Electronic Properties of Phthalocyanines Deposited on H-Si(111)

Dissertation
zur Erlangung des akademischen Grades
doctor rerum naturalium
(Dr. rer. nat.)

vorgelegt
der Fakultät für Naturwissenschaften der Technischen Universität Chemnitz

von M. Sc. Phys. Mihaela Gorgoi

geboren am 27. November 1976 in Zalau

Chemnitz, eingereicht am Dezember 2005

Bibliografische Beschreibung

M.Sc. Phys. Mihaela Gorgoi

Electronic Properties of Phthalocyanines Deposited on H-Si(111)

Technische Universität Chemnitz
Dissertation (in englischer Sprache), 2005

Im Rahmen dieser Arbeit wurden vier Phthalocyanine untersucht: Metallfreies-Phthalocyanin (H_2Pc), Kupferphthalocyanin (CuPc) und Fluor-substituiertes Phthalocyanin (F_4CuPc und $F_{16}CuPc$). Das Ziel dieser Arbeit ist die Charakterisierung der elektronischen und chemischen Eigenschaften der Grenzflächen zwischen diesen Molekülen und Silizium.

Die Moleküle wurden durch organische Molekularstrahldeposition (OMBD) im Ultrahochvakuum auf wasserstoffpassivierte Si(111)-Substrate aufgedampft. Oberflächensensitive Messmethoden wie Photoemissionsspektroskopie (PES), Bremsstrahlung Isochromaten Spektroskopie (BIS oder IPES - Inverse Photoemissionsspektroskopie) und Spektroskopie der Röntgen-Absorptions-Feinstruktur (NEXAFS – Near Edge X-Ray Absorption Fine Structure) wurden zur Charakterisierung eingesetzt. Um eine Zuordnung der verschiedenen Komponenten in PES und IPES zu ermöglichen, wurden Methoden der Dichtefunktionaltheorie zur theoretischen Berechnung eingesetzt.

Die Energieniveauanpassung an der Grenzfläche zwischen der organischen Schicht und der H-Si-Grenzfläche, sowie die Transportbandlücke von H_2Pc, CuPc, F_4CuPc und $F_{16}CuPc$ wurden mit Hilfe von PES und IPES bestimmt.

Die NEXAFS-Messungen ermöglichten eine genaue Bestimmung der Molekülorientierung relativ zum Substrat. Die Auswertung der Daten zeigte unterschiedliche Molekülorientierungen in dünnen und dicken Filmen. Diese Änderungen wurden mit dem bandverbiegungsähnlichen Verlauf der HOMO-und LUMO-Positionen in Verbindung gebracht. Zusätzlich zu diesem Verhalten wiesen die Grenzflächen auch einen Grenzflächendipol auf, welcher durch die unterschiedlichen Austrittsarbeiten der Kontaktmaterialien hervorgerufen wird. Der Einfluss des Grads der Flouridierung wird durch eine ähnlichen Zunahme der Elektronenaffinität (EA), der Austrittsarbeit (ϕ) und der Ionisierungsenergie (IE) bestätigt.

Die elektronischen Eigenschaften von Metall/organische-Schicht-Grenzflächen und von organischen Schichten unter Sauerstoffeinfluss wurden mit Hilfe von PES und IPES untersucht. Die Ag/Pc Grenzflächen zeigten eine Mischung aus HOMO-LUMO-Verschiebungen und Grenzflächendipolbildung. An den Ag/H_2Pc- und Ag/$F_{16}CuPc$- Grenzflächen wurde ein Ladungstransferkomplex gebildet. Auf der CuPc-Schicht physisorbiert das Ag lediglich und im Fall von F_4CuPc wird Ladung zu Ag transferiert, wobei eine andauernde n-Typ-Dotierung an der Grenzfläche erzeugt wird. In Analogie zum Fall der Pc/H-Si Grenzfläche wiesen die Dipole, die hier gefunden wurden, eine lineare Abhängigkeit von EA, ϕ und IE auf und können durch die Differenz zwischen den Austrittsarbeiten vorausgesagt werden.
Das Verhalten der dicken organischen Schichten unter Sauerstoffeinfluss kann in zwei Gruppen eingeteilt werden. Eine Gruppe, bestehend aus H_2Pc und F_4CuPc, wies nur schwache Wechselwirkung auf und der Sauerstoff physisorbiert auf der Pc-Schicht. Die beiden anderen Moleküle, CuPc und $F_{16}CuPc$ konnten einer Gruppe starker Wechselwirkung zugeordnet werden. CuPc bildet einen Ladungstransferkomplex mit Sauerstoff und auf $F_{16}CuPc$ wird eine polarisierte Schicht gebildet.

Schlagwörter:
Phthalocyanin, Organische Moleküle, Organische Molekularstrahldeposition (OMBD), H-Si(111), Ag, Sauerstoff, Grenzfläche, Molekulare Schichten, Photoemissionsspektroskopie (PES), Inverse Photoemission (IPES), NEXAFS.

List of Abbreviations

AFM	Atomic Force Microscopy
BE	Binding energy
BESSY	Berliner Elektronenspeicherring Gesellschaft für Synchrotronstrahlung g.m.b.H.
BIS	Bremstrahlung Isochromat Spektroskopie
CB	Conduction band
CBM	Conduction band minimum
DFT	Density Functional Theory
EA	Electron affinity
ESCA	Electron Spectroscopy for Chemical Analysis
EXAFS	Extended X-Ray Absorption Fine Structure
FWHM	Full Widths at Half Maximum
IE	Ionization Energy
IPES	Inverse Photoemission
HOMO	Highest Occupied Molecular Orbital
LEED	Low Energy Electron Diffraction
LUMO	Lowest Occupied Molecular Orbital
MO	Molecular Orbital
NEXAFS	Near Edge X-Ray Absorption Fine Structure
OMBD	Organic Molecular Beam Deposition
Pc	Phthalocyanine
PES	Photoemission Spectroscopy
PEY	Partial Electron Yield
TEY	Total Electron Yield
UHV	Ultrahigh Vacuum
UPS	Ultraviolet Photoemission Spectroscopy
VBM	Valence Band Maximum
VB-PES	Valence Band Photoemission
VL	Vacuum Level
XAS	X-Ray Absorption Spectroscopy
XPS	X-Ray Photoemission Spectroscopy

Table of Contents

Chapter 1. Introduction

Organic–inorganic structures represent a new class of devices that can combine desirable physical properties characteristic of both organic and inorganic components. Inorganic materials offer the potential for a wide range of electronic properties, substantial mechanical hardness, and thermal stability. Organic molecules, on the other hand, can provide high fluorescence efficiency, large polarizability, mechanical flexibility, ease of processing, structural diversity and lower processing costs. The ability of these materials to transport charges (holes and electrons) due to the π-orbital overlap of neighbouring molecules provides their semiconducting and conducting properties. The self-assembling or ordering of these organic materials enhances this π-orbital overlap and is the key to improvements in carrier mobility. An extensive review of the properties and applications of molecular films displaying semiconducting properties has been published by Forrest [For97]. A couple of directions have been defined such as the development of organic light emitting diodes (OLEDs), organic photovoltaic (OPV) solar cells and organic field-effect transistors (OFETs). In recent years there has been growing interest in the field of OLEDs for their luminous efficiencies [Sha99] and low operating voltages [Bal99]. As an example, ongoing studies of OLEDs [Zho05] prepared by organic vapor phase deposition (OVPD), a method suitable for high volume production of devices, show a quantum efficiency of (7.0±0.1) % at a luminous efficiency of 25 cd/A. This is promising for high-throughput manufacturing of OLED displays.

There has been a tremendous effort to produce white light emission, full colour displays, flexible and transparent devices. Since these aims were achieved, OLEDs are currently brought to market as displays in car radios, mobile phones, mp3 players etc. [Ole04]. The remaining challenge is the fabrication of large area displays.

Simultaneously with the success of OLEDs, interest in organic photovoltaic devices has risen sharply. Therefore quite a large number of studies related to PV solar cells appeared. The photovoltaic effect in molecular materials was first observed in single layers of polyaromatic crystalline materials such as anthracene [Vol13], and phthalocyanine derivatives commonly used as dyes [Sea82]. Pc's close structural relationship to chlorophyll [Mck98], which performs the sunlight harvesting function for the

solar energy conversion process, photosynthesis, gives further encouragement to their use in solar cells. However, new device architectures had to be found to compensate for the poor conversion efficiency and transport properties of these organic layers. In 1986, a breakthrough was realised with Tang's double layer PV cell, based on a perylene derivative, PTCBI, and copper phthalocyanine [Tan86]. It is important to mention that this combination of dyes absorbs up to 70% of the solar spectrum. Nowadays studies have proven that PV solar cells based on organic materials can achieve relatively good efficiencies compared to silicon based ones which reach values of approximately 30%. Xue *et al.* demonstrated that using a structure of an organic tandem PV cell formed by stacking two hybrid planar-mixed heterojunction cells in series based on CuPc and C_{60} can reach power conversion efficiencies of (5.7±0.3)% [Xue04]. Heterostructures containing materials from the perylene class and H_2Pc were also investigated for solar cell applications [Heu02].

In the light of the present investigations of the organic materials application in PV solar cells, the combination of a silicon substrate and Pc is quite promising. Silicon represents the inorganic semiconductor that is the base of the inorganic solar cells produced nowadays. Although the conversion efficiencies reached using only silicon are quite high (approx 26%), the devices are bound to the predicted theoretical limit of about 30% [Mei04]. One of the most important reasons that limit the efficiency of silicon based solar cell is the range of the absorbed light. Carriers are created when the crystalline silicon absorbs photons with energy similar with its band gap of 1.12 eV. However, the higher energy photons are absorbed through different processes depending on their energy range. By introducing another material, an organic layer which has a larger band gap, a wider absorption range for the PV solar cell is enabled. Thus higher conversion efficiency could be obtained.

In addition to OLEDs and PV solar cells, the semiconducting properties of some organic materials enable promising technologies for organic field-effect transistors (OFETs). The Pc class is one of the investigated groups. For example, CuPc is one of the organic materials intensely studied for such applications due to its large charge carrier mobility [Bao96, Zei05].

Due to the rising interest in the development of organic based devices, the need of clarifying studies on the electronic properties of the organic materials appeared. Improving the performance of such devices demands a detailed understanding of the transport and optical processes that take place in the devices. This is achieved only through a fundamental understanding of the electronic structure of the constituent molecules and the molecular thin film. A typical device consists of organic layers sandwiched between a top

metal contact and an inorganic/organic semiconductor with a back metal contact. In this scheme it is very important to be able to predict the relative energies of the highest occupied molecular orbitals (HOMOs) and lowest unoccupied molecular orbitals (LUMOs) of the organic semiconductors at the interface and surface as they represent the barriers for holes and electrons at the interface. Moreover, the difference between HOMO and LUMO determines the transport gap E_t of the organic material.

In the light of the described application of organic materials, this thesis concentrates on describing the interfaces created between four different phthalocyanine (Pc) materials (H_2Pc, CuPc, F_4CuPc and F_{16}CuPc) and hydrogen passivated silicon (H-Si) as hybrid systems for devices such as PV solar cells.

The thesis is structured as follows. Chapter 2 holds a general description of the electronic properties of molecular semiconductors as well as the properties of the materials investigated here: the Pc materials and silicon. A theoretical background of the employed acquisition techniques is presented in chapter 3 as well as a short description of the data analysis. The following chapter 4 depicts the experimental set-ups and the sample preparation e.g. the substrate treatment and the conditions of organic molecular beam deposition (OMBD). Chapter 5 concentrates on determining the electronic properties of Pc/H-Si interfaces correlated with the average molecular orientation in thin and thick layers of Pc. The reactivity of the Pc materials is evaluated in contact with silver and molecular oxygen in chapter 6. Concluding remarks are given in chapter 7.

Chapter 2. Theoretical Background

In the following chapter several basic notions of organic and inorganic semiconductors will be discussed. The organic materials, namely phthalocyanines, involved in this work will be presented, as well as the inorganic substrate – silicon.

2.1 Molecular semiconductors

In contrast to the covalent bonding in inorganic materials, the forces within organic solids are relatively weak. The molecules that compose an organic solid interact via Van der Waals forces and π-π overlapping [Atk94]. The molecules themselves consist of atoms held together by covalent bonds. The atoms are mainly carbon, nitrogen, oxygen and hydrogen. The overlap between the atomic orbitals of the molecule bonding atoms creates bonds which exhibit two types of symmetry: localised σ bonds and delocalised π bonds. Single bonds exhibit σ symmetry while double bonds exhibit one set of σ symmetry and one set of π symmetry.

Molecular semiconductors are a class of organic solids that are generally regarded as materials with poor electrical conductivity [Sim85]. They intrinsically contain few carriers and exhibit poor overlap between orbitals of neighbouring molecules therefore charge cannot pass rapidly from molecule to molecule. Conduction occurs via tunnelling and hopping between molecular sites.

Unfortunately up to now, no complete analytic model was found to describe the behaviour of molecular semiconductors in electric measurements correlated with their electronic structure. One of the most suitable ways in investigating this correlation is studying their interfaces with different inorganic materials using methods that characterize their electronic properties. Such techniques are e. g. photoemission and inverse photoemission. They allow the description of the density of occupied and unoccupied states hence the electronic properties.

2.1.1 Electronic Structure

The electronic properties of the molecular semiconductors are determined by the atomic structure of the molecule and the molecule-molecule interaction. The formation of electronic levels in a single molecule and in a molecular solid is displayed in Figure 2.1 [Ish99]. In the case a), the molecular orbitals are formed by combining the atomic orbitals of all the atoms contained in a molecule. Therefore as the number of atoms comprised in a molecule increases, the complexity of the resulting molecular orbitals increases as well. Figure 2.1 a) shows a sketch of the potential well formed by the atomic nuclei and the electrons. The potential wells of the nuclei are merged in the upper part and form a broad well. The deep atomic orbitals (the core levels) are still localized in atomic wells. The upper atomic orbitals interact and form the localized σ and delocalized π molecular orbitals. The topmost part of the well represents the vacuum level (VL). The difference between the highest occupied molecular orbital (HOMO) and VL corresponds to the ionisation energy (IE). The energy separation from the lowest unoccupied molecular orbital (LUMO) to VL stands for the electron affinity (EA).

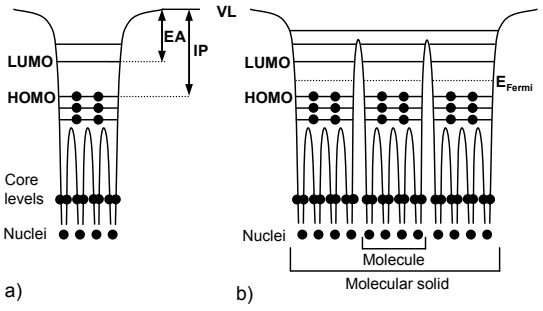

Figure 2.1 Electronic structure of a) a molecule and b) a molecular solid. After Ishii *et al*. [Ish99].

Figure 2.1 b) presents the case of the molecular solid where molecules interact by weak Van der Waals forces. The top part of the occupied valence states and the lower unoccupied states are usually localized in each molecule and have narrow intermolecular bandwidth [Kao81, Gut67]. Thus the electronic structure of an organic solid often preserves that of a molecule and the validity of band theory is limited. The top of the occupied states and the bottom of the unoccupied states are frequently denoted as HOMO and LUMO, reflecting the correspondence with the molecular state. However, experiments have proven that the energy levels are quite different in molecules and organic solid. Schlettwein *et al*. [Sch94] summarizes the HOMO position of several Pcs in gas phase, solution and solid state. The displayed values are different from state to state. The explanation lies in the physics of charged excitation and transport in organic molecular solids, which is dominated by localization and polarization phenomena. Because of the low dielectric constant of organic materials, the electronic polarization has a significant impact on the energy level

of the transport states (HOMO and LUMO). The energy contribution due to polarization can be as large as 1 eV [Hil00]. Several phenomena contribute to polarization and reorganization of molecular levels upon addition or removal of a charged particle: (1) electronic polarization of the surrounding molecules, which accounts for most of the screening of the central charge, (2) molecular relaxation, which accounts for conformational changes of the molecular ion due to the charge, (3) lattice relaxation, which accounts for the response of the structure of the molecular film to the presence of the charge. The molecular relaxation (~100 meV) and the lattice relaxation (~10 meV) are small compared to the electronic polarization component (~1 eV).

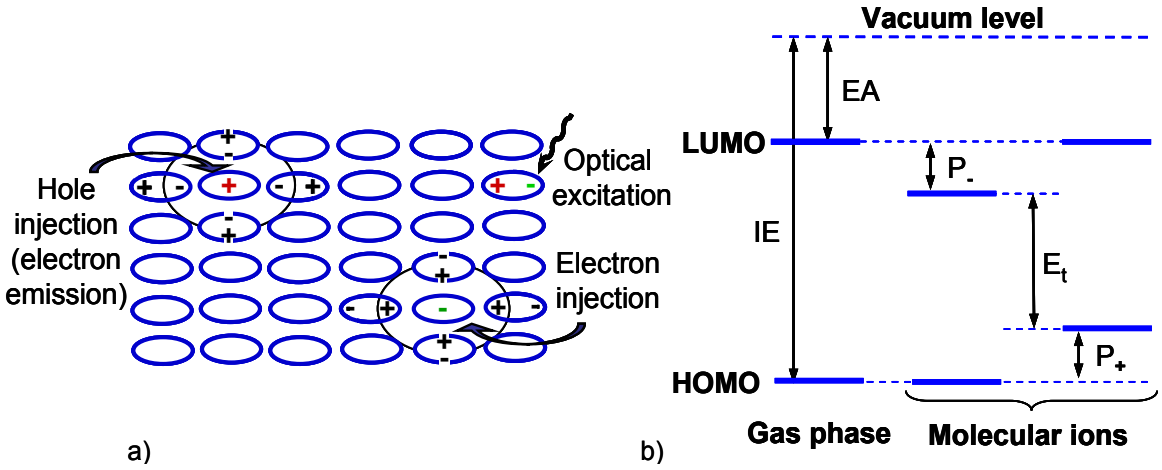

Figure 2.2 a) A molecular solid which suffers ionisation by hole injection (photoemission process) and electron injection (inverse photoemission process); b) ionisation energy (IE) and electron affinity (EA) of the gas phase and the levels of the relaxed molecular ions in the condensed phase, including the polarization energies P_+ and P_- for holes and electrons, respectively.

Similar to inorganic semiconductors, the transport gap E_t, or single-particle gap, of the molecular film is the energy difference between the electron transport state and the hole transport state, and is the minimum energy necessary to create an uncorrelated electron-hole pair infinitely separated in the bulk of the material. As shown it is equal to the difference between the ionisation energy (IE) and the electron affinity (EA) of the gas phase molecule reduced by the sum P of the energies of electronic polarization and molecular lattice relaxation. The IE value in a condensed phase is different from that of an isolated molecule due to the multielectronic effects. When a charge carrier is brought into molecular solid, its field polarizes the surrounding molecules (Figure 2.2 (a)). A secondary polarization field created by polarized molecules contribute to the total self-consistent polarization clouds that surround each charged particle. Formation of these polarization clouds is associated with the stabilization energy P_+ for cations and P_- for anions (Figure 2.2 (b)). The relation between the transport gap E_t and $P= P_+ + P_-$ is given by:

$$E_t = IE - EA - (P_+ + P_-) = \underbrace{(IE - P_+)}_{IE_{condensed\,phase}} - \underbrace{(EA + P_-)}_{EA_{condensed\,phase}} \qquad \text{Eq. 2.1}$$

Since Coulomb interactions are long-ranged, polarization clouds can extend over many lattice constants and P, and hence E_t, can be significantly different at a free surface, near a metal-organic interface, in thin organic layers and in the bulk [Tsi01].

The optical gap (E_{opt}) corresponds to the formation of a Frenkel exciton with the electron and hole on the same molecule. The difference between E_t and E_{opt} yields the binding energy of the exciton [Hil00].

2.1.2 Phthalocyanines

In this thesis, four molecules were studied, namely metal-free phthalocyanine (H_2Pc), copper phthalocyanine (CuPc) and differently fluorinated copper phthalocyanines (F_4CuPc and $F_{16}CuPc$) (Figure 2.3 (a), (b), (c) (d)).

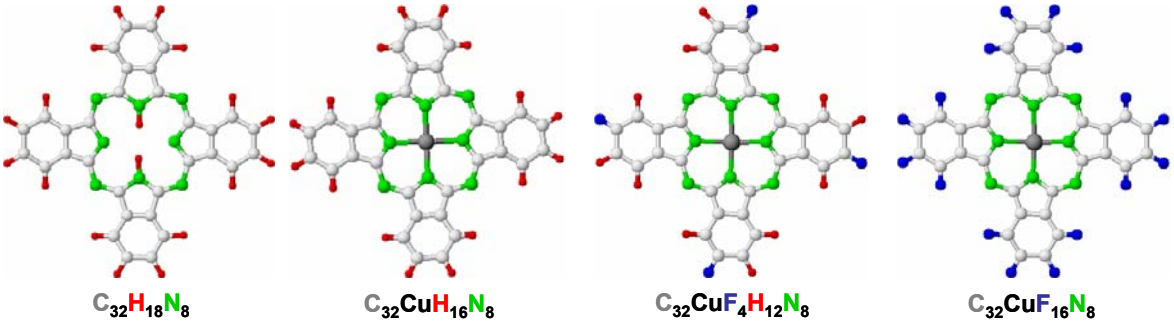

Figure 2.3 a) Metal free phthalocyanine, b) copper phthalocyanine c) and d) fluorinated copper phthalocyanines.

Phthalocyanines are a broad class of molecules which share a common large polyaromatic ring (abbreviated Pc for the phthalocyanato anion $C_{32}H_{16}N_8^{2-}$). Since their discovery by Linstead in 1934 [Lin34], phthalocyanines have been used in applications as diverse as in artist paint, as an ordinary printing dye in colour printing devices and in manufacture of recordable CD's. There is an ongoing research to make use of Pcs in gas sensors [Wri89, Sno89], optoelectronics [Tan86], organic field effect transistors [Tak02] and photodynamic treatment of cancer [Bon95, Coo95]. Their popularity is proven by an overwhelming number of articles and books see e.g. [Mck98, Lez89, Mos83].

Pcs are organometallic complexes that have intense colour, are stable at temperatures up to a few hundreds degrees Celsius and exhibit a high chemical stability (resistance to

chemicals). The central cavity of the Pc ring can accommodate as many as 70 different elemental ions [Mck98], complex oxides such as TiO or VO or hydrogen for the metal-free variety. The geometry of the molecule is planar for small metal phthalocyanines (MPc) and H_2Pc, but a pyramidal configuration is obtained when the ions are too large to be accommodated in the central cavity, as is the case for PbPc, VOPc, etc.

The weakness of the π-π interactions within organic Pc crystals results in a variety of polymorphic forms. Planar phthalocyanines (H_2Pc and MPcs where M = Co^{2+}, Cu^{2+}, Mn^{2+}, Zn^{2+}, Fe^{2+}) are isomorphic and adopt similar polymorphic forms. The major polymorphs are α, β and X-Pcs, but up to 10 crystal species have been identified in literature [Lez89].

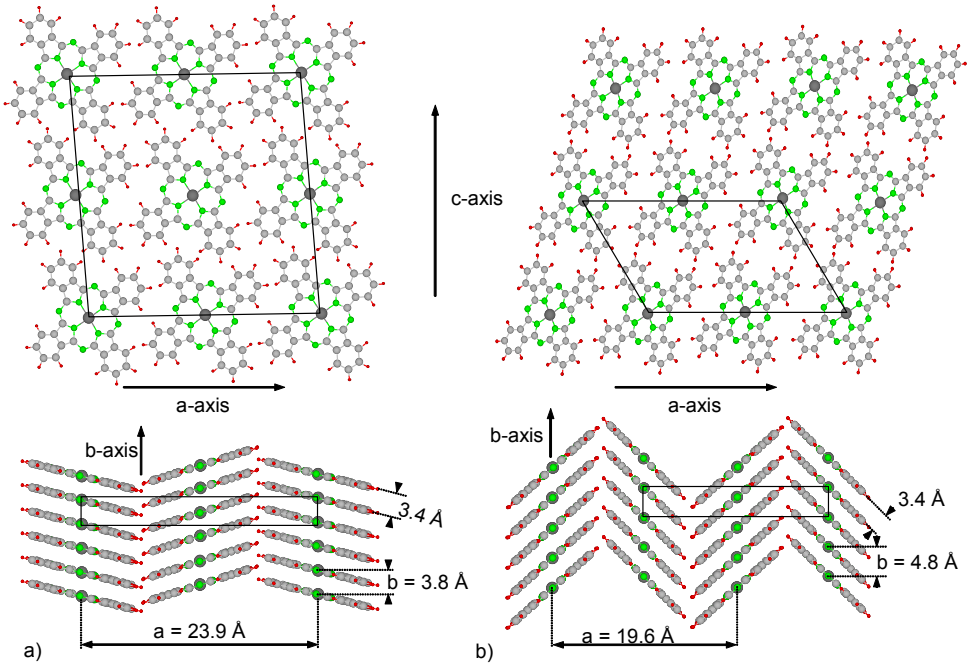

Figure 2.4 Crystal structures of MPc and H_2Pc a) α form, b) β form.

Both the α and β crystallites adopt a herringbone structure in the monoclinic system, where the molecules are stacked along the b-axis (Figure 2.4), while the φ angle between the molecular plane and the stacking axis is different for both forms. The α form crystallises in the C2/c space group [Jan92] while the β form belongs to the P21/a space group [Rob36] and the corresponding φ values are 25° and 45 - 46°, respectively. The unit cell of α form contains four molecules and has the following cell parameters: a=23.9Å, b=3.8Å and c=25.9Å. On the other hand, the β form unit cell contains two molecules and the cell parameters are: a=19.6Å, b=4.8 Å and c=14.6 Å. The α form is metastable and can be obtained as small crystallites by the acid-paste method, precipitation or mechanical grinding [Erc67]. The β form is commercially available and is

the thermodynamically stable phase of MPc; it can usually be obtained by annealing the metastable α form [Sim85].

2.1.2.1 Pc Thin Films

Vacuum deposited thin Pc films were investigated on a large number of different substrates e.g. metals and semiconductors. In the present work, planar Pcs deposited on hydrogen passivated silicon are studied. The UHV deposition usually leads to small spherical crystallites of the α form. The orientation of these crystallites depends on two factors: (i) the nature of the substrate and (ii) the thickness of the film. If there is negligible interaction between the Pc and the substrate, the crystallites adopt a "parallel b-axis configuration" shown in Figure 2.5 (a). This was proven by glancing angle XRD, showing a repeat distance equal to the width of a Pc molecule [Dog92, Has92], and by spectroscopic methods [Kol97, Dow91]. The same configuration was found for CuPc deposited on relatively rough H-Si(111) and H-Si(001) [Nak01]. In thicker films (>1 μm) of H_2Pc [Nes94] and CuPc [Has92], the b-axis is perpendicular to the substrate (Figure 2.5 (b)). Interaction with the substrate can modify the orientation of the phthalocyanine crystallites.

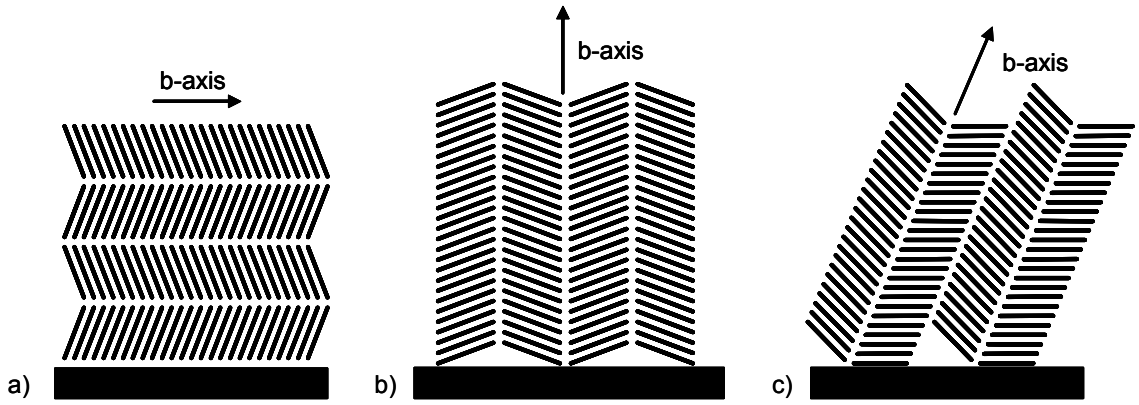

Figure 2.5 Different orientations of α-form a) parallel, b) perpendicular and c) standing b-axis configuration.

Early work by Ashida *et al*. showed that CuPc tends to lie flat when deposited at room temperature on KCl, due to electrostatic forces between K^+ and the electron-rich bridging nitrogens [Ash66]. Although the crystals are still of the α form, they adopt a standing b-axis orientation in that case, where the b-axis is tilted by 26° with respect to the substrate (Figure 2.5 (c)).

Even though it was assumed that Pcs have a tendency to adopt the presented crystalline structures, a recent STM investigation of CuPc on Si (111) revealed that while the lattice parameters of the α-phase are retained the molecules adopt a "slipped-stack" order, i.e. the molecules in adjacent columns have an identical orientation, rather than a herringbone structure (see Figure 2.6 (a)) [Hie00]. On the other hand, one of the chlorinated derivatives of CuPc, namely $CuPcCl_{16}$ was found to lie flat on KCl and graphite [Iri97, Uye72]. The stacks are identical in orientation and the b-axis is in a standing configuration (Figure 2.6 (b)).

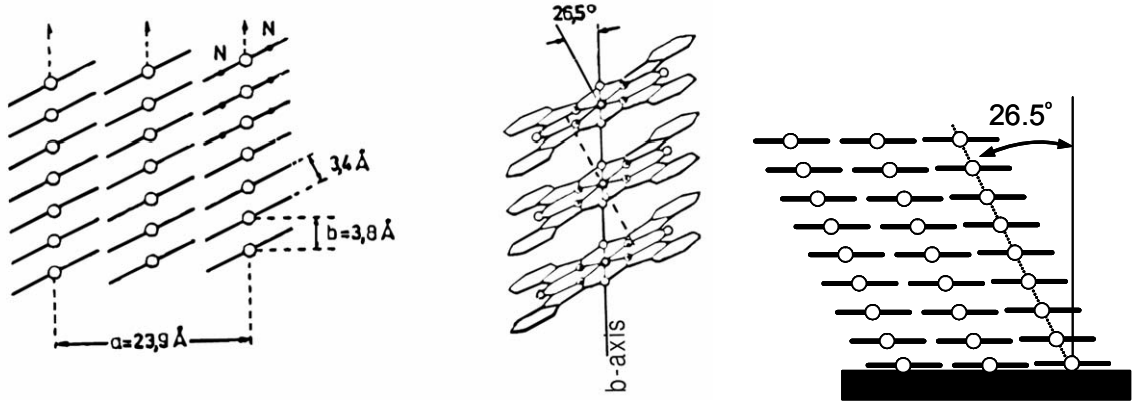

a) b)

Figure 2.6 a) CuPc orientation taken from [Hie00]; b) $CuPcCl_{16}$ orientation as determined in [Iri97].

2.1.2.2 Pc Energy Band Structure

Early studies show calculations of the energy band structure of a few metal Pcs using principally extended Hückel methods [Sin77, Suk69, Mat71, Dev68]. As would be expected from the molecular structure (Figure 2.4), the size of the interaction between the constituent molecules, as measured by the exchange integral, is larger along the b axis (along the stack) than along the other two axes. For example, the energy band structure of H_2Pc has been calculated within the tight binding approximation using Hückel-type molecular orbitals [Che69]. The HOMO belongs to the a_u representation. This labelling is similar to the s-p notation of the atomic orbitals and is based on their symmetry properties. On the other hand, the unoccupied states have several levels in the same energy range and the interaction between bands of the same symmetry must be considered. The lowest empty orbitals b_{2g}^* and b_{3g}^* are separated by only 0.09 eV. Consequently there will be significant mixing of the two levels in the solid state. The bandwidths for H_2Pc were also calculated and they are strongly dependent upon the

direction considered. The reference directions are the three directions of the reciprocal lattice a^*, b^*, c^* in **k** space. The bandwidths are varying from a few meV for directions parallel to a^* and c^* axes, to 30-100 meV along the b^* axis.

The energy band calculations for the other metal Pcs reveal similar assignments as found for H_2Pc. Due to the progress in the theoretical approaches, more advanced studies on Pcs electronic structure appeared. Most of them are based on density functional theory (DFT) methods which provide a more accurate description of the energy levels of the molecules. The calculated energy positions are in better agreement with the experimental data provided by photoemission and inverse photoemission.

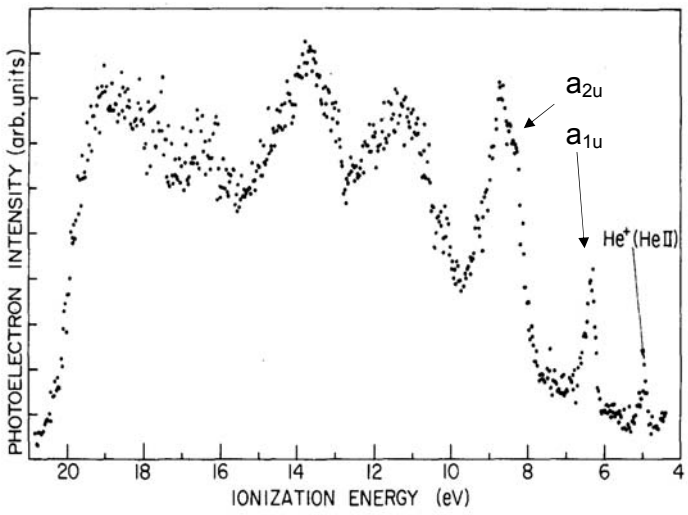

Figure 2.7 Photoemission spectrum of gaseous CuPc (taken from ref. [Ber79]).

The experimental studies on Pc electronic structure started at an early point in time due to the fast development of photoemission and almost simultaneous to the theoretical calculations. In Figure 2.7 we give as an example the photoemission spectrum of gaseous CuPc taken from ref. [Ber79]. The first two peaks are assigned to a_{1u} and a_{2u} symmetries, the first one arising from the carbon rings and the second having some nitrogen character [Ber79]. Quite a high amount of studies followed investigating the occupied states of Pc's. Due to the more recent development of inverse photoemission the unoccupied states were also investigated [Yos01, Gao01]. However, the peak assignments are not yet clearly stated. By comparison with the theoretical calculations one may assign the first peak as mainly arising from the carbon rings.

2.2 Silicon

In the present work, hydrogen passivated silicon (111) was used as substrate. The passivation was obtained by wet chemical etching in hydrofluoric acid solution. The details of preparation will be presented later on, in chapter 4. In the following paragraph some details about silicon and the hydrogen passivated silicon surface will be given.

Silicon is the predominant semiconductor material used in the microelectronics industry, mostly due to several important properties. Silicon can be produced in single crystal form with an extreme purity, it forms an excellent surface oxide and its electronic properties can be tuned through doping. Silicon is a covalent solid that crystallizes in a diamond cubic lattice structure. At the surface, silicon is reactive due to the dangling bonds that remain upon truncating the bulk. Due to these dangling bonds the surface reconstructs, minimizing its energy. The resulting surface structure differs significantly from the bulk. For example, the (111) surface reconstructs into a complex (7x7) structure that contains 49 surface atoms in the new surface unit cell. After reconstruction the resulting surface is highly reactive and thus not stable in air. Therefore any experiments involving such a surface are performed in ultra high vacuum (UHV) conditions. To render it stable in air, the silicon surface can be covered with hydrogen. Several recipes have been developed to terminate the silicon surface with silicon hydride groups (Si-H) [Wel02]. Most of them involve exposure to dilute, aqueous hydrofluoric acid solutions. Most of these recipes are patented and world-wide spread, from research laboratories to large-scale microfabrication facilities.

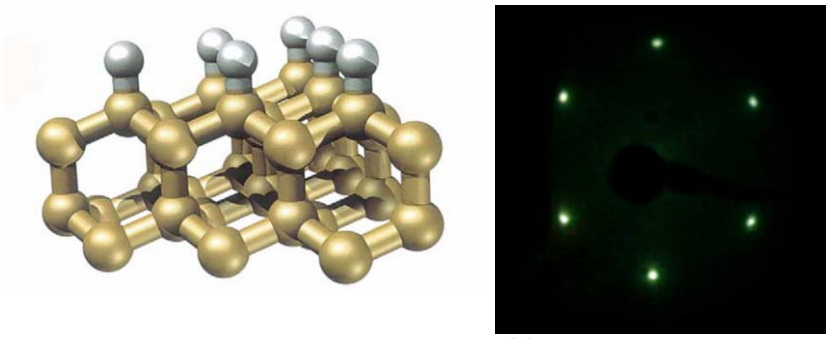

a) b)

Figure 2.8 a) The H-Si(111) surface structure. The golden spheres represent the silicon atoms and the white ones the hydrogen atoms. Reproduced after [Ben02]; b) LEED pattern of H-Si(111)-1x1 obtained at 45 eV.

The presence of hydrogen atop of silicon passivates the surface and changes the surface reconstruction. The silicon atoms terminated with hydrogen do not reconstruct, therefore the surface silicon atoms preserve their bulk like periodicity. In Figure 2.8 (a) the structure of the hydrogen terminated silicon (111) surface (H-Si(111)-1x1) is shown. The low energy electron diffraction (LEED) pattern presented in Figure 2.8 (b) confirms the 1x1 reconstruction of the surface.

Due to its low reactivity, the H-Si surface is preferred for organic molecular beam deposition (OMBD) since it favours ordered arrangement of the organic molecules.

2.2.1 Electronic Structure

The silicon electronic structure has been thoroughly investigated up to now by both theoretical and experimental methods. Figure 2.9 displays the band structure of silicon [Car66]. As shown, the silicon band gap is an indirect one (Γ→X direction), the maximum of the valance band being on the Γ point and the minimum of the conduction band being on the X point.

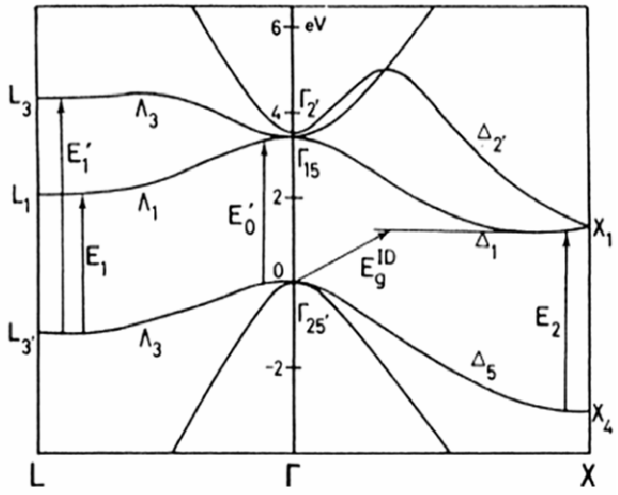

Figure 2.9 Silicon band structure.

The value of the transport gap E_g^{ID} is 1.12 eV. The other interband critical points are observed at the following energy positions: E_0' and E_1 at approximately 3.4 eV, E_2 at about 4.2 eV and E_1' at 5.2 eV.

The electronic structure of the (111) surface of silicon is also well known [Cir75, Sch78]. Moreover, hydrogen chemisorption on this surface has also been systematically investigated [App76, Ho77, Ben02].

The hydrogen passivation by wet chemical treatment raised some difficulties in obtaining a surface equivalent to the one acquired by UHV chemisorption of atomic hydrogen on a silicon (7x7) reconstructed surface. Nevertheless the obstacles were overcome and studies investigated not only the flatness and cleanliness of the surface but also its electronic properties [Bou92, He96].

Chapter 3. Techniques of Investigation

Several acquisition techniques have been employed in the investigation of the Pc systems described in this work. The theoretical background of each method is described, with emphasis on the processing of the experimental data.

3.1 Photoemission Spectroscopy

Photoemission is based on the photoelectric effect, being one of the most used experimental techniques for gaining information on the electronic structure of materials. The sample is irradiated by photons (ideally highly monochromatic) and the emitted electrons are analyzed with respect to their kinetic energy (and to their direction of propagation in angular resolved photoemission).

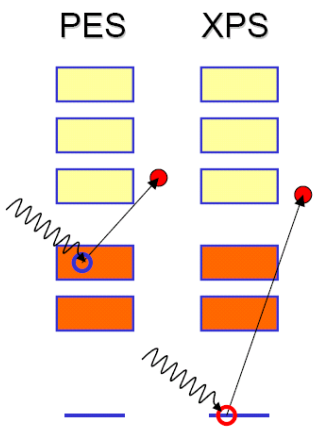

Figure 3.1 Sketch of the photoemission process. Blue - core level, orange - valence band, yellow - conduction band.

A simple sketch of the phenomenon is displayed by Figure 3.1. When photons in the ultraviolet spectral range are used, the technique is called UV photoelectron spectroscopy (UPS). When X-rays are used for excitation, the technique is called X-ray photoelectron spectroscopy (XPS) or ESCA (Electron Spectroscopy for Chemical Analysis). Nowadays, the availability of synchrotron radiation allows the use of a wide spectral range of excitation energies that is why in the present work the valence band photoemission (VB-PES) and core level photoemission (CL-PES) terminology will be used.

In photoemission experiments on solids, only electrons originating from a thin surface layer of the sample are normally used in the analysis of the spectra, which makes photoemission a surface sensitive technique. The reason is that only the electrons which leave the sample without loosing energy are directly carrying information about the electronic structure. The probability for an electron to leave the sample without inelastic

scattering is proportional with the mean free path or electron escape depth. The electron escape depth is a function of the electron kinetic energy, being only in the order of a few nm [Car96]. The large number of electrons which undergo inelastic scattering processes form the secondary electron background in a photoemission spectrum.

In a PES experiment, the photocurrent results from the excitation of electrons by the electromagnetic field from the initial state i (with wave function Ψ_i) to the final state f (with wave function Ψ_f). Considering H_0 the Hamiltonian of the solid in the ground state and the ionizing radiation field as a perturbation H_{int}, the transition probability per unit time is given by Fermi's Golden Rule

$$w_{fi} = \frac{2\pi}{h}\left|\left\langle \Psi_f \left| H_{int} \right| \Psi_i \right\rangle\right|^2 \delta\left(E_f - E_i - \hbar\omega\right) \qquad \text{Eq. 3.1}$$

The Hamiltonian for the interaction between an electron and electromagnetic radiation with a vector potential **A** can be written as:

$$H_{int} = \frac{1}{2mc}\left(\mathbf{A}\cdot\mathbf{p} + \mathbf{p}\cdot\mathbf{A}\right) \qquad \text{Eq. 3.2}$$

where **p** is the momentum of the electron. The vector potential **A** is perpendicular to the propagation direction of the photons. Also it is assumed that the vector potential is not modified by the interaction with the medium into which it penetrates in order to produce the photoemission current. With the explicit **k** – dependence expression 3.1 becomes:

$$w_{fi} = \frac{2\pi}{\hbar}\left|\left\langle \Psi_f, \mathbf{k}_f \left| H_{int} \right| \Psi_i, \mathbf{k}_i \right\rangle\right|^2 \delta(E_f - E_i - \hbar\omega) \qquad \text{Eq. 3.3}$$

Equation 3.3 leads to an expression for the photocurrent. Assuming that the matrix element and the densities of states are constant at fixed $\hbar\omega$ one obtains:

$$\begin{aligned} N(E,\hbar\omega) &\propto \left|\left\langle \Psi_f, \mathbf{k}_f \left| H_{int} \right| \Psi_i, \mathbf{k}_i \right\rangle\right|^2 \sum_i \delta(E_f - E_i - \hbar\omega)\delta(E - E_f + \phi) \\ &\propto \left|\left\langle \Psi_f, \mathbf{k}_f \left| H_{int} \right| \Psi_i, \mathbf{k}_i \right\rangle\right|^2 DOS(E_i)\delta(E - E_f + \phi) \end{aligned} \qquad \text{Eq. 3.4}$$

where ϕ is the work function of the sample. This equation reveals that the distribution of photoemitted electrons in the PES experiment is approximately proportional to the density of initial states $DOS(E_i)$. Also this relation shows a dependence on the various angular momenta of the involved electrons.

For the interpretation of the photoemission process, the so-called 'three-step model' [Bes64] was proven to be useful [Lut93, Huf95]. In this model the photoemission process is separated into three incoherent steps. In a first step the photon is absorbed and the excitation of the electron takes place. In a second step this electron passes through the sample to the surface. In the third step the electron escapes through the

surface into vacuum. A more rigorous theoretical approach to the photoemission process is given by the 'one-step model' [Mah70]. This model considers the excitation from an initial state (Bloch wave in the crystal) into a damped final state near the surface. This damping takes into account the short mean free path of the electrons in the solid. In most of the theoretical treatments of photoemission, an infinitely short time for the removal of the photoelectron is assumed, this being referred to as the sudden approximation. The time for the photoemission process depends on the velocity of the escaping electron and therefore the sudden limit is best suited for high excitation energies [Mar95]. With increasing electron energy the mean free path increases and the electrons come from increasingly larger distances from the surface. Thus the sudden approximation should always be corrected for extrinsic losses [Hed98]. In the case of an interacting N-electron system, the sudden approximation assumes that the photoelectron is decoupled from the (N-1)-electron state and therefore doesn't carry information about it [Kev01].

The absorption of a photon with energy $\hbar\omega$ causes the excitation of an N-electron system which is described by the initial state wave function $\Psi_i(N)$ with energy $E_i(N)$ into a final state ion characterized by $\Psi_f(N\text{-}1,k)$ with $E_f(N\text{-}1,k)$, plus a photoelectron with kinetic energy E_{kin}; k denotes the initial level from which the electron was removed. Thus the conservation of energy is described by

$$E_k = eV_0 + \phi_{cath} - \phi_{sample} \qquad \text{Eq. 3.5}$$

and the binding energy with respect to the vacuum level is expressed as

$$E_B^V(k) = E_f(N-1,k) - E_i(N) \qquad \text{Eq. 3.6}$$

If it is assumed that the remaining (N-1) electrons have the same spatial distributions and energies in the final state as they had in the initial state before the emission of the electron (frozen-orbital approximation), then the binding energy equals the negative orbital energy of the emitted electron.

$$E_B^V(k)_{K.T.} = -\varepsilon_k \qquad \text{Eq. 3.7}$$

This approximation is Koopmans' Theorem [Ert85]. This theorem neglects relaxation of the remaining electrons and also relativistic as well as correlation effects. Hence, in a better description these terms should also be taken into account.

A different approach used in treating the photoemission process is represented by the adiabatic approximation. The adiabatic approximation is approached in the case of threshold ionization of a certain electronic level. Generally this applies for low kinetic energy of photoelectrons. In the adiabatic limit the photoelectron is assumed to leave the system slowly so that the electrons from or near the excited atom change their energy by slowly adjusting to the effective atomic potential in a self-consistent way [Stö83]. Thus, at

any moment, the system is in a state of equilibrium. The correlation between the photoemitted electron and remaining inner electrons is very strong in the case of an adiabatic transition [Tho84].

Further details on the theoretical approaches to photoemission can be found in several dedicated books [Huf95, Sch03].

For a better understanding of the experiment of photoemission let us consider Figure 3.2 which shows schematically how the energy-level diagram and the energy distribution of photoemitted electrons relate to each other. Electrons emitted from the valence band can be found at binding energies of several eV while those from core levels contribute between 10 ~ 1500 eV. In the case of a metal, E_F is in the conduction band (half filled) and has a separation ϕ (work function) from VL. At the low energy end of the spectrum a sharp feature is observed, which originates from emission of electrons that have been inelastically scattered in the solid and no longer contain any specific structural or chemical information. On this background core level lines can be seen. Not shown are the Auger lines which also appear. Because ϕ of solids are usually in the range of a few eV, photons in the ultraviolet and X-ray energy range are necessary for PES experiments.

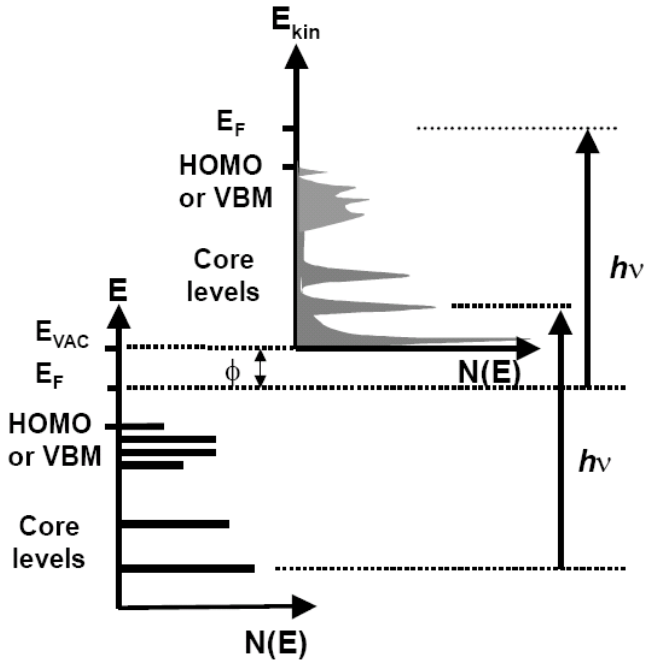

Figure 3.2 Schematic energy level diagram and energy distribution of photoemitted electrons.

Besides the energy levels that can be determined through a photoemission experiment, there are two other parameters that come into play in the evaluation of the data. The first one is the intensity of the peaks in a photoemission spectrum. This intensity depends on the surface density of the corresponding element, the different photoionisation cross-

sections for electrons from various molecular orbitals, the mean free path of the electrons in the sample and spectrometer transmission function. The second parameter is the full width half maximum (FWHM) of the peaks. The FWHM has its origin in intermolecular energy-band dispersion, hole-vibration/phonon coupling, lifetime broadening and dynamic polarisation, and site dependence of the relaxation energy and molecule/substrate interaction. Although the evolution of these parameters may present valuable information due to their origins, one has to be careful when evaluating them.

3.2 Inverse Photoemission Spectroscopy

Unlike photoemission spectroscopy, inverse photoemission spectroscopy (IPES) has a much shorter history. It actually started with the work of the two major promoters of this method Dose [Dos77, Den79] who developed the experimental set-up and Pendry [Pen80, Pen81] who initiated the theoretical work.

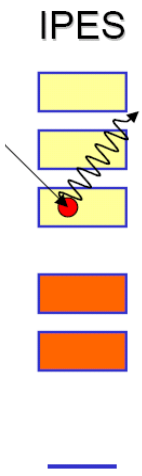

Figure 3.3 Sketch of the inverse photoemission process.

IPES uses the effect that electrons impinging on a solid surface may emit radiation. A sketch of the phenomenon is shown in Figure 3.3. The recorded radiation is in the range of ultraviolet light and the electrons have kinetic energies below 20 eV. Since the energy dependent elastic mean-free path of low-energy electrons is about 10 to 20 Å [Sea79], IPES is very surface sensitive.

IPES gives access to the empty electronic states in the energy region above the Fermi level. An electron with well-defined kinetic energy E_{kin} and well-defined angle of incidence θ impinges on the sample and couples to states in the solid, which are lying above the vacuum level E_{vac} of the sample. From this initial state with energy E_i and wave vector $\mathbf{k}_i$ the electron decays radiatively to lower lying unoccupied electronic final states with energy E_f and wave vector $\mathbf{k}_f$. In the IPES experiment the emitted photons with quantum energy $\hbar\omega$ are detected for a photon take-off angle α. For this process the conservation of energy is

$$E_i = E_f + \hbar\omega \qquad \text{Eq. 3.8}$$

and the momentum conservation is

$$\mathbf{k}_i = \mathbf{k}_f + \mathbf{G} + \mathbf{q} \qquad \text{Eq. 3.9}$$

where **G** – is a reciprocal lattice vector. For photon energies below 100 eV the wave vector of the photon **q** remains small compared to the size of the Brillouin zone, so **G** and **q** can be neglected in Eq. 3.9. Therefore the radiative transition occurs vertically ($\mathbf{k}_i = \mathbf{k}_f$) as a so-called direct transition (Figure 3.4). In an IPES experiment with fixed photon energy $\hbar\omega$ the intensity of the radiation (count rate of the emitted photons) is measured as a function of the final state energy E_f for an angle of incidence θ of the electrons and a photon take-off angle α. In such a spectrum a peak should appear at energies E_f, where a direct transition between two bands separated by $\hbar\omega$ is possible. The natural width of the peaks is determined by the finite lifetime of the final states. A typical spectrum for a metal has its onset at the Fermi level E_F and shows an energy dependent, nearly structureless background, which stems mainly from radiative transitions after electron – hole pair production.

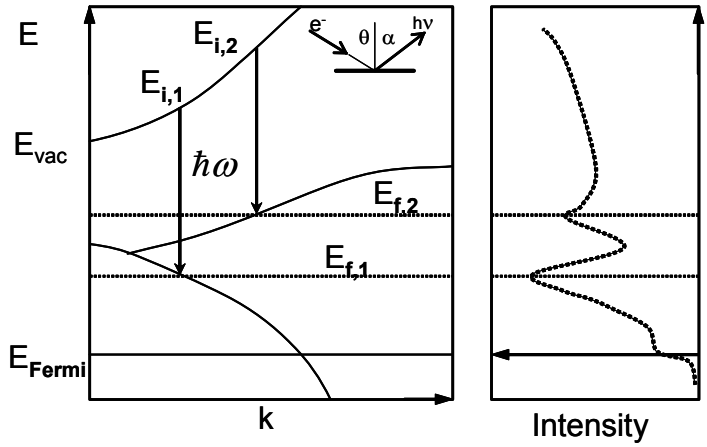

Figure 3.4 IPES process in a metal.

E_F is the Fermi level, below which all states are occupied and above which all states are unoccupied at 0^o K. It should be taken into account that in contrast to the photoemission process, where the initial state is occupied and the final state is unoccupied, the inverse photoemission process involves two initially unoccupied states. Due to a limited number of final states E_f, the count rates are much lower in the case of inverse photoemission spectroscopy than for ultraviolet photoemission spectroscopy.

IPES has two operating modes. The densities of final states are determined either by keeping the energy of photons constant and sweeping the electron energy – the isochromat mode, or by keeping the incident electron energy constant and measuring the photon spectrum – the constant initial state mode.

The experiments presented in this work are performed in the isochromat mode. A more explanatory diagram of the IPES - a specific one for the isochromat mode is presented in Figure 3.5. On the left part and in the middle of the figure the electronic structures for the cathode and for the sample are represented.

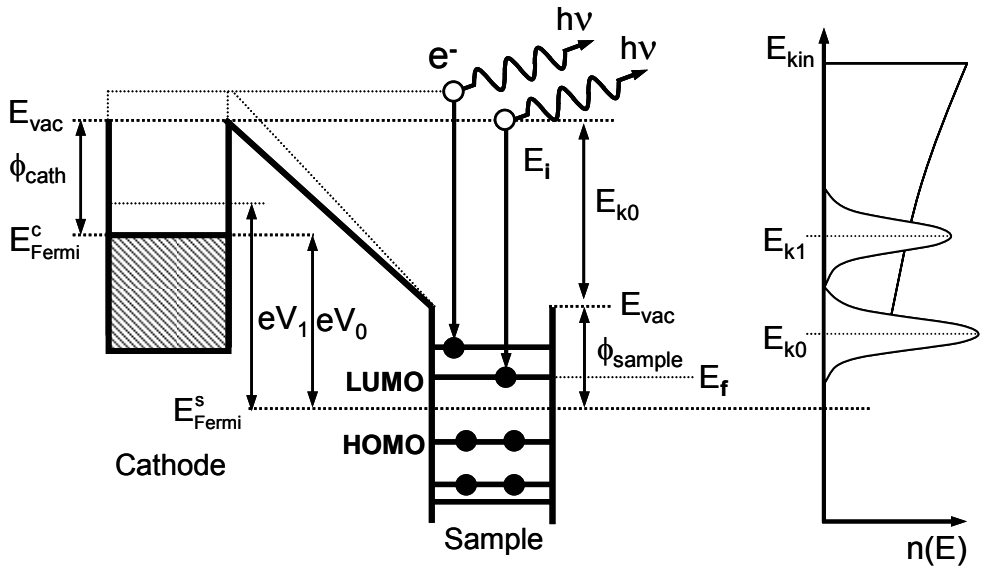

Figure 3.5 Energy diagram for isochromat IPES.

The sample is considered to be an organic semiconductor. ϕ_{cath} and ϕ_{sample} are the work functions of the cathode and of the sample, respectively. In thermal equilibrium the chemical potentials align and therefore the Fermi levels of the sample and the cathode will align. When a voltage V_0 is applied to the cathode, the situation presents itself as shown in Figure 3.4, where the Fermi level of the cathode is displaced upward by an energy eV_0. An electron, which is thermionically emitted from the cathode, is accelerated to the sample, and at the sample it has a kinetic energy

$$E_k = eV_0 + \phi_{cath} - \phi_{sample} \qquad \text{Eq. 3.10}$$

relative to the vacuum level E_{vac}. From the initial state E_i the electron decays to the unoccupied state E_f emitting a photon. E_f in this case is LUMO. The final energy of the electrons becomes:

$$E_f = eV_0 + \phi_{cath} - h\nu \qquad \text{Eq. 3.11}$$

Sweeping the voltage V_0 and recording the resulting photons give rise to an image of the density of unoccupied states between the Fermi and vacuum level, as it is presented in the right-hand side of Figure 3.5. The recorded spectrum shows photon intensity as a function of the kinetic energy of the impinging electrons, hence the peaks corresponding to LUMO and LUMO+1 are placed at E_{k0} and E_{k1}. Thus a certain kinetic energy corresponds to the Fermi level as well. In order to determine the position of the Fermi level, a reference measurement is required, since this level is within the transport gap of the semiconductor sample. The reference measurement is performed on a metal, usually one with unoccupied d levels. A clear shoulder in the photon intensity is expected in the

IPES spectra of metals for the Fermi level [Woo83]. If the starting voltage is set at V_F for the Fermi energy in the above formula, then the following expression is obtained:

$$eV_F = h\nu - \phi_{cath} \qquad \text{Eq. 3.12}$$

and the energy position of the final states with respect to the Fermi level becomes:

$$E_f = eV_0 - eV_F \qquad \text{Eq. 3.13}$$

Based on this equation the densities of final states e.g. LUMO are determined with respect to the Fermi level.

3.2.1 Matrix Elements

For practical and computational reasons, inverse photoemission and photoemission are considered inverse processes in quantum mechanics. By time reversing symmetry, the probability of an incident electron in a solid occupying a state i undergoing a transition to an unoccupied state f and emitting a particular photon is the same as the reversed photoemission process, in which this photon excites the electron from f to i. In each case the current is measured rather than individual states, and this leads to a phase – a space factor between the expressions for the photon flux in inverse photoemission and the electron flux in ultraviolet photoemission, which are also giving the related cross section expressions. Starting with the golden rule (Eq. 3.1), the cross section for the inverse photoemission process is given by

$$\sigma_{ph} \propto \sum_f \left|\langle \Psi_f \left| H_{int} \right| \Psi_i \rangle\right|^2 \qquad \text{Eq. 3.14}$$

where σ_{ph} is the cross section, the sum is taken over all final states, Ψ_f and Ψ_i are the final and initial wave functions, with H_{int} being the interaction Hamiltonian. The transition matrix element:

$$M_{fi} = \left|\langle \Psi_f \left| H_{int} \right| \Psi_i \rangle\right| \qquad \text{Eq. 3.15}$$

is taking into consideration all the possible states after the interaction, representing the weight of any state in a spectrum and is in proportion with the probability of current density linking the final and initial states.

$$M_{fi} = \int \mathbf{A} \cdot J_{fi} d^3r \qquad \text{Eq. 3.16}$$

where **A** is the electromagnetic vector potential and

$$J_{fi} = \frac{1}{2} e(\Psi_f^* \nabla \Psi_i - \Psi_i^* \nabla \Psi_f) \qquad \text{Eq. 3.17}$$

being the probability of current density. The total cross section for the inverse photoemission process is much smaller than the one for ultraviolet photoemission due to the large difference in the total number of final states for the emitted particle in each case. Considering the fact that the cross sections are proportional to the wavelength of the electron and photon for inverse photoemission and for photoemission, respectively, the compared efficiency of these processes can be approximated [Hil97]:

$$\frac{\sigma_{ph}}{\sigma_{el}} \approx \left(\frac{k_{ph}}{k_{el}}\right)^2 = \frac{4\pi^2 E_{ph}^2}{2mc^2 E_{el}^2} \approx 10^{-4} \qquad \text{Eq. 3.18}$$

From an experimental point of view, this value points out that the count rates recorded in the inverse photoemission process are much lower than the ones taken in a photoemission process. In consequence, the detector for IPES must have a high sensitivity.

3.3 VB-PES and IPES Spectra Evaluation

The evaluation of the VB-PES and IPES spectra was performed using the diagram shown in Figure 3.6.

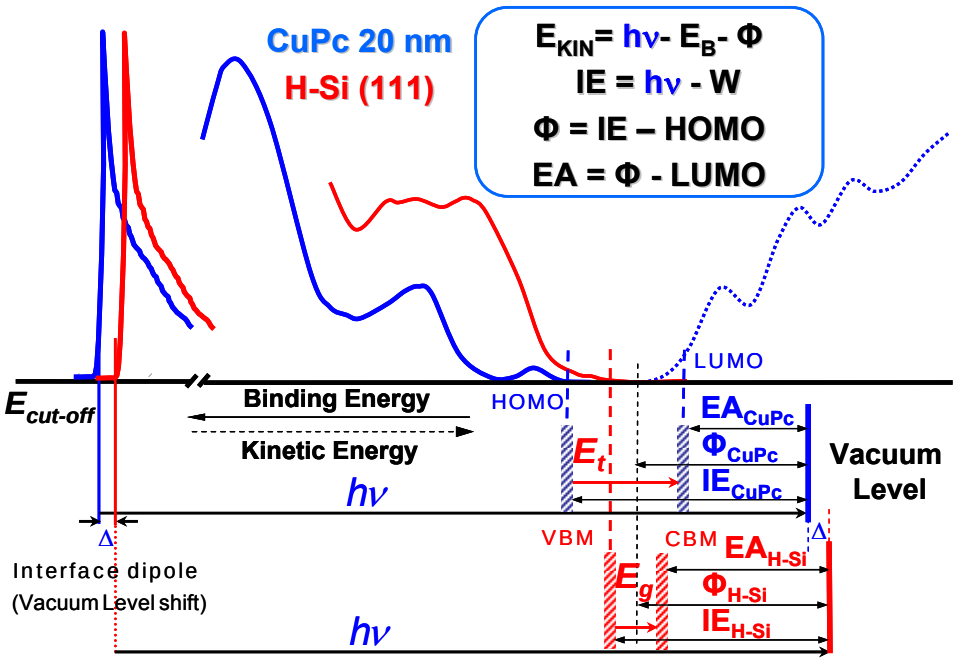

Figure 3.6 Determination of energy band diagram using VB-PES and IPES.

The sketch is based on experimental data recorded for the CuPc/H-Si system. Several electronic properties can be determined for silicon and CuPc. The ionisation energy (IE)

is evaluated by subtracting the width (W) of the PES spectra from the excitation energy of 21.2 eV. Then subtracting the difference between the highest occupied molecular orbital (HOMO) cut-off and the Fermi level position from IE, the work function (Φ) is obtained. The electron affinity (EA) is obtained by deducting from Φ the lowest unoccupied molecular orbital (LUMO) cut-off position after deconvolution measured relative to E_F. Last but not least, the transport gap E_t is evaluated from the HOMO-LUMO cut-offs. In addition, rigid shifts of the secondary electron cut-off positions provide information about interface dipoles between the substrate and the molecular layer.

The IPES spectra require a special treatment due to the poor resolution of the IPES set-up (0.4 eV) which broadens the features extensively. More about the experimental IPES set-up will be described in chapter 4. The treatment of the IPES spectra consists of a deconvolution of the features using a Gaussian function with a full width half maximum (FWHM) of 0.4 eV. A detailed description of the LUMO edge determination for the CuPc case is illustrated in Figure 3.7.

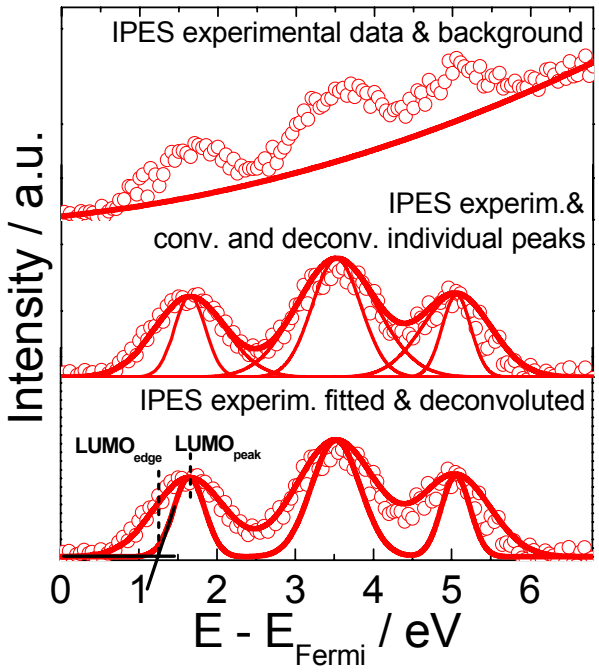

Figure 3.7 The IPES spectrum of CuPc thin film together with convoluted and deconvoluted individual peaks that contribute to the overall intensity.

First the background described by a cubic polynomial function in the IPES spectra (20 nm CuPc deposited onto H-Si(111)) is subtracted. Exponential backgrounds were also investigated. However, the choice of background has a negligible influence on the LUMO energy position. The IPES data were then fitted with Gaussian functions using nonlinear least-squares fitting techniques. The widths of the fitted peaks were then deconvoluted

using a Gaussian function with a FWHM of 0.4 eV accounting for the IPES resolution. Then, the cut-off of the resulting deconvoluted LUMO feature was used in the determination of the transport gap and of the electron affinity.

In the case of the VB-PES spectra no deconvolution was performed since the experimental resolution has a value of 0.15 eV and does not influence to such an extent the recorded features. The FWHM of the peaks in photoemission is much larger than the resolution unlike in IPES where the FWHM of the peaks is in the same range as the experimental resolution.

The evaluation of VB-PES and IPES spectra of the organic/inorganic semiconductor systems requires some introductory remarks about the formation of organic/inorganic interfaces. The most known and documented interfaces are the metal/inorganic semiconductor ones [Mön90] and thus their formation will be shortly described here.

Unfortunately, the metal/organic semiconductor interfaces or organic/inorganic semiconductor interfaces are less detailed. However nowadays, due to the growing interest in the applications of organic semiconductors, there are a large number of articles studying these interfaces. Evidencing different behaviours than the metal/inorganic semiconductor interfaces, the metal/organic semiconductor interfaces created an ongoing debate over their formation.

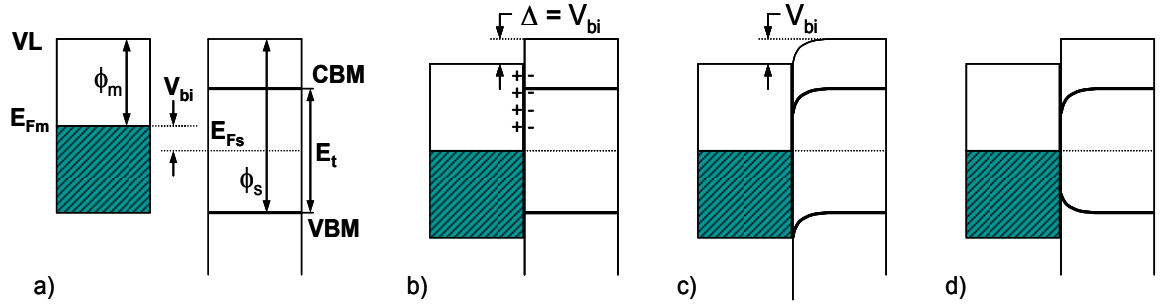

Figure 3.8 Formation of a metal-semiconductor contact. a) the nonequilibrium situation before contact is made. All energies are referred to the vacuum level (VL) b) V_{bi} accommodated over the formation of interface dipole; c) V_{bi} accommodated over band bending; d) same case as b) but including the effect of the image potential (after [Cam03]).

Figure 3.8 summarizes the configurations of the metal-semiconductor contacts. The semiconductor considered here is an intrinsic one. The starting point in the description of the interface between a metal and an inorganic semiconductor [Sze81] is to define the energy difference between the respective Fermi energies of the isolated materials – the built-in potential V_{bi} (Figure 3.8 (a)). When contact is made, equilibrium dictates that charge flows from one material to the other, until the Fermi levels align. There are two extreme cases to consider. The first one shown in Figure 3.8 (b) is the formation of an

interfacial dipole at the interface between the metal and the semiconductor. The second case is the one presented in Figure 3.8 (c) where the transferred charge occupies dopant levels in the bulk. That yields the Schottky-Mott rule [Sze81] which states that the vacuum levels align at the interface, and then the additional charge resides in a depletion region created by ionizing donor or acceptor dopants and causes band bending. In addition, it must be accounted for the image potential [Twa82] that attracts the charges back towards the interface; this case is shown in Figure 3.8 (d).

The difficulty in analysing the experimental data of metal/organic semiconductor interfaces in the light of classic theory (Figure 3.8) occurs from several reasons. One of them is the failure of the Schottky-Mott rule [Ish99, Kah03]. The difference in vacuum levels is attributed to interface dipoles, for which values between 0.2-1 eV were found for several metal-organic interfaces using photoemission spectroscopy. Another reason is the occurrence of a ‘‘band bending’’-like electrostatic energy shift for organic layers which was observed in many metal-organic systems [Hil00-2, Knu04]. In most cases this shift is confined to a regime of only a few nanometres, which cannot be accounted for using the conventional band bending theory of inorganic semiconductors. These issues have been found at the inorganic/organic semiconductor interfaces as well and will be discussed later on for each specific case.

When identifying the cases described in Figure 3.8 (b) (c) and (d), we have to consider Figure 3.6 again. The formation of only an interface dipole (Figure 3.8 (b)) will create in the recorded VB-PES spectra as a function of layer thickness a rigid shift in secondary electron region at the first deposition. No other energy shifts in the HOMO or LUMO position will be present. Thus all the electronic properties that define the deposited material will be constant. However, when a band bending like behaviour is observed as in Figure 3.8 (c), continuous and almost parallel shifts are observed in all VB-PES features: the secondary electron cut-off, the positions of all HOMOs and LUMOs. Consequently the work function will change. The width W of the VB-PES spectra will be constant during the thickness dependent measurements and thus IE will remain constant. EA will be constant as well as the transport gap E_t. In the final case shown in Figure 3.8 (d), due to the effect of the image potential the spectra recorded as a function of thickness will show shifts of the HOMO and LUMO positions towards the Fermi level besides the rigid shift in the secondary electron cut-off. This will result in a variation of the transport gap E_t and of IE and EA. The work function Φ is the only one that remains constant.

3.4 NEXAFS

Near Edge X-Ray Absorption Fine Structure, NEXAFS, spectroscopy refers to the absorption fine structure close to an absorption edge, about 30eV around the actual edge. This region usually shows the largest variations in the X-ray absorption coefficient and is often dominated by intense, narrow resonances [Stö92]. NEXAFS is also called X-Ray Absorption Near Edge Structure, XANES. Today, the term NEXAFS is typically used for soft X-ray absorption spectra and XANES for hard X-ray spectra.

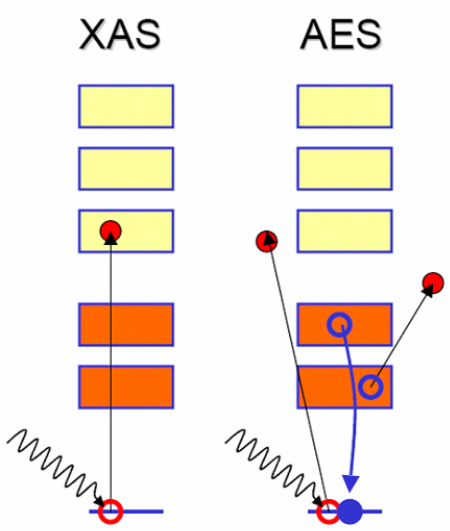

Figure 3.9 X-ray absorption process accompanied by Auger decay.

Opposite to the related X-ray photoemission spectroscopy (XPS or ESCA) technique, where the photon energy is fixed and the electron intensity is measured as a function of electron kinetic energy, in NEXAFS the X-ray energy is scanned and the absorbed X-ray intensity is measured. NEXAFS spectra can be recorded in different ways. The most common methods are transmission and electron yield measurements. The measurements presented here were taken in total electron yield (TEY) detection mode. The absorbed X-ray intensity is not measured directly in TEY measurements, but rather the photoelectrons that are created by the absorbed X-rays. X-rays are absorbed through excitations of core electrons to empty states above Fermi level and the vacuum level (Figure 3.9). The created holes are then filled by Auger decay (dominant in the soft X-ray region over X-ray fluorescence). The intensity of the emitted primary Auger electrons is a direct measure of the X-ray absorption process and is used in so called Auger electron yield (AEY) measurements, which are highly surface sensitive, similar to XPS. As they leave the sample, the primary Auger electrons create scattered secondary electrons which dominate the total electron yield (TEY) intensity.

The TEY cascade involves several scattering events and originates from an average depth, the electron sampling depth L. Electrons created deeper in the sample lose too much energy to overcome the workfunction of the sample and therefore do not contribute to the TEY. The sampling depth L in TEY measurements is typically a few nanometres, while it is often less than 1 nm for AEY measurements.

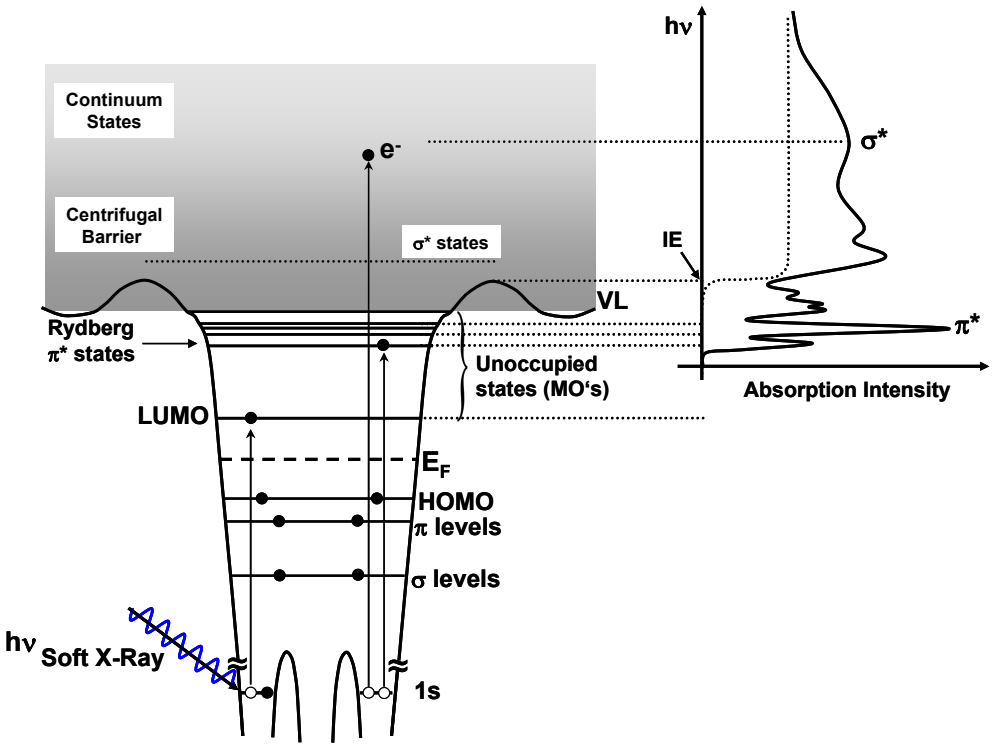

Figure 3.10 Schematic potential of a diatomic molecule that undergoes an absorption process.

The NEXAFS phenomenology is based on the X-ray absorption with the excitation of core electrons into unoccupied atomic/molecular orbitals. Figure 3.10 displays a schematic potential of a diatomic molecule that undergoes an absorption process. The plotted potential assumes positive values at the periphery of the molecule. The barrier is due to an additional centrifugal term $l(l+1)\hbar^2/(2mr^2)$ in the molecular potential which arises when the Schrödinger equation is written in spherical coordinates. The transitions lead to a pronounced fine structure, the so called NEXAFS resonances. A NEXAFS spectrum placed on the right hand side of Figure 3.10 displays a diversity of pronounced resonances which correspond to electronic transitions of a 1s initial state to Rydberg or unfilled final states near VL. At the ionisation energy, corresponding to the threshold for transitions to continuum states a step-like increase in X-ray absorption is expected. The unoccupied molecular orbitals (MO) are marked as σ^* and π^*. For the neutral molecule, the π^* states typically lie above the vacuum level but in this case the π^* states are pulled down by the electron-core hole interaction [Stö92].

Due the localization of the core hole which is created at a certain atom the unoccupied states are projected on this atom. In the soft X-ray regime (K-edges of C, N, O) NEXAFS transitions are governed by dipole selection rules and consequently the absorption cross sections show a polarization dependent angular anisotropy. Consequently, polarization

dependent NEXAFS measurements allow the determination of the orientation of molecular adsorbents.

3.4.1 Molecular Orientation

The NEXAFS resonant intensities show a dependence on the orientation of the electric field vector **E** given by the dipole selection rules. As shown in Figure 3.11 (a), the resonance intensity associated with a specific molecular orbital final state is largest if the **E** vector points in the direction of that molecular orbital. The intensity vanishes if the **E** vector is perpendicular to the direction of the orbital. The spatial orientation of the σ^* and π^* orbitals is presented as well for the benzene molecule. In this case, the atoms are arranged in a plane and thus the σ^* system is characterized by this plane.

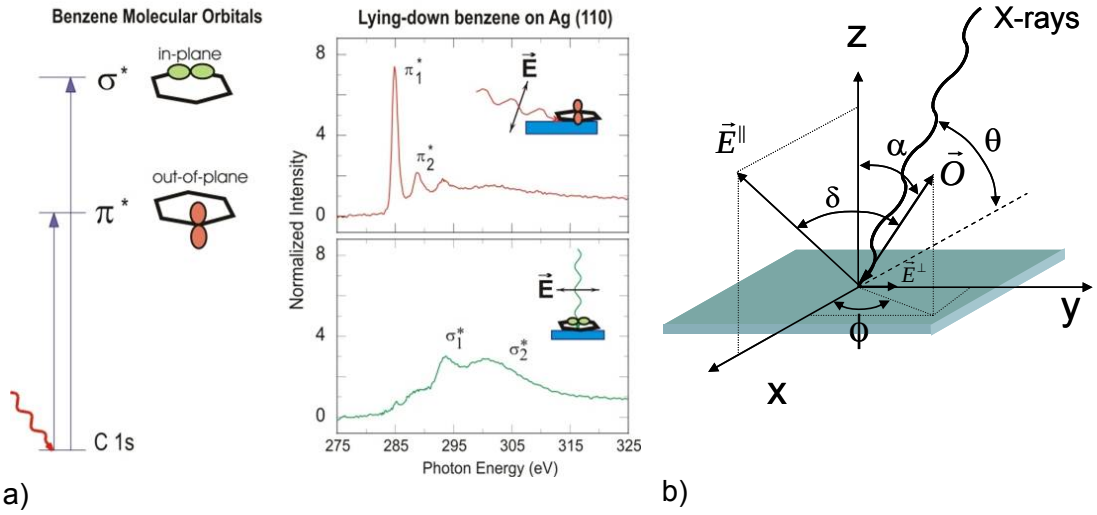

Figure 3.11 a) Polarization dependence on the intensities of σ^* and π^* resonances for benzene lying flat on Ag(110) [Sol91]. b) Coordinate system defining the geometry of π^* orbitals as vectors.

The π^* orbitals can be represented by a vector perpendicular to the plane of the atoms. The mathematical formalism that allows the determination of the molecular orientation is developed for these cases: σ^* orbitals represented by planes and π^* orbitals by vectors.

Since phthalocyanine molecules are planar and thus similar to benzene, the next paragraph will describe the formalism for π^* orbitals as vectors.

The intensity of the resonances I is given by the oscillator strength which is the energy integral of the X-ray absorption cross section σ_x. Considering the angular dependence of specific resonances, it can be assumed that the resonance shape will be constant and only their peak height will change.

As a result the intensity I can be written as

$$I \propto \left|\left\langle f \left| \mathbf{e}\cdot\mathbf{p} \right| i \right\rangle\right|^2 \propto \frac{1}{\left|\mathbf{E}\right|^2}\left|\left\langle f \left| \mathbf{E}\cdot\mathbf{p} \right| i \right\rangle\right|^2 \qquad \text{Eq. 3.19}$$

Where **e** is a unit vector in the direction of the electric field vector **E**, **p** is the momentum operator, $|i\rangle$ is the 1s initial state and $\langle f|$ the molecular orbital final state of transition. For elliptically polarized synchrotron radiation the electric field has two components:

$$\mathbf{E} = \mathbf{E}^{\parallel}\cos(kz - \omega t) + \mathbf{E}^{\perp}\sin(kz - \omega t) \qquad \text{Eq. 3.20}$$

k is the momentum of the X-rays and ω is the frequency of the electromagnetic wave. For expressing the intensity conveniently the degree of linear polarisation P is introduced. P characterises the intensity or energy density of the electromagnetic field in the orbit plane and it has the following expression:

$$P = \frac{\left|\mathbf{E}^{\parallel}\right|^2}{\left|\mathbf{E}^{\parallel}\right|^2 + \left|\mathbf{E}^{\perp}\right|^2} \qquad \text{Eq. 3.21}$$

Then the total resonance intensity is given by

$$I \propto P\left|\left\langle f \left| \mathbf{e}^{\parallel}\cdot\mathbf{p} \right| i \right\rangle\right|^2 + (1-P)\left|\left\langle f \left| \mathbf{e}^{\perp}\cdot\mathbf{p} \right| i \right\rangle\right|^2 \qquad \text{Eq. 3.22}$$

Assuming linearly polarized light, the transition intensity associated with the matrix element of interest can be written as

$$I \propto \left|\mathbf{e}\cdot\left\langle f \left| \mathbf{p} \right| i \right\rangle\right|^2 \qquad \text{Eq. 3.23}$$

For a 1s initial state and a vector final state orbital the matrix element points in the direction of the final state orbital i.e. the direction of maximum orbital amplitude, and thus eq.3.23 becomes

$$\left|\mathbf{e}\cdot\left\langle f \left| \mathbf{p} \right| i \right\rangle\right|_{\nu}^2 \propto I_{\nu} \propto \cos^2\delta \qquad \text{Eq. 3.24}$$

Where the index ν denotes the π^* vector final state and δ is the angle between the electric field vector **E** and the direction $\vec{O}$ of the final state molecular orbital (Figure 3.11 (b)). The orientation of the final state orbital is given by a polar angle α and an azimuthal angle ϕ. The reference frame in Figure 3.11 (b) is the coordinate system (x,y,z) of the sample. The X-rays are incident on the sample in the (x,z) plane which, in practice, is the horizontal plane of the electron orbit in the storage ring. The dominant component $\mathbf{E}^{\parallel}$ of the electric field vector **E** of the elliptically polarized synchrotron radiation lies in this plane. It is tilted from the surface normal by an angle θ which is equal to the X-ray incidence angle. By expressing the angle δ as a function α, ϕ and θ, the resonance intensity becomes:

$$I_v = A\begin{bmatrix} P\left(\cos^2\theta\cos^2\alpha + \sin^2\theta\sin^2\alpha\cos^2\phi + 2\sin\alpha\cos\alpha\sin\theta\cos\theta\cos\phi\right) \\ +(1-P)\sin^2\alpha\sin^2\phi \end{bmatrix} \qquad \text{Eq. 3.25}$$

where A is a constant which describes the absolute angle integrated intensities.

3.4.2 Data Evaluation

The data evaluation in NEXAFS consists of several steps. The first step is the normalization of the recorded spectra to the beam current. It is a necessity since the beam current in a synchrotron facility drops exponentially in time. Then, the spectra are divided by the NEXAFS spectra of the clean substrate prior to the deposition of the organic material. In this way any contribution from the additional absoption from the beamline optical components is subtracted. At this point, depending at which θ angle the π^* resonance have a maxima or a minima, the spectra may be treated in two specific ways that enable minimization of the parameters that enter the fitting procedure. The taken directions will be specified for each Pc in the next chapter. As a final step, using eq. 3.25, the determined resonance intensities are fitted as a function of the unknown parameters: α and ϕ.

It must be noted that parameter A which is a system constant has an already established value of 1.7 determined for the PTCDA molecule in ref. [Gav05]. The NEXAFS measurements were performed on the same UHV chamber and at the same beam line, the Russian –German beam line in BESSY.

3.5 Density Functional Theory

Although this method is not an experimental method of investigation, it is included here since it was employed in the investigation of the phthalocyanines electronic structure.

The density functional theory-based methods derive from the quantum mechanics research from the 1920's, especially the Thomas-Fermi-Dirac model, and from Slater's work in quantum chemistry in the 1950's. The main approach of DFT is modelling the electron correlation via general functionals of the electron density. Following the work of

Kohn and Sham [Koh65], the approximate functionals employed by current DFT methods divide the electronic energy into several terms:

$$E = E^T + E^V + E^J + E^{XC} \qquad \text{Eq. 3.26}$$

where E^T is the kinetic energy term arising form the motion of the electrons, E^V includes terms describing the potential energy of the nuclear-electron attraction and of the repulsion between pairs of nuclei, E^J is the electron-electron repulsion term, and E^{XC} is the exchange correlation term and includes the remaining part of the electron-electron interactions. All terms except the nuclear-nuclear repulsion are functions of ρ, the electron density. $E^T+E^V+E^J$ correspond to the classical energy of the charge distribution ρ. The E^{XC} accounts for the remaining terms in energy: the exchange energy arising from the antisymmetry of the quantum mechanical wavefunction and the dynamic correlation in the motion of the individual atoms. E^{XC} is determined entirely by the electron density and is usually divided into separate parts referred to as the exchange and correlation parts.

$$E^{XC}(\rho) = E^X(\rho) + E^C(\rho) \qquad \text{Eq. 3.27}$$

The two components on the right hand side of Eq. 3.27 are termed exchange functionals and correlation functionals, respectively.

Pure DFT methods are defined by pairing an exchange functional with a correlation functional. For example, the well-known BLYP functional pairs Becke's gradient-corrected exchange functional with the gradient-corrected correlation functional of Lee, Yang and Parr [Lee88]. The B3LYP method employs three parameter hybrid functionals revised by Becke [Bec93] (B3) and uses the non-local correlation provided by the LYP expression [Lee88], and VWN (Vosko, Wilk and Nusair) functional III for local correlation [Vos80].

The computations of Pc molecules performed in this work employed DFT method based on B3LYP functional implemented in Gaussian 98 software package [Gau98]. A more detailed description will be given in each case.

Chapter 4. Experimental

4.1 UHV Set-ups

All the measurements discussed in this thesis were performed in ultra high vacuum (UHV) environment. Three UHV systems were used in the process, from which two are in Chemnitz and the third one at BESSY Berlin. The first UHV system that will be described is the one that served for all the VB photoemission experiments shown here. As shown in Figure 4.1 it consists of five chambers: the analysis chamber (ARUPS 10), the organic molecular beam deposition (OMBD) chamber, current-voltage/capacitance-voltage (IV/CV) measurement and metallization chamber, the sample reservoir chamber and the plasma chamber. The plasma chamber serves as a load-lock as well. The analysis chamber contains an angle resolved electron analyzer (VG ARUPS10), a He discharge lamp, and an X-ray source with Al and Mg dual anodes for photoemission studies, and low electron energy diffraction (LEED). The overall resolution of the spectrometer determined using a polycrystalline Ag(111) film grown on hydrogen-passivated Si(111) surface is 0.15 eV for the He I line (21.2 eV).

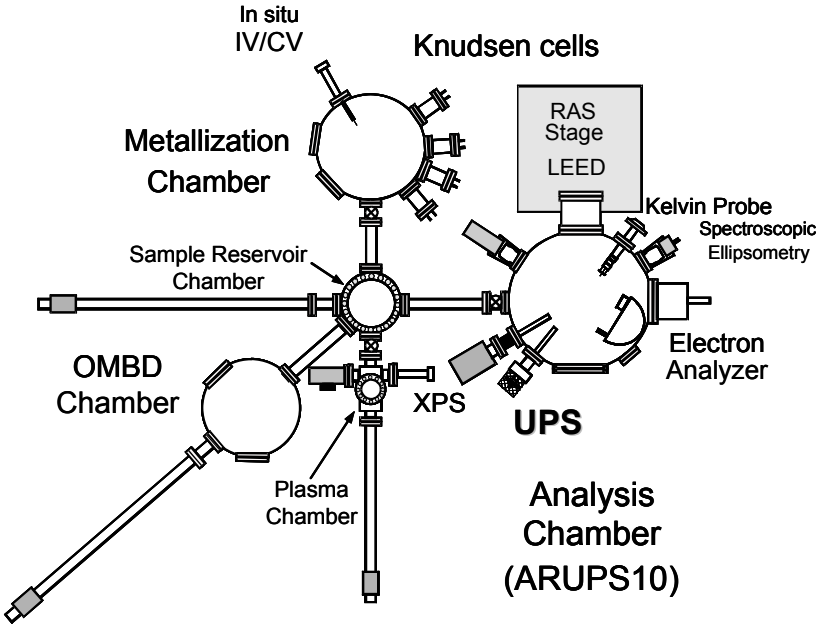

Figure 4.1 UHV system employed in the photoemission experiments.

The base pressure of the analysis chamber is $2 \cdot 10^{-10}$ mbar. OMBD as well as metal evaporation are performed from Knudsen cells in the preparation chamber the base pressure of which is better than $1 \cdot 10^{-9}$ mbar. Samples are introduced into the chamber using the load-lock. The star shape connection between chambers, all connected to the sample reservoir chamber allows transfer of samples without breaking the vacuum. Up to seven samples can be stored in the sample reservoir chamber at once. All the VB-PES spectra taken in ARUPS 10 were recorded in normal emission.

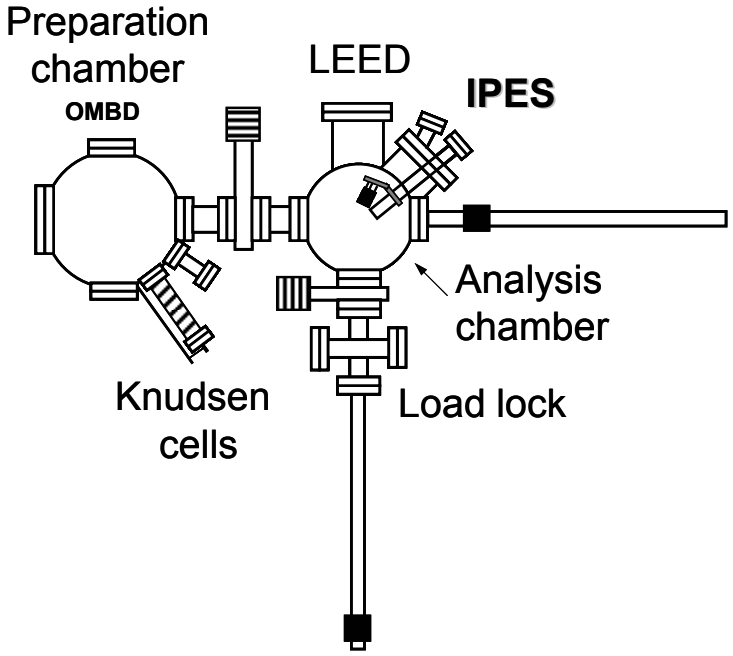

Figure 4.2 UHV system for IPES experiments.

The second UHV system was employed for the inverse photoemission experiments. The system is composed of three chambers: the analysis chamber, the preparation chamber and the load lock (Figure 4.2). The analysis chamber is equipped with the IPES set-up, LEED optics and an argon sputter gun (not shown). The IPES experimental set-up working in the isochromat mode is a "home" built system. The IPES set-up consists of two main components: the low energy electron gun and the Geiger-Müller detector which are mounted on a CF 160 mm flange. The fixed-energy photon detector [Pri88] consists of a Geiger-Müller tube with a magnesium fluoride (MgF_2) window filled with a gas mixture containing ethanol and argon. The ionisation energy of ethanol and the transmission function of the MgF_2 provide a value of 10.9 eV as the nominal detection energy of the detector. A low energy electron gun [Erd82] was used to produce a mono-energetic electron beam. The overall IPES instrumental resolution, estimated from the width of the Fermi edge measured on an Ar sputtered nickel sample is 0.4 eV. All the IPES spectra were recorded at normal incidence of the electron beam with a current density in the range of 10^{-6} A/cm^2. This value is low enough in order not to damage the organic film. The base pressure of the analysis chamber and the preparation chamber is $8.5 \cdot 10^{-10}$ mbar and $1.9 \cdot 10^{-9}$ mbar, respectively. The preparation chamber contains Knudsen cells which are used as evaporation sources for the organic materials and metals.

The third UHV system was the MUSTANG experimental station (Figure 4.3) at BESSY. This chamber was engaged in the NEXAFS measurements presented here. The experiments were performed at the Russian-German Beam Line using a plane-grating monochromator. This beam line provides a linear polarization factor P of 0.98.

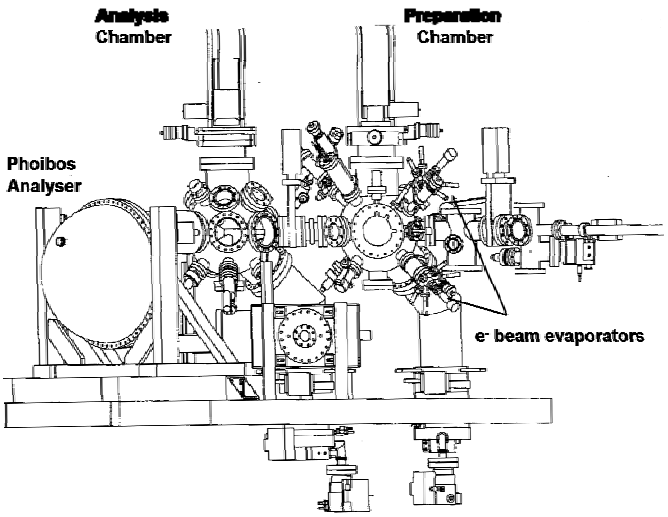

Figure 4.3 MUSTANG experimental station.

MUSTANG is a system consisting of a preparation and an analysis chamber to perform photoemission spectroscopy and NEXAFS measurements. The station is equipped with a SPECS Phoibos 150 analyser. The detector has a mean radius of 150 mm and nine single channel electron multipliers and is arranged at 45° with respect to the incident beam. The preparation chamber is equipped with a LEED system, a differential pumped ion source, two electron beam evaporators, a quartz microbalance, a quadrupole mass spectrometer and a gas inlet system. Inside the load lock chamber there is a sample magazine that can store up to six samples under HV conditions and also inside the preparation chamber it is possible to keep up to four samples under UHV conditions. The base pressure in the analysis and preparation chamber is $2 \cdot 10^{-10}$ mbar.

4.2 Sample Preparation

Silicon p-type, (111) oriented, with a doping concentration of approximately $1.5 \cdot 10^{15}$ cm^{-3} was used as the substrate. The wafers were provided by Siltronic AG. Sublimed H_2Pc and CuPc provided by Sensient Imaging Technologies GmbH (former SynTec) were employed with no further purification. The fluorinated derivatives of CuPc, F_4CuPc and $F_{16}CuPc$, were synthesized and purified by sublimation at the University of Bremen. They were available with the help of Dr. Wilfried Michaelis and Prof. Dr. Derck Schlettwein.

4.2.1 Hydrogen passivation of silicon

The passivation process consists of a wet chemical etching in a HF 40% solution [Yas94]. The detailed steps of the process are shown in Figure 4.4. The first two steps are standard cleaning methods that were developed by Werner Kern at RCA laboratories [Ker78, Ker93]. RCA 1 is a procedure for removing organic residue and films from silicon surface. The decontamination works based on sequential oxidative desorption and complexing with H_2O_2-NH_4OH-H_2O. RCA 2 further cleans the silicon surface by removing any metal ions present there. In between the steps the sample was rinsed with deionised H_2O. The silicon surface was hydrogen terminated by a 30 seconds immersion in a 1:30 mixture of HF 40% and H_2O. The 1x1 reconstruction of the surface was checked by LEED as shown in chapter 2.

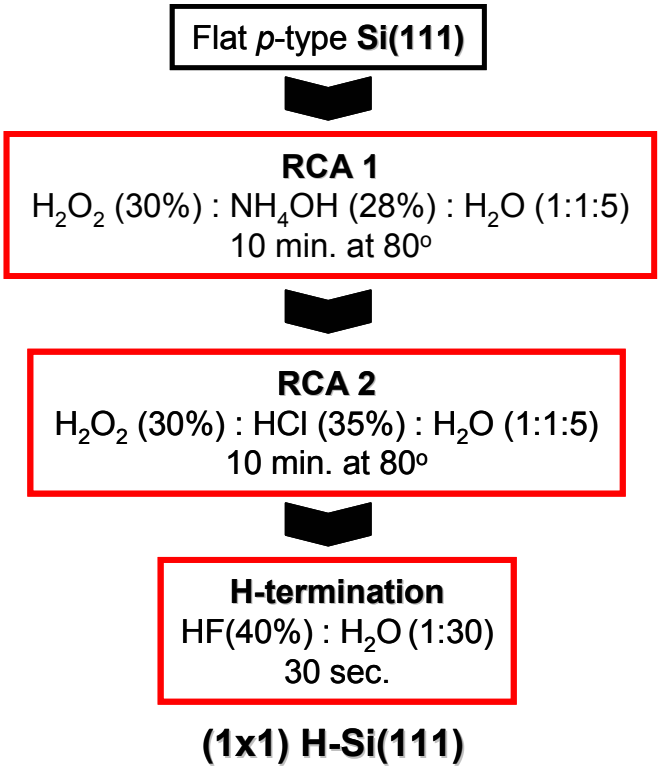

Figure 4.4 The hydrogen passivation procedure.

4.2.2 Molecular and Metal Films

Pc	Temperature (°C)
H_2Pc	310
CuPc	315
F_4CuPc	290
$F_{16}CuPc$	270

Table 4.1 Pcs average evaporation temperatures.

The organic materials were evaporated in UHV from boron nitride crucibles. The Knudsen cells and the crucibles were extensively degassed prior to usage by annealing to temperatures up to 350^0 C. The films were prepared by OMBD on silicon substrates that were kept at room temperature. The organic films were deposited at rates of 0.2-1 nm/min monitored by a quartz microbalance situated in the vicinity of the sample. The

average evaporation temperatures of the Pcs are shown in Table 4.1. The thickness calibration was performed subsequently by means of *ex situ* ellipsometry. The topography of the films was recorded by means of atomic force microscopy (AFM). The AFM topographic image of 20 nm of H_2Pc deposited on H-Si(111) is shown in Figure 4.5 (a). The estimated roughness has a value of 1.35 nm. The crystalline clusters of H_2Pc have a diameter of approximately 0.1 μm estimated from line profiles. The topographic image of 20 nm of CuPc on H-Si (Figure 4.5 (b)) shows the formation of crystalline clusters with sizes of approximately 60-70 nm. Compared to H_2Pc, the film is much smoother, having a roughness of 0.8 nm.

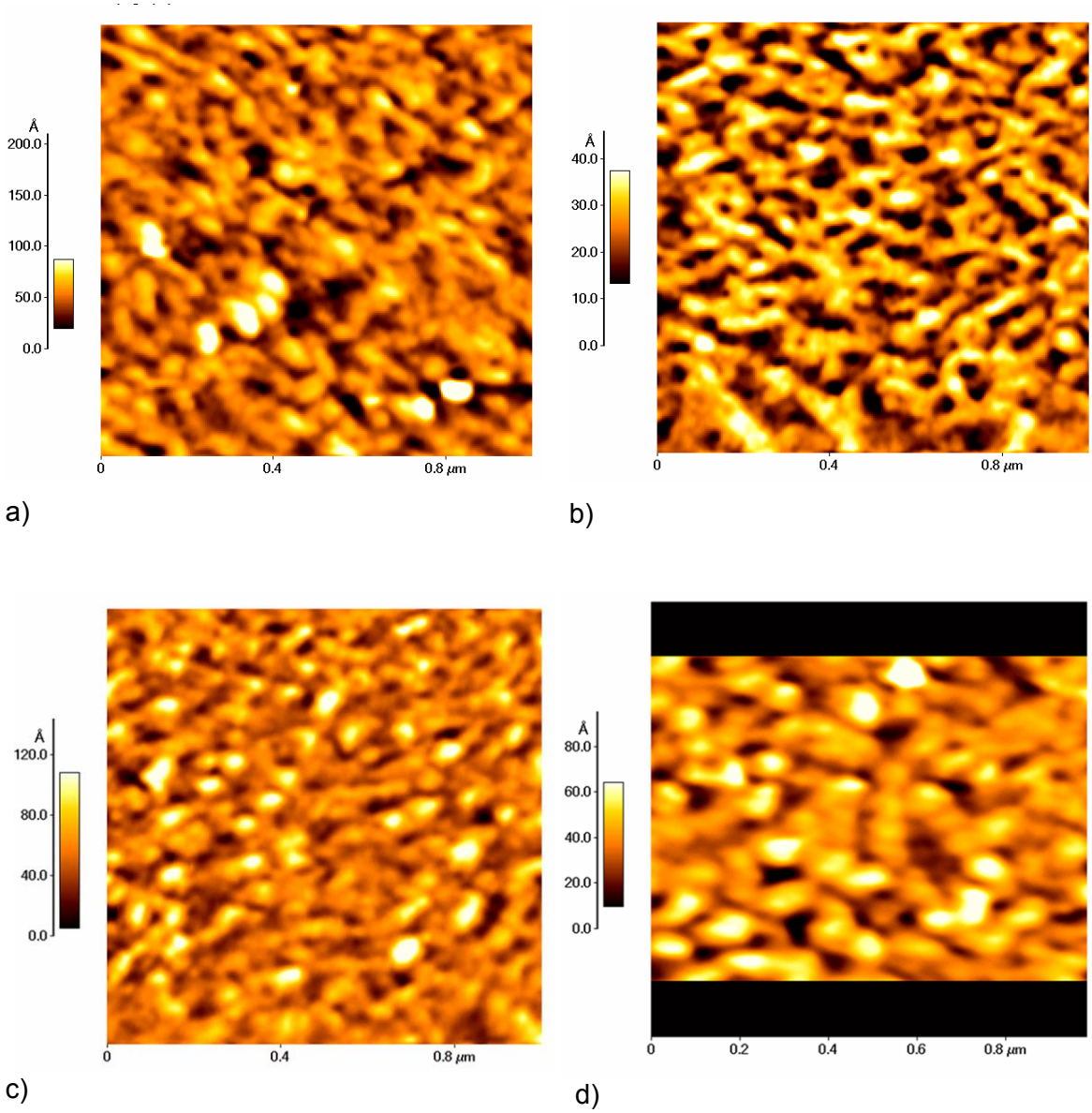

Figure 4.5 AFM topographic image of 20 nm of a) H_2Pc, b) CuPc c) F_4CuPc and d) $F_{16}CuPc$ deposited on H-Si.

The next image (Figure 4.5 (c)) displays the AFM topography of F_4CuPc. The roughness of the film has a value of 2.3 nm value which is quite large compared to the other Pc films. The crystalline clusters of F_4CuPc have sizes of about 0.1 μm. At last Figure 4.5 (d) contains the topographic image of a thin film of F_{16}CuPc. There is quite a large difference in the morphology of this material compared to the others. The main reason is the size of the crystalline clusters which are approximately 0.16 μm in diameter. The roughness estimated from line profiles is found to be approx 1.3 nm.

The metal under study in this thesis is silver provided by ChemPur GmbH and has a purity of 99.9%. Ag was evaporated from the same type of source as used for the organic materials. The temperature of evaporation was around 800^o C and the deposition rate was about 1nm /min.

4.2.3 Gas Exposure

The freshly prepared organic films were exposed *in situ* to molecular oxygen supplied by Messer Griesheim GmbH. The amount of oxygen leaked in the chamber was estimated using a cold cathode pressure gauge in order not to ionize the oxygen molecules. The estimation was expressed in Langmuir units considering the following formula:

$$1L = 1 \cdot 10^{-6}\,\text{torr} \times 1\text{sec} \qquad \text{Eq. 4.1}$$

This formula assumes a sticking coefficient equal to 1 for the gaseous system in discussion.

Chapter 5. Electronic Properties of Pc/H-Si Systems

The following chapter deals with the characterisation of the interface formation between the four phthalocyanines H_2Pc, CuPc, F_4CuPc and $F_{16}CuPc$, and hydrogen passivated silicon. Their electronic properties are determined by means of VB-PES and IPES. Molecular orientation is also estimated by means of NEXAFS.

5.1 H_2Pc/H-Si

Figure 5.1 depicts the thickness dependent photoemission and inverse photoemission spectra of H_2Pc deposited on H-Si(111).

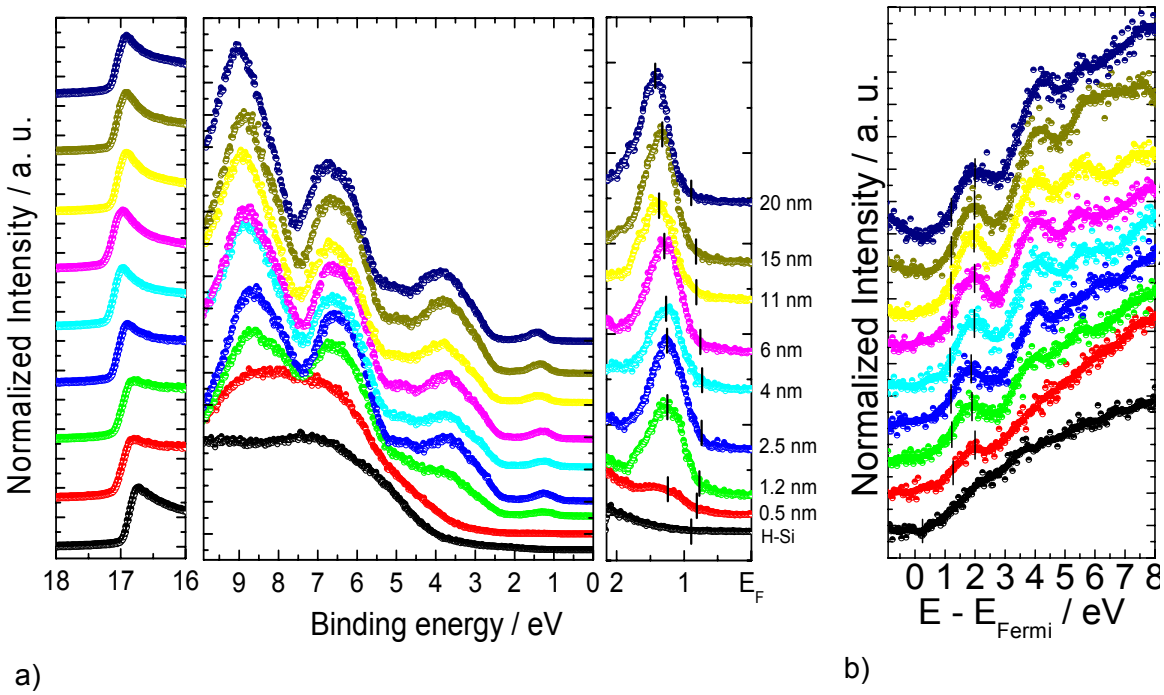

a) b)

Figure 5.1 a) VB-PES thickness dependent measurements on H_2Pc/H-Si(111); b) IPES thickness dependent measurements on H_2Pc/H-Si(111).

The spectra were normalized with respect to the highest peak and shifted vertically for clarity. The HOMO and LUMO peak and onset positions are marked by vertical bars. The

lowest spectra in both images a) and b) of Figure 5.1 correspond to hydrogen passivated silicon. If we analyze the spectra of the first deposited layer of H_2Pc, we observe that only the HOMO and the LUMO features are visible. This may suggest a lying down orientation of the molecules, since the thickness of 0.5 nm corresponds to approximately a monolayer of H_2Pc. The higher binding energy features in VB-PES and in IPES are not visible at this point. In IPES this could be a consequence of either the low cross section of the unoccupied states of H_2Pc in IPES or the low quantum efficiency of the technique (Chapter 3). Further on to the next thicknesses all the characteristic features of H_2Pc become better resolved in both VB-PES and IPES spectra. The full width half maximum (FWHM) of the HOMO feature decreases as the H_2Pc thickness increases, starting from a value of 0.57 eV at 0.5 nm and reaching a value of 0.49 eV at 20 nm of H_2Pc. This indicates a better ordering of the molecules in thicker films. Calculations of the band structure for the β-metal free phthalocyanine suggest that the FWHM of the HOMO and LUMO are in the range of 0.1-0.4 eV along the molecular stacks where the molecules have the greatest π-π overlap [Ort98].

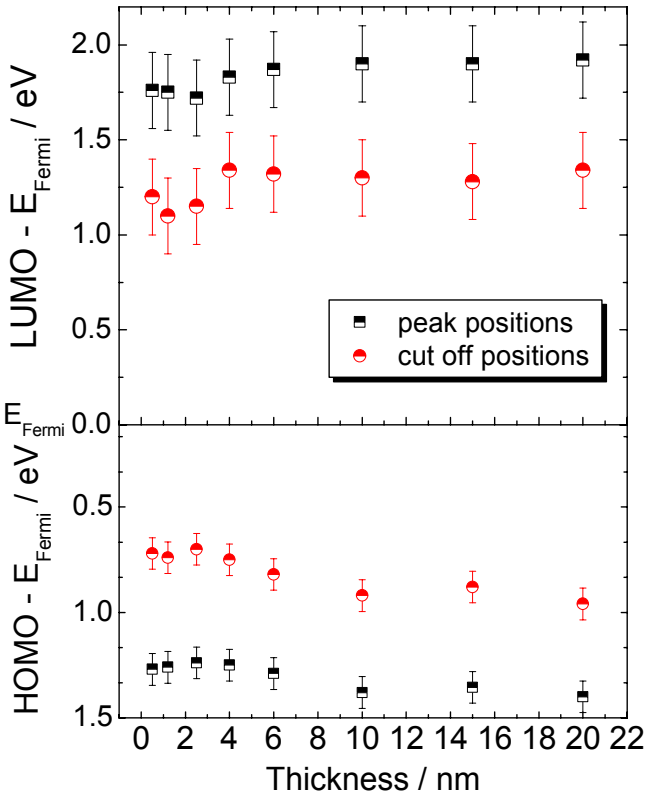

Figure 5.2 Peak and cut-off positions of HOMO and LUMO as a function of H_2Pc layer thickness.

The FWHM of the HOMO observed for individual phthalocyanine molecules in the gas phase has a value of 200 meV [Sch01]. In the gas phase, molecule-molecule interaction is negligible and as a consequence the observed HOMO does not have a contribution from the vibrational coupling of adjacent molecules. Thus, in the present case due to the large values of the FWHM found at 0.5, 1.2 and 2.5 nm of H_2Pc, band formation is observed from the early stages of deposition.

On the other hand, with increasing layer thickness small shifts appear in the HOMO and LUMO positions. These shifts evolve in opposite direction, namely the HOMO feature moves away from the Fermi level and the LUMO moves away as well from the Fermi level. This behaviour is similar to the interface dipole

case that includes the effect of image potential described in the previous chapter 3. Caution must be taken here since this effect is characteristic to organic/metal interfaces. Tsiper et al. [Tsi02] assigned such shifts to different electronic polarization energies found at the interface and at the surface of PTCDA films deposited on Ag and Au.

The evolution of both peak and cut-off positions for HOMO and LUMO as a function of layer thickness is shown in Figure 5.2. Not only HOMO and LUMO shift but also the higher BE features are shifting in similar parallel way. The occurrence of such collective and parallel shifts of the VB-PES and IPES features indicates that no chemical interaction is present at the H_2Pc / H-Si interface. The shape preservation of H_2Pc characteristic features as a function of film thickness also points to negligible chemical interaction.

The HOMO and LUMO cut-offs were determined with respect to the Fermi level by a linear extrapolation of the low energy edge of the HOMO and of the deconvoluted LUMO features (see chapter 3). The shifts show a saturation tendency above 6 nm of H_2Pc thickness, reaching a final value of (0.2 ±0.07) eV. At thicknesses above 6 nm, the transport gap determined as the difference between the onset positions of HOMO and LUMO is found to be (2.2 ± 0.2) eV. The manner in which the transport gap was derived is illustrated by Figure 5.3.

The VB-PES and IPES experimental data for 20 nm of H_2Pc were scaled in order to be plotted in the same graph. Additionally the charge density contours of the HOMO and LUMO are included in the upper panel of the figure.

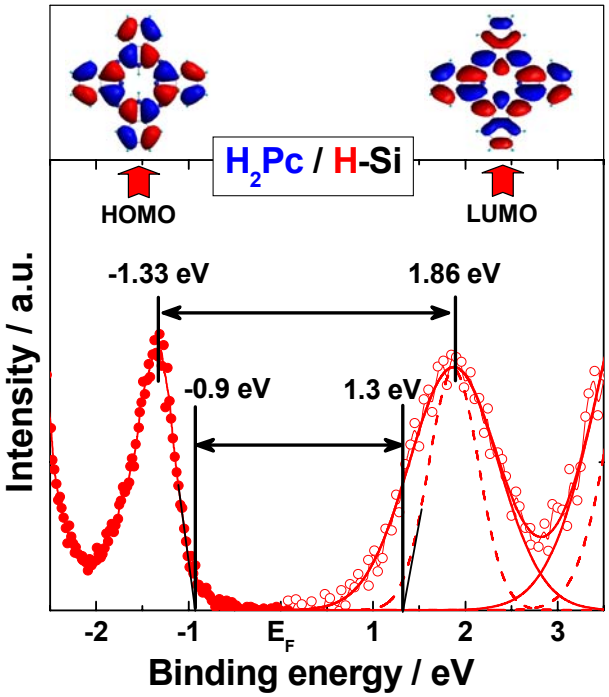

Figure 5.3 E_t determination for H_2Pc.

The contours were determined via a calculation of the density of states (DOS) of one H_2Pc molecule assumed to be in a gaseous state. The code employed for this computation was the Gaussian '98 package [Gau98], using the B3LYP method and 6-31G(d) basis set. Prior to the calculation the geometry optimisation of the molecule was performed using a smaller basis set e.g. 3-21g and the same method. Such a calculation of the DOS is quite important since it can predict the number and nature of the states contributing to each feature in an experimental spectrum

and thus allowing a qualitative assignment of those features. On the other hand, such comparison between calculations for a single molecule and experimental data on films of molecules gives an estimation of the interaction that exists in a molecular solid. Figure 5.4 a) and b) displays a comparison of the VB-PES and IPES experimental spectra and calculated molecular orbitals (MO) of H_2Pc. The experimental spectra correspond to 20 nm thick films of H_2Pc. No cross section effects were included in the simulation of the VB-PES and IPES spectra.

The calculated MO energy positions are obtained with respect to the vacuum level. Their positions were scaled to the Fermi level by subtracting the experimentally determined work function of the organic material. Figure 5.4 (a) contains the experimental and simulated VB-PES spectra. The Gaussian functions used to generate the simulated spectra have a FWHM of 0.5 eV. The calculated positions of MO were shifted away from the Fermi level by 0.48 eV in order to fit the calculated HOMO with its experimentally determined position. The experimental and simulated IPES spectra are shown in Figure 5.4 (b). The experimental data are displayed together with the fit and the deconvoluted spectra.

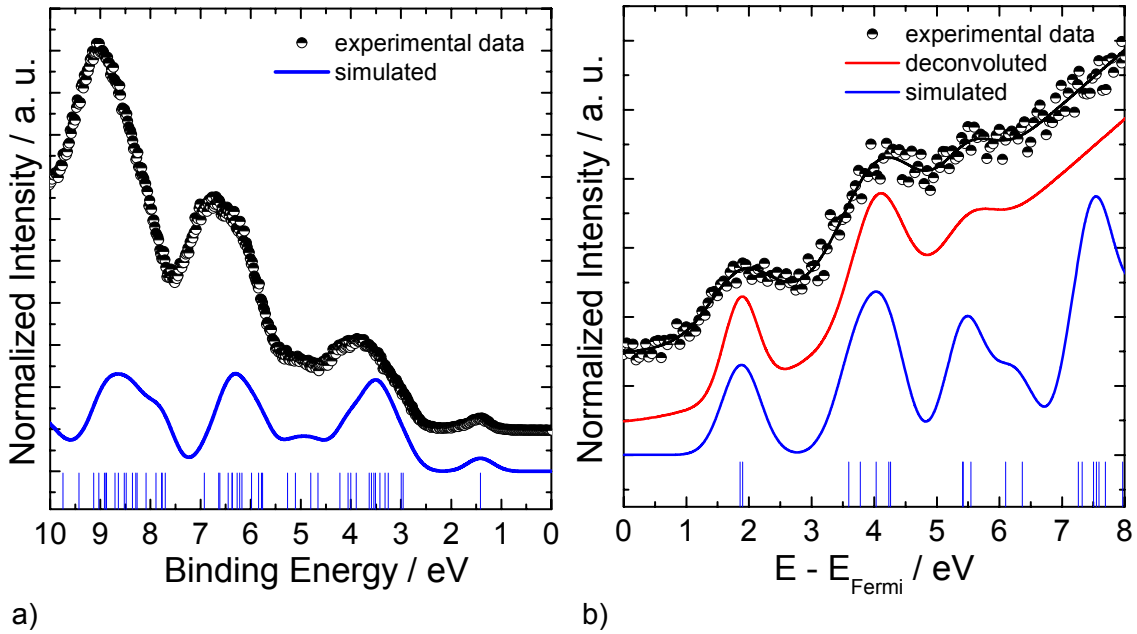

Figure 5.4 a) Experimental and simulated VB-PES spectra of H_2Pc; b) Experimental and simulated IPES spectra of H_2Pc. The vertical lines in figures a) and b) mark the energy positions of the calculated MO.

The FWHM of the deconvoluted LUMO (0.63 eV) was taken into account for the simulation of the calculated MO. The simulated spectra were shifted away for the Fermi level by approximately 0.65 eV for the calculated LUMO peak position to fit with experimental one. However, we have to note that the first peak in the IPES spectra is

composed of two states as judged from the DFT calculation. In the case of the density of unoccupied states the LUMO presented in the upper panel of Figure 5.3 is the lowest energy position occurring from the calculation and shown in Figure 5.4. Both HOMO and double state LUMO have π character and they correspond to a_u and b_{2g}, b_{1g} MOs respectively, in agreement with literature [Ort90]. Although there is a mismatch in the energy positions of the simulated and experimental spectra, in general there is quite a good agreement in their line shapes. This proves the weak inter-molecular interaction present in the organic material.

Going further with the analysis of the experimental data, the evolution of the electronic parameters described in chapter 3 as a function of film thickness is displayed in Figure 5.5 (a). The energy scale is with respect to the vacuum level and thus any present decrease e.g. EA will result in an apparent increase of the data points. At zero coverage the parameters for the hydrogen passivated silicon were introduced in the plot. The top of the valence band (VBM) of H-Si is placed at 0.8 eV from the Fermi level. The bottom position of the conduction band of H-Si was calculated by subtracting from the known transport gap of silicon (1.12 eV) the VBM position. Since silicon is an indirect semiconductor, the position of the conduction band minimum (CBM) is not situated on the perpendicular direction to the (111) plane (see chapter 2 section 2.2.1). Thus IPES at normal incidence does not probe the CBM, but a local minimum of the conduction band.

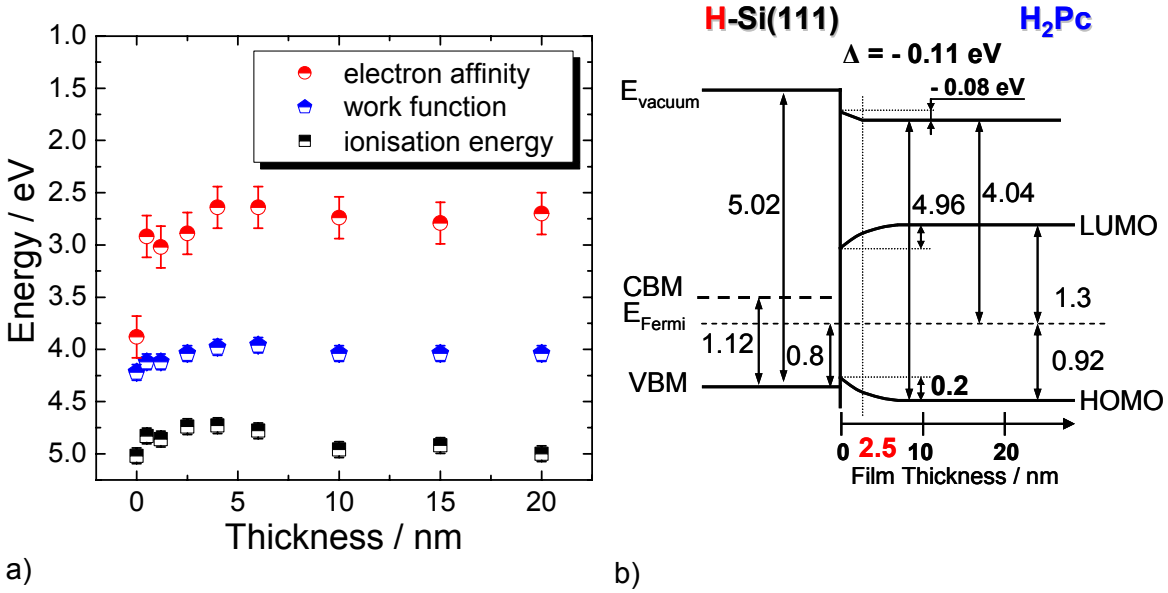

Figure 5.5 a) EA, ϕ, IE as a function of H_2Pc layer thickness; b) Energy band diagram of the H_2Pc/H-Si interface. The surface band bending of the substrate was omitted.

The electron affinity (EA) of the surface shown in Figure 5.5 (a) reveals a sudden decrease upon the first H_2Pc deposition. This indicates a charge transfer at the interface

between the two materials from H_2Pc towards H-Si. EA continues to decrease until the H_2Pc thickness reaches 6 nm. From that thickness on, EA is constant at (2.74±0.2) eV. This suggests a closed H_2Pc layer. The charge transfer at the interface is accommodated by the formation of an interface dipole of Δ=-0.11 eV which is evident from the change displayed by the work function (ϕ) (Figure 5.5 (a)). However, the range in which ϕ changes is smaller than the EA one, ϕ remaining constant at a value of (4.04±0.07) eV after 2.5 nm H_2Pc thickness. The total interface dipole has a value of -0.18 eV. Considering the ϕ of H-Si which has a value of (4.22±0.07) eV and subtracting the ϕ of H_2Pc we can obtain the exact value of the interface dipole. Thus the ϕ of the organic material is the driving force behind the formation of the interface dipole. The IE fluctuations accounting for the changes in the HOMO position and the interface dipole, are resulting in only a slight decrease and then increase of the IE to a value of (4.96±0.07) eV which corresponds to the thick H_2Pc material [Kim00]. In conclusion Figure 5.5 (b) shows the schematic representation of the energy levels at the H_2Pc/H-Si interface which for simplicity does not include the band bending at the H-Si surface. The barrier heights for electrons and for holes at the interface can be estimated to be 0.78 eV and 0.08 eV, respectively.

5.2 CuPc/H-Si

Figure 5.6 depicts the thickness dependent ultraviolet photoemission and inverse photoemission spectra of CuPc deposited on H-Si(111). The spectra in Figure 5.6 (a) middle panel were normalized with respect to the peak placed at 6.5 eV binding energy and shifted vertically for clarity. The H-Si spectrum was normalized to its highest peak in this case. The HOMO and LUMO peak and onset positions are marked by vertical bars. The three VB-PES characteristic peaks for CuPc already appear at very low coverage (0.5 nm) unlike in the H_2Pc case where at this thickness only HOMO is visible. All the peaks shown are gradually shifting with increasing CuPc thickness while the relative distance between the peaks remains unchanged. This indicates that no chemical interaction occurs during the interface formation process. Furthermore, no marked changes in the peak shape of the HOMO as well as LUMO features are observed. The values of the full width half maximum (FWHM) for the HOMO and the LUMO are almost constant as a function of film thickness and have values of 0.50 eV and 1.1 eV without deconvoluting with the instrumental resolution, respectively.

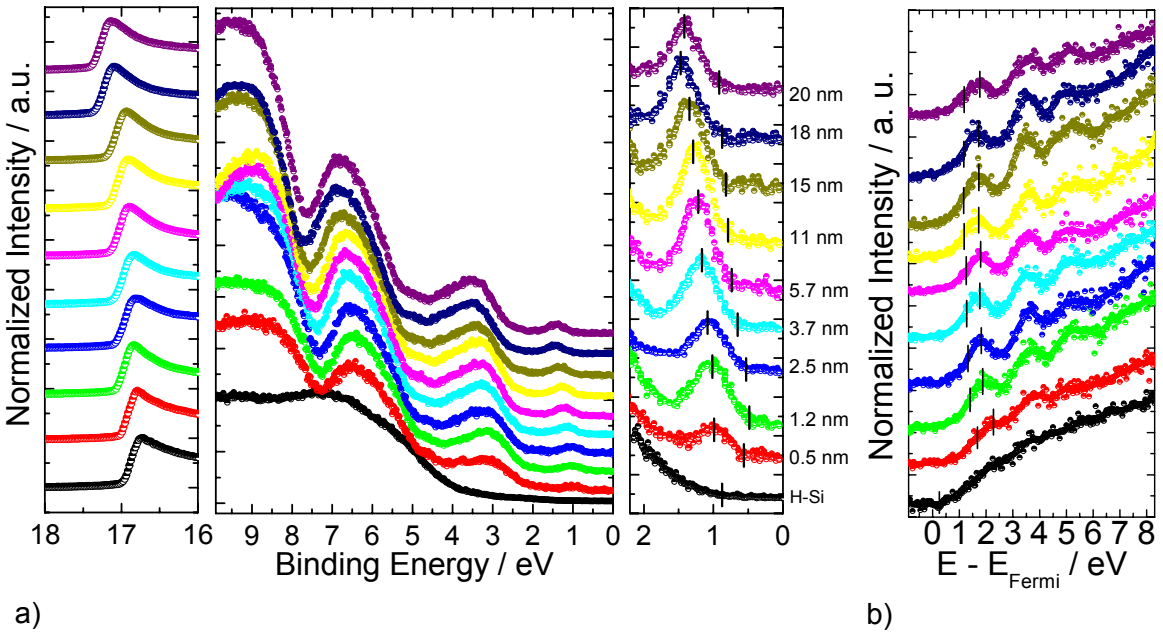

Figure 5.6 a) VB-PES thickness dependent measurements on CuPc/H-Si(111); b) IPES thickness dependent measurements on CuPc/H-Si(111).

As previously discussed for H_2Pc, when band structure is formed, the FWHM of HOMO takes values from 0.1 to 0.4 eV [Ort89]. Consequently the broadening of the HOMO even at a low CuPc coverage suggests the development of a band structure i.e. molecule-molecule interaction. Zooming into the HOMO region as shown on the right hand side of Figure 5.6 (a), a strong shift of the HOMO peak and onset positions towards higher binding energies is observed with increasing thickness. The overall value of the shift is approximately (0.4 ±0.07) eV. The same amount of shift is found in the LUMO position as a function of thickness as shown in Figure 5.6 (b). Similar to the VB-PES case, the CuPc features appear for 0.5 nm and become better resolved for higher thicknesses. The LUMO shifts towards the Fermi level with increasing film coverage. The same shift is observed in the higher binding energy MO's of the IPES spectra. Above 15 nm CuPc coverage the energy shift saturates. At this point the CuPc layer has reached the characteristics of the bulk like organic material. The CuPc molecular bulk configuration presents the HOMO state at ~ 1.6 eV binding energy (BE) and two other molecular levels at higher BE [Sch94] with respect to the Fermi level. On the other hand, in the left hand panel of Figure 5.6 (a) the secondary electrons display a movement of the vacuum level which is in the same range of thicknesses as the HOMO-LUMO shifts.

Figure 5.7 summarizes the resulting HOMO – LUMO peak and onset positions as a function of film thickness and with respect to the Fermi level.

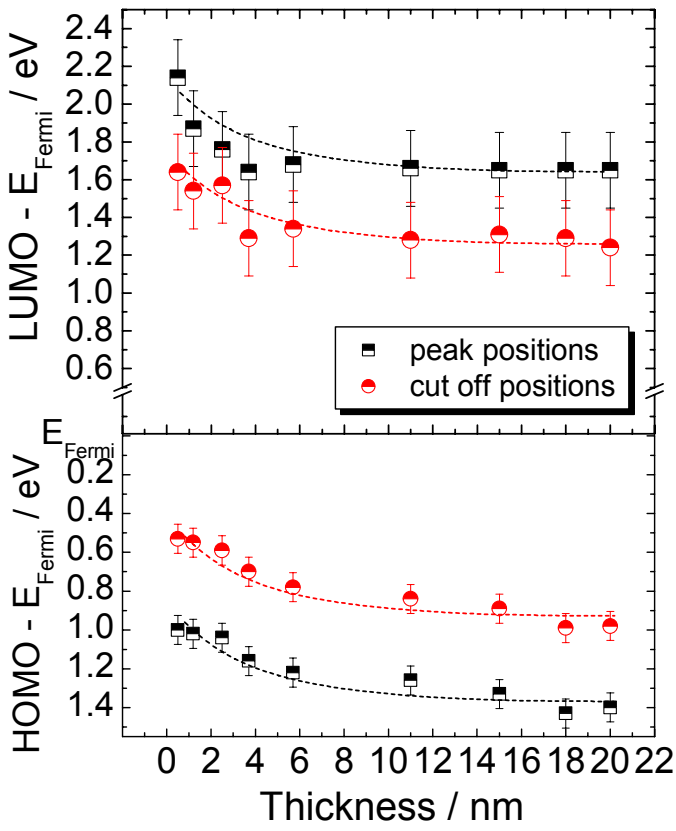

Figure 5.7 Peak and cut-off positions of HOMO and LUMO as a function of H_2Pc layer thickness.

The HOMO – LUMO peak to peak difference calculated for all coverages is approximately (3 ± 0.2) eV.

The transport gap determined as the difference between the onset positions of LUMO and HOMO is found to be approximately (2.2 ± 0.2) eV (Figure 5.8). This value is in rather good agreement with the one determined by Hill *et al.* [Hil00] using UPS-IPES (2.3 ± 0.4) eV, but somewhat larger than the one determined by cyclic voltammetry [Sim85] (1.71 ÷ 1.84 eV). In the upper panel of Figure 5.8 the charge density contours of the HOMO and LUMO are displayed. The HOMO contains two states having almost the same energy. One corresponds to electrons with spin up and one to electrons with spin down (alpha and beta). The LUMO contains four states grouped in two pairs. The states in the pair have the same energy position. Each pair matches the spin up and spin down electrons. Thus the shown contours correspond to the highest and lowest in BE respectively. The two charge density contours were derived from the DFT calculation for a CuPc single molecule. Both HOMO and LUMO have π character. The two and four states correspond to a_{1u} and e_g MO,

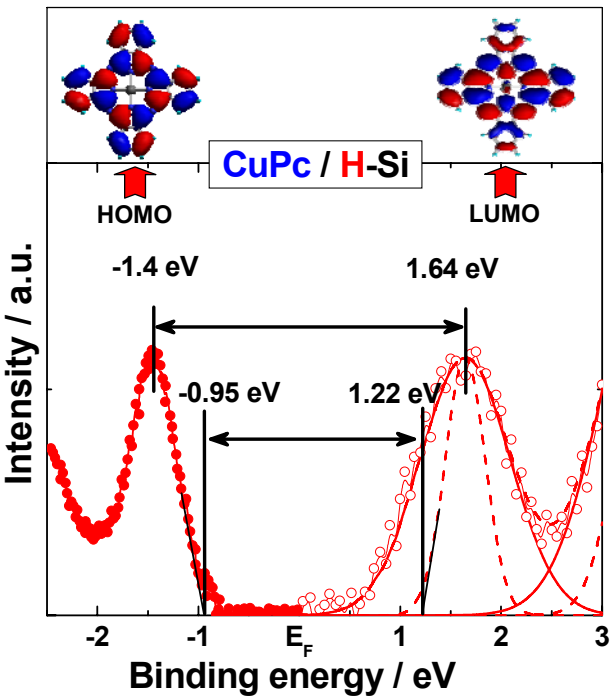

Figure 5.8 E_t determination for CuPc.

respectively. The computation was performed in a similar manner to H_2Pc (subchapter 5.1), but the geometry optimisation procedure was different. To be precise, due to the odd number of valence electrons, CuPc had to undergo a frequency calculation in order to estimate the bonds strength within the molecule. Then, the check point file of this calculation was employed as input in the geometry optimisation calculation of the molecule. Finally the MO's and their energy levels were estimated by the same method and basis set as for H_2Pc. The simulated spectra based on the calculated energy level around the gap compared to the experimental ones are presented in Figure 5.9 (a) and (b). Analogous to H_2Pc, the lineshapes of the simulated spectra are in good agreement with the experimental ones confirming once more the weak intermolecular interaction in the film. However, the expected energy mismatch is found here again. In the first step, the spectra were scaled to the Fermi level by subtracting the experimental work function ϕ.

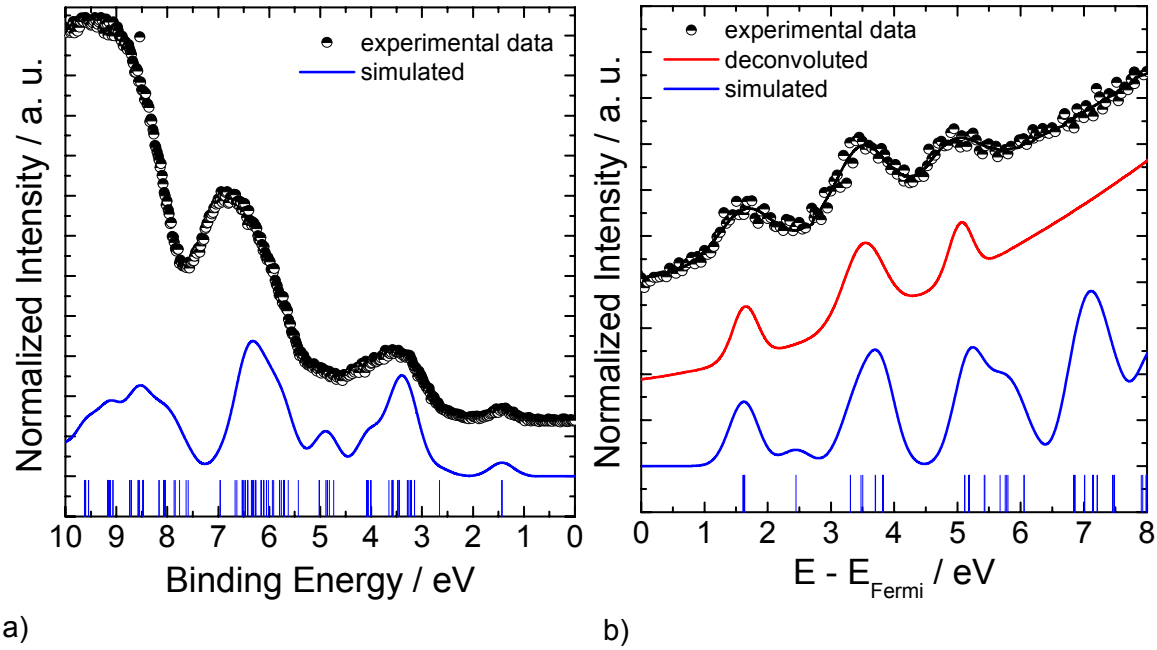

Figure 5.9 a) Experimental and simulated VB-PES spectra of CuPc; b) Experimental and simulated IPES spectra of CuPc. The vertical lines in figures a) and b) mark the energy positions of the calculated MO.

Afterwards, the simulated VB-PES spectrum was shifted by 0.37 eV away from the Fermi level in order to match the calculated HOMO position to the experimental one. Alternatively, the simulated IPES spectrum was shifted by 0.48 eV away from the Fermi level for the computed LUMO position to overlap on the experimental one. Consequently the energy difference between the simulated and experimental states amounts to 0.85 eV. The computer-generated VB-PES and IPES spectra employed Gaussian functions

with FWHM of 0.45 eV. The FWHMs were determined from fitting the experimental HOMO and deconvoluted LUMO.

At the present moment there is an ongoing discussion about the computed states for CuPc. Several articles that present theoretical calculations claim that there is a 3d-like state in the HOMO-LUMO gap [Lia01] placed at the Fermi level [Bia03]. However, there is only one article containing experimental data that sustains this hypothesis [Dow04]. Downes *et al.* show resonant soft X-ray emission data measured on a thick film of CuPc that exhibit a state placed in the HOMO-LUMO gap. In the present work the assumption of the existence of such a state is excluded since no evidence in the experimental data is found whatsoever. This conclusion is sustained by the present DFT calculations and other publications [Loz04, Roc90].

Considering the interface formation of CuPc and H-Si, Figure 5.10 (a) summarizes the electronic properties of the CuPc film surface as a function of the deposited thickness. The dashed lines are plotted as guide to the eye. When 0.5 nm of CuPc is deposited a sudden change of EA and IE occurs. Proceeding to larger CuPc thicknesses EA and IE remain constant. On the other hand, the work function decreases approximately linearly as a function of thickness.

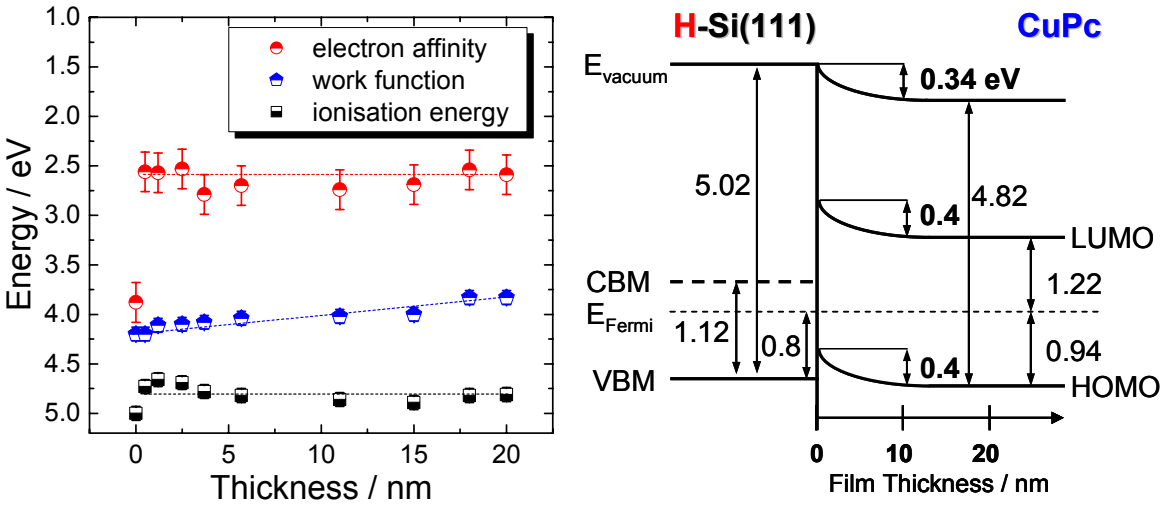

Figure 5.10 a) EA, ϕ, IE as a function of CuPc layer thickness; b) Energy band diagram of the CuPc/H-Si interface. The surface band bending of the substrate was omitted.

Figure 5.10 (b) summarizes the measurements by showing the energy band diagram of CuPc/H-Si(111) interface. The determined values for thick CuPc layer (20 nm) are: IE=(4.82±0.07) eV, Φ=(3.88±0.07) eV and EA=(2.66±0.2) eV. A change of (0.34±0.07) eV in the vacuum level position at the interface is measured as well. There is no rigid shift of the secondary electron cut-off and thus following the definition given in the previous chapter 3, no absolute interface dipole. The onset positions of the HOMO and LUMO

were employed in order to sketch the energy band diagram and to calculate the values of the electronic properties. The determined interface barriers for electrons and for holes are 1.3 eV and 0.26 eV respectively. In the case of H-Si(111), the onset position of the VBM was taken into consideration for determining the IE=(5.02±0.07) eV and Φ=(4.22±0.07) of the surface. The VBM is obtained in the direction perpendicular to the (111) plane of silicon. However, the conduction band minimum is not situated in the same direction [Mön95] as discussed in the previous subchapter 5.1 H_2Pc/ H-Si.

The energy shift that appears at the H-Si(111)/CuPc interface might have several explanations. As already discussed for metal-organic interfaces [Ish99] the formalism of electrostatic band bending model can hardly explain the formation of these interfaces.

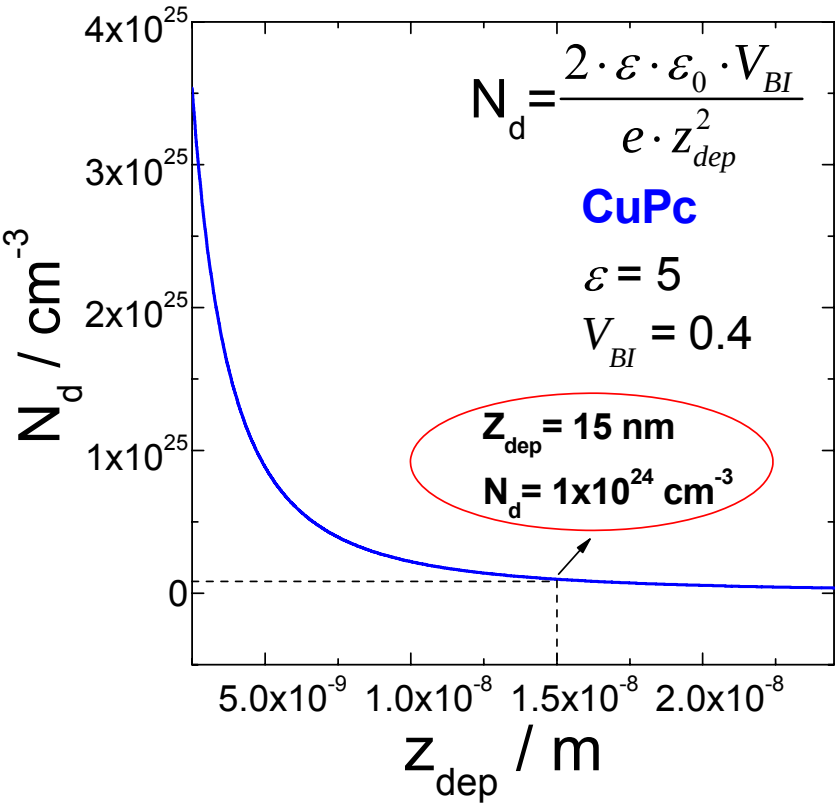

Figure 5.11 The Schottky formula applied in the CuPc case. The charge carrier density as a function of the depletion width.

Figure 5.11 displays the dependence of the charge carrier density as a function of the depletion width for this particular case. Applying Poisson's equation as for inorganic semiconductors, using a depletion width of 15 nm, the built-in potential calculated from the difference of Φ of H-Si and CuPc, and the reported relative dielectric constant of CuPc (about 5) [Deb92], the charge carrier density is found to be very high *i.e.*$1 \cdot 10^{24}$ cm^{-3}. Consequently the results of such an interpretation would be unreasonable since the intrinsic carrier concentration of CuPc [Mck98] was previously estimated to be $\sim 10^7$ cm^{-3}.

Even though the conventional band bending model is quite unlikely to explain the energy shifts at the CuPc/H-Si interface, this model was not completely ruled out in previous publications [Shi98, Paa03]. The formation of inorganic-organic semiconductor interfaces is still under discussion. Possible factors which can affect the interfacial layer are chemical interaction, polarization in the molecular layer and a surface rearrangement. The appearance of the energy shift due to charge transfer occurring as a result of chemical interaction may be excluded since the distance between the gradually shifting peaks as well as their lineshape remains unchanged. In the case of chemical interaction the appearance or disappearance or at least changes in the lineshape of features in the valence band is expected. Polarization in the molecular layer is consistent with such energy shifts in the HOMO position as found by Peisert *et al*. [Pei02] and initially considered for other organic molecules as well i.e. perylene derivatives [Hil00]. The distribution of charge on the molecules changes with the changing of environment from the hydrogen passivated silicon substrate to the thick CuPc film. Moreover, the distribution of charge on the molecules is also influenced by the slightly different arrangement of the molecules in the vicinity of the substrate compared with the ones in the thick film. Furthermore the surface roughness of the substrate may also play a role in the overall molecular arrangement. Nakamura *et al*. [Nak96] determined the growth mode of CuPc on a NH_4F passivated Si(111) substrate. The molecular column of CuPc was found to be parallel to the surface on a relatively rough substrate, while the column was found perpendicular to the Si(111) plane on an atomically flat substrate. The hydrogen passivation involving HF immersion was already proven to produce a relatively rough substrate surface [Bur88, Hig90]. Considering that the FWHM values of the HOMOs are not changing, the adsorption geometry of CuPc molecules may be estimated. The molecules seem to form clusters even at a monolayer coverage, which would grant them already bulk like properties and result in band formation. Peisert *et al.* [Pei02] determined that CuPc on polycrystalline gold behaves in a similar way. Comparing the polycrystalline gold surface and the H-Si(111) surface a common characteristic is found: namely the relative large roughness of both substrates. Although the wet chemical treatment based on HF dip gives an ideally hydrogen terminated surface, this surface is non-uniform [Hig91]. By means of STM the estimated value of the roughness is about 2-3 Å. This may favour the clustering of the molecules in the first monolayers. However, measurements on CuPc/H-Si system using a slightly different hydrogen passivation of silicon show the same energy shifts [Gor05]. This indicates that the surface roughness of the substrate does not play a major role for the energy shifts at the interface.

Several other studies have shown that the molecules change their orientation as a function of layer thickness [Ish98, Pei01, Yam02]. An incomplete overlapping of the CuPc molecules results in a partial superposition of the π orbitals. As a consequence, when a change in molecular orientation occurs, it will result in a change of the intermolecular interaction and will affect of the π-electron system. As determined before from DFT calculations and in agreement with literature HOMO and LUMO features correspond to π-character molecular orbitals [Sch94, Yos01]. Consequently any change of molecular orientation will influence the recorded VB-PES and IPES spectra and the HOMO and LUMO features, respectively. Following this hypothesis angular dependent NEXAFS was performed on the CuPc/H-Si(111) system, namely on two different thicknesses of CuPc. Figure 5.12 displays the CuPc N1s excitation spectra for a) 2 monolayers and b) 20 nm thickness as a function of the angle of incidence θ (normal incidence θ = 90^0) of the synchrotron radiation.

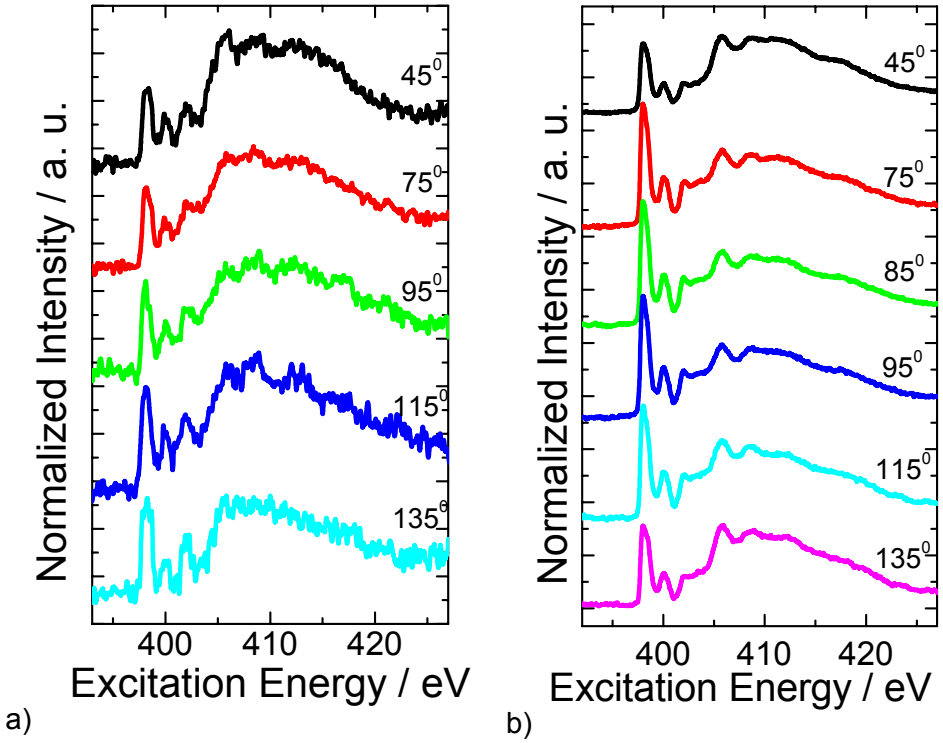

Figure 5.12 a) N1s excitation spectra a) 2 monolayers of CuPc and b) 20 nm of CuPc as a function of θ the angle of incidence; The lower energy features (398-403 eV) represent the π* resonances, whereas those features above 403 eV are related to the σ* resonances.

The intensity of the π* (relative to the σ^* one) resonances has maxima at θ=135^0 (Figure 5.12 (a)) and θ=85^0 (Figure 5.12 (b)). However, the intensity and features of σ^* resonance are still visible at the given incidence angles. This suggests the presence of short range ordering in both cases.

The quantitative analysis of the NEXAFS excitation spectra for CuPc based on the explanations given in chapter 3 is provided in Figure 5.13 (a) and (b). The procedure used for the determination of the normalized intensities consists of several steps. First of all, the NEXFAS spectra were normalized such that they coincide for photon energies far below and far above the N 1s absorption edge. Hence the procedure accounts for the collection efficiency. Subsequently, each π^* region of the NEXAFS N 1s excitation spectra was fitted with Lorentian functions [Stö92]. The intensity of the first π^* peak was then plotted as a function of the radiation incidence angle and the maximum and minimum of the π^* intensities determined. In this case both a) and b) NEXAFS spectra display a clearer maximum in the π^* intensities as a function of incidence angle than a minimum. Consequently, to minimize the parameter number in eq. 3.25, a normalization of all π^* resonant intensities to the maximum one was used in the fitting session.

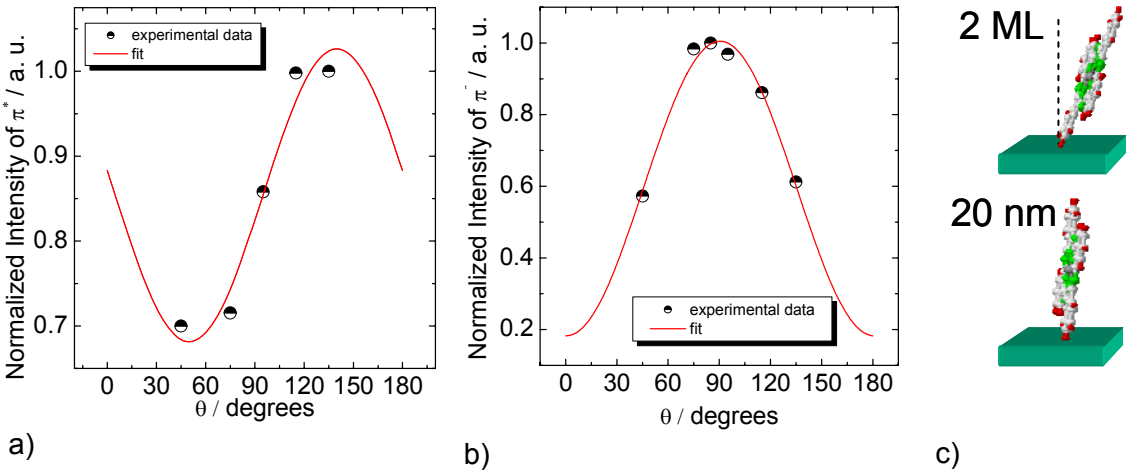

Figure 5.13 Normalized resonance intensity of the π^* orbitals (the highest intensity feature in the N1s excitation spectra in Figure 5.12 (a) ad (b)) as a function of the incidence angle of the synchrotron radiation of a) 2 monolayers and b) 20 nm of CuPc; c) average molecular orientation of CuPc in 2 monolayers (ML) and 20 nm.

Figure 5.13 (a) and (b) exhibits the normalized resonance intensity of the π^* orbitals as a function of the incidence angle of the synchrotron radiation. The data points are fitted using Eq. 3.25 and the average tilt-angle for each case is calculated. The 3-fold symmetry of the silicon substrate is lifted by the surface roughness and as a consequence the model used for the fit contains an azimuthal dependence as well.

	Tilt angle α	**Azimuthal angle ϕ**
2 ML	$70^0 \pm 2^0$	$108^0 \pm 3^0$
20 nm	$90^0 \pm 1^0$	$45^0 \pm 2^0$

Table 5.1 Calculated angles from the fit of the π^* resonance intensities for 2 monolayers and 20 nm of CuPc.

Due to the sampling depth of NEXAFS which is extremely large (approximately 20 nm) compared to the size of a molecule, the determined

molecular orientation is an average one (Figure 5.13 (c)). The calculated values of the tilt angles α and the azimuthal angles ϕ are displayed in Table 5.1. As shown, the CuPc molecules change their orientation above a certain film thickness. This points to weaker interaction strength between the CuPc molecules in a film than between the CuPc molecules and the substrate. If the interactions would be similar in strength, such a change of molecular orientation would not have taken place.

In conclusion NEXAFS spectra reveal a change in the molecular orientation of CuPc from monolayer range to thick films. Thus the rearrangement of the CuPc molecules is most likely the reason for the observed energy shifts at the CuPc/H-Si(111) interface, since the energy shifts are independent of surface treatment and surface roughness.

5.3 F_4CuPc/H-Si

Similarly to H_2Pc and CuPc, VB-PES and IPES experiments were performed on thin films of F_4CuPc deposited on H-Si. The thickness dependent spectra are displayed in Figure 5.14 (a) and (b).

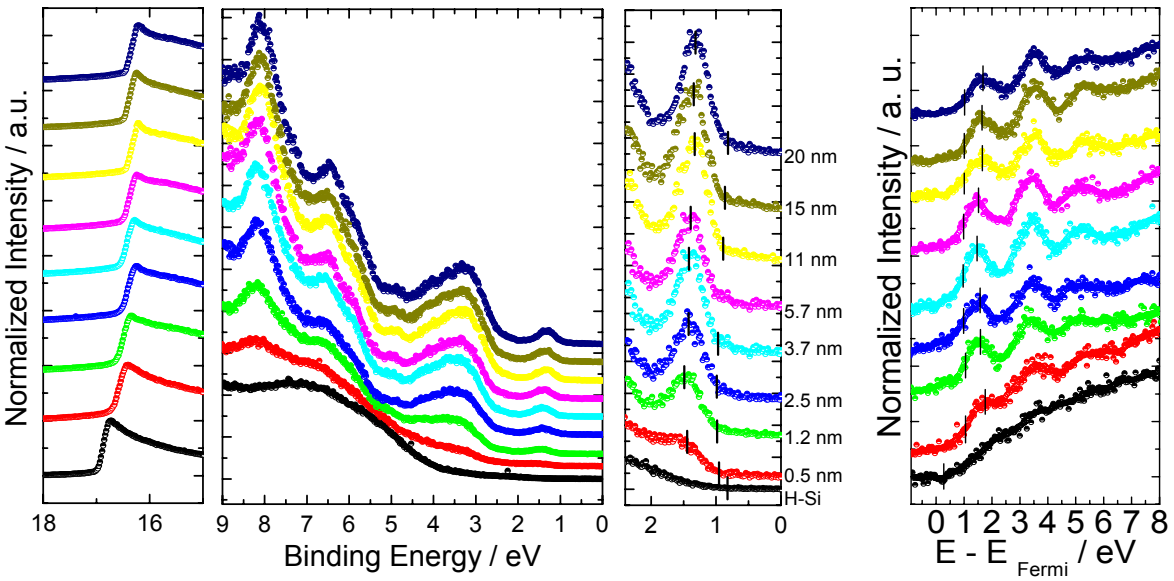

Figure 5.14 a) VB-PES thickness dependent measurements on F_4CuPc/H-Si(111); b) IPES thickness dependent measurements on F_4CuPc/H-Si(111).

The VB-PES spectra corresponding to F_4CuPc were normalized to the peak placed at 6.5 eV BE and then shifted upwards for clarity. The H-Si VB-PES was normalized to its highest peak. The IPES spectra were not normalized. The characteristic features of the material appear at the first deposition and become better resolved at higher thicknesses.

When analysing the shapes of the VB-PES spectra (Figure 5.14 (a)) with respect to the previous systems H_2Pc and CuPc (Figure 5.15), we can observe the high resemblance between them in the low BE region. However, in the high BE energy the shapes are changed. Thus the fluorine atoms contribute mainly to the higher BE components. On the other hand, the shapes of the IPES spectra are highly alike to the ones belonging to H_2Pc and CuPc. The straightforward conclusion would be that fluorine atoms have a much smaller contribution to the unoccupied states.

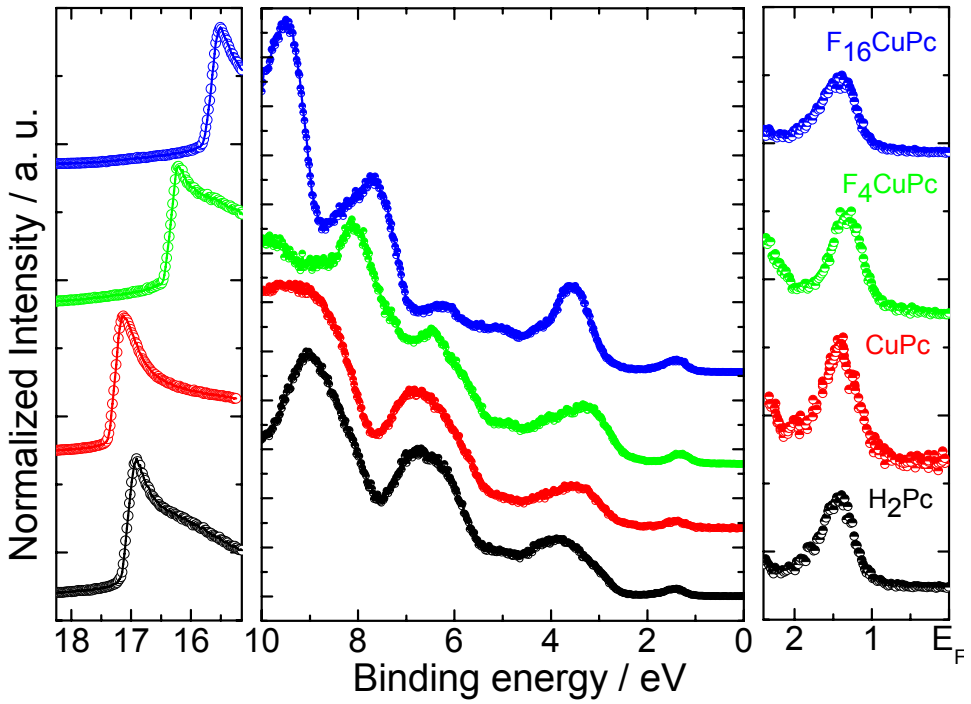

Figure 5.15 VB-PES spectra corresponding to 20 nm of H_2Pc, CuPc, F_4CuPc and $F_{16}CuPc$.

This is somewhat expected due to the high electronegativity of fluorine. In the molecule, fluorine probably has a high tendency to attract the electrons from the core and thus forms negatively charged branches, inducing a quadrupole moment in the molecule.

Advancing in the data analysis, the left hand side of Figure 5.14 (a) displays the secondary electron region. This region detects whether there is any change in the vacuum level position. In this case, an abrupt interface dipole is formed upon the first deposition. The value of the dipole is Δ=0.30 eV. However, the secondary electron cut-off does not remain constant and continues to change until the thickness reaches 3.7 nm where it saturates. The shift has a value of 0.2 eV. The charge flows from H-Si to F_4CuPc. The dipole is formed in an opposite direction to the ones formed by CuPc and H_2Pc. It seems that the presence of fluorine in the molecule reverses the charge flow at the interface. That is again expected due to the high electronegativity of fluorine. The total value of the interface dipole is Δ=0.50 eV.

Considering the right hand panel of Figure 5.14 (a), we detect that the HOMO shifts towards the Fermi level by approximately 0.1 eV as the F_4CuPc thickness is increased. A saturation point is reached above 6 nm thickness. The HOMO FWHM values are decreasing with increasing thickness suggesting a smaller degree of disorder in thicker films and a more defined environment. In the IPES spectra, the LUMO (Figure 5.14 (b)) shows approximately the same behaviour as HOMO. A similar shift occurs in its position with the LUMO moving away from the Fermi level. Figure 5.16 summarizes the resulting HOMO – LUMO peak and onset positions as a function of film thickness with respect to the Fermi level. The HOMO–LUMO peak-to-peak difference calculated for all coverages is approximately (2.85 ± 0.2) eV.

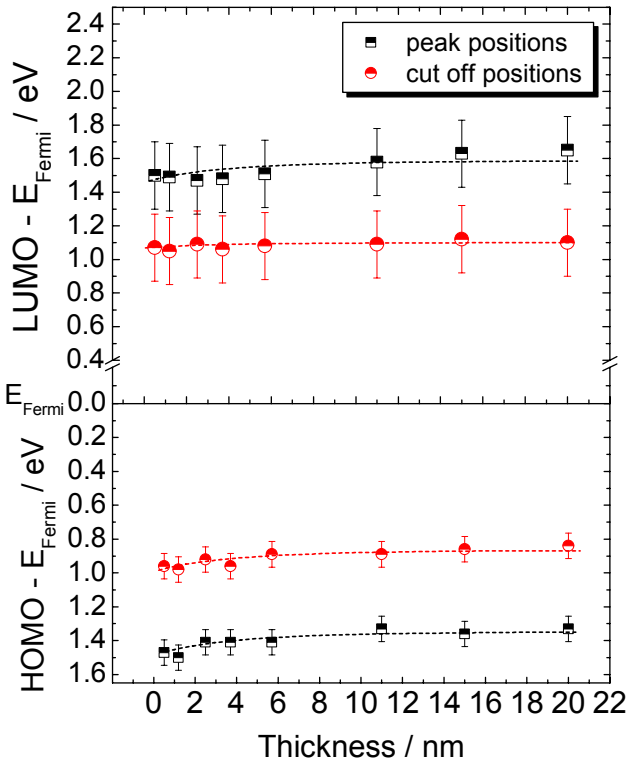

Figure 5.16 Peak and cut-off positions of HOMO and LUMO as a function of F_4CuPc layer thickness.

The transport gap estimated from the HOMO and deconvoluted LUMO onsets (see subchapter 3.3) has a value of (1.95 ± 0.2) eV.

A schematic of the transport gap determination procedure is displayed in Figure 5.17. A DFT calculation on a single F_4CuPc molecule was performed precisely in the same manner as for CuPc using the same type of geometry optimisation procedure, method and basis set (subchapter 5.2).

The charge distribution contours shown in the upper panel of Figure 5.17 were created as a result of this calculation. Exactly as in the case of CuPc, the calculated HOMO and LUMO of F_4CuPc contain two and four states respectively and have π character. The two and four states correspond to a_u and e_g MO, respectively. The simulated spectra based on the calculated energy level around the gap compared to the experimental ones are displayed in Figure 5.18 (a) and (b). The computer generated spectra were rescaled with respect to the Fermi level by subtracting the experimental work function from the computed energy positions. The Gaussian functions used in the convolution of the calculated energy levels have FWHM of 0.46 eV and 0.44 eV for the VB-PES and IPES simulations, respectively. The presented

comparison shows quite good agreement in terms of lineshapes between the simulated and experimental spectra. Nevertheless, in this case as before there is a mismatch between the calculated energy positions and the experimental ones.

The simulated VB-PES spectrum was shifted away from the Fermi level by 0.81 eV in order to match the HOMO position onto the experimental one, while the simulated IPES spectra were shifted towards the Fermi level by 0.05 eV for overlapping the calculated LUMO position with the experimental one. Thus the mismatch in the transport gap mounts to 0.76 eV. This underestimation of the transport gap in DFT calculations is a known issue for this type of computation. Up to now, there has been no publication with detailed theoretical calculations of the F_4CuPc molecule.

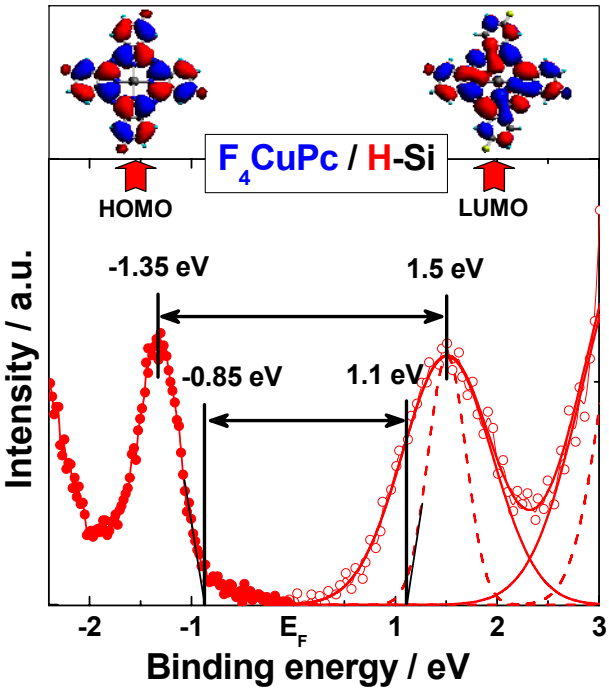

Figure 5.17 E_t determination for F_4CuPc.

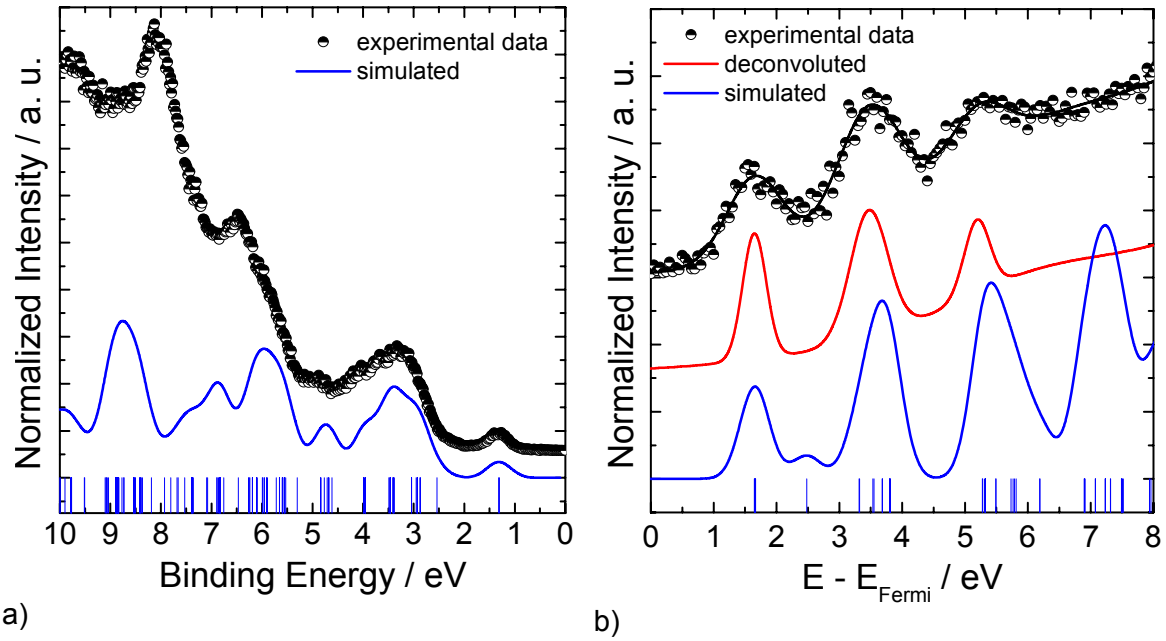

Figure 5.18 a) Experimental and simulated VB-PES spectra of F_4CuPc; b) Experimental and simulated IPES spectra of F_4CuPc. The vertical lines in figures a) and b) mark the energy positions of the calculated MO.

Continuing the experimental data evaluation, Figure 5.19 (a) presents the evolution of the electronic properties of the interface (EA, ϕ, IE) as a function of the F_4CuPc layer thickness. At the zero point of thickness again the experimental data corresponding to H-Si were introduced. Upon the first deposition of F_4CuPc the EA of the surface decreases suddenly. Since the features of F_4CuPc for this thickness are already quite clearly seen in the IPES spectrum, the measured EA corresponds directly to the organic layer with only very little influence from the H-Si. Judging further the change observed in EA, we can estimate the influence of the substrate. For the next thicknesses up to 3.7nm of F_4CuPc, EA increases slightly until it reaches saturation at a value of (3.65±0.2) eV.

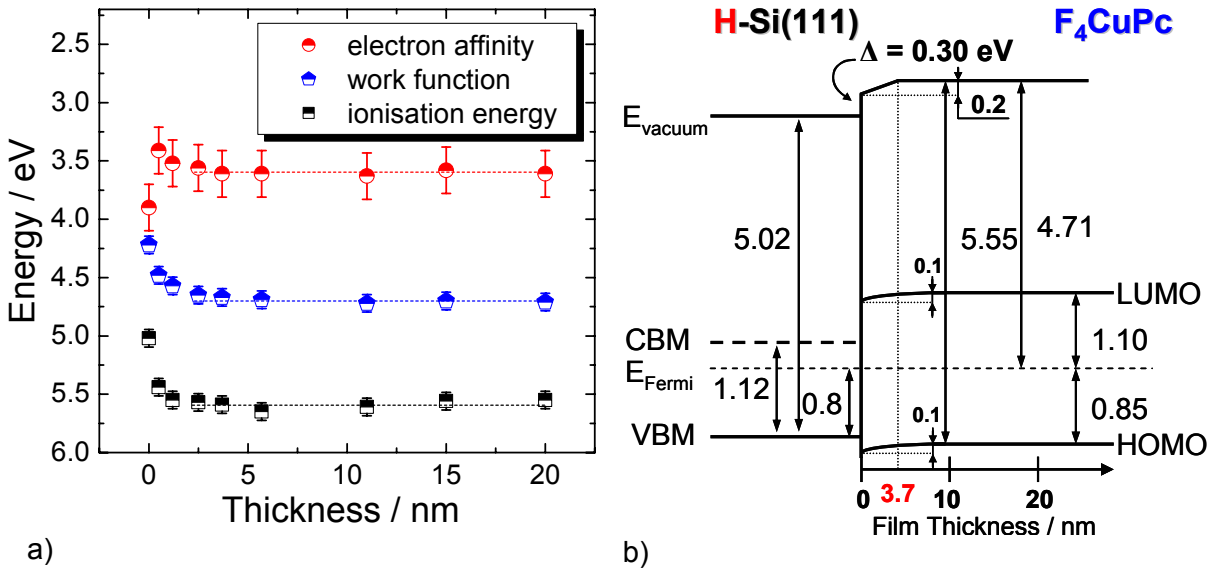

Figure 5.19 a) EA, ϕ, IE as a function of F_4CuPc layer thickness; b) Energy band diagram of the F_4CuPc/H-Si interface. The surface band bending of the substrate was omitted.

This change accounts for the formation of an interface dipole and includes also the LUMO band bending like shift. At this point we can estimate the total barrier for electrons at the interface as being 0.78 eV. ϕ and IE are both increasing as a function of F_4CuPc thickness and reach the saturation values ϕ=(4.71±0.07) eV and IE = (5.55±0.07) eV at 3.7 nm. The change in IE incorporates the vacuum level rigid shift (0.3 eV) and the small HOMO shift (0.1 eV). Further, up to the saturation point it also incorporates the continuous shift found at the vacuum level (secondary electron cut-off). The total barrier for holes can be estimated and has a value of 0.05 eV. ϕ is directly measuring the presence of the total interface dipole (0.5 eV) that relaxes over a charge transfer from H-Si to F_4CuPc. At last, Figure 5.19 (b) summarizes all the determined parameters in the energy band diagram for the F_4CuPc/H-Si interface. The conduction band minimum of H-Si is not included in the band diagram due to reasons previously explained. Compared to

the CuPc/H-Si interface, the F_4CuPc/H-Si interface presents a combination of weak band bending like behaviour and interface dipole formation.

Considering the behaviour of H_2Pc and CuPc in comparison with that of F_4CuPc, such a trend in the interface dipole could be predicted by scaling it to the electronegativity and electron affinity of the substitute atoms when deriving the F_4CuPc molecule from CuPc. When calculating the average value of the electronegativity and electron affinity / molecule (Figure 5.20), we observe the same trend as found in the experimental determination of EA of the molecule. The average electronegativity of the molecules was determined by the geometric mean of the atomic values of their constituents as described by Pauling [Mön95]. On the other hand, the average electron affinity of the molecules was calculated by the arithmetic mean of the atomic values.

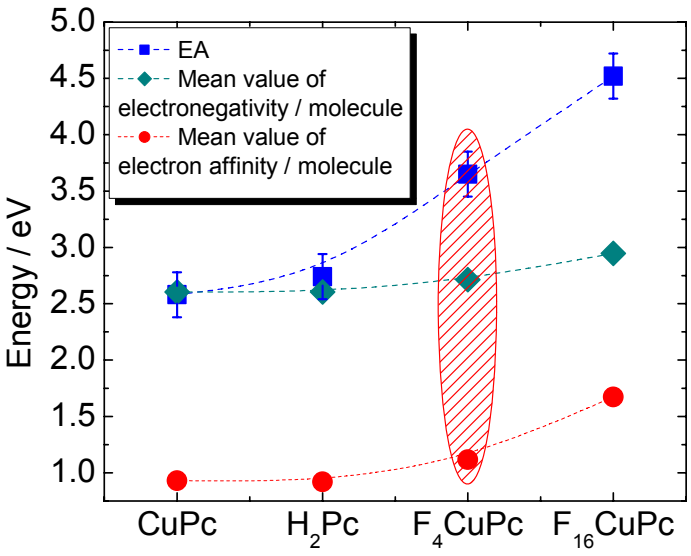

Figure 5.20 Comparison of the experimentally determined EA and the calculated mean values of electronegativity and electron affinity / molecule.

Consequently such a prediction is consistent with the observed linear variation of the interface dipole as a function of EA, ϕ and IE for the different Pcs (Figure 5.36). On the other hand, the change in direction of the energy shifts in the HOMO and LUMO levels at the interface when switching from CuPc to F_4CuPc points to the following conclusion. The fluorine atoms compensate the effect of the copper atom in F_4CuPc. While at the H_2Pc/H-Si interface we find no energy shifts, when Cu atom appears in the H_2Pc molecule forming CuPc, HOMO and LUMO do shift. Similarly, when CuPc is modified by four atoms of fluorine, HOMO and LUMO shift in opposite direction. This type of atom switching leads to a charge redistribution in the molecule and thus influences the π-π overlapping. As a result, a change in the molecular orientation will be induced that produces energy shifts in electronic levels. The direction of the shifts in the HOMO-LUMO positions is influenced by the electron affinity of the atoms that modify the molecules, in this case Cu and F. The values of electron affinities belonging to these atoms are: H: -0.75 eV, Cu: -1.22 eV and F: -3.4 eV. More will be discussed at the end of this chapter, where also a comparison to F_{16}CuPc will be introduced.

Determining the origin of the band bending like behaviour found here also involved testing the classic theory of band bending. A plot of the charge carrier density as a function of the depletion width is shown in Figure 5.21. Applying the Schottky formula in this case yielded the following data: given a shift of 0.1 eV and thus a built-in potential of 0.1 V, and a depletion width of 6 nm, the resulting charge carrier density amounts to 1.4×10^{24} cm^{-3}. This value is totally unrealistic for an organic material. Thus the classic theory of inorganic semiconductor interfaces can not be applied in this case.

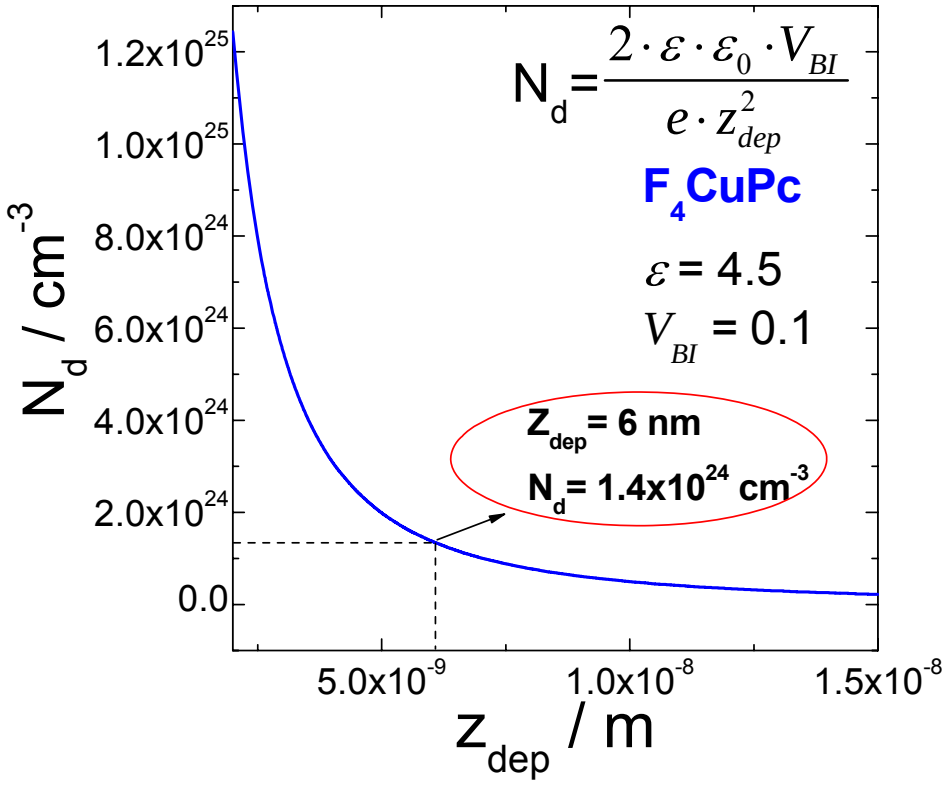

Figure 5.21 The Schottky formula applied in the F_4CuPc case. The charge carrier density as a function of the depletion width.

As previously discussed for CuPc such a shift can have several origins based on the factors which can affect the interfacial layer. The chemical interaction can be ruled out since the appearance or disappearance or at least changes in the lineshape of VB features are not observed. Then polarisation in the molecular layer was another cause discussed for CuPc. It can appear also in this case, however, it can be caused by a change in the molecular orientation in the vicinity of the substrate and in thicker films. Such a change in orientation affects the π-π overlapping and thus the VB-PES and IPES spectra. The result would be shifts in the molecular orbitals as observed here. To confirm the hypothesis of shifts generated by changes in the molecular orientation as a function of thickness, angular dependent NEXAFS measurements were performed at two different F_4CuPc thicknesses.

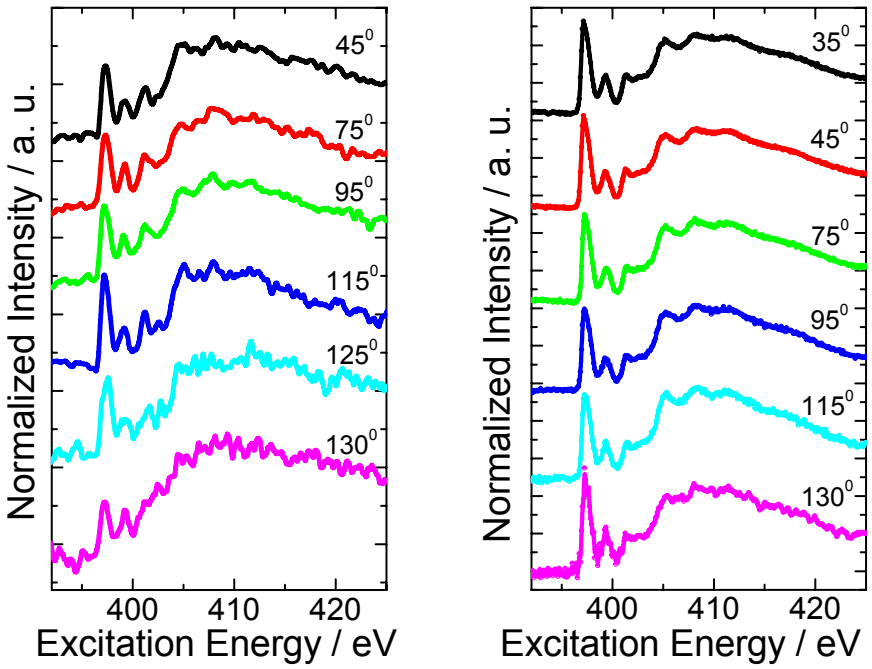

a) b)

Figure 5.22 a) N1s excitation spectra a) 2 monolayers of F_4CuPc and b) 20 nm of F_4CuPc as a function of θ the angle of incidence; the lower energy features (398-403 eV) represent the π* resonances, while those features above 403 eV are related to σ* resonances.

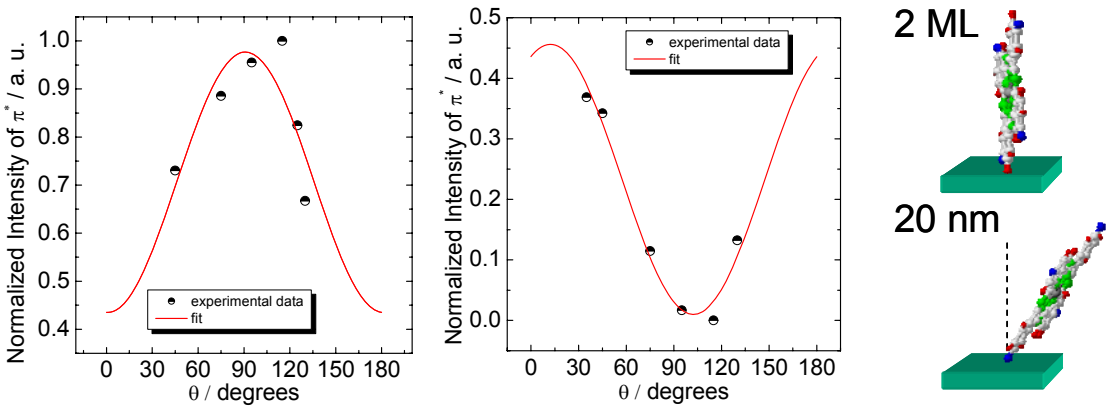

a) b) c)

Figure 5.23 Normalized resonance intensity of the π^* orbitals (the highest intensity feature in the N1s excitation spectra in Figure 5.22 (a) and (b)) as a function of the incidence angle of the synchrotron radiation of a) 2 monolayers and b) 20 nm of F_4CuPc; c) average molecular orientation of F_4CuPc in 2 monolayers (ML) and 20 nm.

The N 1s excitation spectra of a) 2 monolayers and b) 20 nm thickness as a function of the angle of incidence θ of the synchrotron radiation are displayed in Figure 5.22 (a) and (b). As already described for CuPc, the spectra underwent subsequent normalization prior to the final quantitative analysis. The normalization procedure for the 2 monolayers of

F_4CuPc was exactly the same as for CuPc due to the presence of a maxima in the π^* resonance intensities ($\theta=115^0$). Consequently Figure 5.23 (a) displays the ratio of the resonance intensities and the maximum resonance intensity. On the other hand, the resonance intensities for 20 nm of F_4CuPc show only a minimum and therefore the normalization procedure was changed. Instead of the ratio the difference of spectra was used. Namely, the N 1s excitation spectra corresponding to the minimum π^* intensity was subtracted from all the N 1s NEXAFS spectra. This type of procedure is also well documented and widely used [Stö92]. The resulting dependence is shown in Figure 5.23 (b). The fit of the resonant intensities shown in Figure 5.23 for 2 monolayers and 20 nm was performed using Eq. 3.25. Since there was no possibility to obtain a good fit of the resonant intensities by taking into account the 3 fold symmetry of the silicon substrate, the conclusion that the symmetry was lifted by the substrate roughness was reached. Thus the results contain besides the tilt angle α, an azimuthal angle ϕ (Table 5.2). This azimuthal angle may be considered as the angle formed by the in plane projection of the π vector of the molecule and the plane of the incident radiation. Unfortunately this azimuthal angle can not be recalculated with respect to any of the substrate directions due to experimental reasons (the cut directions of the samples are not known).

	Tilt angle α	**Azimuthal angle ϕ**
2 ML	$90^0 \pm 3^0$	$55^0 \pm 5^0$
20 nm	$60^0 \pm 1^0$	$82^0 \pm 4^0$

Table 5.2 Calculated angles from the π^* resonance intensities fit for 2 monolayers and 20 nm of F_4CuPc.

As before the displayed angles are pointing to an average orientation of the molecules. In conclusion, F_4CuPc has a different molecular orientation than CuPc. While CuPc in 2 ML is tilted with respect to the substrate, F_4CuPc adopts a more standing configuration. This suggests a weaker interaction of F_4CuPc with the substrate than found for CuPc. Moreover, in thicker films while CuPc molecules are standing, F_4CuPc molecules are tilting. Such a behaviour definitely points to the fluorine atoms playing the major role in the orientation of the molecules. The change in molecular orientation from thin to thick film points to molecular relaxation achieved above a certain layer thickness. This indicates a larger molecule/substrate interaction than molecule/molecule interaction. If the molecule/molecule interaction would be greater than the molecule/substrate interaction then there would be no change in the molecular orientation as a function of film thickness. Certainly here the strength of the interaction between the F_4CuPc molecule and H-Si can be classified as the weakest when compared to the CuPc/H-Si and $F_{16}CuPc$/H-Si interaction. This assertion can be made due to the

standing geometry of the F_4CuPc molecule in the 2 monolayers film, a geometry which presents the smallest probability of interaction between the π orbitals of F_4CuPc and the σ orbitals of the H-Si surface.

5.4 F_{16}CuPc/H-Si

The last interface discussed here is formed by hexadecafluorinated copper phthalocyanine (F_{16}CuPc) and H-Si. The thickness dependent VB-PES and IPES spectra are displayed in Figure 5.24 (a) and (b) respectively. At the first glance, the spectra show a totally different behaviour when compared to H_2Pc, CuPc and even F_4CuPc. The energy shifts present are large with respect to the previously described ones. In the left hand side panel where the VB-PES spectra are, one can observe that at 0.5 nm thickness the characteristic features of F_{16}CuPc [Knu04] are already present similar to CuPc and opposite to H_2Pc and F_4CuPc. However, at the same thickness in IPES, the features are not as distinct. This could be a consequence of either the low cross section of the unoccupied states of F_{16}CuPc in IPES or the low quantum efficiency of the technique (Chapter 3) as mentioned before. The HOMO and the higher BE states are shifted towards the Fermi level as a function of layer thickness.

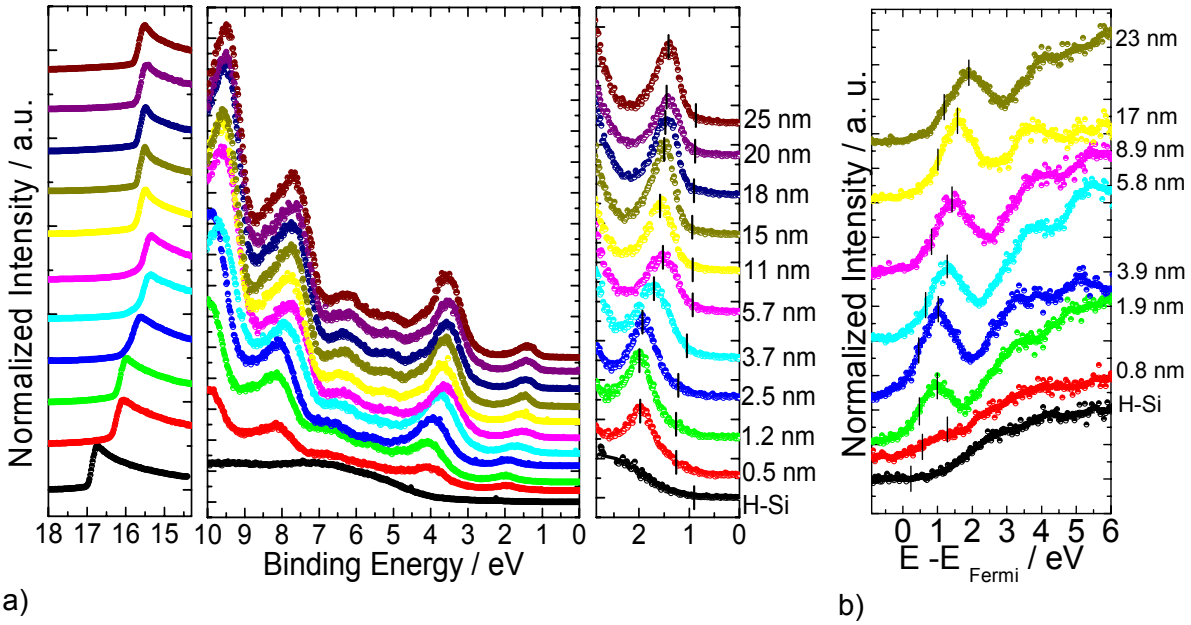

Figure 5.24 a) VB-PES thickness dependent measurements on F_{16}CuPc/H-Si(111); b) IPES thickness dependent measurements on F_{16}CuPc/H-Si(111).

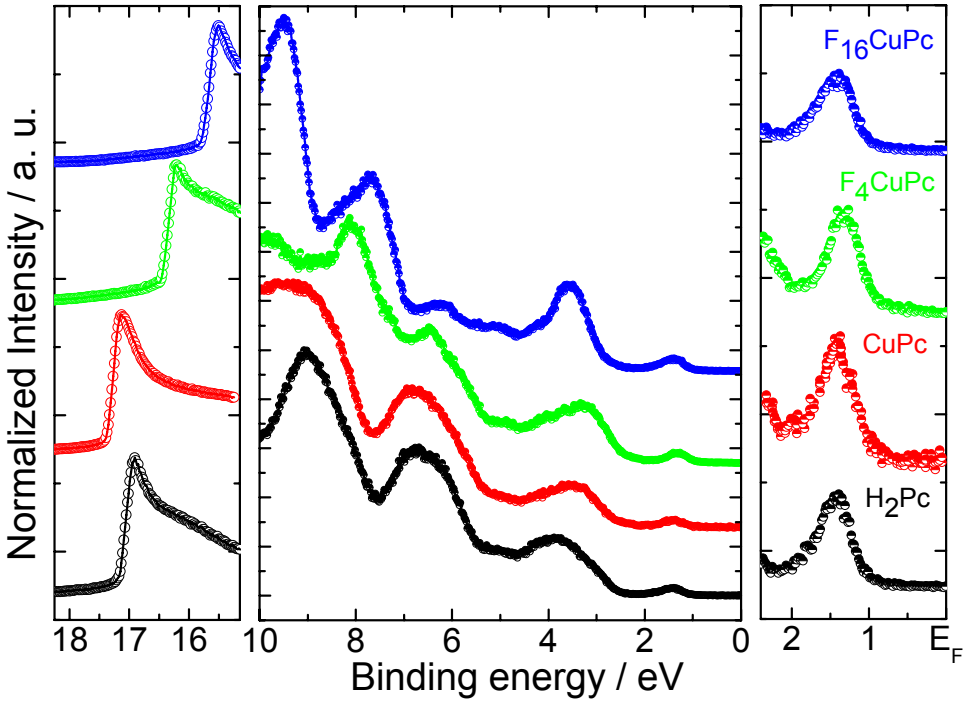

Figure 5.25 VB-PES spectra corresponding to 20 nm of H_2Pc, CuPc, F_4CuPc and $F_{16}CuPc$.

The shape of the VB-PES features is quite distinct from the characteristic ones belonging to H_2Pc, CuPc and even F_4CuPc (Figure 5.25). Thus the higher BE components are modified by the high number of fluorine atoms contained now by the molecule. The energy shift of the HOMO amounts to 0.6 eV. A similar evolution takes place in the IPES spectra where the LUMO shifts away from the Fermi level with the same amount of energy. The shift shows a saturation tendency above 15 nm of $F_{16}CuPc$. Compared to the previously discussed materials, the HOMO-LUMO shift of $F_{16}CuPc$ is opposite to that for CuPc. The transport gap remains approximately constant within the experimental error at a value of (1.8±0.2) eV. The peak-to-peak difference is constant as well and has a value of approximately (2.8±0.2) eV (Figure 5.26). If we consider the secondary electron region, we can observe that when the first layer is deposited a rigid shift is already observable. The shift has a value of 0.60 eV. This type of behaviour is accounted for the formation of an interface dipole at the $F_{16}CuPc$/H-Si interface. At higher thicknesses the secondary electron cut-off continues to shift as a function of thickness reaching a final value for approximately 5.7 nm of $F_{16}CuPc$. The total value of the interface dipole is Δ=1.20 eV and has the same direction as detected for F_4CuPc.

It is opposite to the interface dipoles determined at the H_2Pc/H-Si and CuPc/H-Si interfaces. This clearly indicates that the added fluorine atoms play an important role in the formation of the interface. The presence of a high number of fluorine atoms changes the electronic fingerprint of the molecule as shown in Figure 5.25.

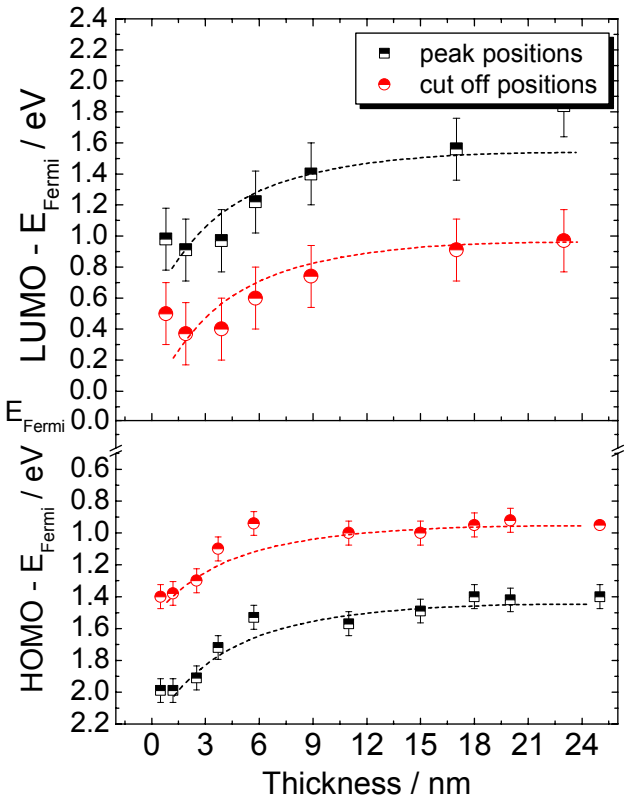

Figure 5.26 Peak and cut-off positions of HOMO and LUMO as a function of F_{16}CuPc film thickness.

The shape of the VB-PES features is different from the ones found for the other Pcs. Consequently the fluorine atoms contribute to all of the MOs that generate the VB-PES features. On the other hand, the band gap of the molecule is also affected by this modification since its determined value (Figure 5.27) is smaller than E_t of CuPc and F_4CuPc.

The DFT calculations performed for this molecule show a contribution of the fluorine atoms to the HOMO and LUMO and predict a smaller band gap as well (2.07 eV). An illustration of this statement can be found in the representation of the HOMO and LUMO charge distributions shown in the upper panel of Figure 5.27.

The shapes of the charge distributions include the fluorine atoms in both cases.

The DFT computation was performed as described for CuPc (one molecule in a gas phase) since the F_{16}CuPc molecule displays the same odd number of valence electrons. A comparison of the calculated states and the VB-PES and IPES experimental spectra is presented in Figure 5.28 (a) and (b). The spectra are referenced to the Fermi level as discussed before. The HOMO and LUMO experimental features are attributed to a_{1u} and e_g MO, respectively. Similarly to CuPc and

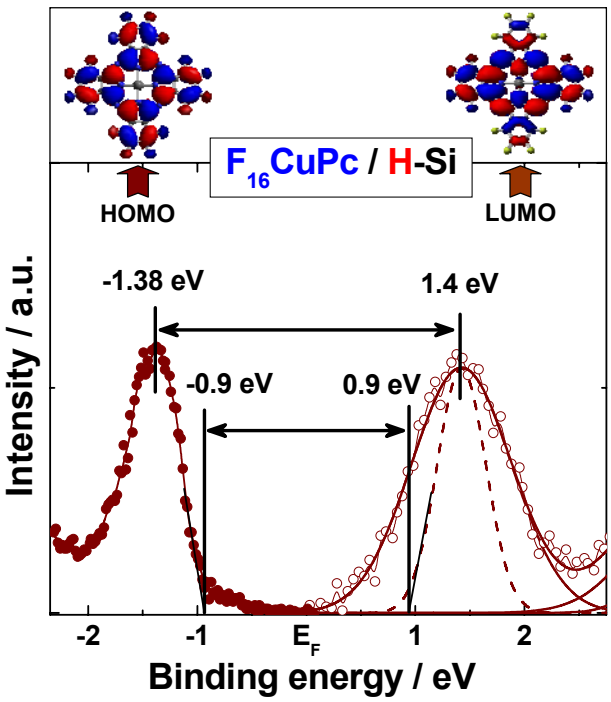

Figure 5.27 E_t determination for F_{16}CuPc.

F_4CuPc, HOMO and LUMO contain two and four states, correspondingly. The VB-PES and IPES simulated spectra employed Gaussian functions with FWHM of 0.51 eV and 0.52 eV as resulted from the fits (see description for the other molecules).

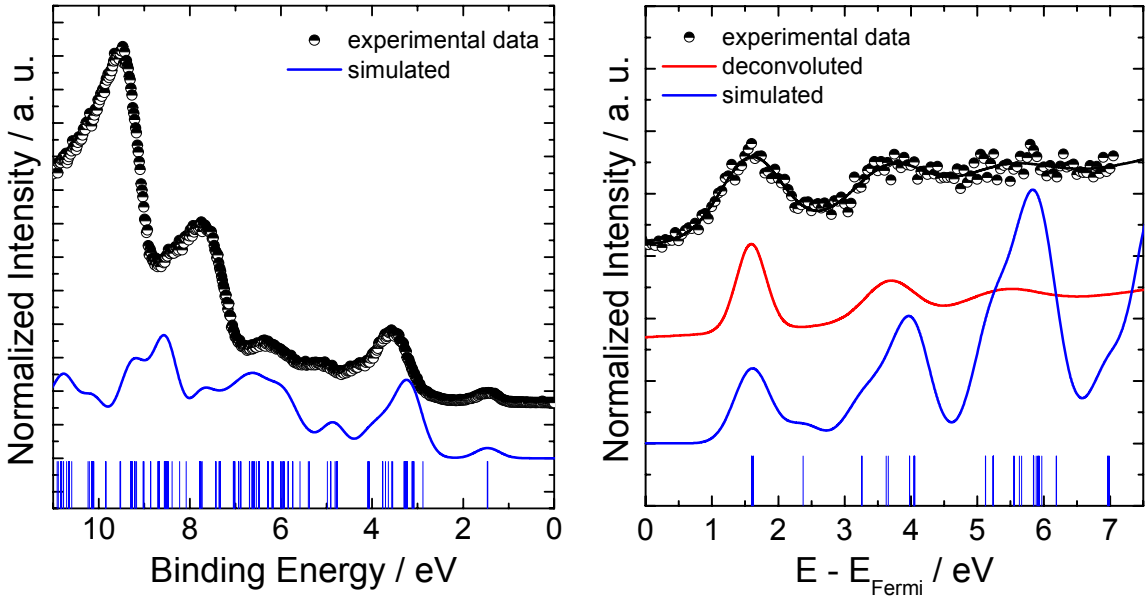

a) b)

Figure 5.28 a) Experimental and simulated VB-PES spectra of F_{16}CuPc; b) Experimental and simulated IPES spectra of F_{16}CuPc. The vertical lines in figures a) and b) mark the energy positions of the calculated MO.

An inequality in the energy positions of the calculated and experimental spectra appeared once more. The HOMO was shifted by 1.2 eV away from the Fermi level and LUMO was shifted towards the Fermi level by 0.22 eV for obtaining the overlap of the spectra. The similar line shapes obtained for both computer-generated and experimental VB-PES and IPES spectra demonstrate that also for this material the inter-molecular bonds are weak. Comparing these simulations to the ones obtained for H_2Pc, CuPc and F_4CuPc, we can assert that here there is less agreement between experiment and theory. This probably indicates that the high number of fluorine atoms needs a slightly different theoretical approach.

No publication has been found that investigates the F_{16}CuPc molecule by means of theoretical calculations.

Moving forward in the analysis of the spectra given in Figure 5.24, one can derive the evolution of the electronic properties as a function of film thickness as displayed in Figure 5.29 (a). At the zero point the electronic properties of H-Si were included once more. The changes that appear in EA, ϕ and IE are opposite to the previously discussed ones of other Pcs. EA, ϕ and IE are all increasing. The difference between the EA value of the first layer of F_{16}CuPc and the one corresponding to H-Si amounts to 0.46 eV. As

the thickness increases, EA increases further. The thickness range of the increase extends to 3.7 nm of F_{16}CuPc. Above this thickness EA becomes approximately constant to a value of (4.52±0.2) eV which corresponds to the organic material. Judging from the energy band diagram shown in Figure 5.29 (b), the EA includes both the large interface dipole and the 0.6 eV shift of LUMO. The total barrier height for electrons amounts to 0.02 eV.

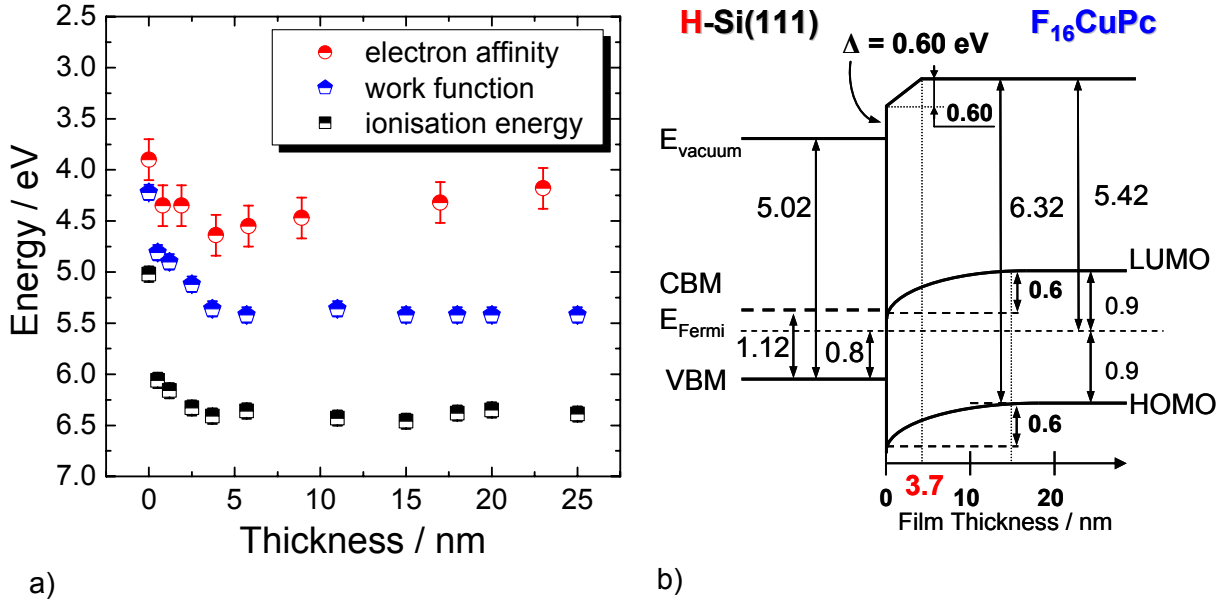

Figure 5.29 a) EA, ϕ, IE as a function of F_{16}CuPc layer thickness; b) Energy band diagram of the F_{16}CuPc/H-Si interface. The surface band bending of the substrate was omitted.

The variation in EA at the interface has a value of about 0.6 eV which is the exact difference between the interface dipole and the LUMO shift. The work function ϕ behaves similarly to EA in terms of direction of change and range of thickness where the change takes place. ϕ increases suddenly by 0.6 eV upon the first deposition indicating the formation of an interface dipole. The extent of the interface dipole can be estimated by the observed continuous increase of ϕ within 3.7 nm. Above 3.7 nm, ϕ is constant at (5.42±0.07) eV. The final value of the interface dipole is Δ=1.20 eV. IE increases in the same range of thickness of 3.7 nm. Upon the first deposition, IE increases by approximately 1.3 eV value which stands for the barrier for holes at the interface (0.7 eV) and the rigid shift of the vacuum level (0.6 eV). Then IE continues to increase. Above 3.7 nm of F_{16}CuPc, IE reaches a constant value of (6.32±0.07) eV which corresponds to that of thick F_{16}CuPc [She01]. Also in this case as determined for EA, IE contains the interface dipole contribution and the HOMO shift, namely the variation observed for IE is given by the 0.6 eV difference between them.

Figure 5.29 (b) summarizes the evolution of the interface between F_{16}CuPc and H-Si. The energy band diagram shows the presence of both interface dipole and band bending like behaviour similar to the previous case of CuPc. The interface dipole formation is driven by the difference in ϕ of the two materials. Thus it can be explained in a similar way to Figure 3.8 (b). However, the additional presence of the energy shifts of the HOMO and LUMO features as a function of layer thickness requires another explanation.

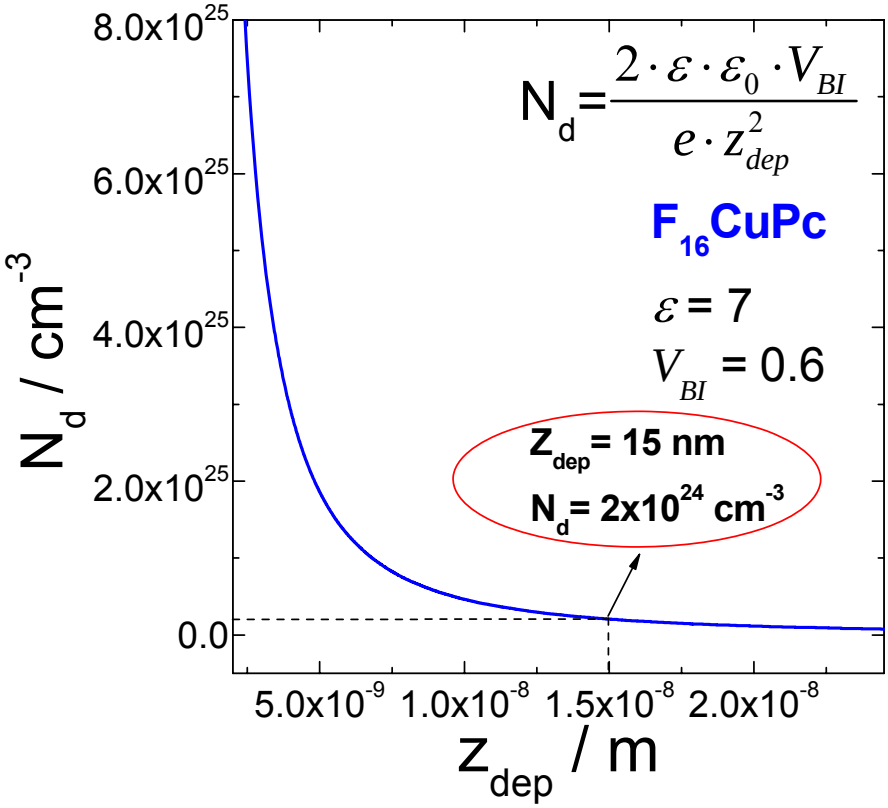

Figure 5.30 The Schottky formula applied in the F_{16}CuPc case. The charge carrier density as a function of the depletion width.

On the other hand, the band bending like energy shifts of the HOMO and LUMO can not be accounted for considering the classical theory of inorganic semiconductors.

As discussed for CuPc which presents the same type of behaviour but bending in opposite direction, the value of the shift in such a range of thickness would give an unreasonable concentration of carriers in the organic material.

Figure 5.30 illustrates the Schottky formula for F_{16}CuPc. Thus the charge carrier density calculated this way amounts to $2 \cdot 10^{24}$ cm^{-3}. Due to the unrealistic value of the charge carrier density obtained this way, we must take into consideration other types of phenomena that could induce such behaviour. In the previous case of F_4CuPc the presence of smaller shifts and in opposite direction to CuPc can be attributed to the presence of fluorine atoms which are compensating the so-called effect of the copper

atom. While in CuPc the change in molecular orientation from monolayer range to thick film is producing the energy shifts around the gap, in F_4CuPc the same observed change in the molecular orientation has a less visible effect due to the presence of four fluorine atoms. However, the situation of the F_{16}CuPc material is quite different.

Since classic theory of band bending can not account for this type of shift, the molecular orientation of the molecules was taken into consideration. As discussed before for CuPc and F_4CuPc, it is known that a change in the orientation of the molecules can influence the energy positions of the molecular orbitals by influencing the π-π overlapping. Therefore NEXAFS measurements were also employed in the characterisation of thin and thick films of F_{16}CuPc.

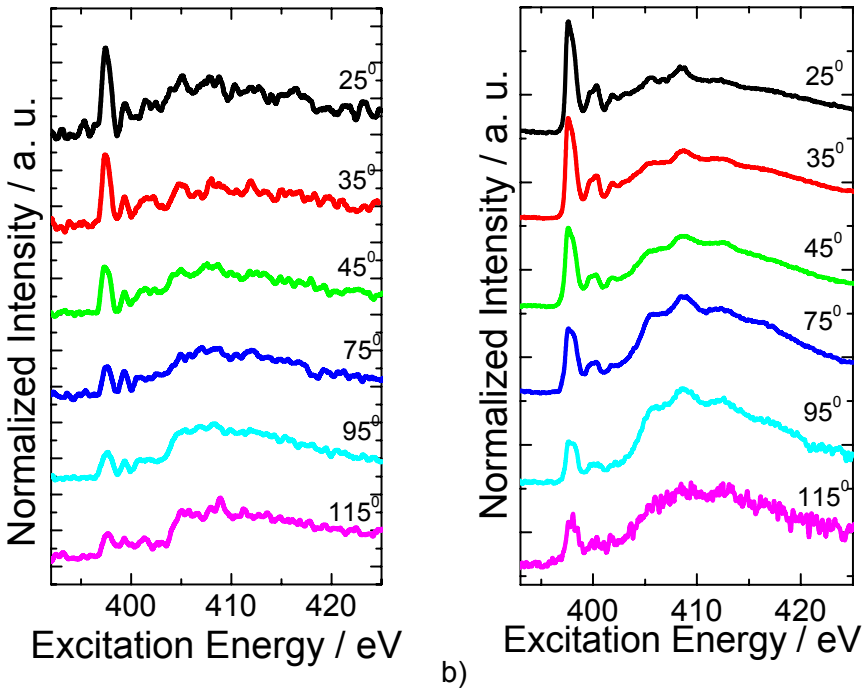

Figure 5.31 a) N1s excitation spectra a) 2 monolayers of F_{16}CuPc and b) 20 nm of F_{16}CuPc as a function of θ the angle of incidence; the lower energy features (398-403 eV) represent the π* resonances, while the features above 403 eV are related to the σ* resonances.

The N 1s excitation spectra of a) 2 monolayers and b) 20 nm thickness as a function of the angle of incidence θ of the synchrotron radiation are displayed in Figure 5.31 (a) and (b). Judging by the small intensity of the π^* features obtained with respect to the σ^* features in both films, the molecules are rather well ordered. The previously discussed molecules CuPc and F_4CuPc show comparable intensities in the π^* and σ^* features and that suggests the presence of short range ordering in both cases. The normalization procedure for the 2 monolayers and 20 nm of F_{16}CuPc was the same as for the thick film (20 nm) of F_4CuPc due to the presence of a minimum in the π^* resonance intensities in

both cases. Consequently Figure 5.32 (a) and (b) display the difference of the resonance intensities and the minimum resonance intensity. Namely, the N 1s excitation spectra corresponding to the minimum π^* intensity was subtracted from all the given N 1s NEXAFS spectra. The fits of the resonant intensities are displayed as well. Also in this case, the substrate symmetry was not helpful for the fits. Any employment of the reduced formulas [Stö92] for substrates with higher symmetry failed. Thus the same conclusion has been reached that the roughness lifts the symmetry of the substrates.

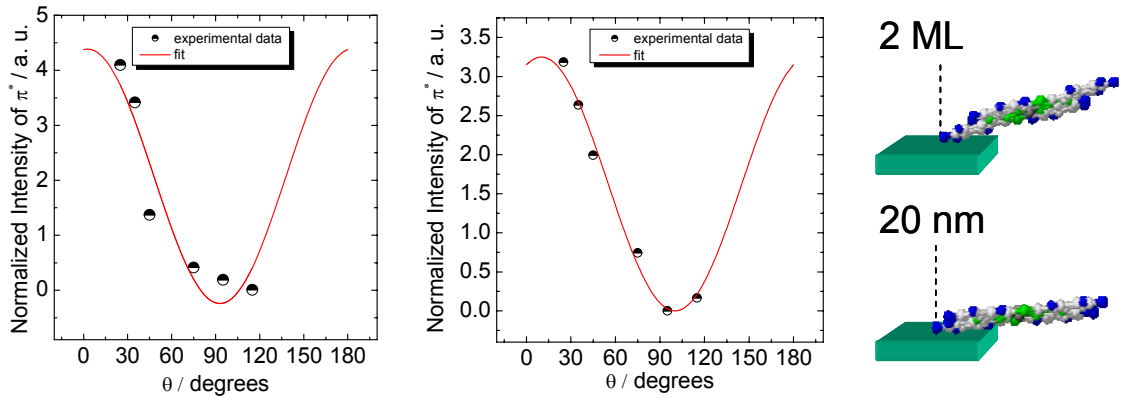

Figure 5.32 Normalized resonance intensity of the π^* features (the highest intensity feature in the N1s excitation spectra in Figure 5.31 (a) and (b)) as a function of the incidence angle of the synchrotron radiation of a) 2 monolayers and b) 20 nm of F_{16}CuPc; c) average molecular orientation of F_{16}CuPc in 2 monolayers (ML) and 20 nm.

Therefore the fits were performed using Eq. 3.25. The resulting tilt angles α and azimuthal angles ϕ are shown in Table 5.3. The listed values can only be considered as representing an average molecular orientation in the films. Opposite to CuPc and F_4CuPc, the F_{16}CuPc molecules are almost lying flat on the substrate.

	Tilt angle α	**Azimuthal angle ϕ**
2 ML	$26^0 \pm 2^0$	$84^0 \pm 5^0$
20 nm	$10^0 \pm 2^0$	$0^0 \pm 0.3^0$

Table 5.3 Calculated angles from the π^* resonance intensities fit for 2 monolayers and 20 nm of F_4CuPc.

However, there is a different molecular orientation when comparing a thin film (2 ML) to a thick one (20 nm). As discussed for the previous two molecules CuPc and F_4CuPc, the strength of the interaction between the molecule and the substrate is larger than the one developed between the F_{16}CuPc molecules in a film. Any other situation would lead to no change in molecular orientation. As for the classification of the interaction strength between the F_{16}CuPc molecule and H-Si compared to the other two

molecules we can say that by far this one is the strongest one. Due to the almost lying flat position of the molecule, the interaction probability between the F_{16}CuPc π orbitals and H-Si σ orbitals is the highest.

The found change in molecular orientation, when passing from a thin to a thick layer, is quite important in the context of the photoemission data since such changes in the molecular orientation may induce energy shifts of the MOs.

5.5 The Influence of the Fluorine Atoms

The starting point in establishing the influence of the fluorination on the interfaces discussed above will be a summary of the electronic properties of all the molecules (Table 5.4).

	Φ / eV	**IE / eV**	**EA / eV**
H_2Pc	(4.04 ± 0.07)	(4.96 ± 0.07)	(2.74 ± 0.2)
CuPc	(3.87 ± 0.07)	(4.82 ± 0.07)	(2.65 ± 0.2)
F_4CuPc	(4.70 ± 0.07)	(5.55 ± 0.07)	(3.60 ± 0.2)
F_{16}CuPc	(5.42 ± 0.07)	(6.32 ± 0.07)	(4.52 ± 0.2)

Table 5.4 Electronic properties of Pcs.

Slightly lower IE, Φ and EA values can be observed for CuPc than for H_2Pc. The difference amounts to approximately 0.15 eV. This is expected when taking into account the electron affinity of the centre Cu atom (1.22 eV) [Hot75, Bil98] which is lower than the EA of the two hydrogen atoms (2·0.756 eV) in H_2Pc.

Thus the addition of a Cu atom to the H_2Pc molecule brings additional charge (valence electrons) and decreases the overall EA of the resulting molecule (CuPc). Then again, the addition of fluorine to the CuPc molecule increases EA as shown in Table 5.4 for the fluorinated Pcs. Considering that the EA of a fluorine atom has a value of 3.2 eV and an electronegativity of 4 eV (Pauling scale), an overall increase in EA of a molecule is expected. To prove this we calculated the mean value of the electron affinity and electronegativity of each molecule based on the corresponding values of each atom. The obtained values are displayed in Figure 5.33. The CuPc and H_2Pc mean values are approximately the same, while the ones belonging to F_4CuPc and F_{16}CuPc are larger, their increase depending on the number of fluorine atoms. Thus we can conclude that the presence of the fluorine atoms increases the EA of the molecule and influences the

interaction mode of the molecule with the H-Si substrate. On the other hand, the resulting transport gaps show a dependence on the degree of fluorination as well.

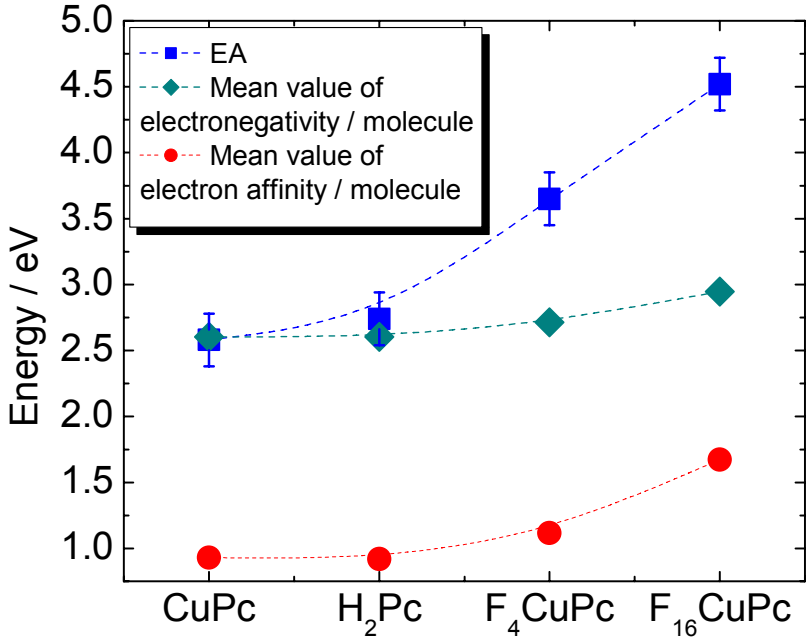

Figure 5.33 Comparison of the experimental determined EA and the calculated values of electron affinity and electronegativity of each molecule. The electron affinity calculus was performed by averaging the known atomic values and the electronegativity calculus by geometric mean of the atomic values.

To be precise E_t of CuPc and H_2Pc has the same value of (2.2±0.2) eV, then E_t decreases with the increasing number of fluorine atoms in the molecule, e.g. (1.95±0.2) eV for F_4CuPc and (1.8±0.2) eV for $F_{16}CuPc$. This trend is more or less preserved in the values of the DFT estimated gaps of these materials (Figure 5.34). Here it is important to mention that the DFT estimated gaps may be better compared to the photoemission peak-to-peak determined band gaps since these have no polarisation contribution (P_- , P_+). The presence of the same value for E_t of CuPc and H_2Pc is expected since there is no metal contribution to their HOMO and LUMO [Yos01]. In addition, the HOMO and LUMO of the fluorinated molecules are extended over the fluorine atoms as shown in the charge distributions from Figure 5.34. This clearly indicates that the fluorine modification of phthalocyanines plays a major part in the band gap, EA and IE modifications. This situation can be analyzed based on the high electronegativity of the fluorine atoms. Fluorine having an electronegativity of 4 eV, which is maximum on the Pauling scale, induces additional charge of positive sign on the π system of the Pc's. Therefore IE increases as a function of the number of fluorine atoms. However, when addressing the EA increase of the Pc molecules upon fluorine modification, the electron affinity of fluorine (EA_F) must be taken into account (Figure 5.33).

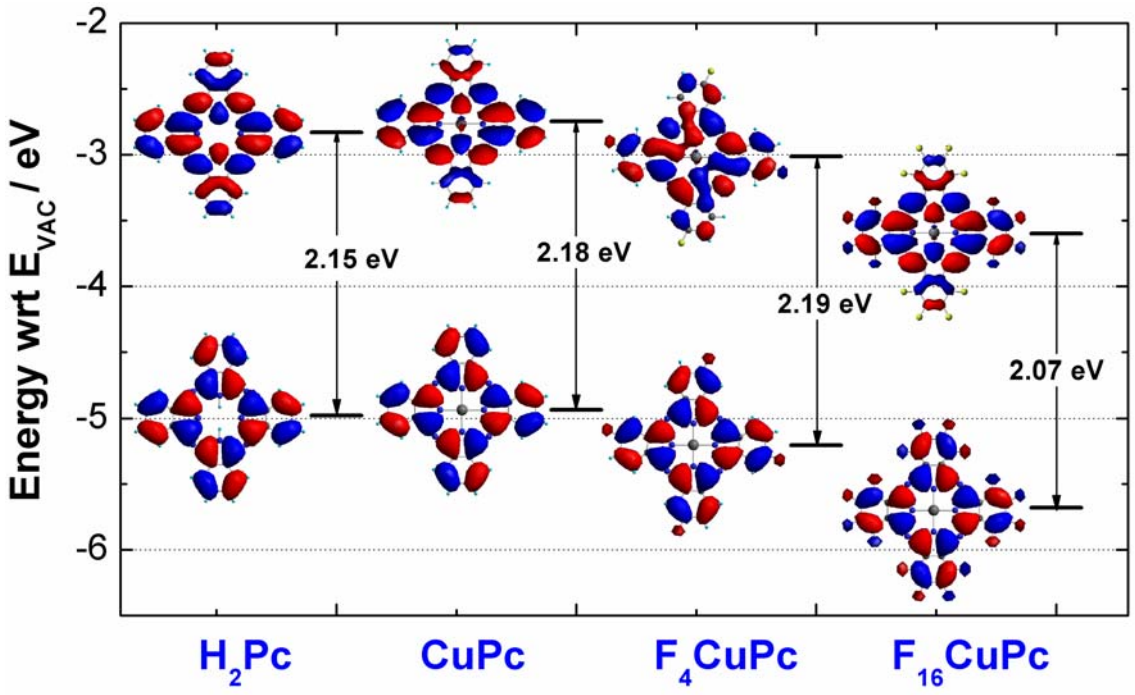

Figure 5.34 The DFT estimated transport gaps of H_2Pc, CuPc, F_4CuPc and $F_{16}CuPc$ and their HOMO and LUMO charge distributions.

The EA_F has a value of 3.2 eV resulting in a different slope of the increasing EA function than the IE one. Thus the transport gap varies with the increasing number of fluorine atoms.

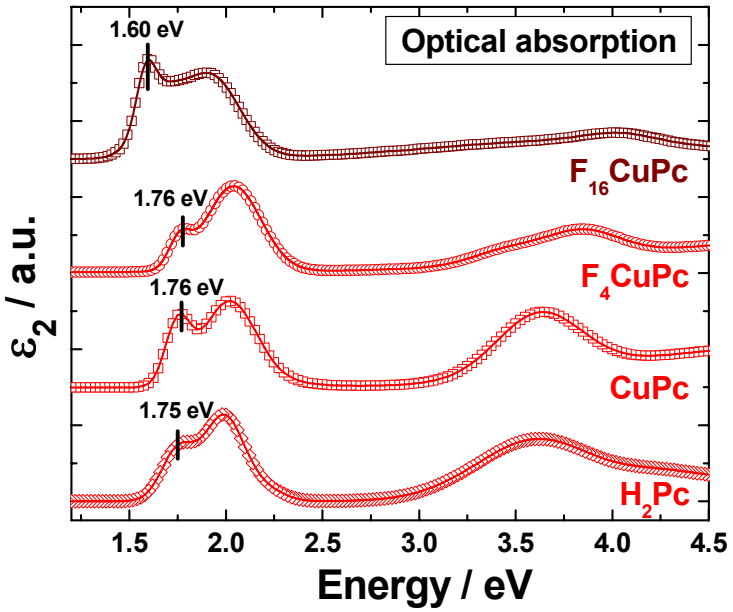

Figure 5.35 Imaginary part of the dielectric function (ε_2) for H_2Pc, CuPc, F_4CuPc and $F_{16}CuPc$. The spectra were rescaled in order to be plotted in the same graph. Marked with vertical line are the first absorption peaks whose positions correspond to the optical gaps.

A similar behaviour is found in the values of the optical gaps. Figure 5.35 contains the imaginary part of the dielectric function ε_2 for the Pcs/H-Si systems obtained from spectroscopic ellipsometry measurements. The H_2Pc and CuPc dielectric functions are taken from ref. [Gor04-1, Gor04-2]. In the energy range of 1.4 eV up to 2.4 eV the Q absorption band of Pcs resides [Lez89]. The first absorption peak placed at lower energy corresponds to the optical gap of the organic material. The determination of the optical gap is not a subject of the present work thus further details can be found in dedicated literature. The values of the optical gaps, calculated gaps as well as the values for the transport gaps and peak to peak gaps are shown in Table 5.5.

	E_t / eV	E_{opt} / eV	E_{calc} / eV	$E_{peak\text{-}to\text{-}peak}$ / eV
H_2Pc	(2.2 ± 0.2)	1.75	2.14	(3.2 ± 0.2)
CuPc	(2.2 ± 0.2)	1.76	2.18	(3 ± 0.2)
F_4CuPc	(1.95 ± 0.2)	1.76	2.19	(2.85 ± 0.2)
$F_{16}CuPc$	(1.8 ± 0.2)	1.60	2.07	(2.78 ± 0.2)

Table 5.5. Transport gaps, optical gaps, DFT estimated gaps and peak-to-peak VB-PES and IPES estimated gap of phthalocyanines.

The change in the total interface dipoles is driven by the change in work function Φ. Thus the total interface dipoles that arise at the interfaces scale linearly with the work function Φ of the Pcs. We considered the total interface dipole as given by the sum of the abrupt dipole that forms at the interface upon the first organic deposition and the continuous shift that appears upon further depositions. Figure 5.36 shows a plot of the total interface dipole formed at Pcs/H-Si interfaces as a function of the EA, Φ and IE of each Pc. The dashed lines are linear fits to the experimental points. The slopes of the linear fits are 0.78, 1 and 1.03, respectively. Such a strong change in the interface dipole due to fluorination was observed as well for the fluorinated Pcs deposited on Au [Pei02-2]. The same linear dependence of IE and Φ was observed, namely the calculated slope for IE has a value of 1. A comparison of the present data and the data obtained for the Pcs/Au interfaces from ref [Pei02-2] is displayed in Figure 5.36. Taking a closer look at the ϕ dependence, we can observe that when the total interface dipole is zero, ϕ has a value of approximately 4.26 eV. This is extremely close to the determined ϕ value for H-Si which is (4.22±0.07) eV.

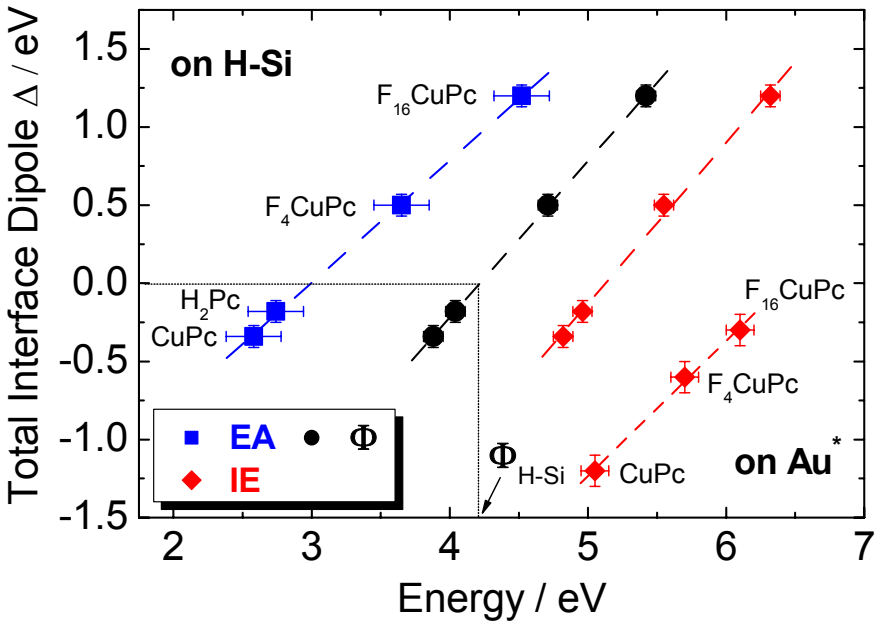

Figure 5.36 Total interface dipoles formed at Pcs/H-Si interfaces as a function of EA, ϕ and IE of the Pcs. Where the total interface dipole is 0, Φ has a value of 4.22 eV which corresponds to H-Si. The data points for Pcs/Au are taken from ref. [Pei02-2].

This is a clear indication that the interface dipole can be predicted by knowing the difference in ϕ of the materials. However, the slope of the linear dependence has another origin proportional to the degree of fluorination.

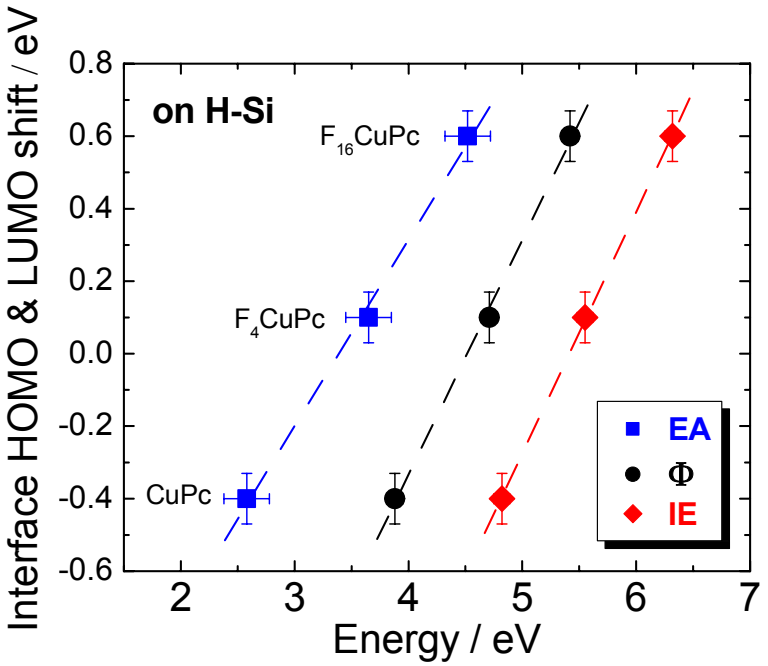

Figure 5.37 The HOMO and LUMO parallel shifts formed at Pcs/H-Si interfaces as a function of EA, ϕ and IE of the Pcs. These continuous shifts are the ones attributed to the band bending-like behaviour.

Comparing the results obtained for the two types of substrates we can conclude that the slope values are quite similar and thus lead to the following assertion. The behaviour of the molecules in contact with different materials e.g. interface energy shifts, is driven by their degree of fluorination.

On the other hand, besides the interface dipole formation found at the interfaces, we also found a band bending like behaviour for the CuPc, F_4CuPc and F_{16}CuPc molecules. A plot of the parallel shifts of HOMO and LUMO as a function of EA, ϕ and IE of the Pcs is shown in Figure 5.37. As observed there is a linear dependence between these shifts and the electronic parameters of the organic materials. As the parameters increase due to the degree of fluorination of the molecule, the HOMO-LUMO shifts are changing direction, basically turning form an upward direction found for CuPc (the negative value here) to a downward one as determined for F_4CuPc and F_{16}CuPc. The slopes of the linear fits of the experimental points are 0.51 for EA, 0.64 for ϕ and 0.66 for IE.

5.6 Summary

In this chapter VB-PES, IPES and NEXAFS were employed in the monitoring of the interface formation between H_2Pc, CuPc, F_4CuPc, F_{16}CuPc and H-Si(111). The energy level alignment was determined in each case and thus parameters such as EA, ϕ, IE and E_t were also estimated within the accuracy of the technique. A comparison was made between the VB-PES and IPES phthalocyanine characteristic spectra and the simulated ones resulting in a rather good agreement. The simulations were convoluted based on the DFT calculation of the energy levels for one molecule. A qualitative assignment of the HOMO and LUMO was achieved. Mixed cases of interface dipole formation and band bending like behaviour were found at these interfaces. Here the interface dipoles can be predicted by the ϕ difference of the Pc and the H-Si substrate. On the other hand, the band bending like behaviour was found to depend on the change in molecular orientation. The NEXAFS results point at a change in the molecular orientation when passing from a thin layer of Pc e.g. 2 monolayers to a thick layer of Pc e.g. 20 nm. Moreover, the direction of the band bending is found to be dependent on the molecular degree of fluorination.

Chapter 6. Chemical Stability of Pcs

The determination of the chemical stability of the phthalocyanine materials was achieved in the present work by studying their interaction with a metal and a gas. The metal chosen for this investigation was silver (Ag) since it is mostly investigated as contact material in electronic devices [Wu04]. The interface properties and energy level alignment are particularly important due to their role in the injection of carriers into the organic layer. Therefore there are many studies concerning this topic. However, most of them concentrate on organic-on-metal systems. For example, the CuPc/Au interface shows low chemical interaction [Pei02], strong shifts of all electronic levels are present for the early stages of CuPc deposition on Au. This behaviour is attributed to final state screening effects. A large interface dipole is present as well. Another case studied is the interface formation of F_4CuPc/Ag(111) and F_4CuPc/polycrystalline Ag [Sch04]. There a new occupied electronic state placed at 0.4 eV confirms a negative charge transfer from the silver substrate to the organic semiconducting material. An extreme case is present at the F_{16}CuPc/Al interface where a strong chemical interaction is present [She01-2]. This leads to the formation of an abrupt insulating $(F_{16}CuPc)_3Al$ layer. On the other hand, the same article describes the interface formation of Al on F_{16}CuPc (metal-on-organic). In this case an extended insulating layer appears. Its thickness is thus found to depend strongly on the interface formation sequence.

The present work concentrates on the metal-on-organic systems studied by means of photoemission and inverse photoemission.

The selected gas was molecular oxygen (O_2) due to several reasons. The most important of them are the following. Being the most important component of the atmosphere, oxygen is also the main factor that could produce degradation of electronic devices containing organic materials. Hence most of the electronic devices are covered by a protective layer. Another more specific reason would be that oxygen acts as a doping material for several phthalocyanines e.g. CuPc, having as a result a large increase in their conductivity [Mck98]. Such behaviour has been established by current-voltage (IV) investigations. However, photoemission investigations have not been employed sufficiently in determining the influence of molecular oxygen on the electronic

properties of the organic materials. Consequently in this work, thick films (~ 20 nm) of Pcs are exposed to molecular oxygen and the change in their electronic properties is monitored.

Before proceeding to the experimental data analysis of the Ag/Pc interfaces, the VB-PES spectrum of Ag/H-Si(111) is described. Figure 6.1 (a) contains such a spectrum. It is important to consider the properties of this system since some of the displayed feature will arise later on in the spectra of thicker Ag films on Pcs. As shown in the middle panel of Figure 6.1 (a) the features appearing in the energy range from 4 to 7 eV are the 4d states of Ag which usually indicate the metallic behaviour of the film. Another sign of such behaviour is the presence of the sp band that gives rise to the Fermi level [Arr02] (Figure 6.1 (a) right hand panel).

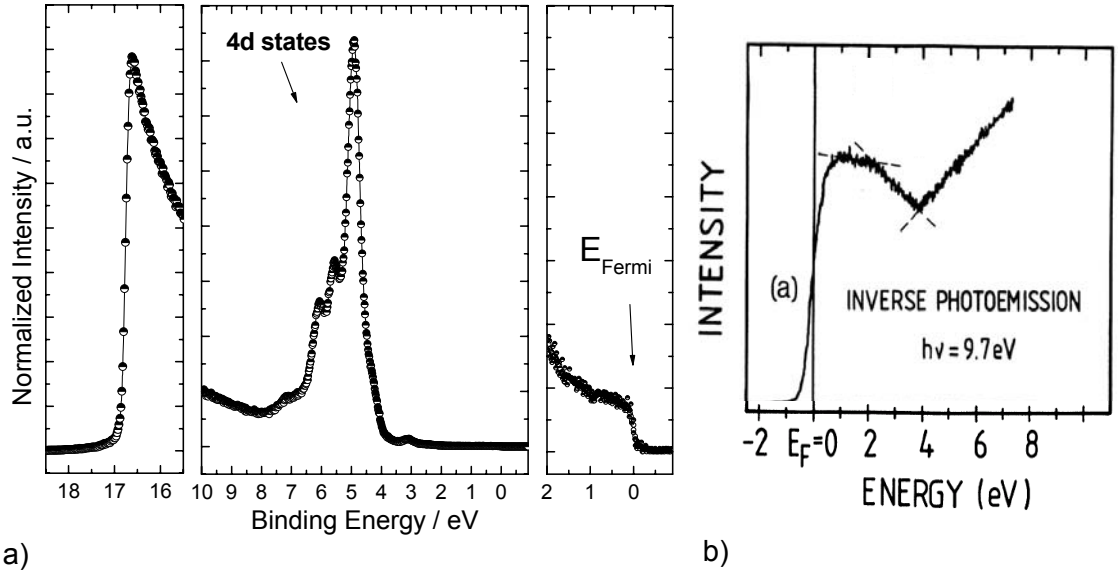

Figure 6.1 a) VB-PES spectrum of Ag/H-Si(111); b) IPES spectrum of polycrystalline Ag – taken from ref. [Rei84].

The work function of Ag obtained from the secondary electron region has a value of (4.35±0.07) eV. This is in agreement with literature, namely the determined value for polycrystalline Ag - 4.27 eV [Dwe71]. On the other hand, Figure 6.1 (b) displays the IPES spectra of polycrystalline Ag. At this point it must be noted that the spectra contain a broad feature centred at approximately 2 eV [Rei84], a feature that will later on appear in the IPES spectra of the Ag deposited on Pc.

At this point several experimental notes are needed. The following chapter discusses the VB-PES and IPES spectra of incremental Ag deposition on Pc thin films and incremental oxygen exposure of Pc thin films. The analysis of these spectra was extended by also plotting the FWHM, intensity and area of HOMO as a function of Ag layer thickness and oxygen exposure. In this case, the intensity and area plots require

careful attention due to the sensitivity of the VB-PES experiment to the alignment of He lamp, sample and analyser. The large scattering present in the intensity points is mostly due to the stepwise type of experiment. Since the Ag deposition was performed in another UHV chamber, the sample position was changed each time. The positioning of the sample was achieved each time by maximising the counts at a given energy position, usually the HOMO peak position. However, there is no guarantee that the same exact position of the sample is obtained and this is visible in the intensity fluctuations that are observed.

6.1 Ag/Pc Interfaces

6.1.1 Ag/H_2Pc

The VB-PES and IPES spectra measured for incremental coverages of Ag on H_2Pc are shown in Figure 6.2 (a) and (b) respectively. The VB-PES spectra were normalized with respect to the intensity at about 6.9 eV and shifted vertically for clarity. In the left hand panel of Figure 6.2 (a) following the secondary electron cut-off, we observe that Φ starts with an initial value of (3.9±0.07) eV.

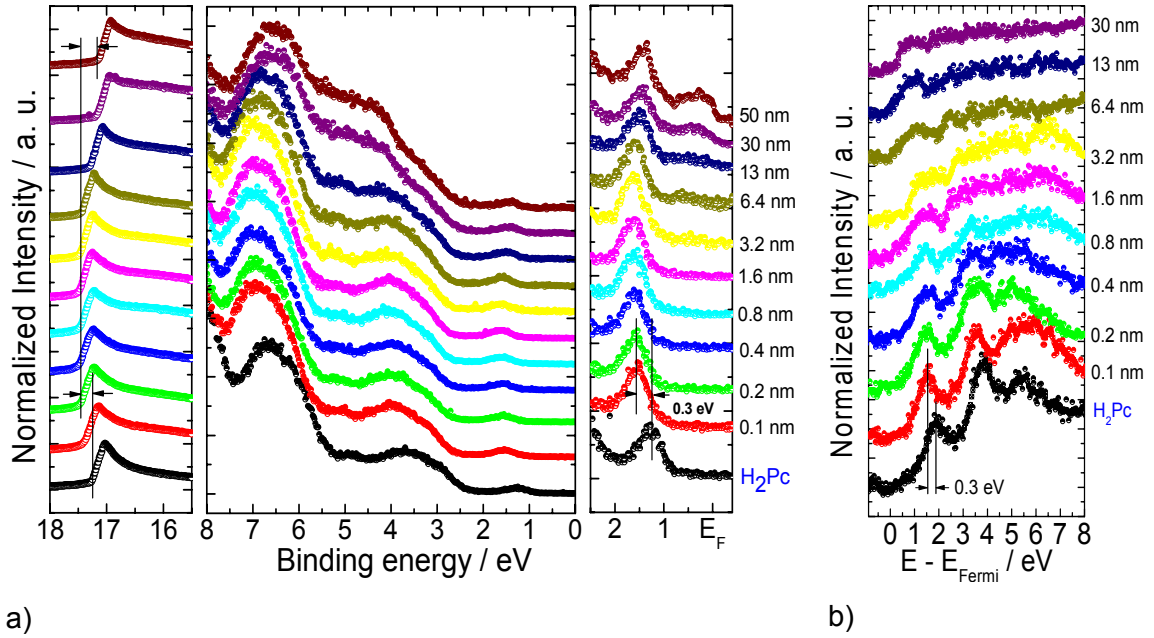

Figure 6.2 a) Thickness dependent VB-PES measurements on Ag/H_2Pc/H-Si(111); b) thickness dependent IPES measurements on Ag/H_2Pc/H-Si(111).

As the Ag thickness increases, Φ decreases to (3.7±0.07) eV, a value which is kept up to 3.2 nm Ag coverage. Above this thickness Φ increases up to a final value of (4.05±0.07) eV at 50 nm. Thus the interface dipole ranges from -0.2 eV to +0.15 eV. The evolution does not show signs of reaching a saturation point. The final Φ value is quite close to that of polycrystalline Ag [Dwe71] as mentioned above. Since that value is not reached, a saturation point for the electronic properties of Ag on H_2Pc is not reached. The middle panel of Figure 6.2 (a) depicts the main features of H_2Pc and their evolution upon Ag deposition. The 4d bands of Ag occurring in the range from 4 to 7 eV BE, become observable from 6.4 nm on and grow in intensity as the Ag thickness increases. Thus metallic Ag is formed. For a better view of the Ag characteristic features we plotted the VB-PES spectra corresponding to the bare H_2Pc film and to 30 nm of Ag on H_2Pc. The Ag spectra was shifted by 0.17 eV in order to overlap the dip present at 7.4 eV BE in both spectra given that this feature was not affected by the Ag deposition. Clear differences generated by Ag can be seen in the BE region from 4 to 7 eV (Figure 6.3). The VB-PES spectra contain overlapped signals from H_2Pc and Ag even at 50 nm of Ag.

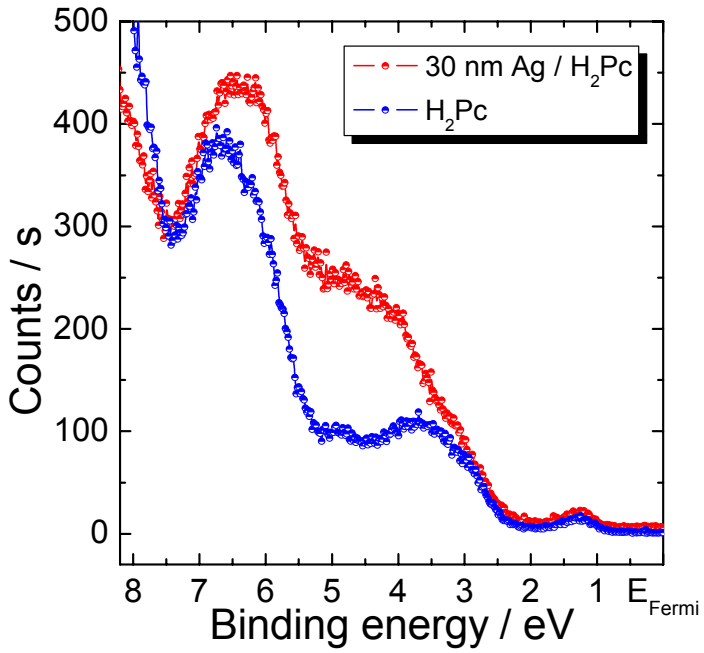

Figure 6.3 Comparison between VB-PES spectra corresponding to bare H_2Pc and to 30 nm of Ag on H_2Pc.

Since the photoelectron escape depth at 10-20 eV kinetic energy is about 1-1.5 nm [Car96] the conclusion can be reached that Ag does not form a closed film. This proves the developing clusters on the organic layer.

In the right hand panel of Figure 6.2 (a) we observe the HOMO of H_2Pc suddenly shifting by 0.3 eV away from the Fermi level upon the first Ag deposition. The HOMO position then remains fixed up to 6.4 nm where a small feature at 0.64 eV B.E. is visible. While this feature grows in intensity and finally develops a clear Fermi step at 50 nm of Ag, the still visible H_2Pc HOMO shifts back towards the Fermi level by about 0.2 eV. Following Figure 6.2 (b) we note that the LUMO presents the same sudden shift of 0.3 eV towards the Fermi level upon the first Ag deposition. This

position is preserved up to 3.2 nm. The characteristic features of the organic material are smeared out by its convolution with the density of unoccupied states of Ag.

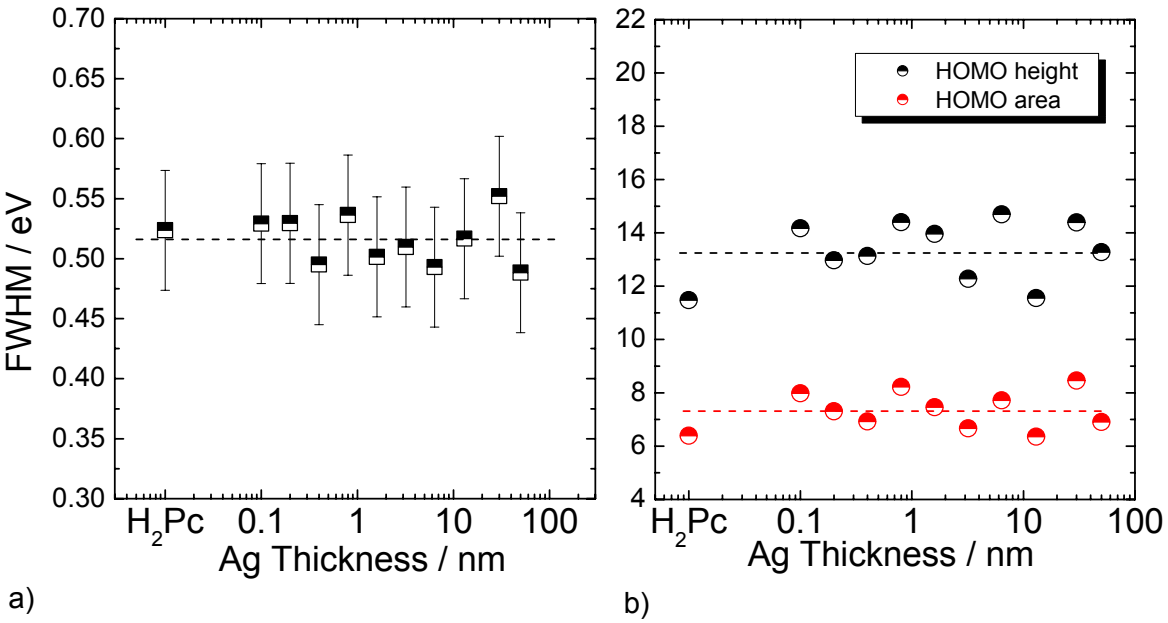

Figure 6.4 a) FWHM of H_2Pc HOMO as a function of Ag thickness; b) the height and area of HOMO as a function of Ag thickness.

However, the smearing out of the features takes place simultaneously with the appearance of the Fermi edge and of the 4d states in VB-PES spectra. This sustains the idea of an overlapping of IPES signals belonging to H_2Pc and Ag. The Fermi level is not resolved in the IPES spectra due to the low electron beam currents used in the experiment. At this point we should note that the beam currents used for obtaining the IPES spectrum of Ag from Figure 6.1 (b) are in range of 15 μA.

The evolution of FWHM of HOMO as a function of Ag thickness is shown in Figure 6.4 (a). The FWHM is approximately constant within the experimental error. Thus there is almost no influence on the HOMO FWHM due to the Ag layer. Moreover, the plot in Figure 6.4 (b) shows the behaviour of the height and area of the HOMO as a function of the Ag thickness. Both height and area of HOMO are almost constant as a function of Ag thickness, although the last Ag thickness reaches 50 nm. There is hardly any attenuation present. Taking into consideration the penetration depth of VB-PES which is 1-1.5 nm and the previous assertion we can conclude that Ag does not form a closed layer on top of H_2Pc. Considering the morphology of the organic one can assume that Ag fills up the gaps in the H_2Pc and afterwards at higher Ag thickness clusters are formed.

Figure 6.5 (a) and (b) summarize the properties of the Ag/H_2Pc interface by presenting the evolution of the electronic properties and the resulting energy level

alignment. As already described for ϕ, its value decreases by 0.2 eV upon the first two Ag depositions. This behaviour indicates the creation of new species on the surface of the H_2Pc film due to the Ag atoms.

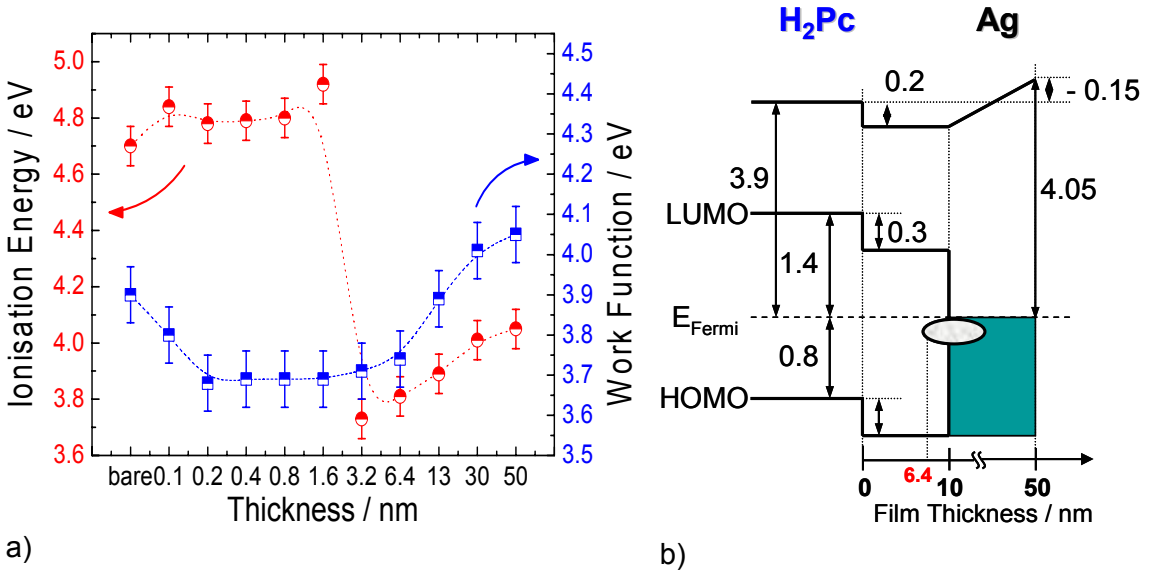

Figure 6.5 a) Evolution of IE and Φ for the Ag/H_2Pc interface as a function of Ag thickness b) energy band diagram of the Ag/H_2Pc interface.

The change in ϕ is simultaneous with the 0.3 eV energy shifts present in the HOMO-LUMO levels. Such sudden shifts in both MO and in the same direction especially towards higher BE indicate a charge transfer from H_2Pc to Ag atoms. Electrons flowing from H_2Pc towards Ag create positively charged organic layers resulting in an increased binding energy for all states (Figure 6.2 (a) middle panel). This is confirmed by the sudden increase of IE upon the first silver deposition (Figure 6.5 (a)). It is quite surprising in view of the fact that that the electron affinity of Ag atom is quite low (1.3 eV) compared to the EA of H_2Pc (2.74±0.2) eV. The interaction of Ag atoms with H_2Pc molecules at early stages of Ag deposition is thus quite strong and unexpected. Such behaviour suggests the formation of a charge transfer complex at the interface. As soon as the quantity of Ag increases and Ag clusters are created, an additional negative charge arises at the surface. In a similar way a small intensity feature appears at 0.64 eV BE. This indicates that the direction of the electron charge transfer is reversed. As a consequence the still visible HOMO of the organic material shifts by 0.2 eV back towards the Fermi level. Thus we can conclude that the Ag/H_2Pc interface formation can not be described only in terms of physisorption. Additional mechanisms are present at the very first deposition step indicating a considerably stronger interaction between the Ag atoms and H_2Pc molecules, i. e. the formation of a charge transfer complex.

6.1.2 Ag/CuPc

Figure 6.6 (a) and b) depicts the thickness dependent VB-PES and IPES spectra of Ag deposited on CuPc. The lowest VB-PES and IPES spectra correspond to 20 nm of freshly prepared CuPc and both exhibit the characteristic peaks of CuPc as shown in the previous chapter. The left hand side panel of Figure 6.6 (a) represents the secondary electron region as a function of Ag thickness. Thus changes of the vacuum level position can be determined and implicitly the variations in the surface work function Φ.

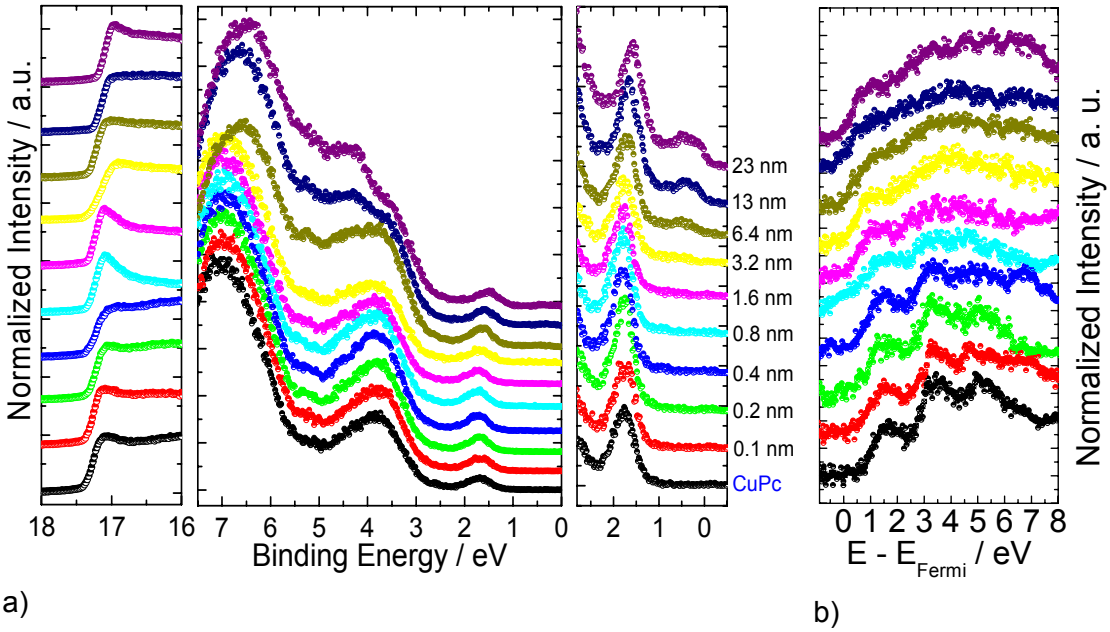

Figure 6.6 a) Thickness dependent PES measurements on Ag/CuPc/H-Si(111); b) thickness dependent IPES measurements on Ag/CuPc/H-Si(111).

In the right hand side panel of Figure 6.6 (a) we observe that the HOMO maintains its position up to 3.2 nm of Ag. Above that thickness, the HOMO shifts continuously towards the Fermi level until the Ag thickness reaches 23 nm. Moreover, the other higher BE HOMOs are also shifting towards the Fermi level (middle panel of Figure 6.6 (a)). The shift has a value of approximately 0.2 eV. It should be noted as well that at 3.2 nm of Ag a small feature arises at about 0.5 eV BE. As the Ag thickness increases, the feature gains intensity and develops into a Fermi step, hence the change in IE. Simultaneously specific Ag features namely the 4d bands arise in the energy region from 4 eV up to 7 eV. The presence of these bands starting with 6.4 nm of Ag proves the formation of metallic Ag. To bring out to light the characteristic features of Ag we plot in Figure 6.7 a comparison

between VB-PES spectra corresponding to bare CuPc and to 23 nm of Ag on CuPc. As before the spectra were shifted in such a way that the dips which are not influenced by the Ag layer and present at approximately at 8 eV BE overlap.

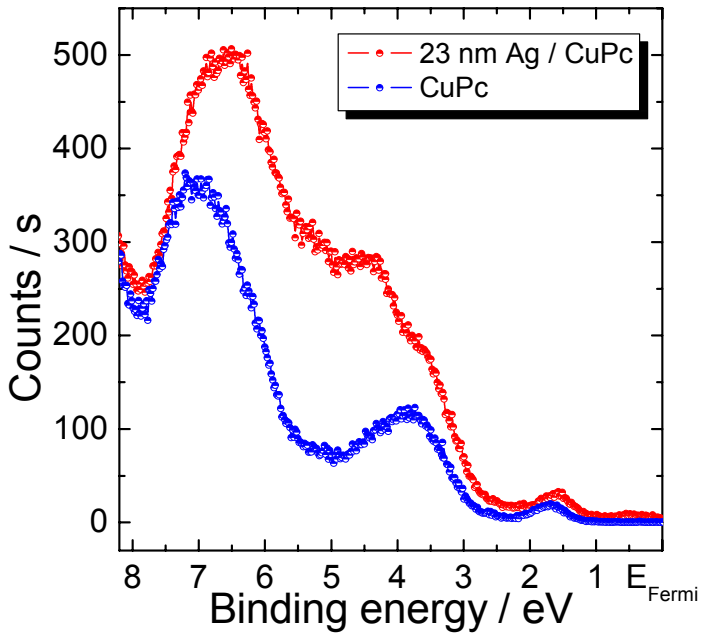

Figure 6.7 Comparison between VB-PES spectra corresponding to bare CuPc and to 30 nm of Ag on CuPc.

Surprisingly the VB-PES characteristic features of CuPc do not smear out in such a manner as the IPES characteristic features do (Figure 6.6 (b)). Still we can observe a similar behaviour of the LUMO in the early stages of Ag deposition. The LUMO resides at its value with respect to the Fermi level up to 1.6 nm of Ag, where the CuPc features are already diminishing. Since the IPES spectrum of polycrystalline Ag contains a rather broad feature centred at 2 eV [Rei84], we can not assume that at thicker Ag films the peak at 1.25 eV is still the LUMO of CuPc. Moreover, the Fermi edge is not resolved here as well as found before for H_2Pc. Therefore we conclude that also in this case the IPES spectra show a convolution of unoccupied CuPc and Ag states.

The evolution of the FWHM, height and area of CuPc HOMO is also plotted in Figure 6.8 a) and b). When comparing the data to H_2Pc, here we find a larger scattering in the experimental points in both plots. FWHM is constant within 0.1 eV, a value which is lower than the experimental resolution. The height and the area of HOMO are also constant as the Ag thickness is increasing which again point to cluster formation atop the organic and no diffusion into the CuPc film.

The evolution of Φ and IE as a function of Ag coverage as well as the energy band diagram are displayed in Figure 6.9 (a) and (b), respectively. In this case Φ initially has a value of (3.8±0.07) eV which is approximately constant up to 3.2 nm of Ag. Then Φ evolves to a final value of (4±0.07) eV for 23 nm of Ag which is quite close to the reported value for polycrystalline Ag (4.27±0.07) eV [Dwe71].

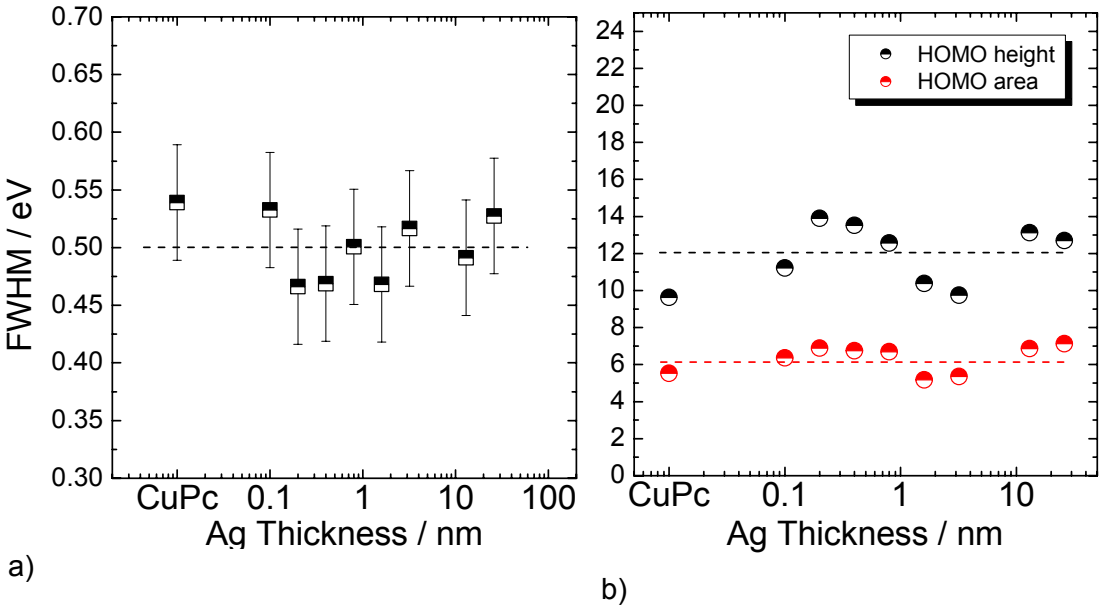

Figure 6.8 a) FWHM of CuPc HOMO as a function of Ag thickness; b) the height and area of CuPc HOMO as a function of Ag thickness.

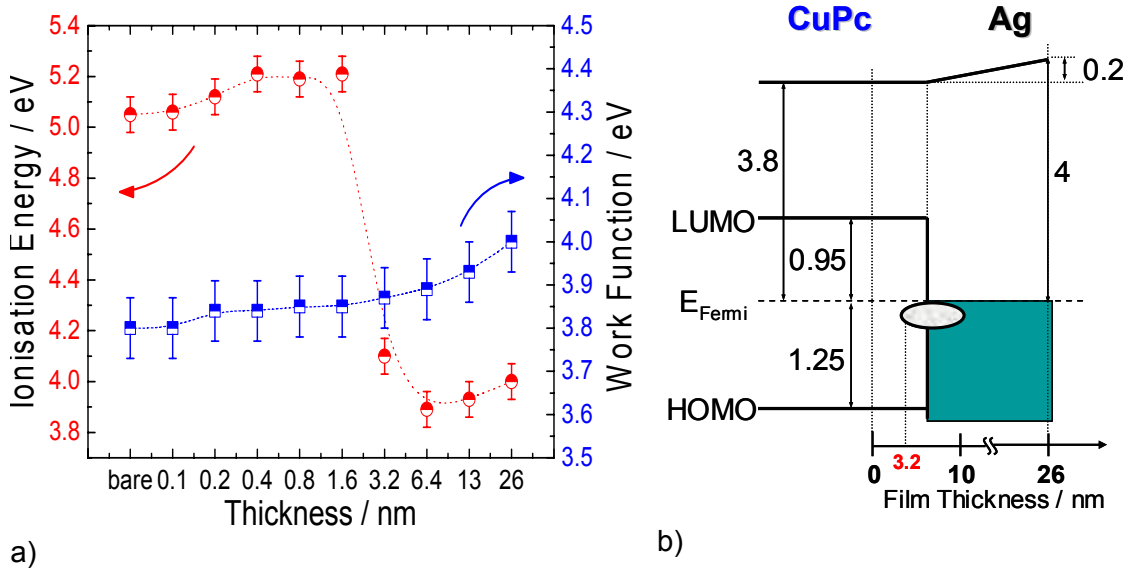

Figure 6.9 a) Evolution of IE and Φ for the Ag/CuPc interface as a function of Ag thickness; b) energy band diagram of the Ag/CuPc interface.

This suggests the existence of a similar morphology of Ag on CuPc and H_2Pc and that further Ag depositions are needed to reach a saturation point in the electronic properties of the Ag layer on top of CuPc. The interface dipole estimated from the change in Φ has a value of 0.2 eV. The IE only varies slightly as a function of Ag thickness up to 1.6 nm. When the 3.2 nm Ag thickness is reached, metallic Ag is present and consequently IE is identical to ϕ.

On the other hand, no chemical reaction is present at this interface since there is no sign of filling of unoccupied states of CuPc from an early stage of Ag deposition. The energy shift of all the higher B.E. HOMOs towards the Fermi level starting from 3.2 nm of Ag indicates the presence of a negatively charged layer at the surface. The appearance of a small intensity feature at 0.5 eV B.E. for 3.2 nm of Ag indicates charge transfer from Ag to the CuPc molecules. The additional negative charge provided by the Ag clusters acts as an accelerating electric field for the photoelectrons, resulting in shifts of the VB-PES features towards Fermi level. This interaction is rather weak since the overall shift of the molecular orbitals amounts to 0.2 eV. Thus we can presume that Ag is physisorbed on the surface of CuPc.

6.1.3 Ag/F_4CuPc

Following the same description procedure as for the other two Pcs, in Figure 6.10 (a) and (b) the thickness dependent VB-PES and IPES spectra of Ag deposited on F_4CuPc are presented.

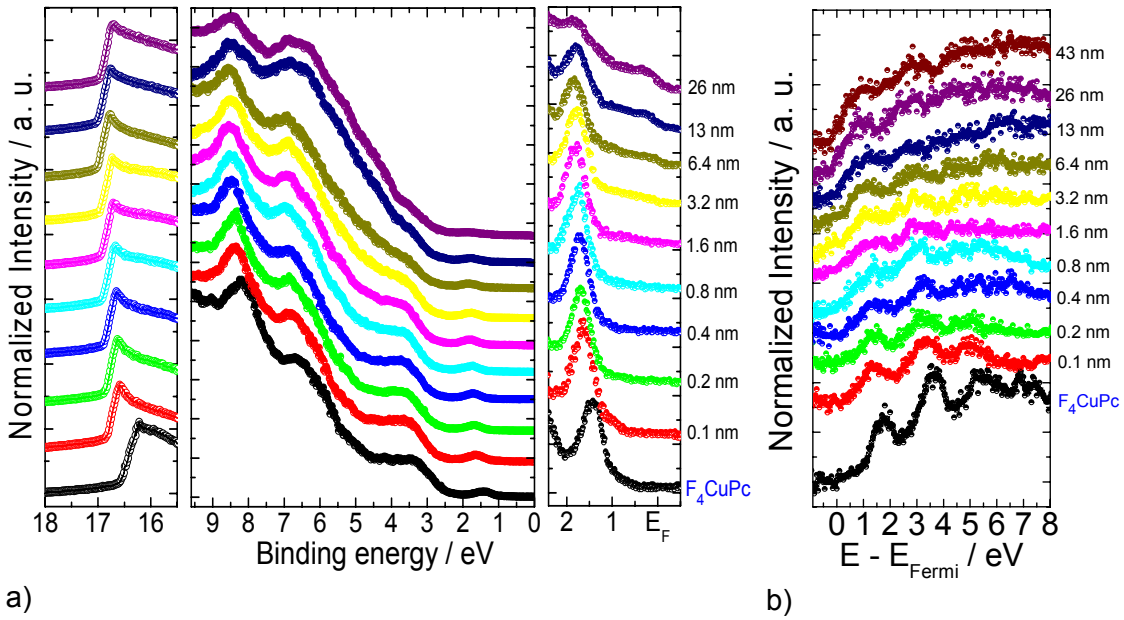

Figure 6.10 a) Thickness dependent VB-PES measurements on Ag/F_4CuPc/H-Si(111); b) thickness dependent IPES measurements on Ag/F_4CuPc/H-Si(111).

A sudden change in the secondary electron region (left hand panel of Figure 6.10 (a)) as well as in the HOMO position is visible after the first Ag deposition. This is quite similar to the shifts found at the Ag/H_2Pc interface. In the VB characteristic features of F_4CuPc

displayed in the middle panel of Figure 6.10 (a), one can observe a shift away from the Fermi level of all of them including HOMO upon the first Ag deposition.

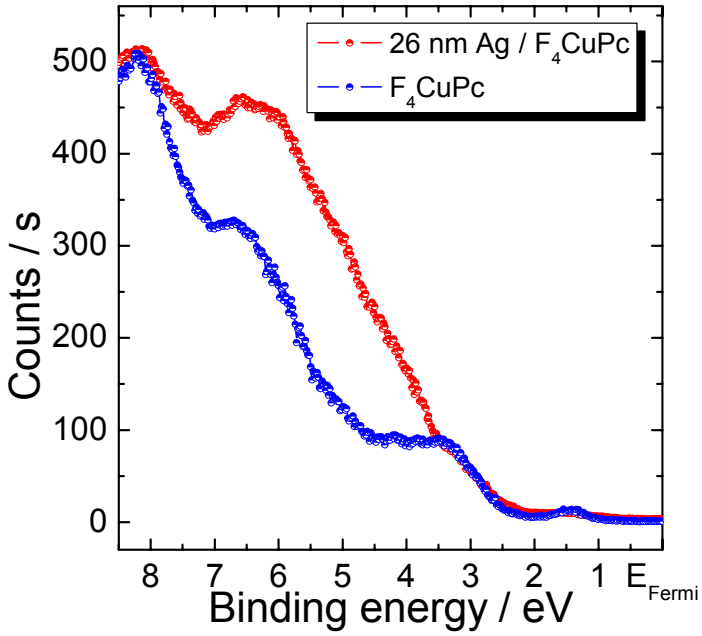

Figure 6.11 Comparison between VB-PES spectra corresponding to bare F_4CuPc and to 26 nm of Ag on F_4CuPc.

The shift amounts to 0.2 eV. Above 0.1 nm of Ag, the HOMOs continue to shift away from the Fermi level until approximately a thickness of 3.2 nm of Ag is reached. The additional shift has a value of 0.1 eV. Consequently the final value of the change in the HOMO position amounts to 0.3 eV. When the Ag thickness attains 3.2 nm, a small intensity feature arises at approximately 0.67 eV BE. Further on, this feature develops into the Fermi edge while in the range of 4 to 7 eV BE the 4d states of Ag emerge. An illustration of the 4d states is found in the comparison of the freshly prepared F_4CuPc layer and the thickest Ag film on F_4CuPc (Figure 6.11).

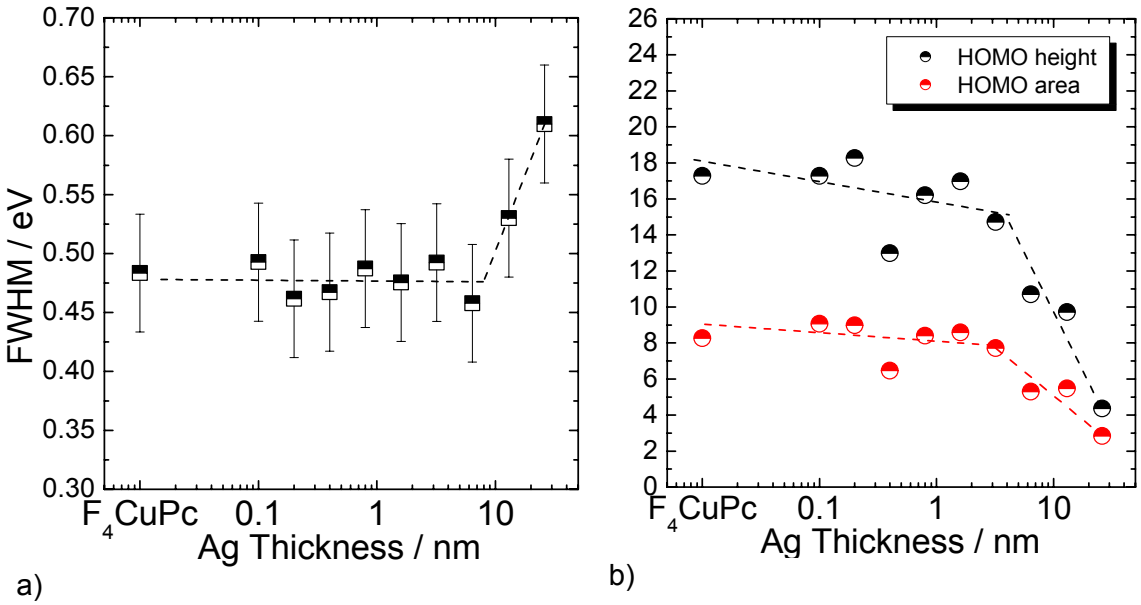

Figure 6.12 a) FWHM of F_4CuPc HOMO as a function of Ag thickness; b) the height and area of F_4CuPc HOMO as a function of Ag thickness.

In this case unlike in the previous two organic materials, the spectra of the Ag layer was shifted horizontally as to overlap the feature found at 8 eV, feature which is not affected by the Ag deposition.

At this point at 3.2 nm of Ag, metallic Ag is formed on the surface of the organic film. Since the recorded VB-PES spectra show features from both materials F_4CuPc and Ag even at 26 nm Ag coverage, we can conclude that the Ag layer is not closed and Ag clusters are formed. This conclusion is also sustained by the FWHM, height and area behaviour showed in Figure 6.12. Unlike the previous cases, here FWHM (Figure 6.12 (a)) is constant at about 0.47 eV up to 6.4 nm Ag thickness and subsequently is increasing to 0.61 eV. The height and area of HOMO (Figure 6.12 (b)) are dropping following functions with two different slopes. These findings point to a slight diffusion of the Ag atoms into the organic layer. The slope found from a thickness higher than 3.2 nm of Ag has a larger value than the one found at lower Ag thicknesses. This indicates the formation of larger Ag clusters than in the previous cases H_2Pc and CuPc. However, the morphology of the F_4CuPc film does not seem to account for the smearing out of the HOMO feature above 6.4 nm of Ag. Judging by the high roughness of the organic film, the feature should be at least at the same intensity displayed in the VB-PES spectra of the same thickness of Ag on H_2Pc or CuPc. Since this is not the case (Figure 6.12), one can conclude that the chemistry of the interface is slightly different from the previously investigated ones.

Turning our attention back to Figure 6.10 (b), the shifts in the HOMO levels are reproduced in the LUMO levels of the IPES spectra as well. Of course at thicker Ag coverage we deal with the same overlapping of the two IPES signals – one due to the F_4CuPc and the other one coming from the Ag film. Above 1.6 nm of Ag the IPES features are smeared out. In conclusion the analysis of the interface properties considering both VB-PES and IPES spectra will concentrate on the Ag thicknesses up to 3.2 nm.

Studying the changes in ϕ, a total interface dipole of 0.37 eV can be determined. Figure 6.13 (a) shows the evolution of ϕ and IE as a function of Ag thickness. Therefore, it can be observed that upon the first Ag deposition there is a drop in ϕ by 0.2 eV, similar to the energy shifts of the HOMO-LUMO level. ϕ has an initial value of (4.55$\pm$0.07) eV. While the Ag thickness increases, ϕ continues to decrease reaching a final value of (4.18$\pm$0.07) eV. Thus the interface dipole formed at this interface has a value of 0.37 eV. The secondary electron cut-offs seem to reach a saturation level when 6.4 nm Ag thickness is reached. ϕ determined for the final Ag layer is close to the previous ϕ value for the H_2Pc

and CuPc cases, indicating an analogous morphology of Ag atop the organic layer. On the other hand, IE is constant up to the point when the critical Ag thickness is reached (3.2 nm).

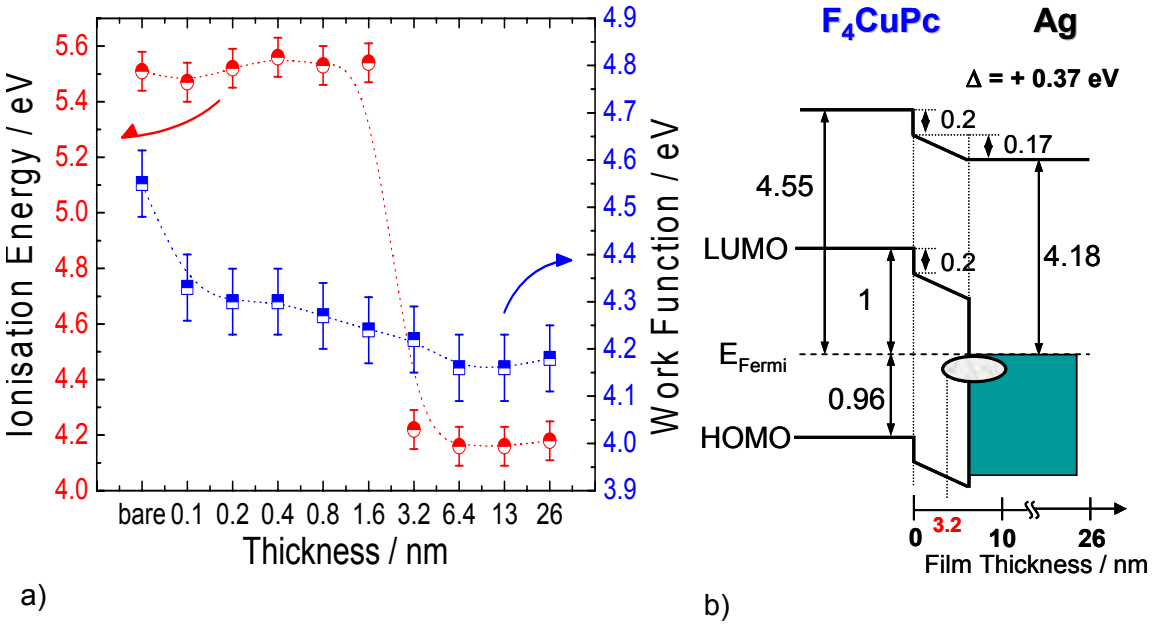

Figure 6.13 a) Evolution of IE and Φ for the Ag/F_4CuPc interface as a function of Ag thickness; b) energy band diagram of the Ag/F_4CuPc interface.

This finding is highly important since it proves that here there is no case of charge transfer complex formation as shown for Ag/H_2Pc interface.

The presence of simultaneous energy shifts of the HOMO and LUMO levels with respect to the Fermi level and towards a higher BE is similar to the already discussed Ag/H_2Pc interface. Only a charge transfer from the F_4CuPc molecules to Ag can justify such behaviour. This was previously assigned to the formation of a charge transfer complex. However such a “modification” of the molecules would immediately alter IE. This is not the case here as mentioned above. Thus Ag atoms are doping the organic materials conferring it a more n-type character. Moreover, the continuous shift of HOMO-LUMO levels to higher BE over a range of Ag thicknesses is due to a continuous input of Ag atoms diffusing into the organic material. The electronic properties of the interface are summarized in Figure 6.13 (b).

6.1.4 Ag/F_{16}CuPc

For the final Ag interface, the VB-PES and IPES spectra as a function of incremental Ag thickness are shown in Figure 6.14 (a) and b), respectively. The middle

panel of Figure 6.14 (a) contains the characteristic features of $F_{16}CuPc$ that upon Ag deposition shift towards higher BE in a similar way to H_2Pc and F_4CuPc. However, the value of the shift is slightly smaller – 0.17 eV.

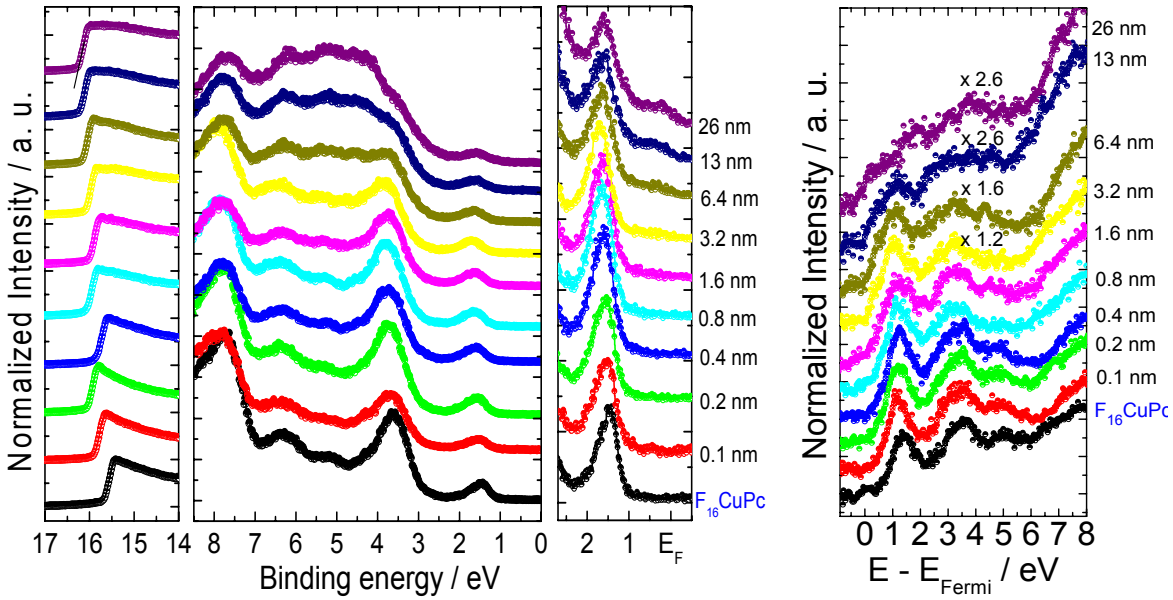

Figure 6.14 a) Thickness dependent VB-PES measurements on Ag/F_{16}CuPc/H-Si(111); b) thickness dependent IPES measurements on Ag/F_{16}CuPc/H-Si(111).

The critical Ag thickness above where the 4d states arise is the same as before – 3.2 nm of Ag. A better view of the 4d region placed within 4 to 7 eV is given in the comparison of the freshly deposited $F_{16}CuPc$ and the thickest Ag film shown in Figure 6.15. Similarly to previous plots of this type, the spectrum belonging to the Ag film of 26 nm was shifted in order to overlap the dip placed at approximately 9 eV BE, since this feature is placed outside the influence of Ag 4d features.

In the right hand panel of Figure 6.14 (a), for 3.2 nm Ag thickness there is a small intensity feature arising at approximately 0.4 eV. However, this feature is no well defined into a Fermi edge until the Ag thickness reaches 13 nm.

In the IPES spectra the same value of shift as in the HOMO position is found. The LUMO shifts towards the Fermi level and thus following the movement of the HOMO in the direction of higher BE. Unexpectedly, the IPES characteristic features of $F_{16}CuPc$ are still visible up to 6.4 nm and even 13 nm when enhancement is employed. Such behaviour may be due to a different morphology of Ag atop the organic material. However, the features are diminishing, namely their FWHM is increasing and their intensity decreasing. As already established for the other Pcs, the IPES spectra are a convolution of two signals. This case also subscribes to this assertion.

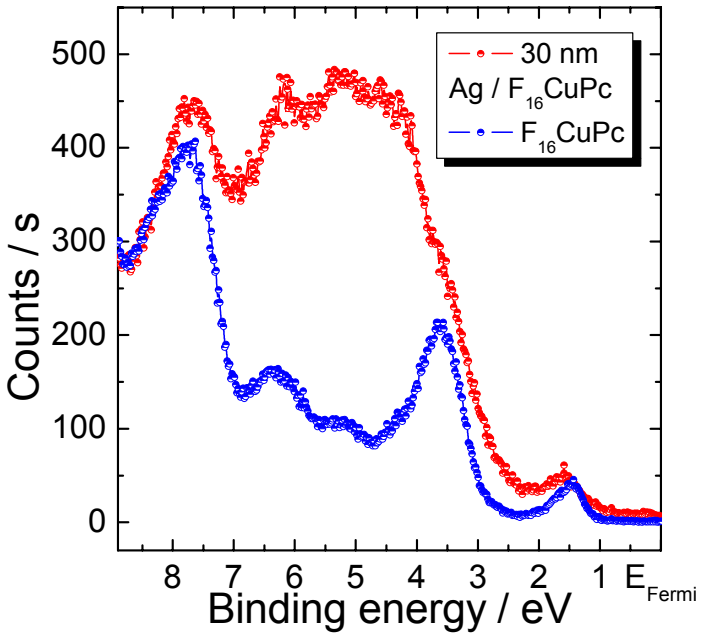

Figure 6.15 Comparison between VB-PES spectra corresponding to bare F_{16}CuPc and to 26 nm of Ag on F_{16}CuPc.

Considering the electron escape depth we can conclude once more that also here the surface of the F_{16}CuPc film is not completely covered with Ag when the thickness reaches 26 nm. However, metallic Ag is created starting with 3.2 nm thickness. Thus we can deduce that Ag clusters are formed on top of the organic film.

Analysing the FWHM, height and area of the F_{16}CuPc HOMO Figure 6.16 can be obtained. The FWHM increases by about 0.05 eV compared to the original value (Figure 6.16 (a)). This reveals an undefined environment, a lower degree of ordering at the surface upon Ag deposition than in the F_{16}CuPc film and a slight diffusion of the Ag atoms into the organic.

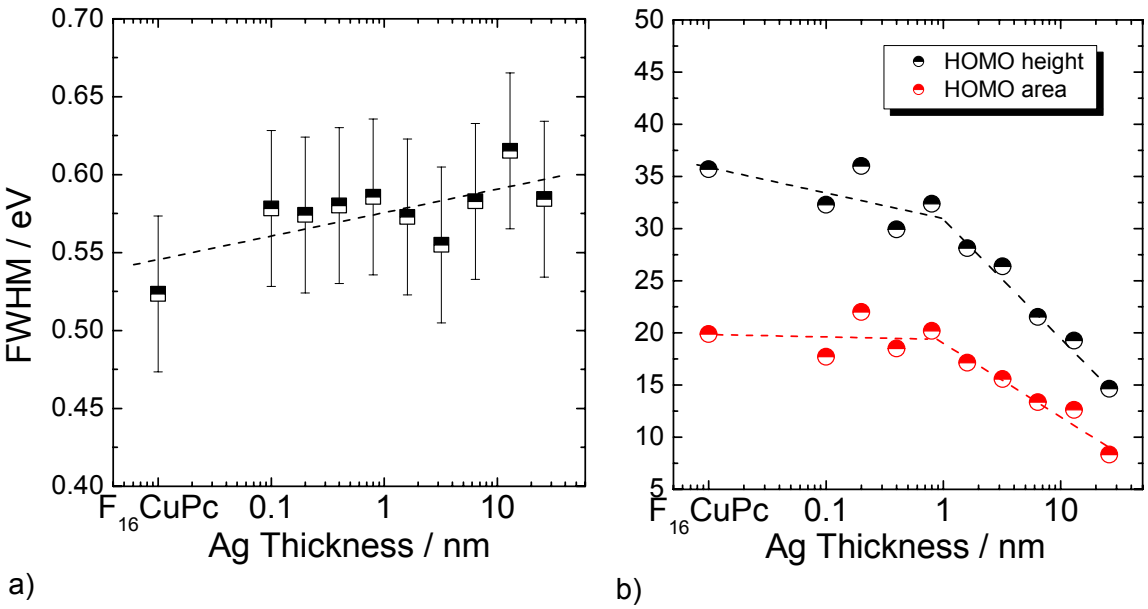

Figure 6.16 a) FWHM of F_{16}CuPc HOMO as a function of Ag thickness; b) the height and area of F_{16}CuPc HOMO as a function of Ag thickness.

The height and area of HOMO show a linear decrease having two different slopes as a function of Ag thickness in a similar way to F_4CuPc. This attenuation of the HOMO feature

points to continuously growing clusters of Ag on the surface of the film evolving towards a closed layer of Ag. Since HOMO is still visible at 23 nm of Ag, it is clear that a close layer is not formed yet.

Proceeding further with the analysis of the experimental data, the electronic properties of the interface are calculated as a function of Ag thickness and displayed in Figure 6.17 (a). Altogether with this representation, the energy band diagram corresponding to the Ag/F_{16}CuPc interface is shown in Figure 6.17 (b).

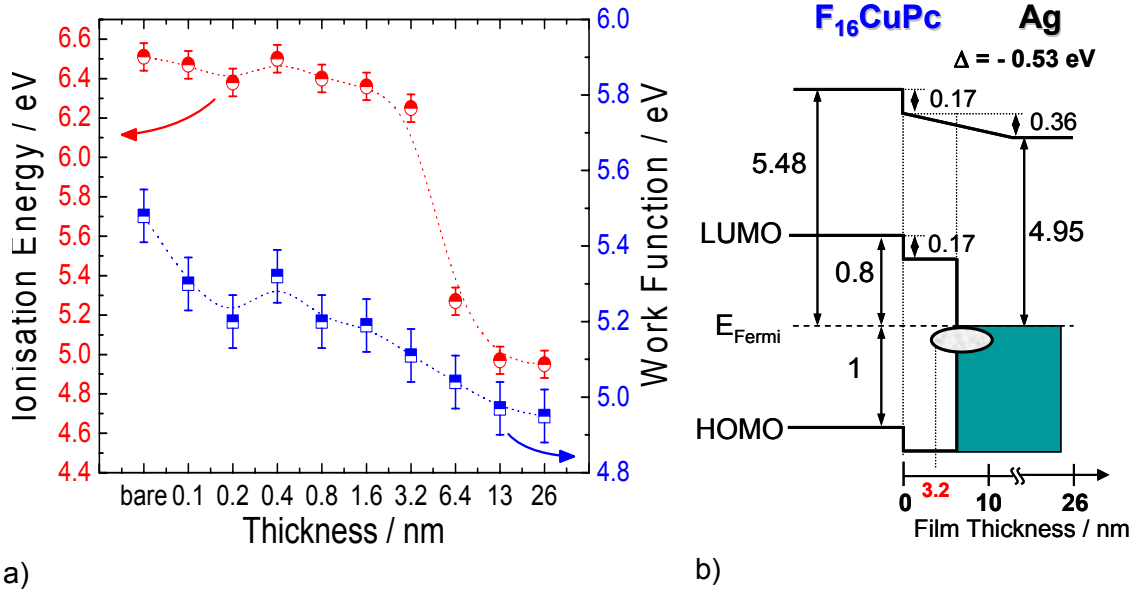

Figure 6.17 a) Evolution of IE and Φ for the Ag/F_{16}CuPc interface as a function of Ag thickness; b) energy band diagram of the Ag/F_{16}CuPc interface.

Focussing on the evolution of ϕ, it can be observed that it has an initial value of (5.48±0.07) eV. Upon the first Ag deposition, there is a sudden shift of 0.17 eV of the secondary electron cut-off which then drops the value of ϕ to (5.31±0.07) eV. Further deposition of Ag layers decreases ϕ even more. A saturation point is reached at 13 nm of Ag. ϕ takes a value of (4.95±0.07) eV. Surprisingly, this value is closer to the published ϕ value of Ag(111) 4.74 eV [Dwe73]. This indicates that Ag on top of F_{16}CuPc forms a much more ordered structure than when deposited on the other molecules. Considering the morphology of the organic (Figure 4.5 (d)) which shows larger crystallites than in the other Pcs, a better ordering of the Ag may be favored. The interface dipole that forms at this interface has a total value of 0.53 eV. It is important to note that the shift by 0.17 eV of the secondary electrons take place simultaneously with the energy shift of HOMO and LUMO. This behaviour suggests a similarity between this system and Ag/F_4CuPc, which is a slight n-type doping for the first layer, i.e. the Fermi level is moving within the gap. Diffusion of Ag atoms is also expected. However, following the evolution of ϕ we can see

that ϕ decreases with increasing Ag thickness. This is also found for IE. Therefore we can conclude that at thicker Ag films, charge transfers from $F_{16}CuPc$ to Ag. A charge transfer complex is formed.

6.1.5 The Influence of the Fluorine Atoms

As starting point we can consider the comparison between the VB-PES spectra of the freshly deposited organic materials and the spectra of the thick Ag films displayed in the two figures Figure 6.18 and Figure 6.19.

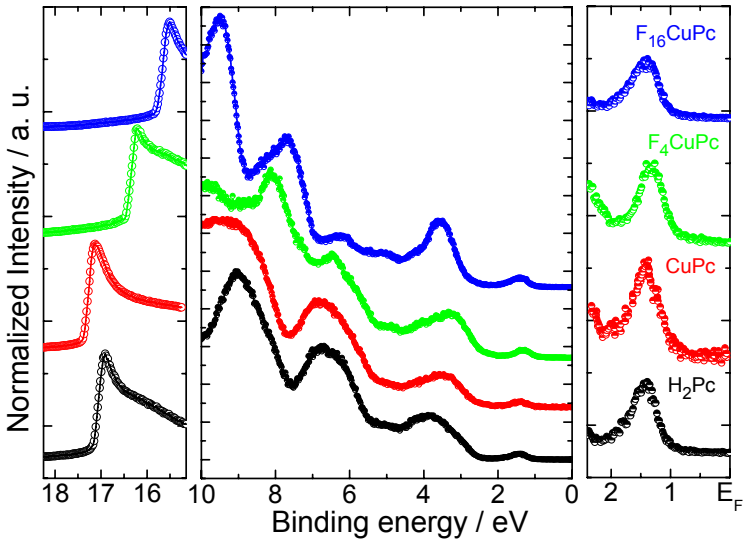

Figure 6.18 VB-PES spectra corresponding to 20 nm of H_2Pc, CuPc, F_4CuPc and $F_{16}CuPc$.

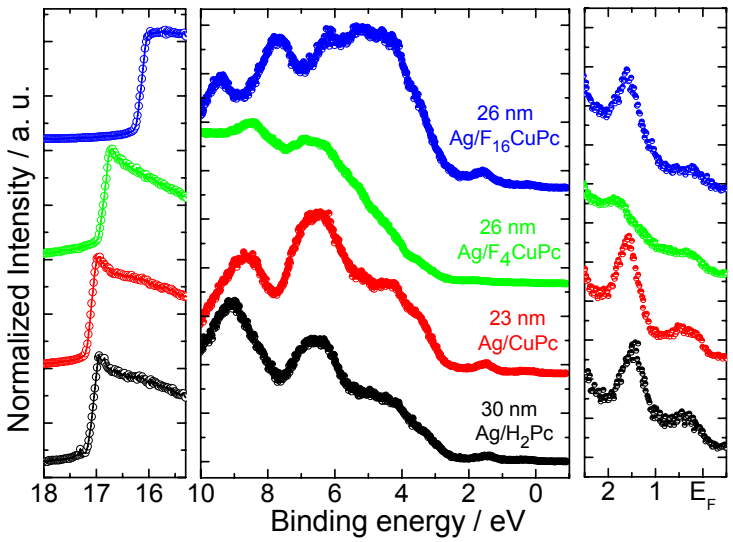

Figure 6.19 VB-PES spectra corresponding to 30, 23, 26 and 26 nm of Ag on H_2Pc, CuPc, F_4CuPc and $F_{16}CuPc$, respectively.

As observed in the region extending from 4 to 7 eV BE (Figure 6.19 middle panel) the 4d bands (Figure 6.1 (a)) are visible. Their intensity is quite similar for H_2Pc, CuPc and F_4CuPc, but in the case of $F_{16}CuPc$ the intensity of the 4d bands is more pronounced. The Fermi level is observable in all cases. Metallic Ag is formed on top of all the organic films. On the other hand, the features of the organic materials are still visible at the shown Ag thicknesses which are larger than 20 nm. This is a clear proof that Ag does not form a closed film atop the Pcs. The HOMO feature seems to have different intensities in each case. The largest attenuation is present in the case of F_4CuPc.

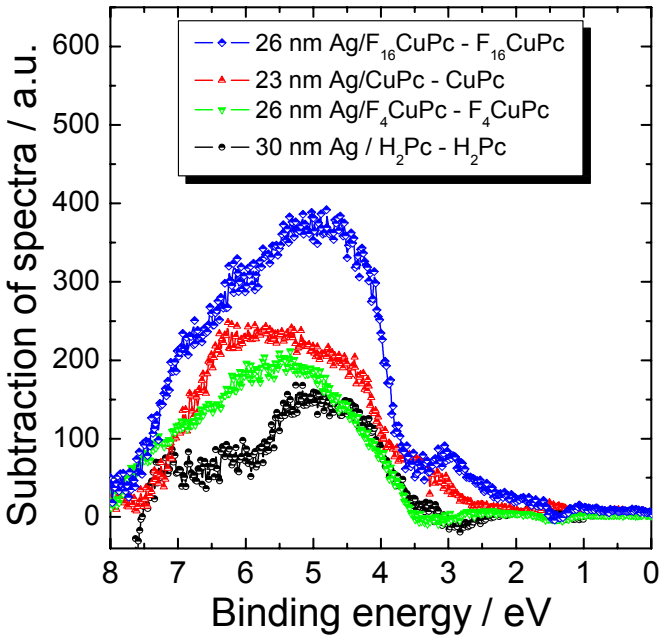

Figure 6.20 Subtracted VB-PES spectra. For each organic material the VB-PES spectrum of the freshly prepared film was subtracted from the corresponding VB-PES spectrum of the thick Ag film.

Figure 6.20 shows the difference obtained by subtracting the freshly prepared VB-PES organic film from the thick Ag layer performed for each material. The trend displayed by this figure may be associated with the size of the organic crystallites determined by AFM (Figure 4.5). The dimension of the crystallites for H_2Pc, CuPc and F_4CuPc is approximately 100 nm while the $F_{16}CuPc$ crystallites are about 160 nm. This larger crystallite size in the case of $F_{16}CuPc$ may favour a much more ordered structure for the deposited Ag and thus resulting in an increase in the intensity of the Ag VB-PES features. Such an assertion is sustained by the determined ϕ of $F_{16}CuPc$ which is closer as value to the Ag(111) one [Dwe73].

As shown already for the interfaces with H-Si, the fluorination plays a major role in the chemistry of the interface. Even though here, at the Ag/Pc interfaces, the behaviour found is profoundly different from the Pc/H-Si ones, the interface dipole shows a linear dependence on the EA, ϕ and IE of the molecules. Figure 6.21 (a) and (b) display the dependence. The slopes of the linear functions used to fit the experimental data of interface dipoles as a function of EA, ϕ and IE are 0.38, 0.49, and 0.49, respectively. Similarly to the previously discussed interfaces Pc/H-Si, the interface dipole found at the Ag/Pc interface is increasing as a function of the number of fluorine atoms.

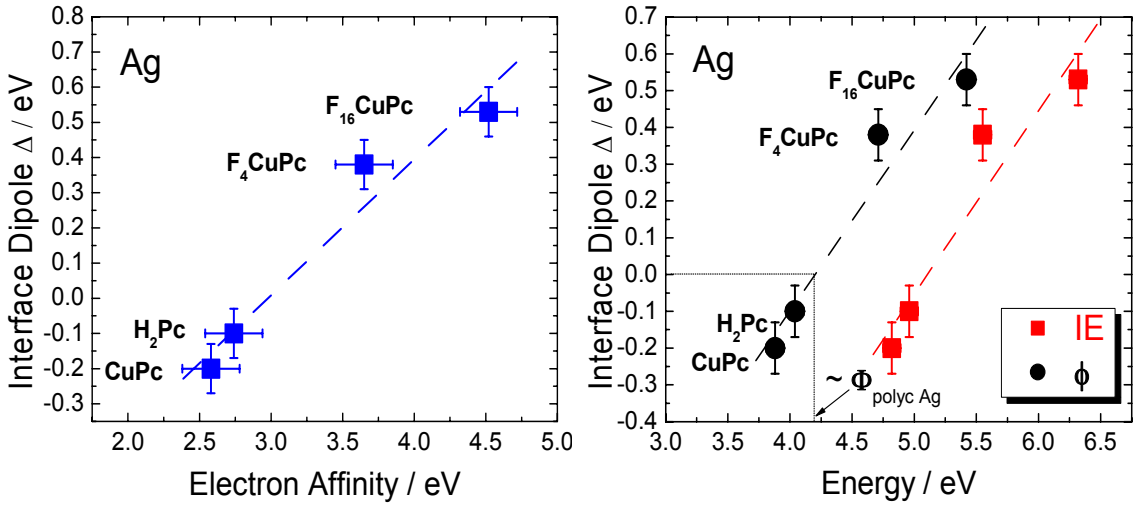

Figure 6.21 Interface dipoles formed at Ag/Pcs interfaces a) as a function of EA of the Pcs and b) as a function of ϕ and IE of the Pcs.

However, the slopes are almost half of the values determined in the previous case indicating a different type of interaction at the Ag/Pc interfaces. Considering the linear function that describes the variation of the interface dipole as a function of ϕ, we can obtain ϕ for which the interface dipole would be zero. The resulting ϕ has a value of 4.19 eV, which is close to the one determined for polycrystalline Ag - 4.27 eV [Dwe71]. Hence, knowing the difference in ϕ of the materials, one can predict the interface dipole that might appear at the interface.

Since the increasing number of fluorine atoms in the Pc molecules induces an increase in their EA, they will also play a role in the interaction found at the interface with Ag. It seems that here the estimated charge transfers are much stronger than in the H-Si case. This can be understood by considering the electron affinity of Ag atom (1.21 eV) and the electron affinity of H-Si (3.9 eV). As EA increases when changing the contact material from Ag to H-Si, also the slopes are increasing but not in the same proportion. In conclusion, the electron affinity of the atoms is the driving force of the changes found at the Ag/Pc interfaces.

6.2 Oxygen Exposed Phthalocyanines

A survey of the literature points out that most of the phthalocyanine materials are quite stable under the influence of molecular oxygen and that the conductivity of the films is usually increased by the presence of oxygen. Early work reports an enhancement in the photoconductivity of H_2Pc and CuPc as a function of oxygen exposure [Bor57]. The explanation of such behaviour comes much later when Dahlberg *et al*. discussed the formation of electron acceptor surface states on CuPc and NiPc films exposed to oxygen [Dah80]. Their experimental data sustain the theoretical model of charge transfer from the Pc ring to O_2, and thus the formation of charge transfer species at the surface of the film. This behaviour has been exploited further in investigations of CuPc for gas sensing applications [Zho98]. However, the techniques involved in the characterisation of Pc layers seldom contained photoemission and inverse photoemission although this combination allows the determination of the electronic properties at the exposed surface.
In the following paragraph the oxygen exposed phthalocyanines are investigated by means of VB-PES and IPES. Figure 6.22, Figure 6.23, Figure 6.24 and Figure 6.25 (a) and (b) contain the experimental spectra of VB-PES and IPES of H_2Pc, CuPc, F_4CuPc and $F_{16}CuPc$. The characteristic features for all Pcs are present in the lower spectra of VB-PES and IPES plotted in black.

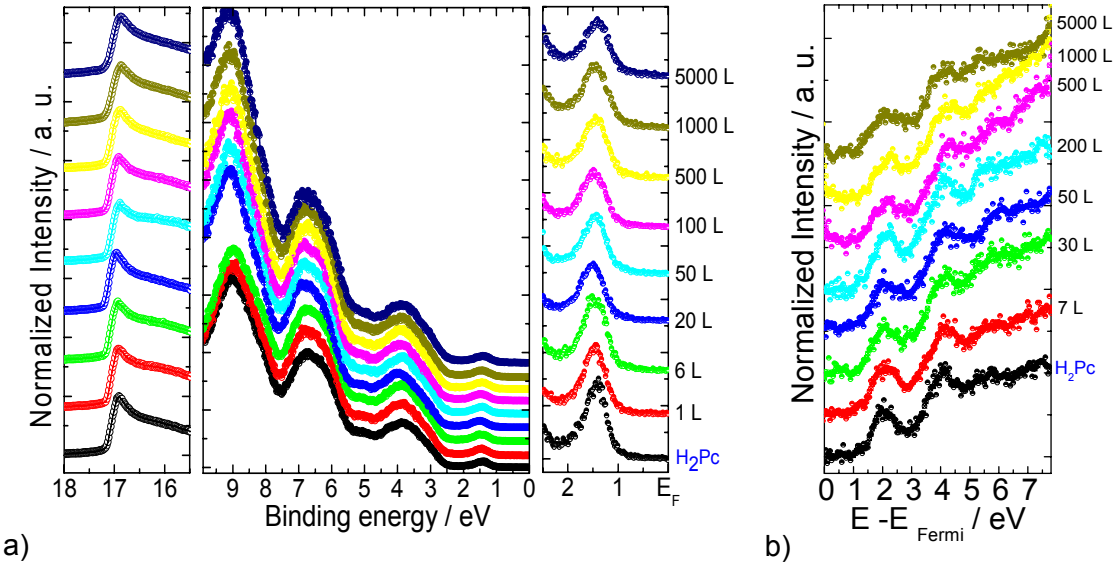

Figure 6.22 Incremental oxygen exposure of H_2Pc a) VB-PES and b) IPES spectra.

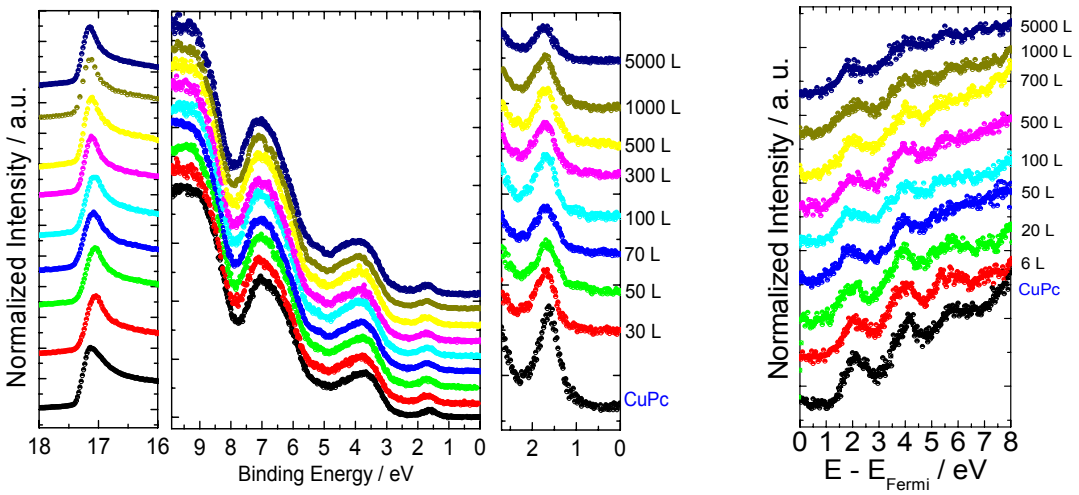

a) b)

Figure 6.23 Incremental oxygen exposure of CuPc a) VB-PES and b) IPES spectra.

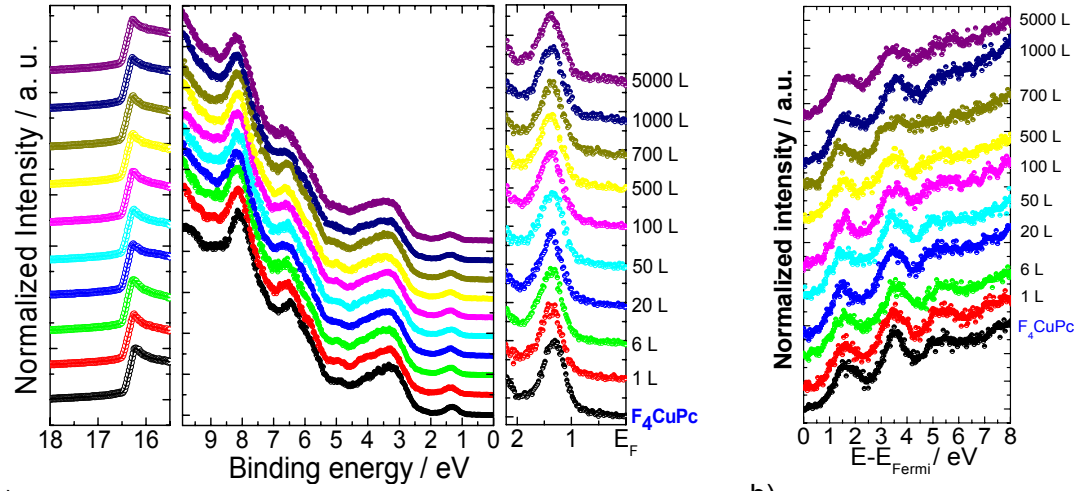

a) b)

Figure 6.24 Incremental oxygen exposure of F_4CuPc a) VB-PES and b) IPES spectra.

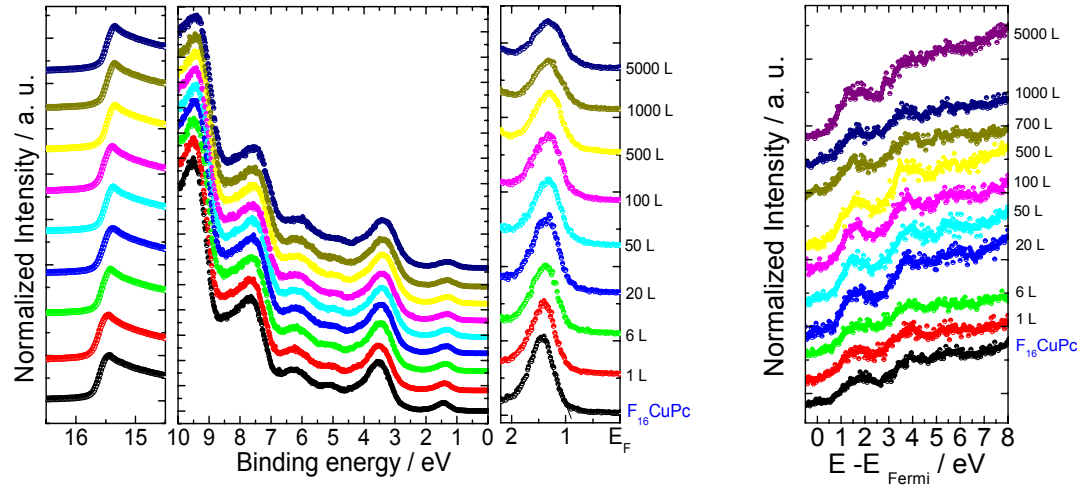

a) b)

Figure 6.25 Incremental oxygen exposure of F_{16}CuPc a) VB-PES spectra; b) IPES spectra.

At the first glance, one can say that the specific Pc features hardly change upon oxygen exposure. There are no new features arising due to oxygen presence and thus no strong interaction. As the oxygen quantity increases, the only observable change is the decrease in the intensity of the HOMO and LUMO features and a slight increase of their FWHM.

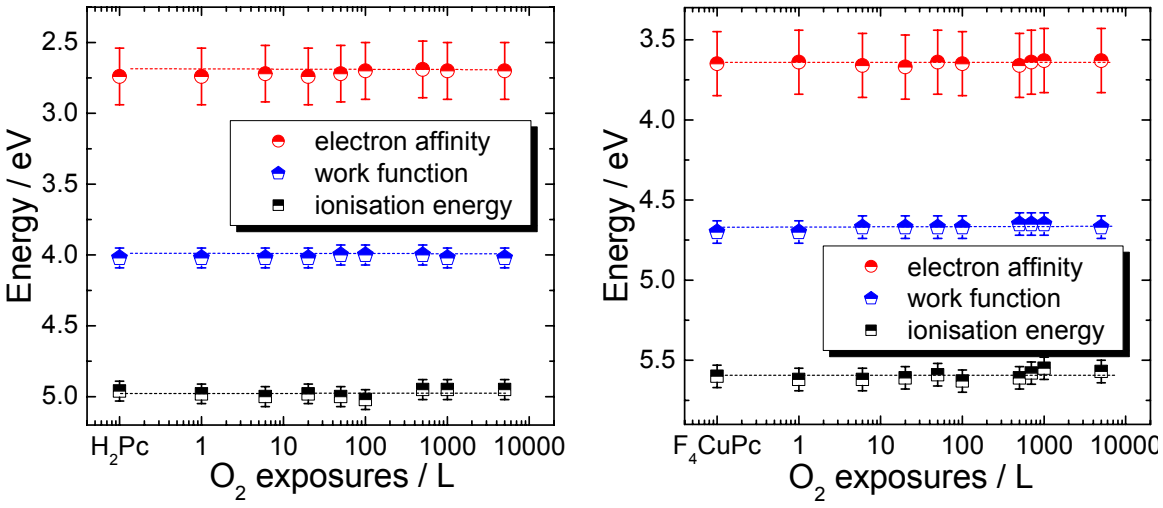

Figure 6.26 a) H_2Pc and b) F_4CuPc EA, ϕ and IE of the surface as a function of the oxygen exposures.

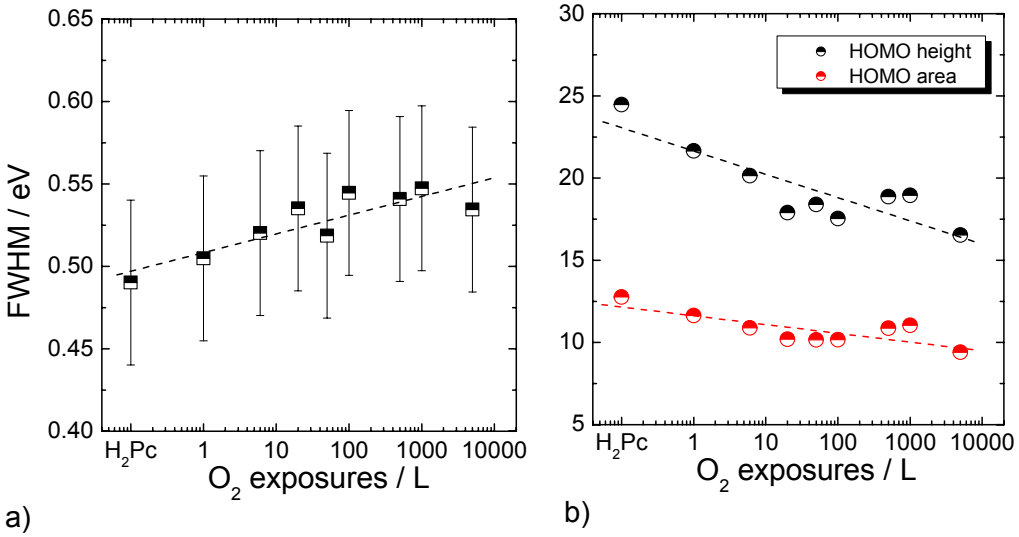

Figure 6.27 a) FWHM of H_2Pc HOMO as a function of oxygen exposure; b) the height and area of H_2Pc HOMO as a function of oxygen exposure.

This behaviour is consistent with the assessment that the oxygen molecules adsorb on the surface of the organic layer without any chemical interaction whatsoever. The physisorption model is valid for the H_2Pc and F_4CuPc molecules where no other shifts in the HOMO-LUMO energy positions occur. Figure 6.26 (a) and (b) shows the electronic properties of the surface as function of oxygen exposure for these two molecules. No changes are present. In addition for both molecules an increase of approximately 0.05 eV

is observed in the FWHM and a similar slope decrease in height and area of HOMO (Figure 6.27 (a) (b), Figure 6.28 (a) (b)).

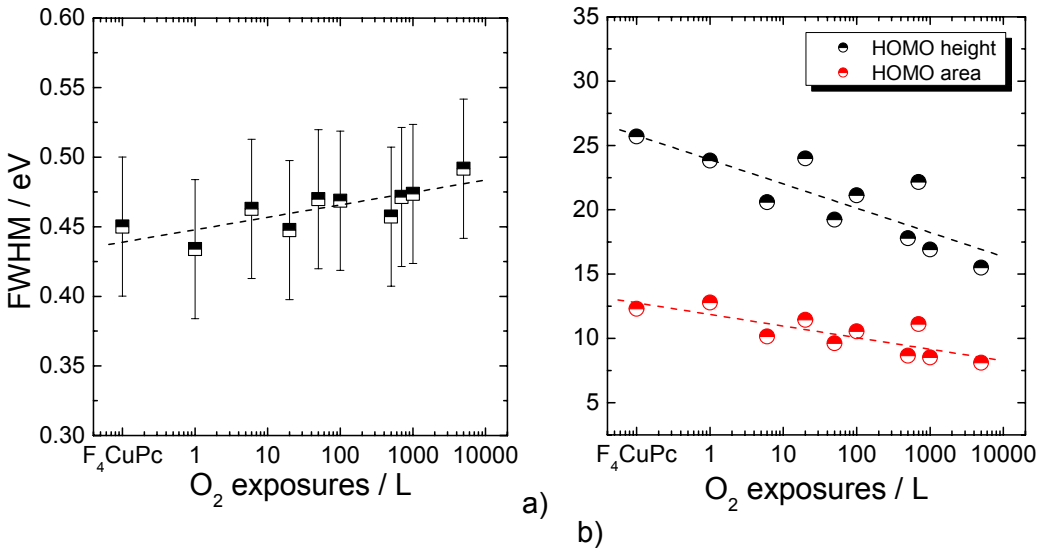

Figure 6.28 a) FWHM of F_4CuPc HOMO as a function of oxygen exposure; b) the height and area of F_4CuPc HOMO as a function of oxygen exposure.

However, in the case of CuPc and F_{16}CuPc a different situation appears. Analysing in a greater detail the VB-PES and IPES spectra of CuPc one can observe that the HOMO-LUMO levels are both shifting by 0.1 eV upon the first oxygen exposure. The HOMO is shifting away from the Fermi level and LUMO is shifting towards the Fermi level.

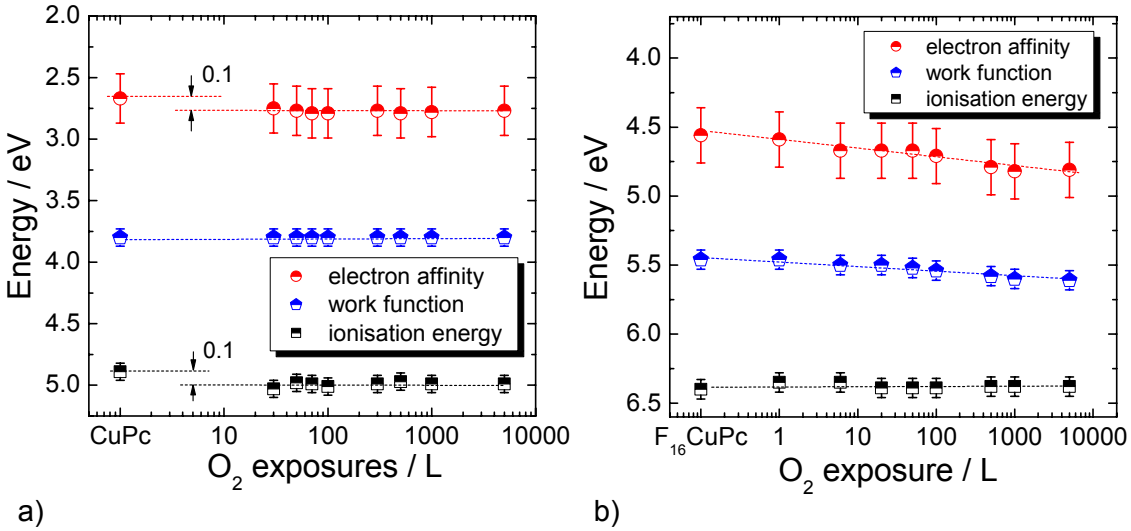

Figure 6.29 a) CuPc and b) F_{16}CuPc EA, ϕ and IE of the surface as a function of the oxygen exposures.

Such behaviour is consistent with a charge transfer from the CuPc molecules to the oxygen ones. Since upon further oxygen exposure no other energy shift occurs, the probability of a charge transfer complex formation on the surface is quite high. The

evolution of the surface electronic parameters is displayed in Figure 6.29 (a). Both IE and EA increase by 0.1 eV and afterwards remain constant. ϕ is invariable along the oxygen exposures of the organic film.

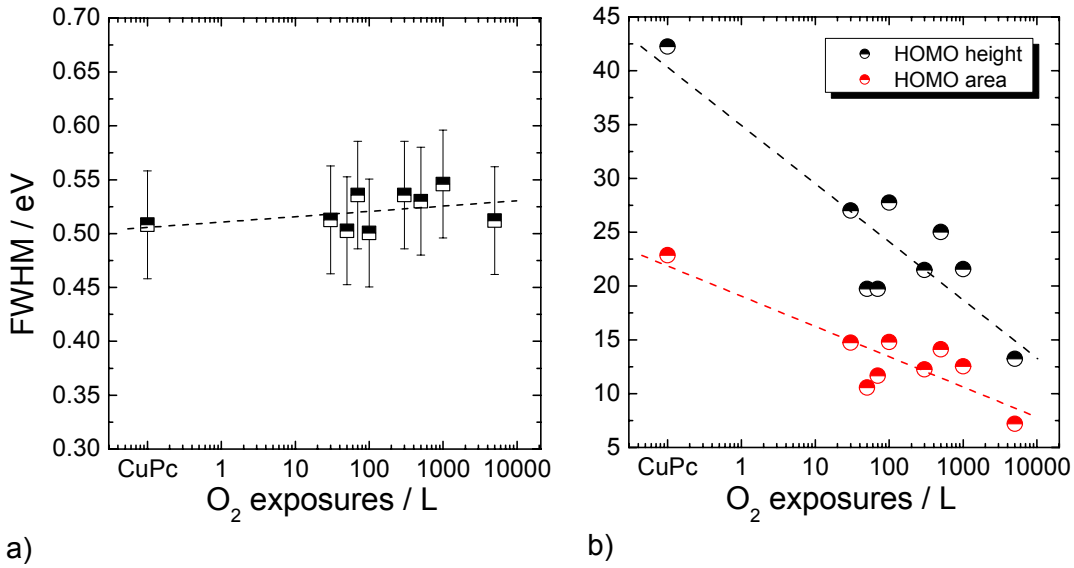

Figure 6.30 a) FWHM of CuPc HOMO as a function of oxygen exposure; b) the height and area of CuPc HOMO as a function of oxygen exposure.

Besides this, the HOMO presents a stronger drop in intensity as a function of the oxygen exposure (Figure 6.30 (b)) than H_2Pc and F_4CuPc show and this indicates a larger interaction between oxygen molecules and CuPc. While the FWHM of H_2Pc and F_4CuPc HOMO display an increase of about 0.05 eV, here the FWHM of CuPc HOMO increases only by half 0.025 eV.

On the other hand, for the fluorine derivative of CuPc, $F_{16}CuPc$ the surface interaction with oxygen is more complicated. Here, HOMO and LUMO levels are both shifting simultaneously as a function of oxygen exposure and towards the Fermi level. This leads to a decrease of the band gap at the surface by 0.25 eV. The HOMO FWHM is increasing here more than found for the other oxygen exposed Pcs, namely by 0.1 eV (Figure 6.31 (a)). The height and area of HOMO are dropping faster than found for H_2Pc and F_4CuPc but lesser than in the CuPc case (Figure 6.31 (b)). Thus the strength of the interaction between the oxygen molecules and $F_{16}CuPc$ is also classified as stronger than what was found for H_2Pc and F_4CuPc and weaker than found for CuPc. Moreover, the surface work function ϕ is increasing with the oxygen exposure by 0.15 eV (Figure 6.29 (b)). As a result of this band gap change, IE is almost constant within the experimental error and EA is increasing by 0.13 eV.

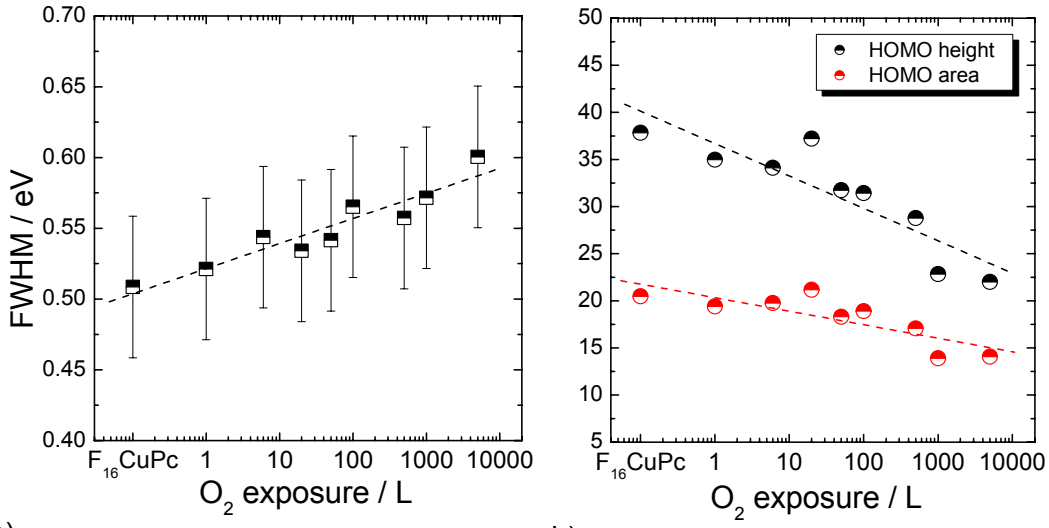

Figure 6.31 a) FWHM of F_{16}CuPc HOMO as a function of oxygen exposure; b) the height and area of F_{16}CuPc HOMO as a function of oxygen exposure.

This behaviour is characteristic to the creation of a polarized layer at the surface of the film. It is somewhat expected since both oxygen and fluorine are atoms that have extremely high electron affinities.

It seems that the interactions found between molecular oxygen and phthalocyanines can be divided into two groups. The first group could be the one of the lowest interaction. The lowest interaction is found on the surface of H_2Pc and F_4CuPc where oxygen is physisorbed. Then the second group may include CuPc and F_{16}CuPc which show a stronger interaction with oxygen. CuPc forms a charge transfer complex with oxygen and on the surface of F_{16}CuPc a polarized layer occurs. The presence of these two groups can not be predicted by calculating the phthalocyanines electronegativities since the values found scale with the degree of fluorination (Figure 5.33). However the charge redistribution within the molecule due to the copper atom and the fluorination might be a factor that contributes to the formation of these two groups.

6.3 Summary

This chapter investigated the chemical stability of the Pc's under incremental metal deposition and gas exposure. Here, the metal used was Ag and the gas was molecular oxygen. The techniques involved in the characterisation of these interfaces were VB-PES and IPES.

In the case of the Ag/Pc interfaces, the energy level alignment was determined for each organic material. Changes in the electronic parameters EA, ϕ and IE were also evaluated. Metallic Ag was formed on all the organic materials and the Fermi level was observed. In all the cases, since the features of the Pc are still visible at Ag thicknesses larger than 20 nm it can be concluded that Ag does not form a closed layer atop the organic. On the other hand, interface dipoles form at all the Ag/Pc interfaces and show a linear dependence on the electronic parameters. The determined ϕ for a 0 interface dipole is close to the polycrystalline Ag value and thus the ϕ difference is the driving force behind the interface dipole formation. Charge transfer complexes are formed at the Ag/H_2Pc and Ag/F_{16}CuPc interfaces. A weak interaction is found between Ag and CuPc and thus Ag may be considered as physisorbed on the CuPc surface. Charge transfer from F_4CuPc to Ag and a continuous n-type doping are determined in this case.

In the case of the oxygen exposed Pcs, the evolution of electronic properties of the surfaces was followed as function of oxygen exposure. Two groups were found, classified by their interaction strength with oxygen. H_2Pc and F_4CuPc form the group which shows the weakest interaction with oxygen. Consequently oxygen is physisorbed atop the organic. The second group is composed of the other two Pc, CuPc and F_{16}CuPc. CuPc shows the strongest interaction with oxygen and thus forms a charge transfer complex. F_{16}CuPc displays a weaker interaction than CuPc, however showing a band gap modification. A polarized layer is formed atop of F_{16}CuPc. No link has been found between these two types of groups and the degree of fluorination of the molecules. However the redistribution of charges in the molecules due to the copper and fluorine atoms might play a role in the formation of these two types of groups.

Chapter 7. Conclusions

The primary aim of this work was the *in situ* investigation of the energy level alignment of the interfaces formed by four phthalocyanine materials – H_2Pc, CuPc, F_4CuPc and $F_{16}CuPc$ and H-Si(111) as hybrid structures, e.g. for solar cells. In addition, the chemical stability of these organic materials in contact with Ag and molecular oxygen was also studied. The techniques involved in the investigations were mainly surface sensitive VB-PES and IPES. However, further insight was given by the NEXAFS investigation which determined the molecular orientation of CuPc, F_4CuPc and $F_{16}CuPc$ on H-Si.

For the preparation of the hydrogen passivated silicon a standard cleaning and passivating procedure was used [Yas94]. The surface reconstruction was investigated by LEED and the surface roughness by STM. The organic films as well as the metal ones were prepared *in situ* by OMBD. The surface morphology of the Pcs was studied by AFM. The interface formation of Pc/H-Si, Ag/Pc and oxygen/Pc was probed by incremental variation of the thickness/quantity of material. Each step was investigated by means of VB-PES and IPES. The NEXAFS excitation spectra were recorded at different organic film thickness, thus allowing the detection of changes in molecular orientation from thin to thick film.

The energy level alignment at the H_2Pc, CuPc, F_4CuPc, $F_{16}CuPc$ and H-Si(111) interfaces was determined by following the HOMO, LUMO and secondary electron cut-off evolution as a function of Pc thickness. Implicitly the progress of the electronic properties EA, ϕ and IE of the surface was pursued. Since there is a very small amount of publications dealing with IPES investigations of Pcs compared to the PES ones, the EA evolution is a new element that comes into play in the description of interfaces. The final values obtained for IE for all the molecules are in close agreement to the published ones [Kim00, Pei03]. The transport gaps for thick Pc films were calculated along with EA, ϕ, IE, and the barriers for holes and electrons at the interfaces. CuPc and H_2Pc transport gap are in close agreement with previous publications [Hil00]. However, for the F_4CuPc and $F_{16}CuPc$ molecules there are no records of their transport gaps. Electronic properties of single molecules were calculated using density functional theory methods. The calculated

densities of occupied states and unoccupied states were compared and discussed with respect to the experimental ones and proved to be in rather good agreement with them. When compared to published results, H_2Pc calculations are well established [Ort90] and in agreement with the present DFT calculation. On the other hand, the CuPc computed states are in an ongoing debate at present due to the presence of the copper atom which complicates the situation. Some theoretical calculations claim a 3d-like state in the gap placed at the Fermi level [Lia01, Bia03]. However, there is only one article containing experimental data that sustain this hypothesis [Dow04]. In the present work the experimental data excludes the presence of such a state. This is sustained by the present DFT calculations for CuPc and other publications [Loz04, Roc90]. In the case of F_4CuPc and $F_{16}CuPc$ molecules no records containing detailed theoretical calculations were found. A qualitative assignment of HOMO and LUMO was performed based on the DFT computations.

For all three molecules CuPc, F_4CuPc and $F_{16}CuPc$, the molecular orientation with respect to the substrate was determined in 2 monolayer and 20 nm thick films. The evaluation of the data showed different molecular orientation in the thin and thick films. This type of approach was scarcely employed in past publications. Considering hydrogen passivated silicon as substrate, there are several studies that probe H_2Pc [Nes94] and CuPc [Nak01, Has92] configuration. However, the film thicknesses employed in these studies is much larger than in the present study and thus no direct comparison can be made. Still, it is important to point out that different orientations emerged in thin films (about 50 nm) and in thick films (>1 μm). Consequently the present results complete the picture of orientation of organic molecules on inorganic semiconductor surfaces. The change in orientation was correlated with the band bending like behaviours that emerged at these interfaces. In addition to the band bending like behaviour, the interfaces show also an interface dipole which is driven by the work function difference between the contact materials. The influence of the degree of fluorination is confirmed in the similar increase of the EA, ϕ and IE as well as of the calculated electron affinity and electronegativity/molecule. The found band gap modification due to fluorination is also discussed. These types of changes were also found at the interfaces formed between a gold substrate and CuPc, F_4CuPc, $F_{16}CuPc$ [Pei02, Pei03] and thus prove the similar influence of the fluorination upon the interfaces.

The incremental Ag deposition on phthalocyanines was investigated in a similar way to the Pc/H-Si interfaces. Ag was chosen since it is one of the mostly investigated contact materials in electronic devices [Wu04]. The tools of choice were VB-PES and IPES. The energy level alignments of the Ag/Pc interfaces were determined and the

evolution of ϕ and IE was probed. The interfaces show a mixture of HOMO-LUMO shifts and interface dipole formation. Ag clusters are formed atop all the organic layers. A charge transfer complex is formed in the case of Ag/H_2Pc and Ag/F_{16}CuPc interfaces. Ag is physisorbed atop the CuPc. Charge transfers from F_4CuPc to Ag creating a continuous n-type doping at the interface. The charge transfer found at Ag/F_4CuPc interface is analogous to the one found at F_4CuPc/Ag discussed in ref. [Sch04]. Similar to the Pc/H-Si interfaces, the interface dipoles found here show a linear dependence on the EA, ϕ and IE and can be predicted by the difference in the work functions. In a comparable way as found for Pc/H-Si interfaces, this result shows the influence of the fluorination.

The stepwise oxygen exposure of thick films of H_2Pc, CuPc, F_4CuPc and F_{16}CuPc was studied by VB-PES and IPES. The data evaluation provided the evolution of EA, ϕ and IE. Two groups of behaviours were determined. The weak interaction group is represented by H_2Pc and F_4CuPc, Pcs on which oxygen is physisorbed. The strong interaction group contains the other two molecules CuPc and F_{16}CuPc. CuPc forms a charge transfer complex with oxygen and on top of F_{16}CuPc a polarized layer is formed. CuPc behaviour in the presence of oxygen is in agreement with published data [Dah80]. No link was found between these two types of groups and the degree of fluorination of the molecules. However the charge redistribution within the molecules due to the copper and fluorine atoms might play a role in the formation of these two types of groups.

In summary, the present results constitute a comprehensive database on the electronic properties of four phthalocyanines: H_2Pc, CuPc, F_4CuPc, and F_{16}CuPc and their different interfaces. Tracking the evolution of the electronic parameters as a function of the functionalisation of the molecules in three different cases (Pc deposition on H-Si, Ag deposition on Pc films and Pc oxygen exposure) allowed information extraction on the influence of fluorination.

References

[App76] J. A. Appelbaum, D. R. Hamann, Rev. Mod. Phys. 48 (1976) 479.

[Arr02] A. Arranz, J. F. Sanchez-Royo, J. Avila, V. Perez-Dieste, P. Dumas, M. C. Asensio, Phys. Rev. B 65 (2002) 075405.

[Ash66] M. Ashida, Bull. Chem. Soc. Jpn. 39 (1966) 2632.

[Atk94] P. W. Atkins, *Physical Chemistry*, 5th edition, Oxford University Press 1994.

[Bal99] M. A. Baldo, S. Lamansky, P. E. Burrows, M. E. Thompson, and S. R. Forrest, Appl. Phys. Lett. 75 (1999) 4.

[Bao96] Z. Bao, A. J. Lovinger, A. Dodabalapur, Appl. Phys. Lett.69 (1996) 3066.

[Bec93] A. D. Becke, J. Chem. Phys. 98 (1993) 5648.

[Ben02] Stacey F. Bent, Surf. Sci. 500 (2002) 879.

[Ber79] J. Berkowitz, J. Chem. Phys. 70 (1979) 2819.

[Bes64] C. N. Berglund, W. E. Spicer, Phys. Rev. 136 (1964) 1030, 1044.

[Bia03] B. Bialek , I. G. Kim , J. Il Lee, Thin Solid Films 436 (2003) 107.

[Bil98] R. C. Bilodeau, J. Phys. B 31 (1998) 3885.

[Bon95] R. Bonnett, Chem. Soc. Rev. (1995) 19.

[Bor57] J. Bornmann, J. Chem. Phys. 27 (1957) 604.

[Bou92] S. Bouzidi, F. Coletti, J. M. Debever, P. A. Thiry, P. Dumas, Y. J. Chabal, Phys. Rev. B 45 (1992) 1187.

[Bur88] V. A. Burrows, Y. J. Chabal, G. S. Higashi, K. Raghavachari and S. B. Christman, Appl. Phys. Lett. 53 (1988) 998.

[Cam03] J. Campbell Scott, J. Vac. Sci. Technol. A 21 (2003) 521.

[Car66] M. Cardona, F. H. Pollak, Phys. Rev. B 27 (1966) 7466.

[Car96] M. Cardona and P. Y. Yu, *Fundamentals of Semiconductors*, Springer-Verlag Berlin 1996.

[Che69] I. Chen, J. Chem. Phys. 51 (1969) 3241.

[Cir75] S. Ciraci, I. P. Batra, W. A. Teiller, Phys. Rev. B 12 (1975) 5811.

[Coo95] M. J. Cook, I. Chambrier, S. J. Cracknell, D. A. Mayes, and D. A. Russel, Photochem. Photobiol. 62 (1995) 542.

[Dah80] S. C. Dahlberg, M. E. Musser, J. Chem. Phys. 72 (1980) 6706.

[Deb92] M. K. Debe, J. Vac. Sci. Technol. A 10 (1992) 2816.

[Den79] G. Denninger, V. Dose, H. Scheidt, appl. Phys. 18 (1979) 375.

[Dev68] P. Devaux, G. Delacote, Chem. Phys. Lett. 2 (1968) 337.

[Dog92] S. Dogo, J. P. Germain, C. Maleysson, and A. Pauly, Thin Solid Films 219 (1992) 244.

[Dos77] V. Dose, Appl.Phys. 14, (1977) 117.

[Dow04] J. E. Downes, C. McGuinness, P-A. Glans, T. Learmonth, D. Fu, P. Sheridan, K. E. Smith, Chem. Phys. Lett. 390 (2004) 203.

[Dow91] J. Dowdy, J. J. Hoagland, and K. W. Hipps, J. Phys. Chem. 95 (1991) 3751.

[Dwe71] A.W. Dweydari, C.H.B. Mee, Phys. Status Solidi A 27 (1971) 223.

[Dwe73] A.W. Dweydari, C.H.B. Mee, Phys. Status Solidi A 17 (1973) 247.

[Erc67] C. Ercolani, C.Neri, and P. Porta, Inorg. Chim. Acta 1 (1967) 415.

[Erd82] P. W. Erdman, E.C. Zipf, Rev. Sci. Instrum. 53 (1982) 225.

[Ert85] G. Ertl, J. Kuppers, *Low Energy Electrons and Surface Chemistry*, VCH Verlagsgesellschaft, Weinheim, 1985.

[For97] S. R. Forrest, Chem. Rev. 97 (1997) 1793.

[Gao01] W. Gao, A. Kahn, Appl. Phys. Lett. 79 (2001) 4040.

[Gau98] Gaussian 98 (Revision A.1), M. J. Frisch, G. W. Trucks, H. B. Schlegel, G. E. Scuseria, M. A. Robb, J. R. Cheeseman, V. G., Zakrzewski, J. A. Montgomery, R. E. Stratmann, J. C. Burant, S. Dapprich, J. M. Millam, A. D. Daniels, K. N. Kudin, M. C. Strain, O. Farkas, J. Tomasi, V. Barone, M. Cossi, R. Cammi, B. Mennucci, C. Pomelli, C. Adamo, S. Clifford, J. Ochterski, G. A., Petersson, P. Y. Ayala, Q. Cui, K. Morokuma, D. K. Malick, A. D. Rabuck, K. Raghavachari, J. B. Foresman, J. Cioslowski, J. V., Ortiz, B. B. Stefanov, G. Liu, A. Liashenko, P. Piskorz, I. Komaromi, R. Gomperts, R. L. Martin, D. J. Fox, T. Keith, M. A.,Al-Laham, C. Y. Peng, A. Nanayakkara, C. Gonzalez, M. Challacombe, P. M. W. Gill, B. G. Johnson, W. Chen, M. W. Wong, J. L., Andres, M. Head-Gordon, E. S. Replogle and J. A. Pople, Gaussian, Inc., Pittsburgh PA, 1998.

[Gav05] G. Gavrila, PhD thesis TU Chemnitz, Germany, 2005.

[Gor04-1] O. Gordan, M. Friedrich, D. R. T. Zahn, Thin Solid Fims 455-456 (2004) 551.

[Gor04-2] O. Gordan, M. Friedrich, D. R. T. Zahn, Organic Electronics 5 (2004) 291.

[Gor05] M. Gorgoi, D. R. T. Zahn, Organic Electronics 6 (2005) 168.

[Gut67] F. Gutmann, L. E. Lyons, Organic semiconductors, Wiley, New York 1967.

[Has92] A. K. Hassan and R. D. Gould, Physica Status Solidi A, Applied Research 132 (1992).

[He96] Y. He, S. Bouzidi, B.-Y. Han, L.-M. Yu, P. A. Thiry, R. Caudano, J. M. Debever, Phys. Rev. B 54 (1996) 17654.

[Hed98] L. Hedin, J. Michiels, J. Inglesfield, Phys. Rev. B 58 (1998) 15565.

[Heu02] S. Heutz, PhD Thesis, University of London, 2002.

[Hie00] R. Hiesgen, M. Räbisch, H. Böttcher, and D. Meissner, Sol. Energ. Mat. Sol. C. 61 (2000) 73.

[Hig90] G. S. Higashi, Y. J. Chabal, G. W. Trucks and K. Raghavachari, Appl. Phys. Lett. 56 (1990) 656.

[Hig91] G. S. Higashi, R. S. Becker, Y. J. Chabal, and A. J. Becker, Appl. Phys. Lett. 58 (1991) 1656.

[Hil97] I. G. Hill, PhD thesis, Queen's University, Canada, 1997.

[Hil00] I. G. Hill, A. Kahn, Z.G. Soos, R.A. Pascal, Jr., Chem. Phys. Lett. 327 (2000) 181.

[Hil00-2] I.G. Hill, A.J. Makinen, Z.H. Kafa, Appl. Phys. Lett. 77 (2000) 1825

[Ho77] K. M. Ho, M. Cohen, Phys. Rev. B 15 (1977) 3888.

[Hot75] H. Hotop and W. C. Lineberger, J. Phys. Chem. Ref. Data 14 (1975) 731.

[Huf95] S. Hüfner, *Photoelectron Spectroscopy-Principles and Applications* Springer Series in Solid-State Sciences 82, Springer-Verlag, 1995.

[Iri97] S. Irie, A. Hoshino, K. Kuwamoto, S. Isoda, M. J. Miles, T. Kobayashi, Appl. Surf. Sci. 113/114 (1997) 310.

[Ish98] H. Ishii, K. Sugiyama, D. Yoshimura, E. Ito, Y. Ouchi, K. Seki, IEEE J-STQE 4 (1998) 24.

[Ish99] H. Ishii, K. Sugiyama, E. Ito, K. Seki, Adv. Mater. 11 (1999) 605.

[Jan92] J. Janczac and R. Kubiac, J. Alloys Comp. 190 (1992) 121.

[Kah03] A. Kahn, N. Koch, W. Gao, J. Pol. Sci.: Part B: Pol. Phys. 41 (2003) 2529.

[Kao81] K. C. Kao, W. Hwang, *Electrical transport in solids*, Pergamon, Oxford 1981.

[Ker78] W. Kern and J. Vossen, Eds., *Thin Film Processes*, Academic Press: New York, 1978, Ch V-1.

[Ker93] W. Kern, Ed., *Handbook of Semiconductor Cleaning Technology*, Noyes Publishing: Park Ridge, NJ, 1993, Ch 1.

[Kev01] S. D. Kevan, E. Rotenberg, J. Electron Spectrosc. Rel. Phenom. 117-118 (2001), 57.

[Kim00] T. Kimura, M. Sumimoto, S. Sakaki, H. Fujimoto, Y. Hashimoto, S. Matsuzaki, Chem. Phys. 253 (2000) 125.

[Knu04] M. Knupfer, H. Peisert, Phys. Stat. Sol. (a) 201 (2004) 1055.

[Koh65] W. Kohn, L. J. Sham, Phys. Rev. 140 (1965) A1133.

[Kol97] B. A. Kolesov, T. V. Basova, and I. K. Igumenov, Thin Solid Films 304 (1997) 166.

[Lee88] C. Lee, W. Yang, and R. G. Parr, Phys Rev B 37 (1988) 785.

[Lez89] C. C. Leznoff and A. B. P. Lever, *Phthalocyanines - Properties and Applications*, VCH, New York, 1989-96.

[Lia01] M. -S. Liao, S. Scheiner, J. Chem. Phys. 114 (2001) 9780.

[Lin34] R. P. Linstead, J. Chem. Soc. (1934) 1016.

[Loz04] L. Lozzi, S. Santucci, S. La Rosa, B. Delley, S. Picozzi, J. Chem. Phys. 121 (2004) 1883.

[Lut93] H. Lüth, *Surfaces and Interfaces of Solids* Springer Series in Surface Sciences 15, Springer-Verlag, 1993.

[Mah70] G. D. Mahan, Phys. Rev. B 2 (1970) 4334.

[Mar95] N. Mårtensson, A. Nilsson in W. Eberhardt (Ed.), *Applications of Synchrotron Radiation–High Resolution Studies of Molecules and Molecular Adsorbates on Surfaces*, Springer Series in Surfaces Sciences 35, Springer-Verlag, 1995.

[Mat71] S. C. Mathur, J. Singh, D. C. Singh, J. Phys. C Solid State Phys. 4 (1971) 3122.

[McK98] N. B. McKeown, *Phthalocyanine materials: synthesis, structure and function*, Cambridge University Press, Cambridge, 1998.

[Mei04] F. Meillaud, A. Shah, C. Droz, E. Vallat-Sauvain, C. Miazza, to be published in Solar Energy Materials and Solar Cells, presented at the 14th International Photovoltaic Science and Engineering Conference, PVSEC14, Bangkok, Thailand, January, 2004.

[Mön90] W. Mönch, Rep. Prog. Phys. 53 (1990) 221.

[Mön95] W. Mönch, *Semiconductor Surfaces and Interfaces*, Springer-Verlag Berlin Heidelberg 1995.

[Mos83] F. H. Moser and A. L. Thomas, *The Phthalocyanines*, CRC Press, Boca Raton, Florida, 1983.

[Nak01] M. Nakamura, T. Matsunobe, H. Tokumoto, J. Appl. Phys. 89 (2001) 7860.

[Nak96] M. Nakamura, Y. Morita, Y. Mori, A. Ishitani and H. Tokumoto, J. Vac. Sci. Technol. B 14 (1996) 1109.

[Nes94] S. Nespurek, H. Podlesak, and C. Hamann, Thin Solid Films 249 (1994) 230.

[Ole04] http://www.oled-info.com/devices.html

[Ort89] E. Orti, J. L. Bredas, Synth. Met. 29 (1989) 115.

[Ort90] E. Orti, J. L. Bredas, C. Clarisse, J. Chem Phys. 92 (1990) 1228.

[Paa03] G. Paasch, H. Peisert, M. Knupfer, J. Fink, S. Scheinert, J. Appl. Phys. 93 (2003) 6084.

[Pei01] H. Peisert, T. Schwieger, J. M. Auerhammer, M. Knupfer, M. S. Golden, J. Fink, P. R. Bressler M. Mast, J. Appl. Phys. 90 (2001) 466.

[Pei02] H. Peisert, M. Knupfer, T. Schwieger, J. M. Auerhammer, M. S. Golden, J. Fink, J. Appl. Phys. 91 (2002) 4872.

[Pei02-2] H. Peisert, M. Knupfer, J. Fink, Appl. Phys. Lett. 81 (2002) 23.

[Pei03] H. Peisert, M. Knupfer, T. Schwieger, G. G. Fuentes, D. Olligs, J. Fink, Th. Schmidt, J. Appl. Phys. 93 (2003) 9683.

[Pen80] J.B. Pendry, Phys. Rev. Lett. 45 (1980) 1356.

[Pen81] J. B. Pendry, J. Phys. C14 (1981) 1381.

[Pri88] K. C. Prince, Rev. Sci. Instrum. 59 (1988) 741.

[Rei84] B. Reihl, R. R. Schlittler, Phys. Rev. B 29 (1984) 2267.

[Rob36] J. M. Robertson, J. Chem. Soc. (1936) 1195.

[Roc90] M. L. M. Rocco, K.-H. Frank, P. Yannoulis, E.-E. Koch, J. Chem. Phys. 93 (1990) 6859.

[Sch01] D. Schlettwein, K. Hesse, N. E. Gruhn, P. A. Lee, K. W. Nebesny, N.R. Armstrong, J. Phys. Chem. B 105 (2001) 4791.

[Sch03] W. Schattke, M. A. Van Hove, *Solid-State Photoemission and Related Methods: Theory and Experiment*, Wiley-VCH Verlag GmbH & Co. 2003.

[Sch04] T. Schwieger, H. Peisert, M. Knupfer, Chem Phys. Lett. 384 (2004) 197.

[Sch78] M. Schlüter, M. L. Cohen, Phys. Rev. B 17 (1978) 716.

[Sch94] D. Schlettwein, N. R. Armstrong, J. Phys. Chem. 98 (1994) 11771.

[Sea79] M. P. Seah, W. A. Dench, Surf. Interface Analysis 1 (1979) 2.

[Sea82] D. A. Seanor, in *Electrical Properties of Polymers*, Academic Press, New York, 1982.

[Sha99] S. E. Shaheen, G. E. Jabbour, B. Kippelen, Appl. Phys. Lett. 74 (1999) 3212.

[She01] C. Shen and A. Kahn, J. Appl. Phys. 90 (2001) 4549.

[She01-2] C. Shen, A. Kahn, J. Schwartz, J. Appl. Phys. 90 (2001) 6236.

[Shi98] T. Shimada, K. Hamaguchi, A. Koma, F. S. Ohuchi, Appl. Phys. Lett. 72 (1998) 1869.

[Sim85] J. Simon, J.-J. Andre, *Molecular Semiconductors*, Springer Verlag Berlin Heidelberg 1985.

[Sin77] J. Singh, J. Phys. Status Solidi B 82 (1977) 263.

[Sno89] A. W. Snow and W. R. Barger, *Phthalocyanines - Properties and Applications* (VCH publishers, New York, 1989).

[Sol91] J. L. Solomon, R. J. Madix, J. Stöhr, Surf. Sci. 255 (1991) 12.

[Sto83] J. Stöhr, R. Jaeger, J. J. Rehr, Phys. Rev. Let. 51 (1983), 821.

[Stö92] J. Stöhr, *NEXAFS Spectroscopy*, Springer Series in Surfaces Sciences 25, Springer-Verlag, 1992.

[Suk69] M. Sukigara, R. C. Nelson, Mol. Phys. 17 (1969) 387.

[Sze81] M. Sze, *Physics of Semiconductor Devices*, Wiley, New York, 1981.

[Tak02] M. Takada., H. Yoshioka, H. Tada, K. Matsushige, Jpn J. Appl. Phys. Vol. 41, (2002) L73-L75.

[Tan86] C. W. Tang, Appl. Phys. Lett. 48 (1986) 183.

[Tho84] T. Darrah Thomas Phys. Rev. Let. 52 (1984), 417.

[Tsi01] E.V. Tsiper and Z.G. Soos, Phys. Rev. B 64 (2001) 195124.

[Tsi02] E.V. Tsiper, Z.G. Soos, W. Gao, A. Kahn, Chem. Phys. Lett. 360 (2002) 47.

[Twa82] A. Twarowski, J. Chem. Phys. 77(3) (1982) 1458.

[Uye72] N. Uyeda, T. Kobayashi, E. Suito, Y. Harada, M. Watanabe, J. Appl. Phys.43 (1972) 5181.

[Vol13] M. Volmer, Ann. Physik 40 (1913) 775.

[Vos80] S. H. Vosko, L. Wilk, M. Nusair, Can. J. Phys. 58 (1980) 1200.

[Wel02] M. K. Weldon, K. T. Queeney, J. Eng. Jr., K. Raghavachari, Y. J. Chabal, Surf. Sci. 500 (2002) 859.

[Woo83] D. F. Woodruff, P. D. Johnson and N. V. Smith, J. Vac. Sci. Technol. A 1 (1983) 1104.

[Wri89] J. D. Wright, Prog. Surf. Sci. 31 (1989) 1.

[Wu04] Z. Wu, S. Chen, H. Yang, Y. Zhao, J. Hou, S. Liu, Semicond. Sci. Technol. 19 (2004) 1138.

[Xue04] J. Xue, S. Uchida, B. P. Rand, S. R. Forrest, Appl. Phys. Lett. 85 (2004) 5757.

[Yam02] H. Yamane, S. Kera, S. Tanaka, H. Honda, T. Nakamura, H. Setoyama, K. K. Okudaira, N. Ueno, PC74, ERPOS, Prague, 2002.

[Yas94] T. Yasuda, D. E. Aspnes, D. R. Lee, C. H. Bjorkman, G. Lucovsky, J. Vac. Sci. Technol. A 12(4) (1994) 1152.

[Yos01] H. Yoshida, K. Tsutsumi, N. Sato, J. El. Spec. and Rel. Phenom. 121 (2001) 83.

[Zei05] R. Zeis, T. Siegrist, Ch. Kloc, Appl. Phys. Lett. 86 (2005) 022103.

[Zho05] T. X. Zhou,T. Ngo, J. J. Brown, M. Shtein, S. R. Forrest, Appl. Phys. Lett. 86 (2005) 21107.

[Zho98] Q. Zhou, R. D. Gould, Thin Solid Films 317 (1998) 432.

List of Tables

List of Figures

Erklärung

Ich erkläre, dass ich die vorliegende Arbeit selbständig und nur unter Verwendung der angegebenen Literatur und Hilfsmittel angefertigt habe.

2005

M.Sc. Phys. Mihaela Gorgoi

Curriculum Vitae

MIHAELA GORGOI

Date of birth: 27 November 1976

Place of birth: Zalau, Romania

Nationality: Romanian

Gender: Female

Languages: Romanian (native), English, French, German

Education:

2001-2005 **PhD** (not defended yet) – Institute of Physics, University of Technology Chemnitz, Germany in ***D**esigning **I**norganic / **O**rganic **DE**vices* (**DIODE**) *Human Potential Research Training Network* funded by *EU.* Subject: *"Electronic Properties and Chemical Stability of Phthalocyanines on Hydrogen Passivated Silicon"*. Supervisor: Prof. Dr. D. R. T. Zahn

01.04.2001 - 30.09.2001 *Socrates-Erasmus Student Grant* for Master Studies at University of Technology Chemnitz, Germany. Subject: **"***Inverse Photoemission Spectroscopy*". Supervisor: Prof. Dr. D. R. T. Zahn

2000-2001 **Master of Science** - Faculty of Physics, Babes-Bolyai University, Cluj-Napoca (Romania). Master Subject: "*Inverse Photoemission Spectroscopy*"

1995-2000 **Batchelor of Science** - Technological Physics Department, Faculty of Physics, Babes-Bolyai University, Cluj-Napoca (Romania)
Diploma Subject: "*EXAFS studies on La-Al-B-O systems*"
Supervisor: Dr. Nicolae Aldea.

1991-1995 Theoretic Highschool, Zalau (Romania)
Mathematics-Physics-English Profile

1983-1991 Elementary School "Simion Barnutiu", Zalau (Romania)

Workshops:

16-28.09.2001 WE Heraeus-summer school for physics *"Organic surface and Interface – the interface to bioworld",* Chemnitz, Germany

22-26.04.2002 DIODE training workshop
"STM, AFM and Theoretical Simulations"
Madrid, Spain.

09-14.06.2003 DIODE training workshop
"Theoretical Summer School"
Paderborn, Germany.

27.09-08.10.2004 WE Heraeus-summer school for physics
"New materials for tomorrow and the day after tomorrow in experiments and simulations", Chemnitz, Germany

List of Publications

1. G.N. Gavrila, **M. Gorgoi**, T.U. Kampen, B. Tepper, W. Braun, D.R.T. Zahn: ***Electronic Properties and Chemistry of 3, 4, 9, 10-Perylenetetracarboxylic dianhydride (PTCDA) upon Mg Deposition,*** BESSY Jahresbericht 2003, 211.
2. **M. Gorgoi**, W. Michaelis, T.U. Kampen, D. Schlettwein, D.R.T. Zahn: ***Thickness dependence of the LUMO position for phthalocyanines on hydrogen passivated silicon (111),*** Applied Surface Science 234 (2004) 138–143.
3. **M. Gorgoi**, G.N. Gavrila, W. Braun, D.R.T. Zahn: ***Orientation of Perfluorinated Phthalocyanines: from Ultra-low Coverages on Hydrogen Passivated Silicon to Thick Layers,*** BESSY Jahresbericht 2004, 165.
4. G.N. Gavrila, **M. Gorgoi**, W. Braun, D.R.T. Zahn: ***Chemistry of Metal/Organic Interface Revealed by High Resolution Photoemission Spectroscopy,*** BESSY Jahresbericht 2004, 190.
5. **M. Gorgoi**, D.R.T. Zahn: ***"Band bending" in Copper Phthalocyanine on Hydrogen Passivated Si(111)*** Organic Electronics 6 (2005) 168-174.
6. P. Bressler, F. Schäfers, **M. Gorgoi**, W. Braun, M. Sperling, M. Mertin, G. Öhrwall, S. Svensson, W. Eberhardt, **HIKE experiment at KMC1: Progress and Proposed Experiments,** BESSY Jahresbericht 2005.
7. **M. Gorgoi,** D.R.T. Zahn, ***Charge Transfer at Silver/Phthalocyanines Interfaces***, proceedings to ICTF 13 / ACSIN 8 Sweden 2005, Applied Surface Science 252 (2006) 5453-5456.
8. **M. Gorgoi,** D.R.T. Zahn, ***Density of Occupied and Unoccupied States Monitored during Metal Deposition onto Phthalocyanine Layers*** proceedings to ICFSI-10 2005, Journal de Physique IV, 132 (2006) 337-340.
9. D.R.T. Zahn, **M. Gorgoi**, O. Gordan, ***Organic Layers on Silicon with Potential Application in Hybrid Solar Cells,*** proceedings to SREN 2005, Solar Energy Journal 80 (2006) 707-714.
10. W. Braun, G. Gavrila, **M. Gorgoi**, D.R.T. Zahn, ***Influence of the Molecular Structure on the Interface Formation between Magnesium and Organic Semiconductors*** Radiation Physics and Chemistry 75 (2006) 1869-1871.
11. D. R. T. Zahn, G. Gavrila, **M. Gorgoi**, ***The Transport Gap of Organic Semiconductors Studied Using the Combination of Direct and Inverse Photoemission*** Chemical Physics 325 (2006) 99-112.

Acknowledgements

First of all I would like to thank Prof. D. R. T. Zahn for the supervision of my work and for giving me the opportunity to join the Semiconductor Physics Group in Chemnitz. I also thank Dr. T. U. Kampen for fruitful discussions and for introducing me to the UHV technique. My special thanks go to Mr. Axel Fechner for his guidance and help in testing and developing the IPES technique. Without his support this work would not have been possible.

I would like to thank Prof. Michael Hietschold and Prof. Derck Schlettwein for correcting and refereeing my thesis.

I am grateful to Mrs. Sybille Raschke and to Mrs. Kornelia Dostmann for their help in the administrative problems.

I express my gratitude to Dr. H. Kupfer for the AFM measurements, Mike Sperling for his unconditional help and to Dr. Walter Braun for the good collaboration during the BESSY beamtimes. I thank Simona and Ovidiu for the ellipsometry measurements.

I would like to show my appreciation to all the people involved in the DIODE network for the experience exchange via meetings and workshops.

My special thanks go to Giani and Simo for being true friends and always being there for me. Thank you!

I would like to thank to all the former and present colleagues: Andreea, Andrei, Arindam, Beynor, Cami, Daniel, Dirk, Geta, Giang, Hendrik, Henry, Ilja, Lica, Lori, Marion, Michal, Matthias, Miruna, Ovidiu, Reinhard, Robi, Sascha, Sandrine, Sungook, Stefan, Steve, Tomas, Yu for the nice moments spent together. Henry, thank you for the salsa lessons and the fun we had dancing.

The financial support provided by the EU funded Human Potential Research Training Network DIODE (Contract No.: HPRN-CT-1999-00164) is gratefully acknowledged.

Last but not least, I would like to express my love to my mother who is an infinite source of energy, wisdom and motivation.

Erratum

The following part contains corrections to the present work concerning an error that occurred in the deconvolution software used in the evaluation of the IPES spectra. The code error was found after the defence took place. The error generated a wrong estimate of the LUMO cut-off and thus the derived electronic parameters i.e. the band gap E_t and EA based on these values required corrections.

List of Changes:

Figure 3.7 Chapter 3. Techniques of Investigations, Subchapter 3.3 VB-PES and IPES Spectra Evaluation at page 28 should be displayed as:

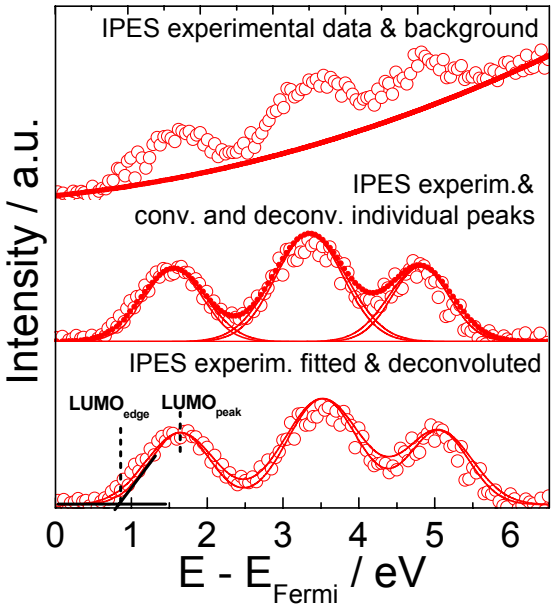

Figure 13.1 The IPES spectrum of CuPc thin film together with convoluted and deconvoluted individual peaks that contribute to the overall intensity.

Figure 5.1 a) b) Chapter 5. Electronic properties of Pc/H-Si System, Subchapter 5.1 H_2Pc at page 43 should be displayed as:

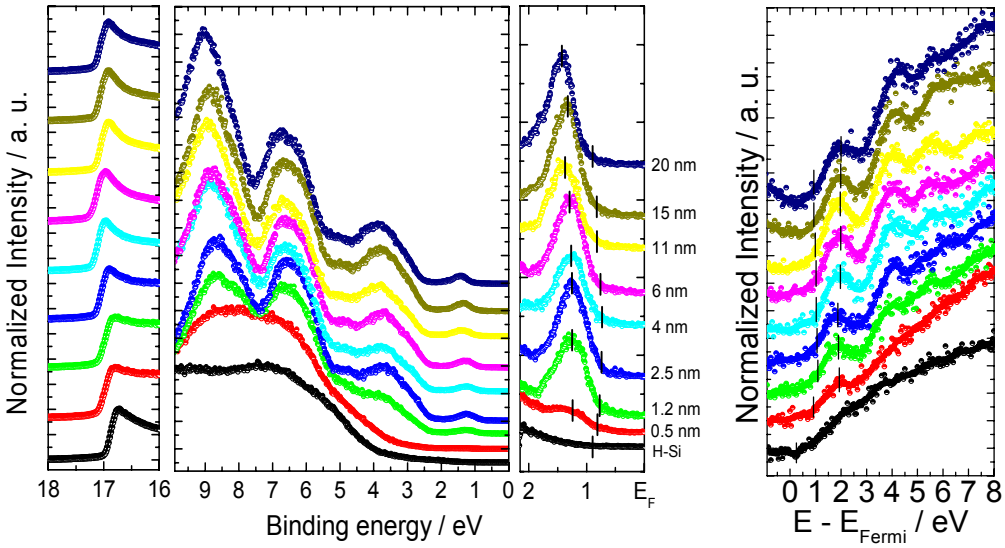

Figure 13.2 a) VB-PES thickness dependent measurements on H_2Pc/H-Si(111); b) IPES thickness dependent measurements on H_2Pc/H-Si(111).

where the cut-off positions in the IPES are closer to the Fermi level.

Figure 5.2 Chapter 5. Electronic properties of Pc/H-Si System, Subchapter 5.1 H_2Pc at page 44 should be displayed as:

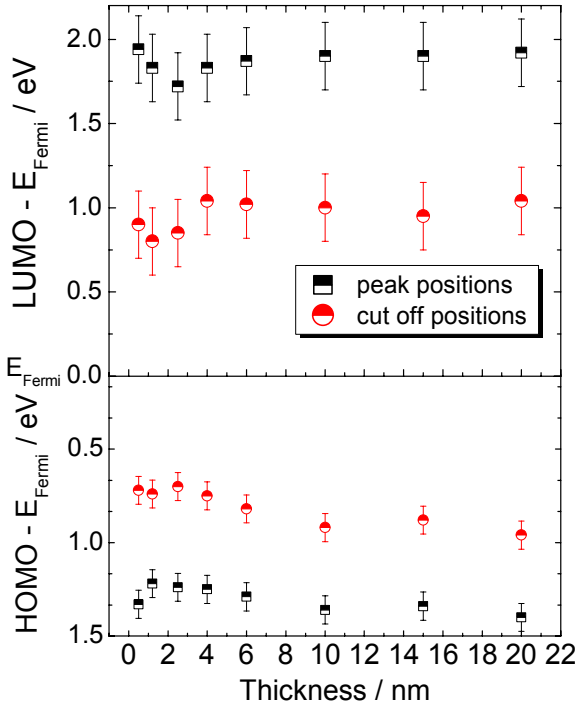

Figure 13.3 Peak and cut-off positions of HOMO and LUMO as a function of H_2Pc layer thickness.

The following paragraph on page 45: "*At thicknesses above 6 nm, the transport gap determined as the difference between the onset positions of HOMO and LUMO is found to be (2.2 ± 0.2) eV.*" should be read as:

"*At thicknesses above 6 nm, the transport gap determined as the difference between the onset positions of HOMO and LUMO is found to be (1.9 ± 0.2) eV.*"

Figure 5.3 Chapter 5. Electronic properties of Pc/H-Si System, Subchapter 5.1 H_2Pc at page 45 should be displayed as:

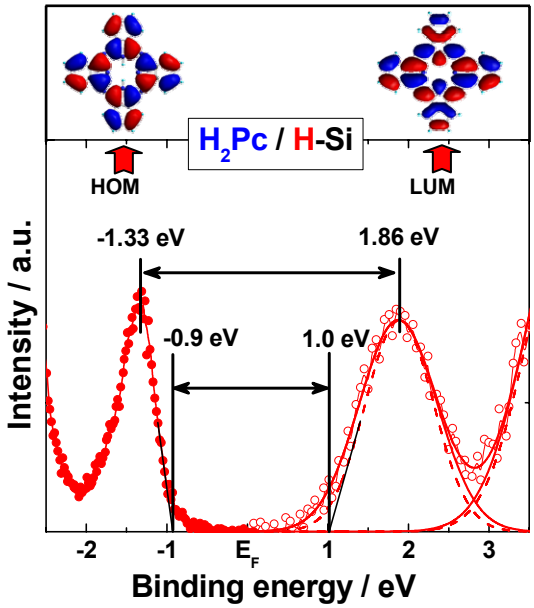

Figure 13.4 E_t determination for H_2Pc.

Figure 5.4 b) Chapter 5. Electronic properties of Pc/H-Si System, Subchapter 5.1 H_2Pc at page 46 should be displayed as:

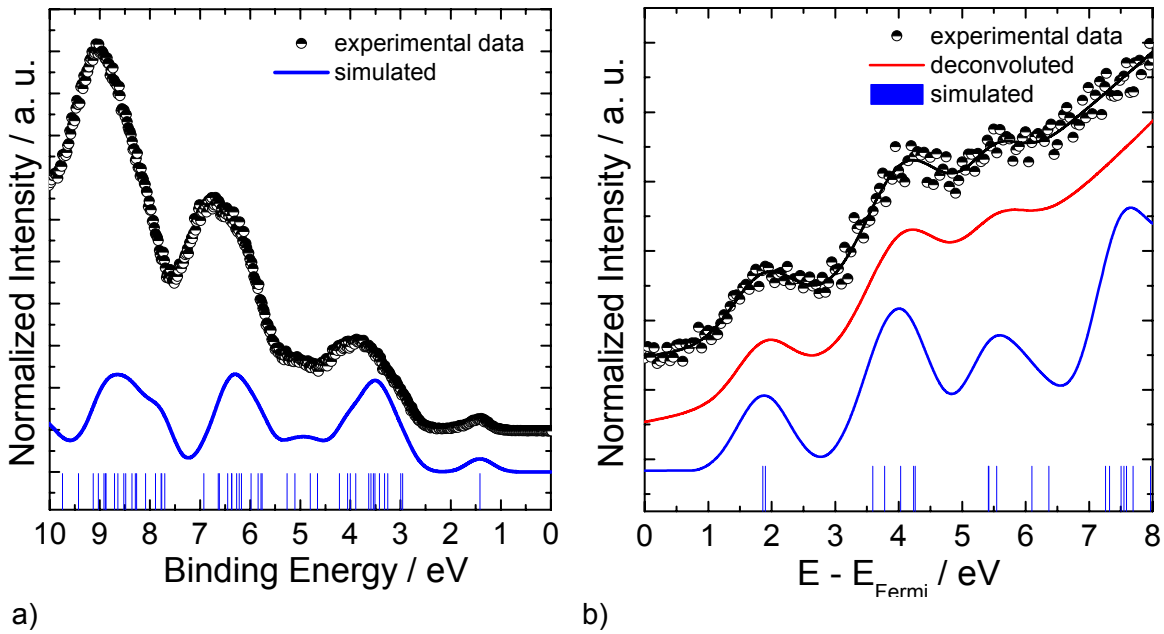

Figure 13.5 a) Experimental and simulated VB-PES spectra of H_2Pc; b) Experimental and simulated IPES spectra of H_2Pc. The vertical lines in figures a) and b) mark the energy positions of the calculated MO.

The following phrase at page 46:"*The FWHM of the deconvoluted LUMO (0.63 eV) was taken into account for the simulation of the calculated MO.*" should be read as: "*The FWHM of the deconvoluted LUMO (0.84 eV) was taken into account for the simulation of the calculated MO.*"

Figure 5.5 a) and b) Chapter 5. Electronic properties of Pc/H-Si System, Subchapter 5.1 H_2Pc at page 47 should be displayed as:

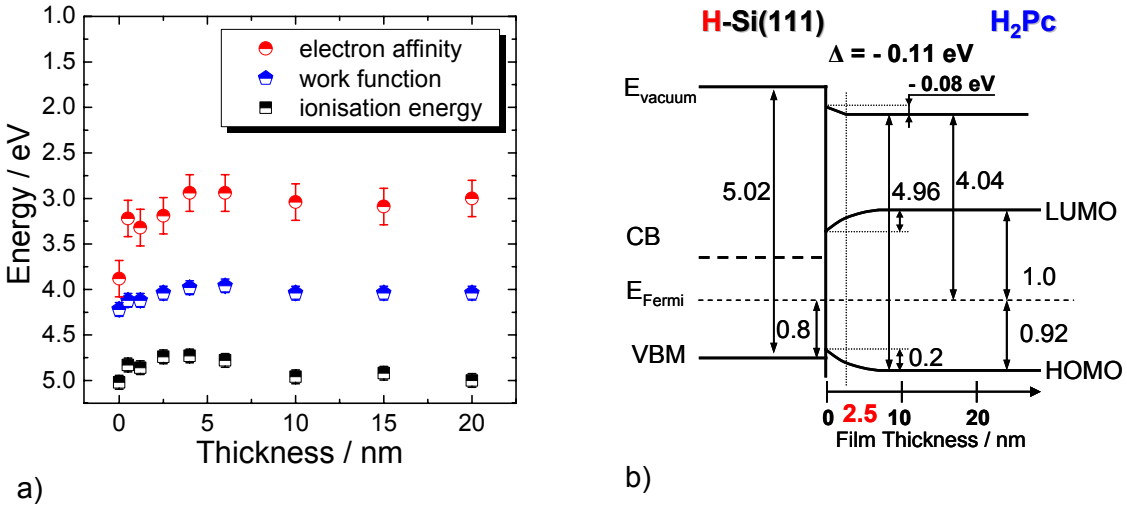

Figure 13.6 a) EA, ϕ, IE as a function of H_2Pc layer thickness; b) Energy band diagram of the H_2Pc/H-Si interface. The surface band bending of the substrate was omitted.

The following phrase at page 47: *"From that thickness on, EA is constant at (2.74±0.2) eV."* should be read as: "*From that thickness on, EA is constant at (3.0±0.2) eV."*

The following phrase at page 48: "*The barrier heights for electrons and for holes at the interface can be estimated to be 0.78 eV and 0.08 eV, respectively*." should be read as: "*The barrier heights for electrons and for holes at the interface can be estimated to be 0.38 eV and 0.08 eV, respectively*."

Figure 5.6 b) Chapter 5. Electronic properties of Pc/H-Si System, Subchapter 5.2 CuPc/H-Si at page 49 should be displayed as:

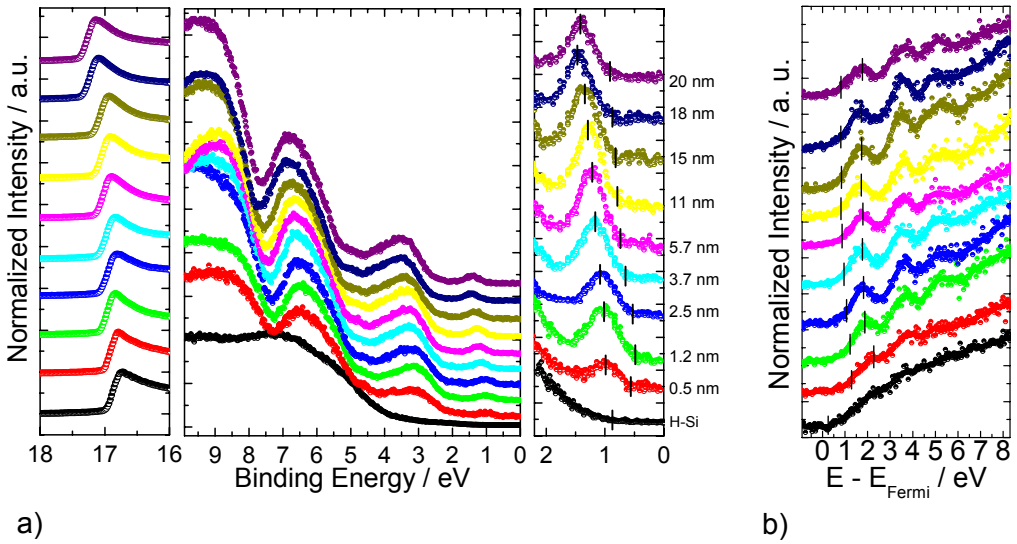

Figure 13.7 a) VB-PES thickness dependent measurements on CuPc/H-Si(111); b) IPES thickness dependent measurements on CuPc/H-Si(111).

The following phrase at page 50:" *The transport gap determined as the difference between the onset positions of LUMO and HOMO is found to be approximately (2.2 ± 0.2) eV (Figure 5.8). This value is in rather good agreement with the one determined by Hill et al. [Hil00] using UPS-IPES (2.3 ± 0.4) eV, but somewhat larger than the one determined by cyclic voltammetry [Sim85] (1.71 ÷ 1.84 eV).*" should be read as: "*The transport gap determined as the difference between the onset positions of LUMO and HOMO is found to be approximately (1.8 ± 0.2) eV (Figure 5.8). This value is somewhat smaller than the one determined by Hill et al. [Hil00] using UPS-IPES (2.3 ± 0.4) eV, but in rather good agreement with the one determined by cyclic voltammetry [Sim85] (1.71 ÷ 1.84 eV).*"

Figure 5.7 Chapter 5. Electronic properties of Pc/H-Si System, Subchapter 5.2 CuPc/H-Si at page 50 should be displayed as:

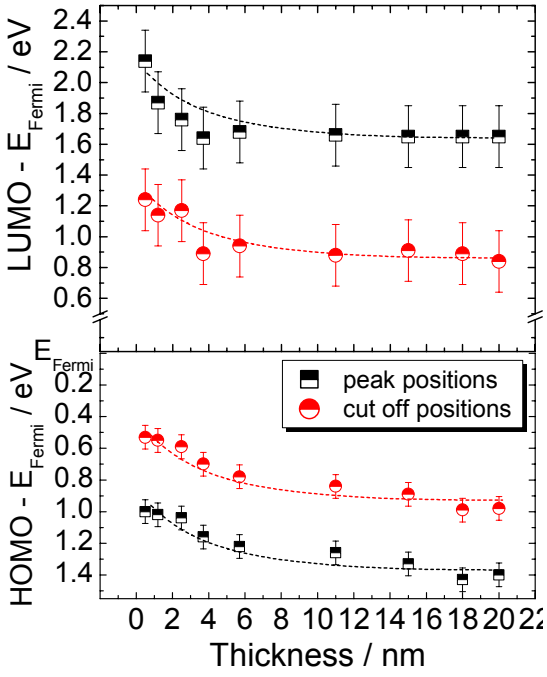

Figure 13.8 Peak and cut-off positions of HOMO and LUMO as a function of H_2Pc layer thickness.

Figure 5.8 Chapter 5. Electronic properties of Pc/H-Si System, Subchapter 5.2 CuPc/H-Si at page 50 should be displayed as:

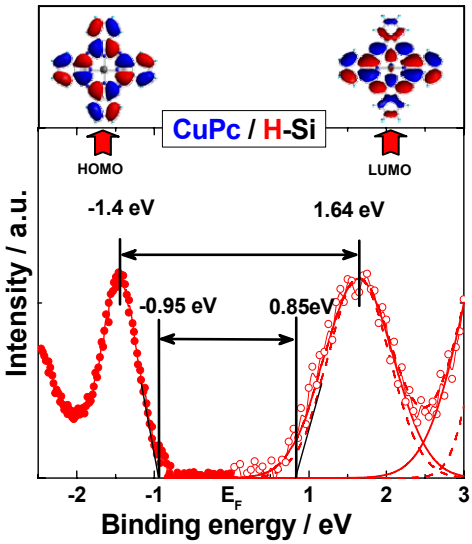

Figure 13.9 E_t determination for CuPc.

The following phrase at page 51: "*The computer-generated VB-PES and IPES spectra employed Gaussian functions with FWHM of 0.45 eV.*" should be read as: *"The computer-generated VB-PES and IPES spectra employed Gaussian functions with FWHM of 0.45 eV and 0.8 eV respectivey."*

Figure 5.9 b) Chapter 5. Electronic properties of Pc/H-Si System, Subchapter 5.2 CuPc/H-Si at page 51 should be displayed as:

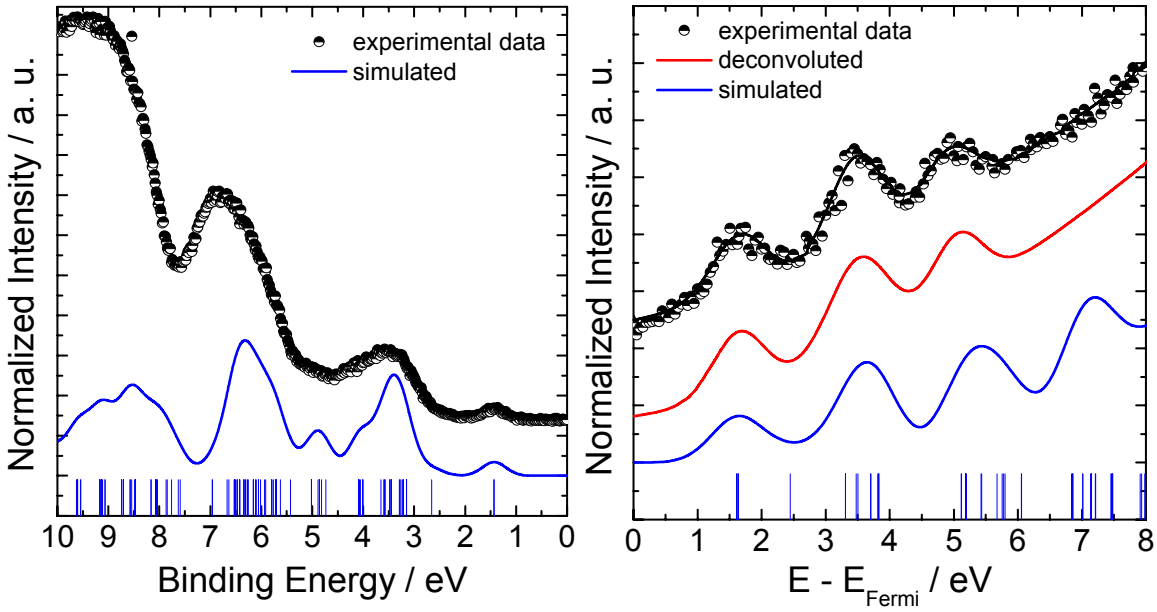

Figure 13.10 a) Experimental and simulated VB-PES spectra of CuPc; b) Experimental and simulated IPES spectra of CuPc. The vertical lines in figures a) and b) mark the energy positions of the calculated MO.

Figure 5.10 a) and b) Chapter 5. Electronic properties of Pc/H-Si System, Subchapter 5.2 CuPc/H-Si at page 52 should be displayed as:

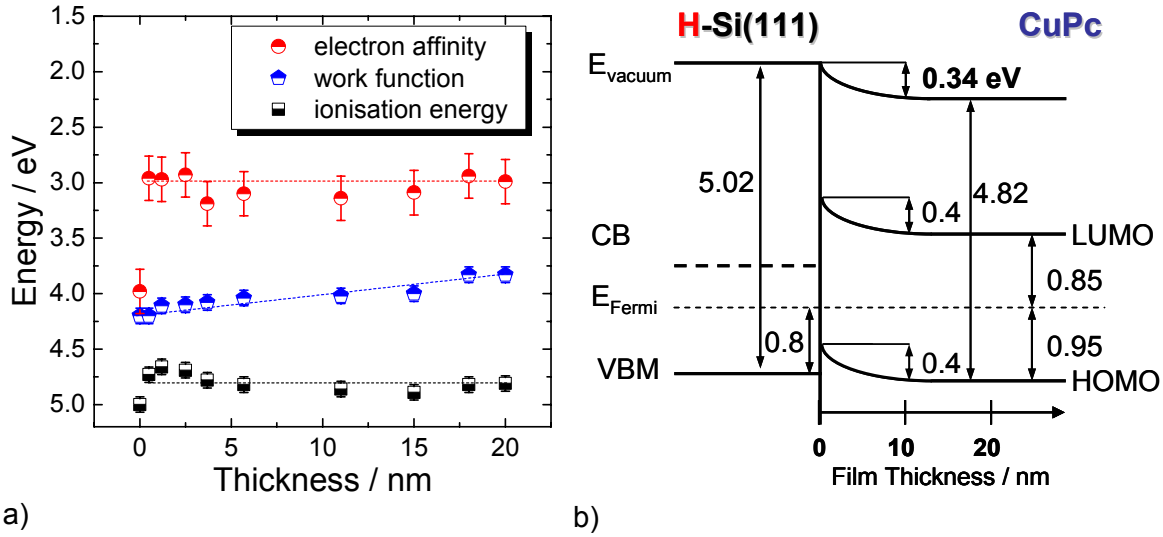

Figure 13.11 a) EA, ϕ, IE as a function of CuPc layer thickness; b) Energy band diagram of the CuPc/H-Si interface. The surface band bending of the substrate was omitted.

The following phrases at page 52-53:"*The determined values for thick CuPc layer (20 nm) are: IE=(4.82±0.07) eV, Φ=(3.88±0.07) eV and EA=(2.66±0.2) eV.[…] The determined interface barriers for electrons and for holes are 1.3 eV and 0.26 eV respectively.*" should be read as: *"The*

determined values for thick CuPc layer (20 nm) are: IE=(4.82±0.07) eV, Φ=(3.88±0.07) eV and EA=(3.0±0.2) eV.[…] The determined interface barriers for electrons and for holes are 0.93 eV and 0.26 eV respectively."

Figure 5.14 b) Chapter 5. Electronic properties of Pc/H-Si System, Subchapter 5.3 F_4CuPc/H-Si at page 57 should be displayed as:

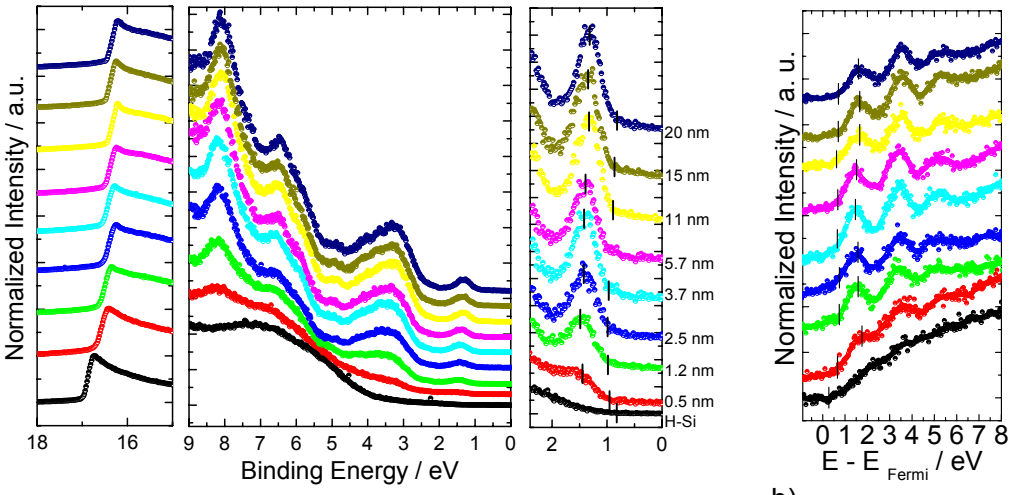

a) b)

Figure 13.12 a) VB-PES thickness dependent measurements on F_4CuPc/H-Si(111); b) IPES thickness dependent measurements on F_4CuPc/H-Si(111).

Figure 5.16 Chapter 5. Electronic properties of Pc/H-Si System, Subchapter 5.3 F_4CuPc/H-Si at page 59 should be displayed as:

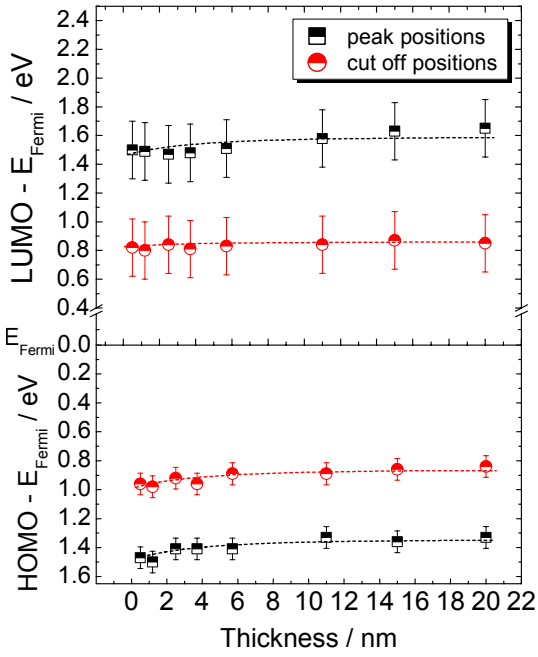

Figure 13.13 Peak and cut-off positions of HOMO and LUMO as a function of F_4CuPc layer thickness.

The following phrase at page 59: "*The transport gap estimated from the HOMO and deconvoluted LUMO onsets (see subchapter 3.3) has a value of (1.95 ± 0.2) eV.*" should be read as: "*The transport gap estimated from the HOMO and deconvoluted LUMO onsets (see subchapter 3.3) has a value of (1.85 ± 0.2) eV.*"

The following phrase at page 59: "*The Gaussian functions used in the convolution of the calculated energy levels have FWHM of 0.46 eV and 0.44 eV for the VB-PES and IPES simulations, respectively.*" should be read as: "*The Gaussian functions used in the*

convolution of the calculated energy levels have FWHM of 0.46 eV and 0.60 eV for the VB-PES and IPES simulations, respectively."

Figure 5.17 Chapter 5. Electronic properties of Pc/H-Si System, Subchapter 5.3 F_4CuPc/H-Si at page 60 should be displayed as:

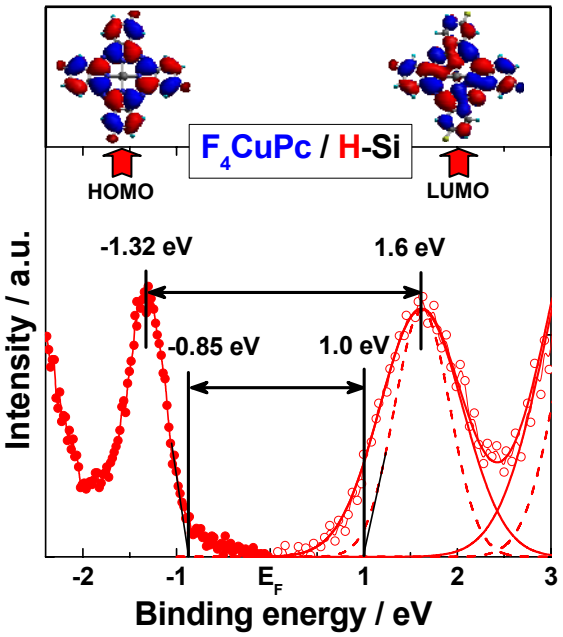

Figure 13.14 E_t determination for F_4CuPc.

Figure 5.18 b) Chapter 5. Electronic properties of Pc/H-Si System, Subchapter 5.3 F_4CuPc/H-Si at page 60 should be displayed as:

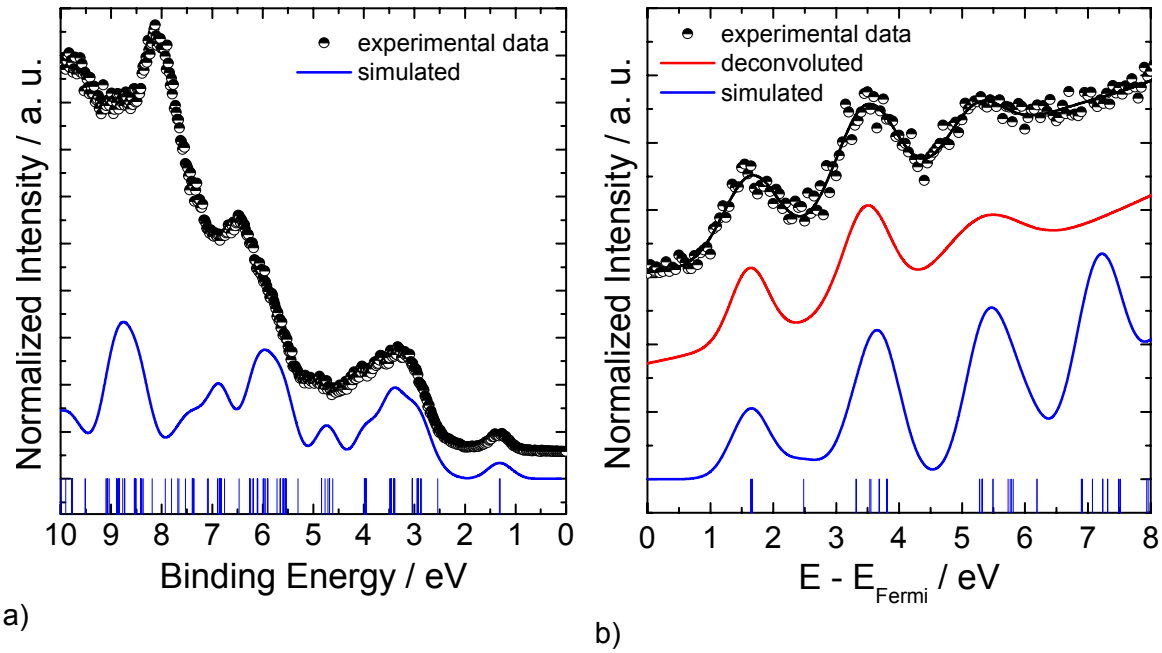

Figure 13.15 a) Experimental and simulated VB-PES spectra of F_4CuPc; b) Experimental and simulated IPES spectra of F_4CuPc. The vertical lines in figures a) and b) mark the energy positions of the calculated MO.

The following phrase at page 61: "*For the next thicknesses up to 3.7nm of F_4CuPc, EA increases slightly until it reaches saturation at a value of (3.65±0.2) eV*." should be read as: "*For*

the next thicknesses up to 3.7 nm of F_4CuPc, EA increases slightly until it reaches saturation at a value of (3.7±0.2) eV."

Figure 5.19 a) b) Chapter 5. Electronic properties of Pc/H-Si System, Subchapter 5.3 F_4CuPc/H-Si at page 61 should be displayed as:

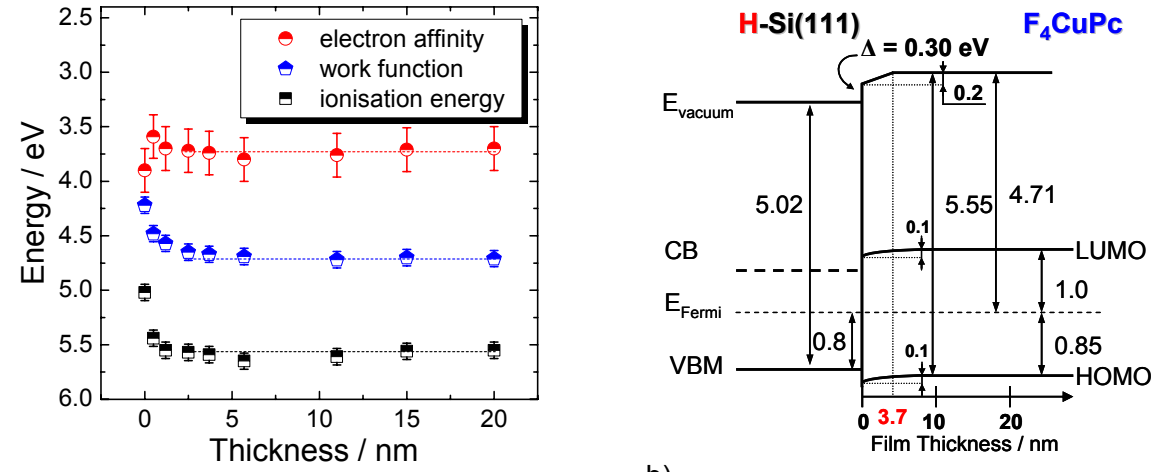

a) b)

Figure 13.16 a) EA, ϕ, IE as a function of F_4CuPc layer thickness; b) Energy band diagram of the F_4CuPc/H-Si interface. The surface band bending of the substrate was omitted.

The following phrase at page 61: "*At this point we can estimate the total barrier for electrons at the interface as being 0.78 eV.*" should be read as: "*At this point we can estimate the total barrier for electrons at the interface as being 0.58 eV.*"

Figure 5.20 Chapter 5. Electronic properties of Pc/H-Si System, Subchapter 5.3 F_4CuPc/H-Si at page 62 should be displayed as:

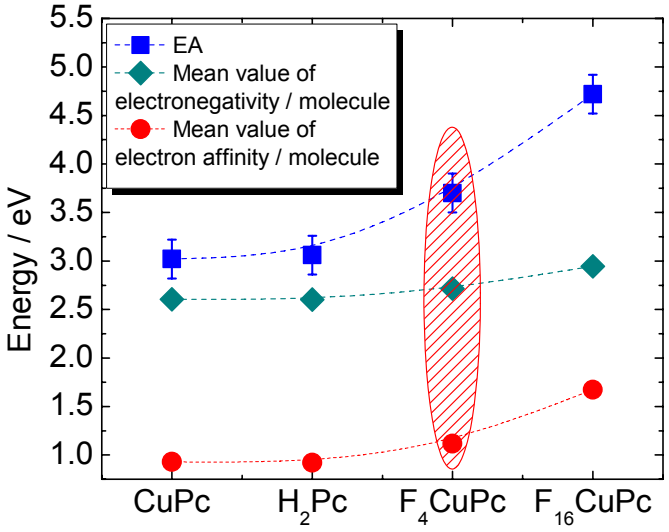

Figure 13.17 Comparison of the experimentally determined EA and the calculated mean values of electronegativity and electron affinity / molecule.

Figure 5.24 b) Chapter 5. Electronic properties of Pc/H-Si System, Subchapter 5.4 F_{16}CuPc/H-Si at page 66 should be displayed as:

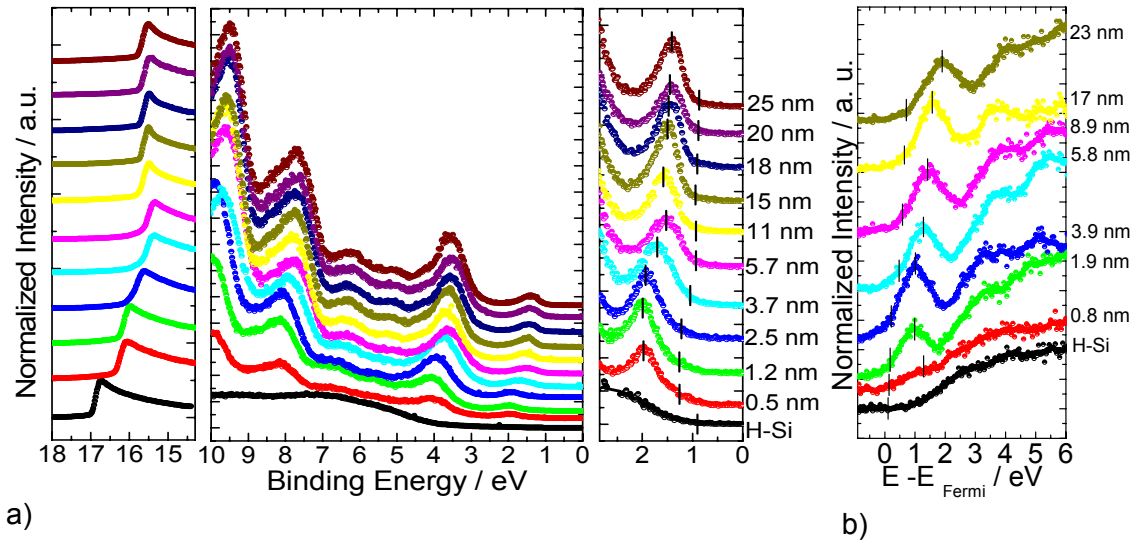

Figure 13.18 a) VB-PES thickness dependent measurements on F_{16}CuPc/H-Si(111); b) IPES thickness dependent measurements on F_{16}CuPc/H-Si(111).

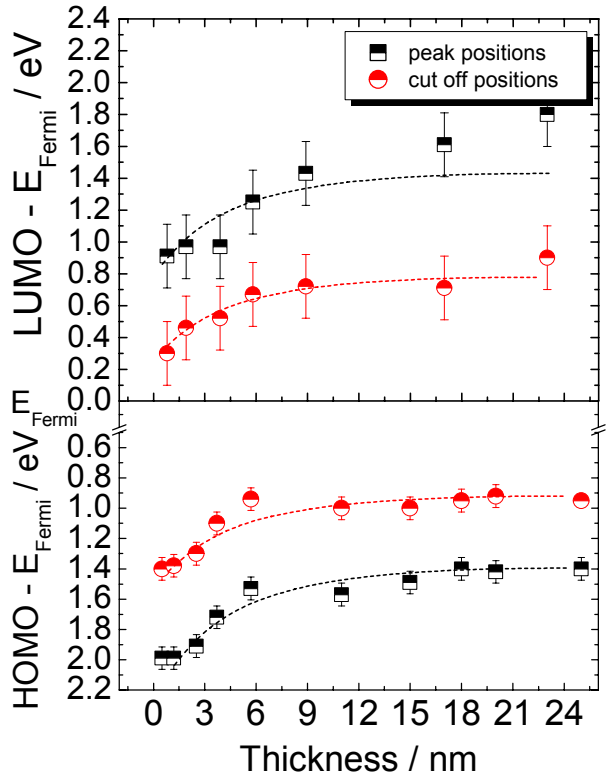

Figure 13.19 Peak and cut-off positions of HOMO and LUMO as a function of F_{16}CuPc film thickness.

Figure 5.25 Chapter 5. Electronic properties of Pc/H-Si System, Subchapter 5.4 F_{16}CuPc/H-Si at page 67 should be displayed as:

The following phrase at page 67: "*The transport gap remains approximately constant within the experimental error at a value of (1.8±0.2) eV.*" should be read as: "*The transport gap remains approximately constant within the experimental error at a value of (1.6±0.2) eV.*"

Figure 5.26 Chapter 5. Electronic properties of Pc/H-Si System, Subchapter 5.4 F_{16}CuPc/H-Si at page 68 should be displayed as:

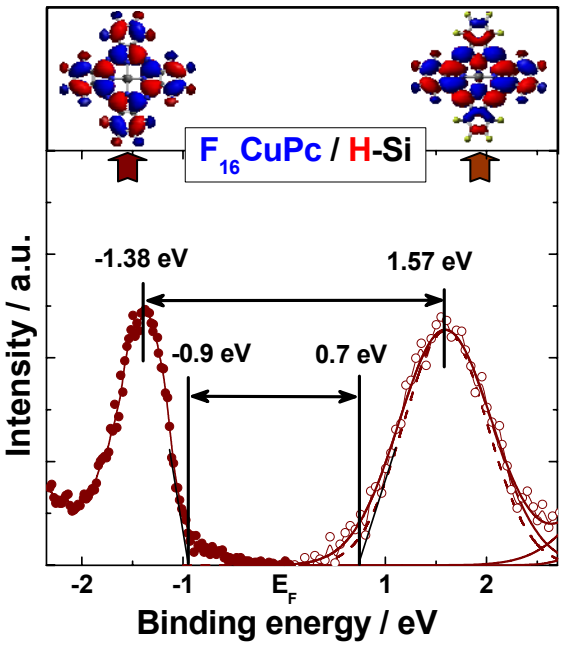

Figure 13.20 E_t determination for F_{16}CuPc.

The following phrase at page 69: "*The VB-PES and IPES simulated spectra employed Gaussian functions with FWHM of 0.51 eV and 0.52 eV as resulted from the fits (see description for the other molecules).*" should be read as: "*The VB-PES and IPES simulated spectra employed Gaussian functions with FWHM of 0.51 eV and 0.82 eV as resulted from the fits (see description for the other molecules).*"

Figure 5.27 b) Chapter 5. Electronic properties of Pc/H-Si System, Subchapter 5.4 F_{16}CuPc/H-Si at page 69 should be displayed as:

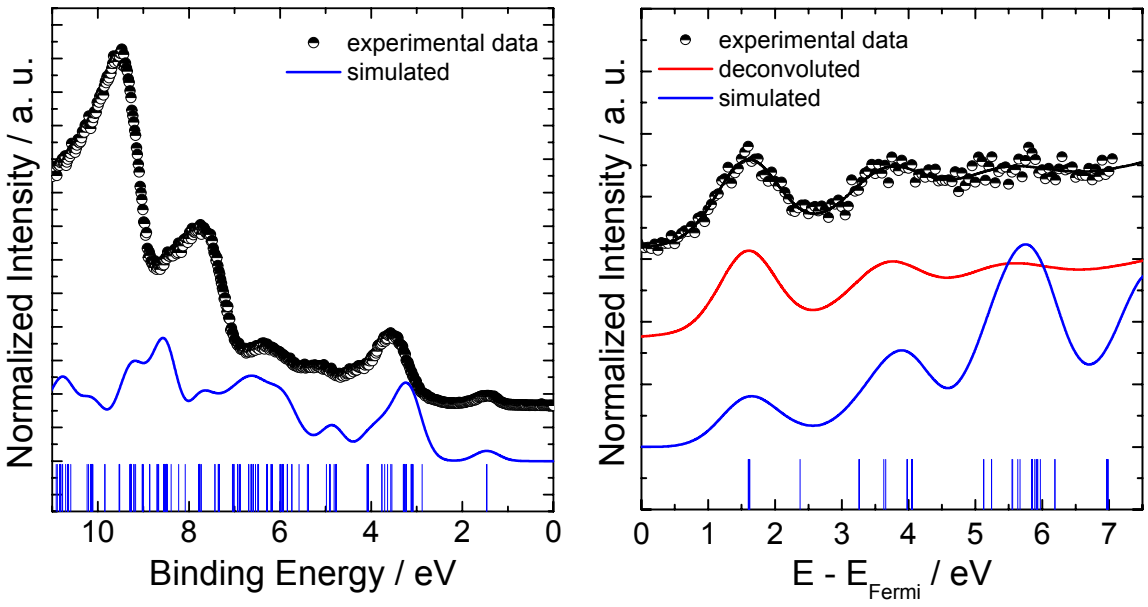

a) b)

Figure 13.21 a) Experimental and simulated VB-PES spectra of F_{16}CuPc; b) Experimental and simulated IPES spectra of F_{16}CuPc. The vertical lines in figures a) and b) mark the energy positions of the calculated MO.

The following phrase at page 69: "*The difference between the EA value of the first layer of F_{16}CuPc and the one corresponding to H-Si amounts to 0.46 eV. As the thickness increases, EA*

increases further. The thickness range of the increase extends to 3.7 nm of F_{16}CuPc. Above this thickness EA becomes approximately constant to a value of (4.52 ± 0.2) eV which corresponds to the organic material. Judging from the energy band diagram shown in Figure 5.29 (b), the EA includes both the large interface dipole and the 0.6 eV shift of LUMO. The total barrier height for electrons amounts to 0.02 eV." should be read as: "*The difference between the EA value of the first layer of F_{16}CuPc and the one corresponding to H-Si amounts to 0.85 eV. As the thickness increases, EA increases further. The thickness range of the increase extends to 3.7 nm of F_{16}CuPc. Above this thickness EA becomes approximately constant to a value of (4.72 ± 0.2) eV which corresponds to the organic material. Judging from the energy band diagram shown in Figure 5.28 (b), the EA includes both the large interface dipole and the 0.6 eV shift of LUMO. The total barrier height for electrons amounts to 0.22 eV.*"

Figure 5.28 a) and b) Chapter 5. Electronic properties of Pc/H-Si System, Subchapter 5.4 F_{16}CuPc/H-Si at page 70 should be displayed as:

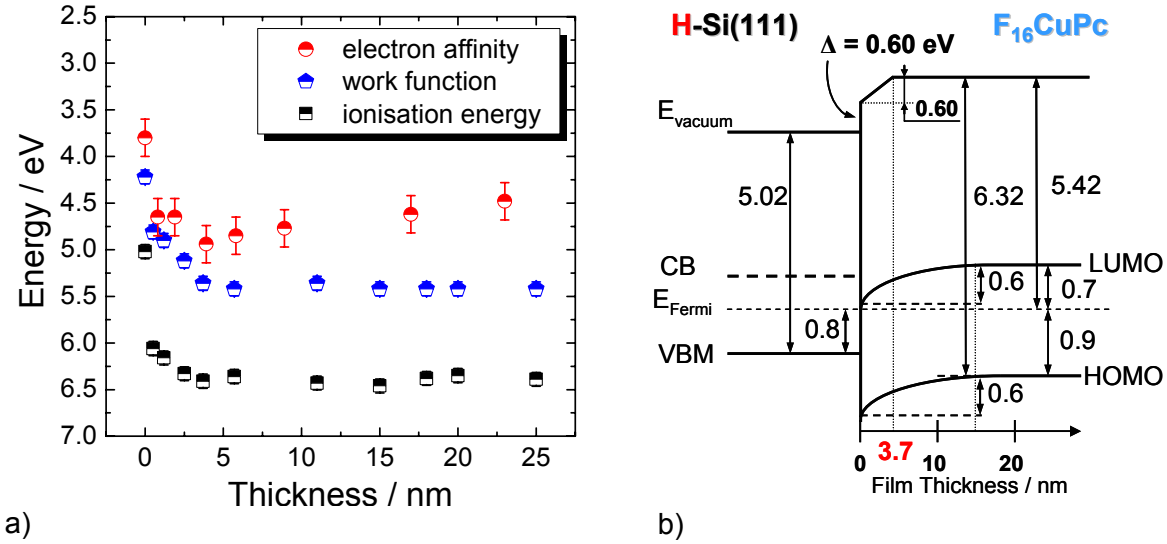

Figure 13.22 a) EA, ϕ, IE as a function of F_{16}CuPc layer thickness; b) Energy band diagram of the F_{16}CuPc/H-Si interface. The surface band bending of the substrate was omitted.

Table 5.4 Chapter 5. Electronic properties of Pc/H-Si System, Subchapter 5.5 The Influence of the Fluorine Atoms at page 74 should be displayed containg these values:

	Φ / eV	**IE / eV**	**EA / eV**
H_2Pc	(4.04 ± 0.07)	(4.96 ± 0.07)	(3.06 ± 0.2)
CuPc	(3.87 ± 0.07)	(4.82 ± 0.07)	(3.02 ± 0.2)
F_4CuPc	(4.71 ± 0.07)	(5.55 ± 0.07)	(3.70 ± 0.2)
F_{16}CuPc	(5.42 ± 0.07)	(6.32 ± 0.07)	(4.72 ± 0.2)

Table 13.1 Electronic properties of Pcs.

Figure 5.32 Chapter 5. Electronic properties of Pc/H-Si System, Subchapter 5.5 The Influence of the Fluorine Atoms at page 74 should be displayed as:

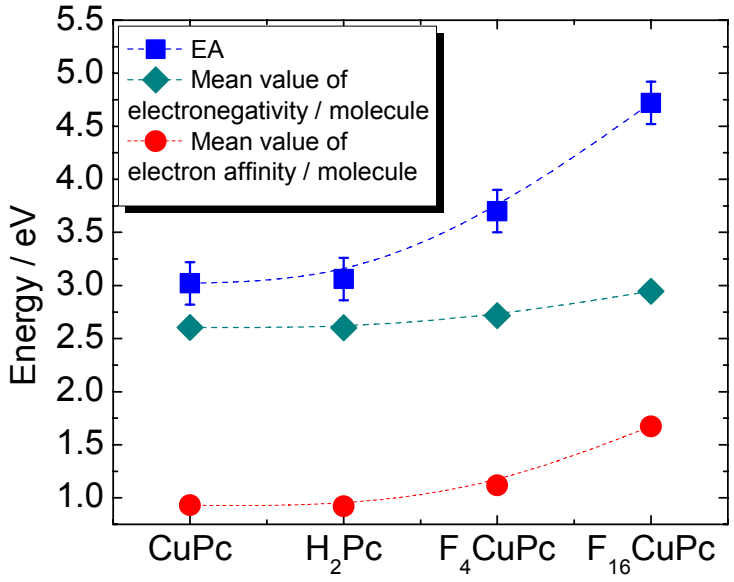

Figure 13.23 Comparison of the experimental determined EA and the calculated values of electron affinity and electronegativity of each molecule. The electron affinity calculus was performed by averaging the known atomic values and the electronegativity calculus by geometric mean of the atomic values.

Table 5.5 Chapter 5. Electronic properties of Pc/H-Si System, Subchapter 5.5 The Influence of the Fluorine Atoms at page 76 should be displayed containg these values:

	E_t / eV	E_{opt} / eV	E_{calc} / eV	$E_{peak\text{-}to\text{-}peak}$ / eV
H_2Pc	(1.9 ± 0.2)	1.75	2.14	(3.2 ± 0.2)
CuPc	(1.8 ± 0.2)	1.76	2.18	(3.04 ± 0.2)
F_4CuPc	(1.85 ± 0.2)	1.76	2.19	(2.92 ± 0.2)
$F_{16}CuPc$	(1.6 ± 0.2)	1.60	2.07	(2.95 ± 0.2)

Table 13.2. Transport gaps, optical gaps, DFT estimated gaps and peak-to-peak VB-PES and IPES estimated gap of phthalocyanines.

The following phrase at page 77: "*The slopes of the linear fits are 0.78, 1 and 1.03, respectively*." should be read as: "*The slopes of the linear fits are 0.87, 1 and 1.03, respectively.*"

Figure 5.36 Chapter 5. Electronic properties of Pc/H-Si System, Subchapter 5.5 The Influence of the Fluorine Atoms at page 78 should be displayed as:

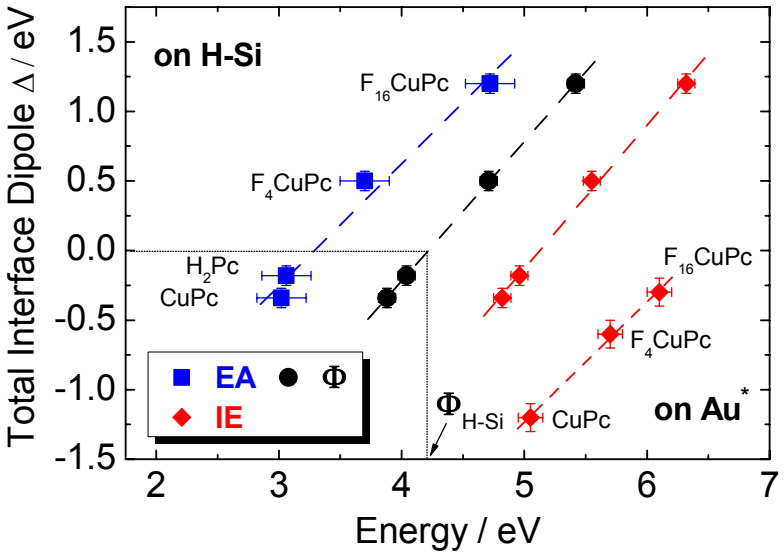

Figure 13.36 Total interface dipoles formed at Pcs/H-Si interfaces as a function of EA, ϕ and IE of the Pcs. Where the total interface dipole is 0, Φ has a value of 4.22 eV which corresponds to H-Si. The data points for Pcs/Au are taken from ref. [Pei02-2].

Figure 5.37 Chapter 5. Electronic properties of Pc/H-Si System, Subchapter 5.5 The Influence of the Fluorine Atoms at page 78 should be displayed as:

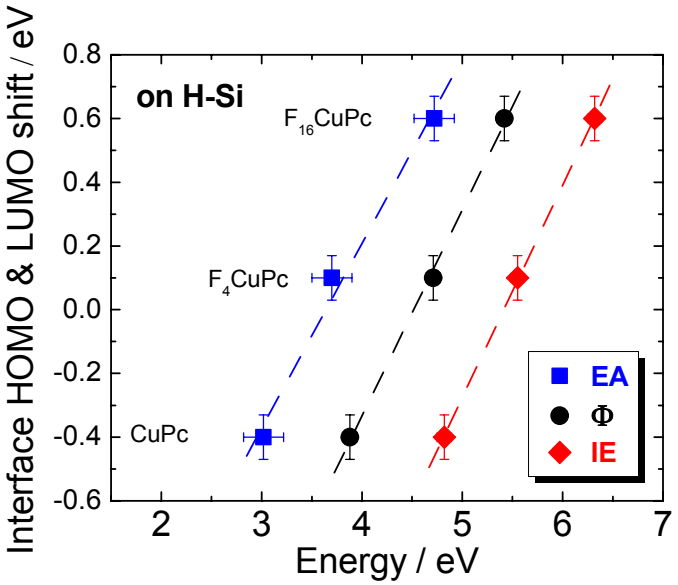

Figure 13.24 The HOMO and LUMO parallel shifts formed at Pcs/H-Si interfaces as a function of EA, ϕ and IE of the Pcs. These continuous shifts are the ones attributed to the band bending-like behaviour.

The following phrase at page 78: "*The slopes of the linear fits of the experimental points are 0.51 for EA, 0.64 for ϕ and 0.66 for IE.*" should be read as:"*The slopes of the linear fits of the experimental points are 0.58 for EA, 0.64 for ϕ and 0.66 for IE.*"

The following phrase at page 85:"*It is quite surprising in view of the fact that that the electron affinity of Ag atom is quite low (1.3 eV) compared to the EA of H_2Pc (2.74±0.2) eV.*" should be read as: "*It is quite surprising in view of the fact that that the electron affinity of Ag atom is quite low (1.3 eV) compared to the EA of H_2Pc (3.06±0.2) eV.*"

Figures 6.5 b), 6.9 b), 6.13 b) and 6.17 b) Chapter 6. Chemical stability of Pcs, pages 85, 88, 92 and 95 should be displayed as:

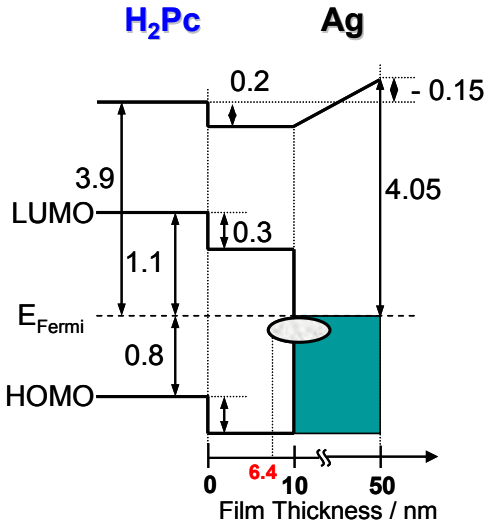

Figure 13.25 b) energy band diagram of the Ag/H_2Pc interface.

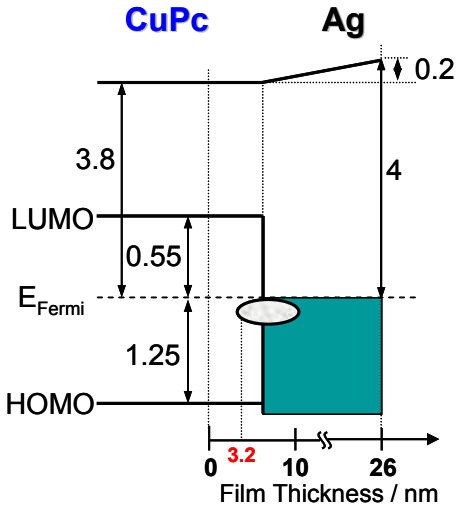

Figure 13.26 b) energy band diagram of the Ag/CuPc interface.

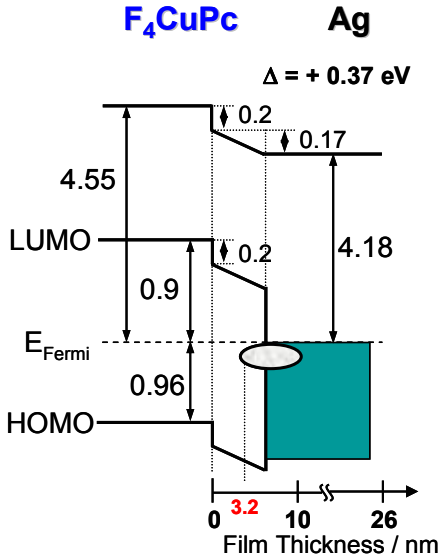

Figure 13.27 b) energy band diagram of the Ag/F_4CuPc interface.

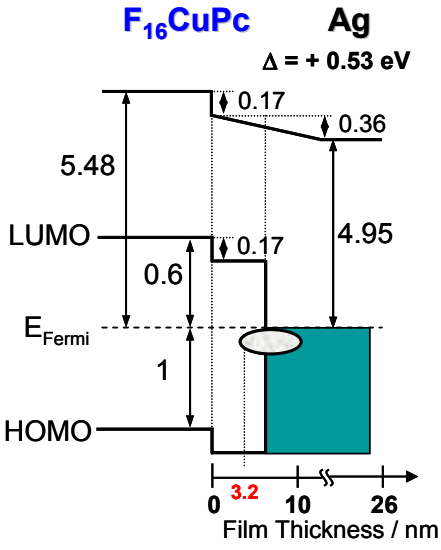

Figure 13.28 b) energy band diagram of the Ag/F_{16}CuPc interface.

The following phrase at page 97: "*The slopes of the linear functions used to fit the experimental data of interface dipoles as a function of EA, ϕ and IE are 0.38, 0.49, and 0.49, respectively.*" should be read as: "*The slopes of the linear functions used to fit the experimental data of interface dipoles as a function of EA, ϕ and IE are 0.41, 0.49, and 0.49, respectively.*"

Figure 6.21 Chapter 6. Chemical stability of Pcs, Subchapter 6.1.5 The Influence of the Fluorine Atoms at page 98 should be displayed as:

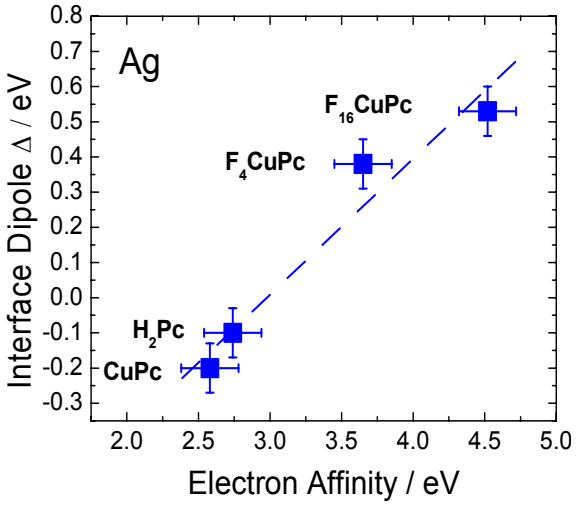

Figure 13.29 Interface dipoles formed at Ag/Pcs interfaces a) as a function of EA of the Pcs.

Figure 6.26 a) and b) Chapter 6. Chemical stability of Pcs, Subchapter 6.2 Oxygen Exposed Phthalocyanines page 101 should be displayed as:

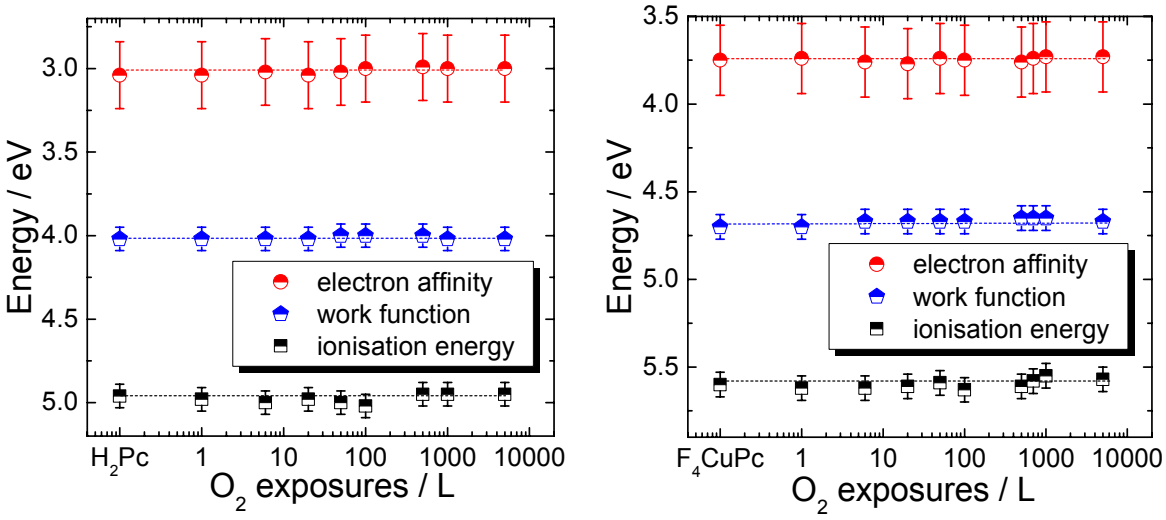

a) b)

Figure 13.30 a) H_2Pc and b) F_4CuPc EA, ϕ and IE of the surface as a function of the oxygen exposures.

Figure 6.29 a) and b) Chapter 6. Chemical stability of Pcs, Subchapter 6.2 Oxygen Exposed Phthalocyanines page 102 should be displayed as:

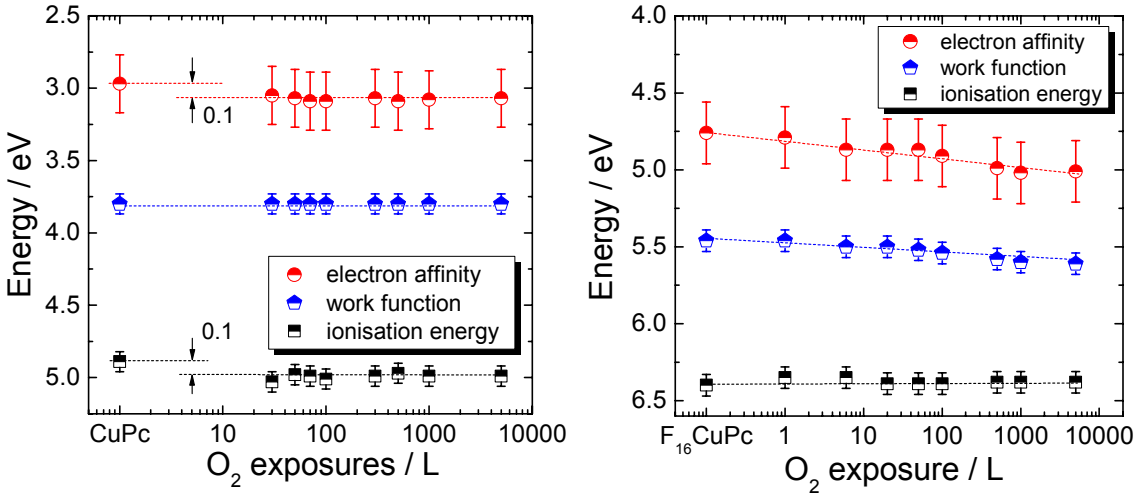

Figure 13.31 a) CuPc and b) F_{16}CuPc EA, ϕ and IE of the surface as a function of the oxygen exposures.